Numerical Study of Coronal Mass Ejections, Shocks, and Turbulence: from Chromosphere to 1 AU

by

Meng Jin

A dissertation submitted in partial fulfillment
of the requirements for the degree of
Doctor of Philosophy
(Space and Planetary Physics & Scientific Computing)
in The University of Michigan
2014

Doctoral Committee:

Professor Tamas I. Gombosi, Co-Chair
Research Associate Professor Ward B. Manchester IV, Co-Chair
Associate Research Scientist Bartholomeus van der Holst
Associate Research Scientist Richard A. Frazin
Associate Professor Justin C. Kasper
Professor Kenneth G. Powell

To my family,

and in memory of my grandmother,

Guihua Zhang (1931-2007)

ACKNOWLEDGEMENTS

After I started writing this part of the thesis, I immediately realized that it will be the easiest and hardest part of my thesis. It is easy because my graduate life here is grateful and I have a lot to say about the great people I met and extraordinary education I received in the last five years. At the same time, I realized that this dissertation would not be possible without the help and support of a great number of people. It is very hard to list them all. Therefore, I would like to express my sincerest gratitude to all the people that helped and supported me during my graduate life at the beginning of this acknowledgement. You all have my thanks even if I cannot list you here.

I would like to express my special thanks to my advisors: Professor Chip Manchester and Professor Tamas Gombosi. I am grateful to Professor Manchester for his invaluable guidance and consistent encouragement throughout my graduate life. His insight and knowledge of solar physics always enlighten me and help me through when I met difficulties in the research. I also want to thank him for his patience on my grammar mistakes and his tremendous help on all of my papers/proposals that dramatically improved their quality. Professor Gombosi guided me into the field of space physics. I learned a lot from him and his "bible of space physics" about how to think as a physicist and how to excel in this field. His enthusiasm for space science as well as his great sense of humor will remain my source of amusement and inspiration for many years. I would like to extend my gratitude to Dr. Bartholomeus van der Holst for teaching and helping me a lot, not only on writing code but also on the MHD

turbulence. I would like to thank my dissertation committee Dr. Richard Frazin, Professor Justin Kasper, and Professor Kenneth Powell for taking time from their busy schedules to read my thesis and offer invaluable comments and suggestions. I would like to extend my thanks to Professor Mingde Ding, my former advisor in Nanjing University. He first introduced me into the intriguing solar physics world and kept encouraging me during my PhD years. I am also indebted to Professor Pengfei Chen for first introducing me into the numerical simulation world and Professor Cheng Fang for his guidance and encouragement in the past years.

I am also indebted to CSEM members: Dr. Gábor Tóth for teaching me the essence of SWMF and helpful comments on my papers; Dr. Enrico Landi for teaching me a great deal of solar spectra observations and his encouragement on my research; Dr. Igor Sokolov for teaching me how to understand the physics behind the model; Dr. Darren De Zeeuw for helping me on many visualization and computer issues; Dr. Daniel Welling for introducing me into the Python world; Dr. Kenneth Hansen, Dr. Xianzhe Jia, Dr. Raluca Ilie, Dr. Valeriy Tenishev, and Dr. Shasha Zou for their helpful discussions on space sciences.

I also want to express my gratitude to the professors both inside and outside our department who taught me space physics and scientific computing: Professor Paul Drake, Professor Lennard Fisk, Professor Robert Krasny (Mathematics), Professor Susan Lepri, Professor Michael Liemohn, Professor Mark Moldwin, Professor Andrew Nagy, Professor Aaron Ridley, Professor Philip Roe (Aerospace), Professor James Slavin, Professor Quentin Stout, Professor Bram van Leer (Aerospace), Professor Divakar Viswanath (Mathematics), Professor Thomas Zurbuchen.

I would like to thank AOSS administrative and IT staff for their kind help during my graduate study: Jan Beltran, Darren Britten-Bozzone, Deborah Eddy, Sue Griffin, Kristi Hansen, Sandee Hicks, Rachel Long, Allison Lyons, Marti Moon, Mary Nehls-Frumkin, Kathy Norris, Faye Ogasawara, Sandra Pytlinski, Margaret Reid, Nicholas

Stauder, Melissa Tenwilliger, Eidilia Thomas, Marcia Wallin, Bryan White.

There are also many people outside U of M who helped me during my graduate life. I would like to thank my collaborators over years for their invaluable discussion and help on my researches: Dr. Xin Cheng, Dr. Curt de Koning, Dr. Rebekah Evans, Dr. Jacob Gruesbeck, Dr. Yang Guo, Professor Roussev Ilia, Professor Shinsuke Imada, Dr. Xudong Sun, Dr. Alberto Vásquez, Dr. Angelos Vouridas, and Dr. Chun Xia. I am also indebted to Professor Xueshang Feng from Chinese Academy of Science, who invited me to give a talk to his group. His knowledge and enthusiasm in computational space physics always make the discussion inspiring. I also would like to express my gratitude to Professor Jie Zhang from George Mason University who provided me a lot of important guidances both in science and in career development. I also want to thank Professor Ying Liu from Chinese Academy of Science for his kind help and enlightening discussion of ICMEs. I would like to give special thanks to Dr. Qingrong Chen, Dr. Cooper Downs, Dr. Fan Guo, Dr. Kamen Kozarev, Dr. Wei Liu, Dr. Loé Lugaz, Dr. Cohen Ofer, Dr. Hui Tian, and Dr. Junwei Zhao for their helpful scientific discussions during meetings and over phone/emails. Special thanks also go to Umbe Oliveira-Cantu, who took care of us so well in the annual SHINE meetings over years.

My life would have been much less pleasant without my friends here. I would like to express my great thanks to my officemates: Dmitry Borovikov, Sidney Ellington, Zhenguang Huang, Xing Meng, Erica Morgan, Rona Oran, and Judit Szente who made our office a great place both for science and for friendship. I also would like to extend my thanks to all my friends in AOSS and in U of M: Ercha A, Rebort Alexander, Yuqiang Bi, Alexander Bryan, Theresa Carranza-Fulmer, David Chen, Xi Chen, Xinyang Chen, Yuntao Chen, Yuxi Chen, Huiwen Chuang, Shannon Curry, Gina DiBraccio, Aron Dodger, Chuanfei Dong, Fang Fang, Julie Feldt, Nicolas Fougére, Ye Gao, Dan Gershman, John Haiducek, Fei He, I-Ning Hu, Qiaona Hu, Quanyuan Hsu,

Chaoyi Jiao, Blake Johnson, Roxanne Katus, Yuni Lee, Hui Li, Yang Li, Guangxing Lin, Chi-Mei Liu, Xiaojian Liu, Yue Ma, Jonathan Nickerson, Stav Ofer, Doğacan Öztürk, Fang Pan, Lingyu Peng, Gang Kai Poh, Jim Raines, Kevin Reed, Kela Shang, Yinsi Shou, Lois Smith, Wei Tian, Paul Ulrich, Catherine Walker, Chunpeng Wang, Jun-Chieh Wang, Ziqi Wu, Jianping Xiao, Li Xu, Shaosui Xu, Xun Yang, Weiye Yao, Bo Yu, Yiqun Yu, Yuxing Yun, Colin Zarzycki, Yiting Zhang, Xiangyun Zhang, Liang Zhao, Cheng Zhou, and Jie Zhu.

I would like to express my great gratitude to Dr. Karel Schrijver at LMSAL, who will be my postdoc advisor in the next two years. I appreciate Dr. Schrijver's invaluable help and comments during the Jack Eddy Fellowship application process that make the proposal outstanding at last. I still remember that I was assigned a paper by Dr. Schrijver about the solar sympathetic events for my oral qualification exam three years ago. I am really grateful to be able to work on this new adventure three years later with him.

Finally, I would like to express my deepest thanks to my family: my father Xianlu Jin and mother Yunxia Fu, who raised me up and supported every decision I made. Their deep belief in me is one of the strongest motivations during my PhD years in US. I would like to thank my fiancée Dong Wang for sharing and enriching my life. Without her company and the delicious food, this dissertation would not be possible. I also want to thank my cousins Ying Feng (in Georgia) and Tengfei Fu (in Oregan). They make me feel that the family is not far away. Especially, I would like to dedicate this dissertation to my grandmother, Guihua Zhang, who loved me and took care of me for many many years. I hope this dissertation can make her happy and wish her peace in heaven.

TABLE OF CONTENTS

LIST OF FIGURES

Figure

LIST OF APPENDICES

Appendix

ABSTRACT

Numerical Study of Coronal Mass Ejections, Shocks, and Turbulence: from Chromosphere to 1 AU

by

Meng Jin

Co-Chairs: Ward B. Manchester IV & Tamas I. Gombosi

My dissertation focuses on one of the major source of destructive space weather: coronal mass ejections (CMEs). This explosive activity has been observed and studied for decades. However, due to insufficient observations, our understanding of CMEs and the physical processes involved during their interplanetary propagation is still limited. Numerical models that are physically self-consistent (no ad hoc coronal heating functions) play a vital role in interpreting observations, testing theories, and providing forecasts. By helping develop and utilizing a new data-driven global MHD model: The Alfvén Wave Solar Model (AWSoM) in the Space Weather Modeling Framework (SWMF), we achieve a more realistic CME event simulation from the chromosphere to 1 AU. A detailed investigation of the CME, CME-driven shock, and CME associated turbulence is conducted based on the numerical simulation results.

First, we perform a multi-spacecraft validation study for the new solar wind model in solar minimum conditions. By using *in situ* observations from the STEREO A/B, ACE, and Venus Express spacecraft, we compare the observed plasma parameters and magnetic field of the heliosphere with that predicted by the model. Near the Sun, the

solar rotational tomography of SOHO/LASCO C2 data, differential emission measure tomography of STEREO data, and Hinode/EIS data are used. Moreover, for the first time, we compare ionic charge states of carbon, oxygen, silicon, and iron observed with ACE/SWICS with those predicted by our model. The validation results suggest that most of the model outputs can fit the observations very well, which will lead to a great improvement for CME and CME-driven shock modeling.

By employing the validated background solar wind model in both one-temperature (1T) and two-temperature (2T) modes, we present a numerical study of an event that occurred on 2011 March 7. We compare the propagation of fast CMEs and the thermodynamics of CME-driven shocks in both the 1T and 2T CME simulations. Because there is no distinction between electron and proton temperatures, heat conduction in the 1T model creates an unphysical temperature precursor in front of the CME-driven shock and makes the shock parameters (e.g., shock Mach number, compression ratio) incorrect. Our results demonstrate the importance of electron heat conduction in conjunction with proton shock heating in order to produce the physically correct CME structures and CME-driven shocks.

By separating electron and proton temperature, as well as implementing collisionless heat conduction, we simulate CME propagation from the chromosphere to 1 AU. A comprehensive validation study of the CME model is performed using remote as well as *in situ* observations from SOHO, SDO, STEREO A/B, ACE, and WIND. Our results show that the new model can reproduce most of the observed features near the Sun and in the heliosphere. By fitting the CME speeds near the Sun with observations, the CME-driven shock arrival time is within 1 hour of the observed arrival time and all the *in situ* parameters are correctly simulated, which suggests the forecasting capability of the new model. Also, by applying a fully physical description of Alfvén wave turbulence (wave propagation, reflection and dissipation calculated self-consistently) in the model, for the first time, we capture the CME turbulence

interaction in the global MHD model. Alfvén wave reflection is evident in front of the CME-driven shock, which leads to the enhanced turbulence dissipation.

In general, the numerical study of CME, CME-driven shocks, and CME turbulence greatly advances our understanding of the physical processes of CME propagation near the Sun and in the heliosphere. These results illustrate the new capability of the model, which is a large step towards accurate space weather forecasting.

CHAPTER I

Introduction: An Odyssey of Coronal Mass Ejections from the Sun to the Earth and Beyond

"Begin at the beginning," the King said, gravely, "and go on till you come to an end; then stop."

– Lewis Carroll, *Alice in Wonderland*

Dear Professor: We are in the sixth grade. In our class we are having an argument. The class took sides. We six are on one side and 21 on the other...The argument is whether there would be living things on earth if the sun burnt out...We believe there would be...Will you tell us what you think? Love and Lollipops, Six Little Scientists

Dear Children: The minority is sometimes right – but not in your case. Without sunlight there is: no wheat, no bread, no grass, no cattle, no meat, no milk, and everything would be frozen. No LIFE.

– Correspondence between schoolchildren and Albert Einstein, *1951*

1.1 Space Weather and Sun-Earth Connection

With human activities expanding to outer space, the "weather" is no longer limited to the lower atmosphere of our Earth. Space weather refers to the conditions

of geospace that are largely driven by plasma flows, electromagnetic emission, and energetic particles originating from the Sun. Coronal mass ejections (CMEs) are the largest of these expulsions in which 10^{15}-10^{16} g of plasma is ejected from the Sun with a kinetic energy of order 10^{31}-10^{32} ergs (*Hundhausen*, 1993). When the CMEs propagate into interplanetary space, they are called interplanetary CMEs (ICMEs). Fast CMEs can be supersonic and drive shocks that are linked with storms of energetic particles flooding interplanetary space.

When arriving at Earth, the magnetic field carried by ICMEs can interact with Earth's magnetosphere. Since the geomagnetic field has a northward nature (relative to the ecliptic plane of the solar system), a southward magnetic field carried by the ICMEs will trigger magnetic reconnection in the magnetosphere, which causes closed field lines to open and expose the Earth's atmosphere to the solar wind plasma. At the same time, the increased solar wind pressure compresses the Earth's magnetosphere and leads to a further expansion of the auroral ovals. The compression and magnetic reconnection can lead to strong and variable changes to the currents and magnetic fields in geospace lasting for days. Energetic particles in interplanetary space can penetrate into the Earth's atmosphere along the open field lines. The above-mentioned geomagnetic activity caused by ICMEs is called a geomagnetic storm. There is a widely used index for classifying the severity of geomagnetic activity called Dst index (Disturbance storm time index). It is expressed in nT and based on the average value of the horizontal component of the Earth's magnetic field. During the geomagnetic storm, the intensity of the magnetospheric ring current increases, which leads to a decrease of the Dst. Note that many other indices are also used for measuring the geomagnetic storm (e.g., Kp index).

In Figure 1.1, the configuration of the Earth's magnetosphere is shown, in which we can see its interaction with the interplanetary magnetic field. The solar wind compresses the sunward side magnetosphere to ∼6-10 R_E. A supersonic shock wave

is created called bow shock, which forms the outermost layer of the magnetosphere. Behind the bow shock, it is a region called magnetosheath. The particles in this region originate from the shocked solar wind plasma. Also, both the magnitude and direction of the magnetic field in this region change frequently, which leads to magnetic turbulence. The magnetopause is a layer where the pressure from the Earth's magnetic field is balanced with the dynamic pressure from the solar wind plasma. The solar wind drags out the anti-sunward magnetosphere to $\sim$1000 R_E known as magnetotail. It contains two lobes and separated by a plasma sheet (an area with lower magnetic field and denser hot plasma). The radiation belts contain at least two layers of energetic charged particles that are held by the Earth's magnetic field[1]. The innermost of magnetosphere is called plasmasphere (or inner magnetosphere) that consists low energy plasmas.

[1]The Van Allen Probes discovered the third radiation belt recently(*Baker et al.*, 2013).

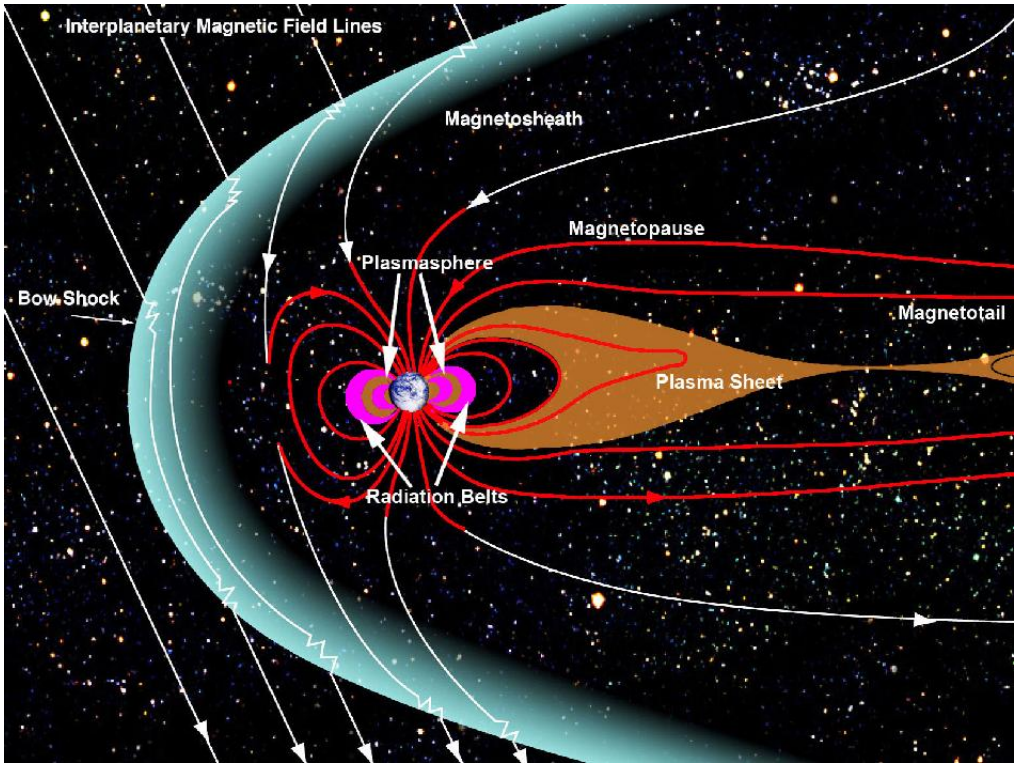

Figure 1.1: Earth's magnetosphere and its interaction with the interplanetary magnetic field in the case of an IMF with a significant southward component (Credit: NASA/Goddard/Aaron Kaase).

There are many consequences of geomagnetic storms. Some of them can significantly affect our daily lives. Economists estimate that the adverse impact of space weather is \$200-\$400 million per year, and the potential exists for significantly larger losses[2]. In Figure 1.2, a simple diagram is shown for the technological systems that can be affected by space weather. The major effects of space weather events can be summarized as follows:

- Damage to spacecraft hardware by direct solar energetic particle (SEP) impact or spacecraft charging. Space weather related losses to satellite companies range from thousands of dollars for temporary data outages to over \$200 million to replace one satellite.

[2]NRC, Severe space weather events – understanding societal and economic impacts workshop report, Tech. Rep. ISBN: 0-309-12770-X, Committee on the Societal and Economic Impacts of Severe Space Weather Events, National Research Council, 2008.

- Increased atmospheric drag on orbiting spacecraft causing them to drop to lower altitudes.

- Threat to the lives of astronauts due to the exposure to energetic particles and high radiation doses.

- Increased radiation exposure to high-latitude commercial aircraft. Due to the rapidly increasing use of transpolar flights, the influence of space weather on commercial flights is becoming more and more important. The polar flights are diverted due to loss of radio communications.

- Degraded or lost high-frequency radio signals, which can disturb telecommunications between phone lines or satellites/Global Positioning System (GPS).

- Induced current generation in power lines, resulting in power systems failures. A geomagnetic storm in March 1989 caused a failure in the Hydro-Quebec electric power system and the electric blackout lasted for 9 hours with 6 million people affected. Moreover, any large conductor on Earth (e.g., oil pipelines) can experience these induced currents.

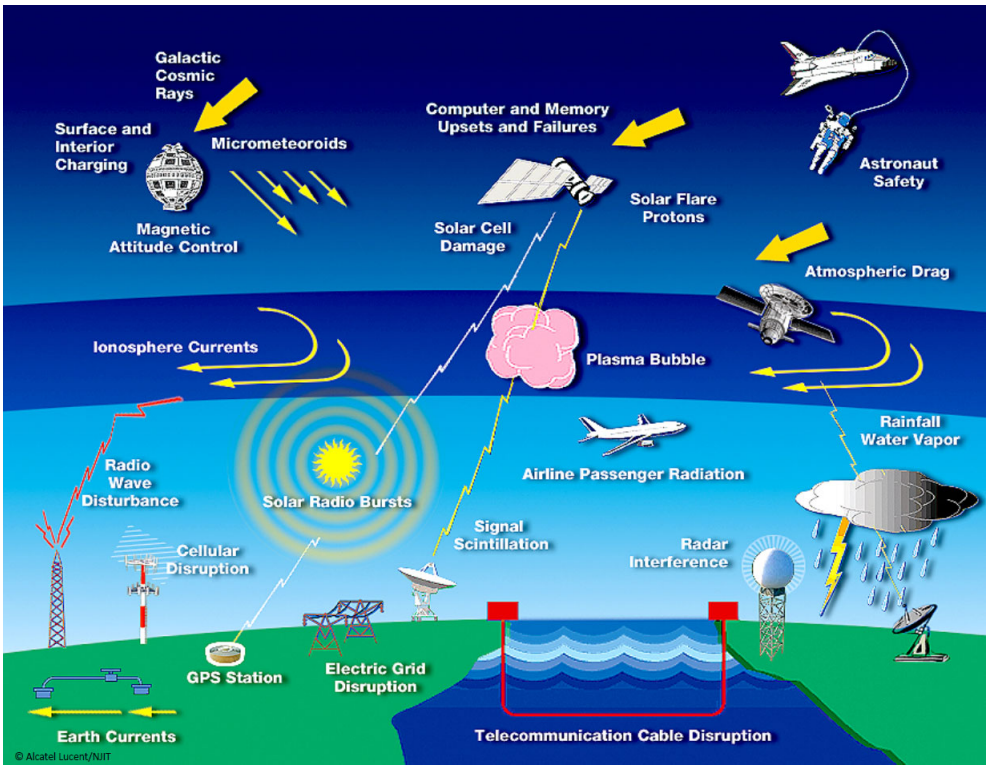

Figure 1.2: A simple diagram that shows the technological systems affected by space weather (*Lanzerotti*, 2011).

Given these effects, it is in the national interest to understand space weather related phenomena. However, compared with traditional weather forecasting, space weather prediction lags greatly behind. The development of a reliable space weather forecast model is a high national priority for both civilian and national security purposes. This dissertation will focus on the major sources of the destructive space weather: CMEs and CME-driven shocks. Before describing my dissertation work, I would like to briefly describe the life cycle of CMEs and the major physical processes involved during the whole evolution in Chapter I. In Chapter 1.2, the solar wind, with which the CMEs interact, is briefly introduced. In Chapter 1.3 and 1.4, an introduction of CMEs and ICMEs is given, followed by the motivations and opening questions in Chapter 1.5. The organization of the dissertation is in Chapter 1.6.

1.2 The Solar Wind

1.2.1 Historical Background

Different opinions may exist on when the study of the solar wind started. But I would like to start the story in the year 1859 when the British astronomer Richard Carrington first observed a super event (i.e., Carrington event) from a projected image of the Sun (*Carrington*, 1859). He saw two patches of peculiarly intense light appear and fade within 5 minutes in the largest sunspot group visible. The phenomenon he saw is called "white-light solar flare" (the energy release is so large that the flare can be seen in white light on the disk of the Sun). About 18 hours later, large disturbances appeared on the Earth: telegraph systems failed, and intense auroras spread over most of the world. Carrington suggested the solar event and the phenomenon on the Earth are connected. And this idea was taken seriously by some physicists at the end of the nineteenth century (George Fitzgerald, 1892, Sunspots and magnetic storms). The Carrington event brought the first concept of solar wind, that the Sun can emit sporadic beams separated by a vacuum. Figure 1.3 shows the sunspots sketch recorded by Richard Carrington on September 1, 1859.

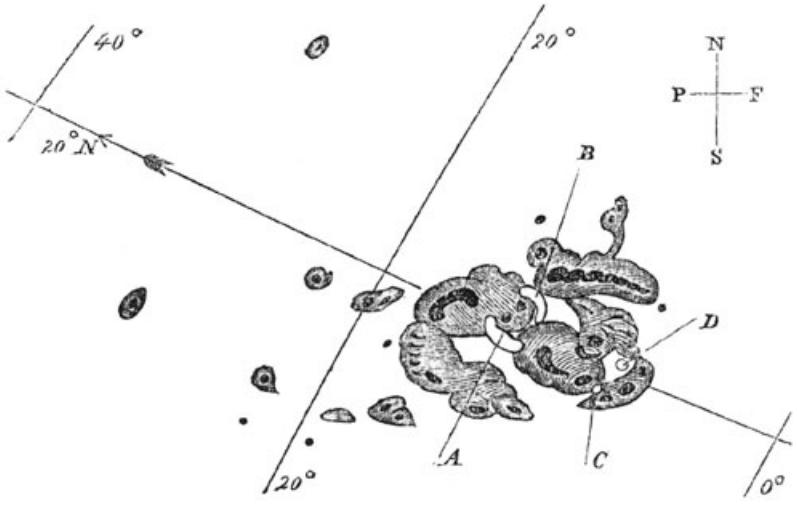

Figure 1.3: Sunspots of September 1, 1859, as sketched by Richard Carrington. A and B mark the initial positions of an intensely bright event, which moved over the course of 5 minutes to C and D before disappearing.

The concept of solar wind was championed by the Norwegian physicist Kristian Birkeland (*Birkeland and Dall*, 1915). Based on the observation of auroral and geomagnetic activity, he suggested that the Sun emits a continuous flux of charged particles filling up the whole interplanetary space. The Earth is also surrounded by these charged particles. This was a great change for the solar wind concept at that time and is very close to the modern solar wind definition. However, this new idea was strongly rejected by Lord Kelvin who argued that the Sun could not produce geomagnetic disturbances. Therefore, Birkeland's work was largely ignored by the scientific community at that time.

At the middle of the twentieth century, another astronomical phenomenon made people rethink Birkeland's idea about solar wind: comets. People observed that comets have two kinds of tails: one is nearly straight and made of plasma; the other has a curved shape and is made of dust as seen in Figure 1.4, which shows an image of comet Hale-Bopp. The curved dust tail is produced by solar radiation pressure and gravity. However, the straight tail could not be understood. It always points away from the Sun and shows acceleration features from the irregularities. The explanation of solar radiation pressure fails by several orders of magnitude. In the 1950s, German physicist Ludwig Biermann developed a model for the interaction of cometary particles with those coming from the Sun that can reproduce the straight tail of comets if they are surrounded by a permanent flux of charged particles from the Sun (*Biermann*, 1951). Although his original arguments about the interaction process between particles were later known to be incorrect, his work made a critical step in the study of the solar wind. Since the orbits of comets cover all the heliospheric latitudes, Biermann's work naturally leads to the conclusion that the Sun is continuously emitting particles at all directions.

Figure 1.4: Image of comet C/1995 O1 (Hale-Bopp), taken on 1997 April 04 (E. Kolmhofer, H. Raab; Johannes-Kepler-Observatory, Linz, Austria).

Four years later, English physicist Sydney Chapman, who had made major contributions to the kinetic theory of gases, published another completely different theory to explain the solar atmosphere around the Earth (*Chapman and Zirin*, 1957). He found that the hot ionized solar atmosphere can conduct heat so well that it should remain hot to very large distances. Therefore, the solar particles have large enough thermal speed to escape the solar gravity, which leads to a slowly declining density. The solar atmosphere should extend well beyond the Earth's orbit so that the Earth is surrounded by a static solar atmosphere.

The modern solar wind concept was proposed by Eugene Parker in 1958, who tried to unify Chapman and Biermann's theories."However unlikely, it seemed, the only possibility was that Biermann and Chapman were talking about the same thing" (*Parker*, 1997). Parker showed that Biermann's continuous flux of solar particles was just Chapmen's extended solar atmosphere expanding away in space as a supersonic flow. Due to the hot solar atmosphere, neither solar gravity nor the pressure of the interplanetary medium can confine it. Parker's non-static solar atmosphere was so novel

that his paper (*Parker*, 1958) encountered difficulty publishing in the Astrophysical Journal[3].

In order to prove Parker's solar wind theory, *in situ* observations from space were needed. At the end of 1950s, it was still a challenge for rocket-borne instruments to get the measurement from space. It took four Russian missions and seven American ones to finally get an unambiguous result. The most successful Russian mission is Lunik II, which was launched in 1959. It detected a flux of positive ions. However, due to the lack of velocity information, the conclusion cannot be conclusive. The final proof came from the American mission Mariner II (*Neugebauer and Snyder*, 1962). On its way to Venus, the plasma instrument onboard detected a continuously flowing solar wind. Moreover, the fast and slow streams that have a repeating rate of 27 days are detected suggesting their solar origin. This measurement finally ended the debate that lasted for almost a century about the existence of the continuous solar wind[4].

1.2.2 Observations and Models

In the Section, we will start with the famous Parker solar wind solution, followed by a brief introduction of the solar wind structures. At the end of the section, a brief review of the global MHD solar wind modeling is given.

1.2.2.1 Parker's Solar Wind Solution

Assume the solar wind is spherically symmetric, single fluid, fully ionized, and quasi-neutral plasma including electrons and protons, the hydrodynamic equations can be written as (*Gombosi*, 2004):

$$\frac{1}{r^2}\frac{d}{dr}(r^2\rho u) = 0 \tag{1.1}$$

[3]The referee stated that the author was not familiar with the subject. However, as the editor of the journal, Subrahmanyan Chandrasekhar decided to publish it at last (*Parker*, 2014)

[4]Marcia Neugebauer said:"We had data ! Lots of it! There was no longer any uncertainty about the existence and general properties of the solar wind."(*Neugebauer*, 1997)

$$\rho u \frac{du}{dr} + \frac{dp}{dr} + \rho G \frac{M_\odot}{r^2} = 0 \tag{1.2}$$

$$\frac{3}{2} u \frac{dp}{dr} + \frac{5}{2} p \frac{1}{r^2} \frac{d}{dr}(r^2 u) = 0 \tag{1.3}$$

With the hydrostatic assumption, the above equations can be simplified as:

$$\frac{dp_s}{dr} + \rho_s G \frac{M_\odot}{r^2} = 0 \tag{1.4}$$

where p_s and ρ_s represent the pressure and mass density at an arbitrary point away from the Sun. The isothermal hydrostatic solution of Eq 1.4 can be written as:

$$p_s = p_\odot \exp\left[\frac{m_p g_\odot}{2kT} R_\odot \left(\frac{R_\odot}{r} - 1\right)\right] \tag{1.5}$$

where $g_\odot$ is the gravitational acceleration at the surface of the Sun. With this solution, at very large distance from the Sun, the pressure does not vanish: $r \to \infty$, $p_\infty / p_\odot \approx 3 \times 10^{-4}$. However, the estimated pressure of the interstellar medium is at least 10 orders of magnitude smaller. Therefore, the hydrostatic solution cannot represent an equilibrium solution for the hot solar corona.

If the nonzero velocities are allowed, then the isothermal solution becomes:

$$\frac{1}{2} u^2 - {a_s}^2 \ln u = 2{a_s}^2 \ln r + g_\odot \frac{{R_\odot}^2}{r} + C \tag{1.6}$$

where ${a_s}^2 = 5p/3\rho$ is the local sound speed (it is a constant in the isothermal assumption). C is a constant. The solution is shown in Figure 1.5. There are five classes of solutions. The Class I & II solutions are immediately dropped due to the double solution nature. The Class III solution is also unrealistic because the solar wind is supersonic at the solar surface. The Class V solution is called the solar breeze solution. This solution has a similar problem as the hydrostatic solution, that the pressure at infinity is finite and far exceeds the pressure of the interstellar medium.

The Class IV solution is Parker's solar wind solution. We notice that the pressure will vanish at large distance. Figure 1.6 shows the velocity evolution with different temperatures. In reality, the solar wind temperature decreases with distance with a polytropic index less than 5/3. Therefore, some heating mechanism is needed to maintain the slowly decreasing temperature. We will discuss this topic more at the end of this section.

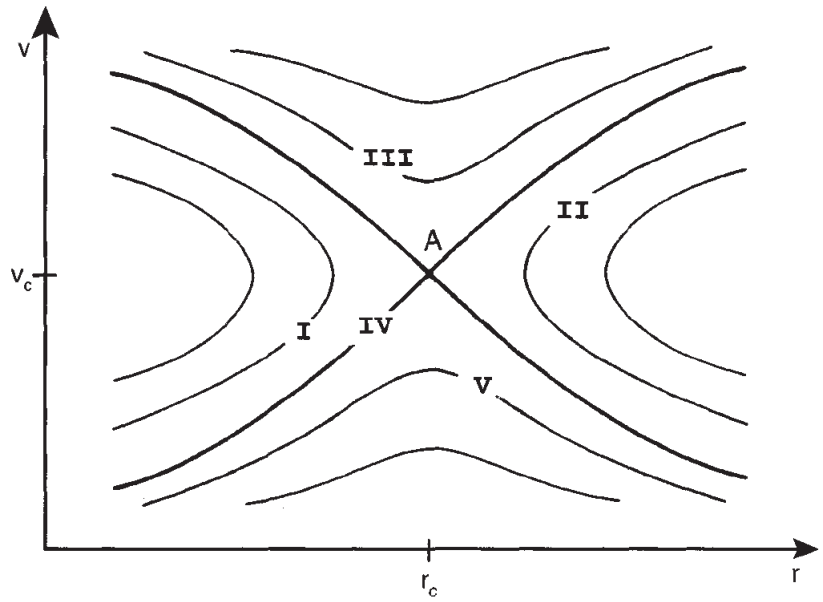

Figure 1.5: Mathematically admissible classes of isothermal solutions of an expanding corona (*Gombosi*, 2004).

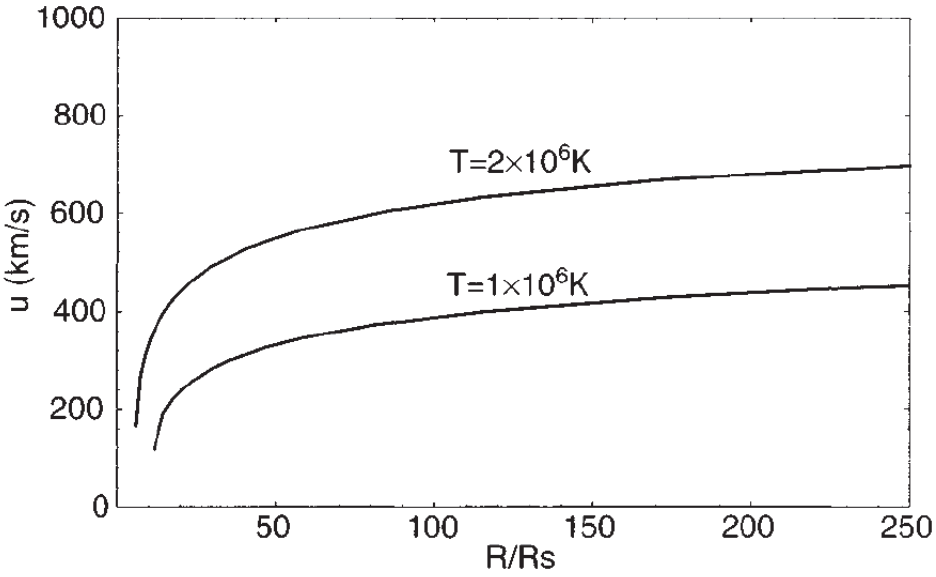

Figure 1.6: Parker's solar wind solution with different temperatures (*Gombosi*, 2004).

1.2.2.2 Interplanetary Magnetic Field (IMF)

Parker's solar wind solution does not include the magnetic field. In order to understand how the solar magnetic field extends into the interplanetary medium, one can start from the magnetic induction equation:

$$\frac{\partial \mathbf{B}}{\partial t} = \nabla \times (\mathbf{u} \times \mathbf{B}) \tag{1.7}$$

In the reference frame that rotating with the Sun, we find $\mathbf{u}' \times \mathbf{B} = 0$, which means the magnetic field and plasma flow are always parallel to each other. When considering the non-rotating frame, it leads to the Parker spiral solution of the magnetic field (*Gombosi*, 2004):

$$\mathbf{B} = B_s \left(\frac{R_s}{r}\right)^2 \mathbf{e_r} - B_s \left(\frac{{R_s}^2}{r}\right) \frac{\Omega_\odot \sin\Theta}{u_{sw}} \mathbf{e}_\phi \tag{1.8}$$

where the subscript s refers to a source surface past the sonic point, $\Omega_\odot$ is the rotation rate of the Sun, Θ is the spherical polar angle. The Parker spiral solution of IMF is shown in the left panel of Figure 1.7. In the right panel, the 3d IMF structure of a global MHD solar wind model is shown (*van der Holst et al.*, 2010). The observed average magnetic field at 1 AU is $\sim$7 nT, which is consistent with the expected value by the Parker spiral solution of IMF (assuming a few Gauss magnetic field at the source surface).

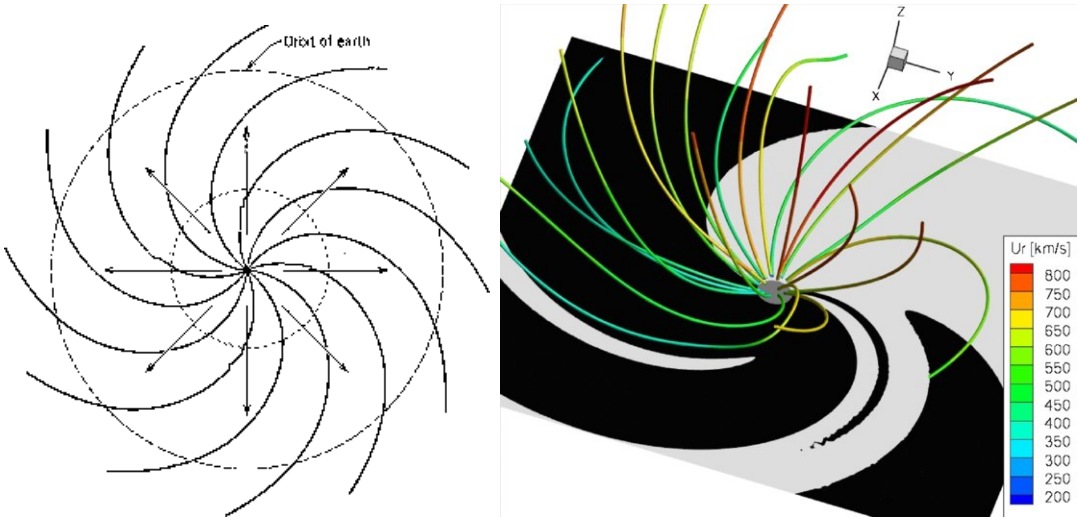

Figure 1.7: Left panel: Parker spiral solution of IMF. Right panel: IMF in the global MHD solar wind model (*van der Holst et al.*, 2010).

In situ observations from space that cover wide heliocentric distances and heliographic latitudes appear to be in reasonable agreement with Parker's highly idealized solution (e.g., *Smith* 1979; *Burlaga et al.* 1982; *Smith and Phillips* 1997). However, some discrepancies still exist between the model and data. Some assumptions may be invalid for realistic solar wind conditions. For example, in the Parker spiral model, all field lines are fixed on the surface of the Sun. But in reality, the field lines can move in response to convection in the solar photosphere (e.g., *Jokipii and Parker* 1968), differential solar rotation (e.g., *Fisk* 1996), or interchange reconnection (magnetic reconnection between the open and closed field lines; e.g., *Fisk et al.* 1998; *Crooker*

et al. 2002). *Fisk* (1996) proposed a revision for Parker's spiral model: at high magnetic latitudes, the new model incorporates a rigidly rotating magnetic dipole tilted relative to the solar rotation axis. This model is based on the non-radial expansion of the fast solar wind from polar corneal holes (*Smith et al.*, 1995) and the differential rotation of the footpoints of magnetic field lines (*Snodgrass*, 1983).

1.2.2.3 Coronal Structure and Heliospheric Current Sheet (HCS)

In order to understand the coronal structure as well as the formation of the heliospheric current sheet (HCS), we need to consider the effect of the magnetic field. In the single fluid ideal MHD assumption:

$$\nabla \cdot (\rho \mathbf{u}) = 0 \tag{1.9}$$

$$\rho(\mathbf{u} \cdot \nabla)\mathbf{u} + \nabla p + \rho G \frac{M_\odot}{r^2}\mathbf{e_r} - \mathbf{j} \times \mathbf{B} = 0 \tag{1.10}$$

$$\nabla \times (\mathbf{u} \times \mathbf{B}) = 0 \tag{1.11}$$

$$\mathbf{j} = \frac{1}{\mu_0}\nabla \times \mathbf{B} \tag{1.12}$$

The above equations were solved by *Pneuman and Kopp* (1971) in 2D starting from dipole field. The result is shown in the left panel of Figure 1.8. The result shows that the first open field lines are quite close together near the equator and extend radially outward, which suggests that there is a thin sheet with very high current density $\mathbf{j} = \frac{1}{\mu_0}\nabla \times \mathbf{B}$ pointing in the azimuthal direction. This current sheet is called the heliospheric current sheet (HCS) that separates fields of different polarity as well as the plasma flows from different hemispheres.

The dipole field assumption is valid for solar minimum conditions, since the solar dipole moment tends to be nearly aligned with the rotation axis at that time. However, the dipole moment tends to be inclined substantially relative to the solar

rotation axis at non-minimum conditions. The HCS becomes wrapped into a global structure that resembles a ballerina's twirling skirt (as shown in the right panel of Figure 1.8). In each solar rotation, the Earth crosses the HCS at least twice. Each crossing will change the observed IMF polarity. Due to the complexity of the realistic solar magnetic field, there can be multiple HCS crossings in the observation (*Crooker et al.*, 1993).

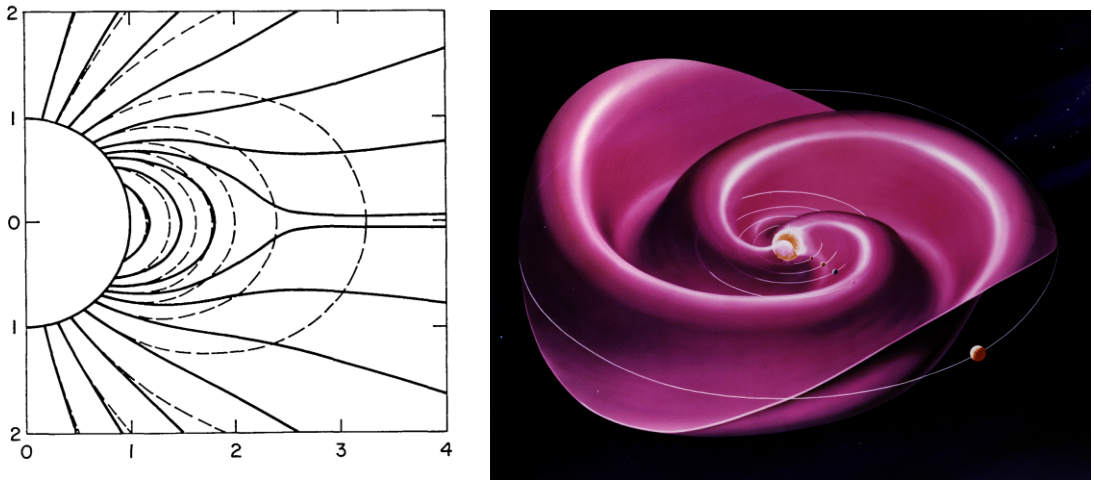

Figure 1.8: Left panel: idealized heliospheric current sheet. Right panel: heliospheric current sheet results from the influence of the Sun's rotating magnetic field.

1.2.2.4 Solar Wind Stream Structure

The global solar wind stream structure was extensively examined by the *Ulysses* mission due to its unique orbit. By using Jupiter's large gravitational field, *Ulysses* was accelerated out of the ecliptic plane to high heliographic latitudes (Figure 1.9 shows the third orbit of *ulysses*). By now, there are three orbits including two orbits (first and third) near the solar minimum conditions and one orbit (second) near solar maximum. In Figure 1.10, the polar plots of the solar wind speed over all three Ulysses' orbits are shown. For the solar minimum condition, there is a nearly constant fast solar wind ($\sim$750-800 km s^{-1}) at high latitudes. This fast solar wind originates

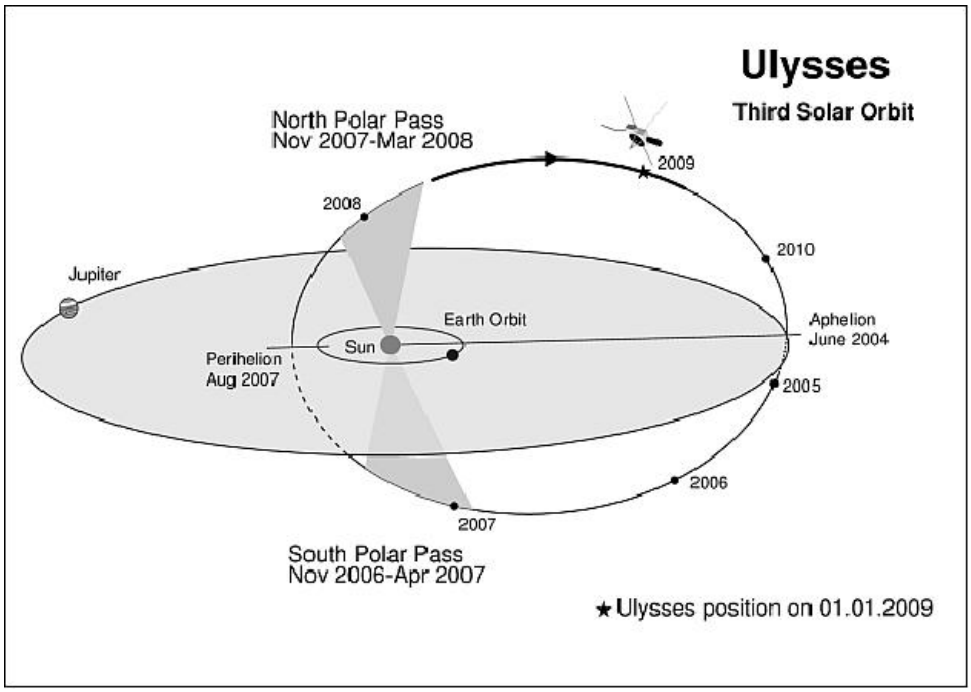

Figure 1.9: The third orbit of *Ulysses*.

in the coronal holes, which are large, nearly unipolar regions in the solar atmosphere. The slow solar wind was found to have a width of about ±20° to ±35° (first orbit) or ±37° (third orbit). The typical slow wind speed is ∼350 km s^{-1} (*McComas et al.*, 2008). The slow solar wind originates from the boundaries of the coronal streamers that straddle the region of magnetic polarity reversal. During the second orbit (from the rising phase to the maximum of solar cycle 23), the structure of the solar wind was much more complex, which reflects a more complex coronal structure (*McComas et al.*, 2001, 2002). Mixtures of slow and fast solar wind streams were observed at all heliographic latitudes, which come from different sources (e.g., streamers, CMEs, small coronal holes, and active regions).

1.2.2.5 Corotating Interaction Region (CIR)

Spatial variations in the solar atmosphere can result in the formation of recurring interplanetary structures. When a fast solar wind stream interacts with a slow solar

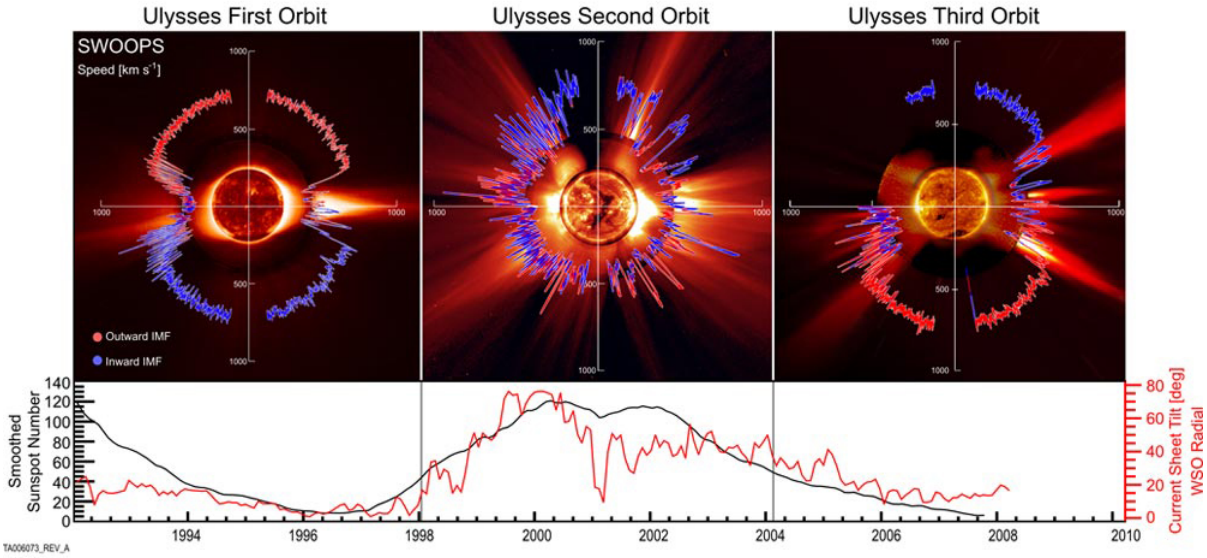

Figure 1.10: Polar plots of the solar wind speed over all three of Ulysses' orbits.

wind stream, the fast stream compresses the plasma and produces a high pressure region that separates the slow and fast solar wind streams. This region is called a corotating interaction region (CIR). Since the solar wind temperature gradually decreases with distance while the velocity keeps increasing. The leading edge of the fast stream will keep steepening and form a pair of forward and reverse shocks at a certain distance from the Sun, which bounds the CIR. In the left panel of Figure 1.11, the cartoon sketch shows the interaction of fast and slow streams. In the right panel, the CIRs in a global MHD solar wind model is shown (*van der Holst et al.*, 2010).

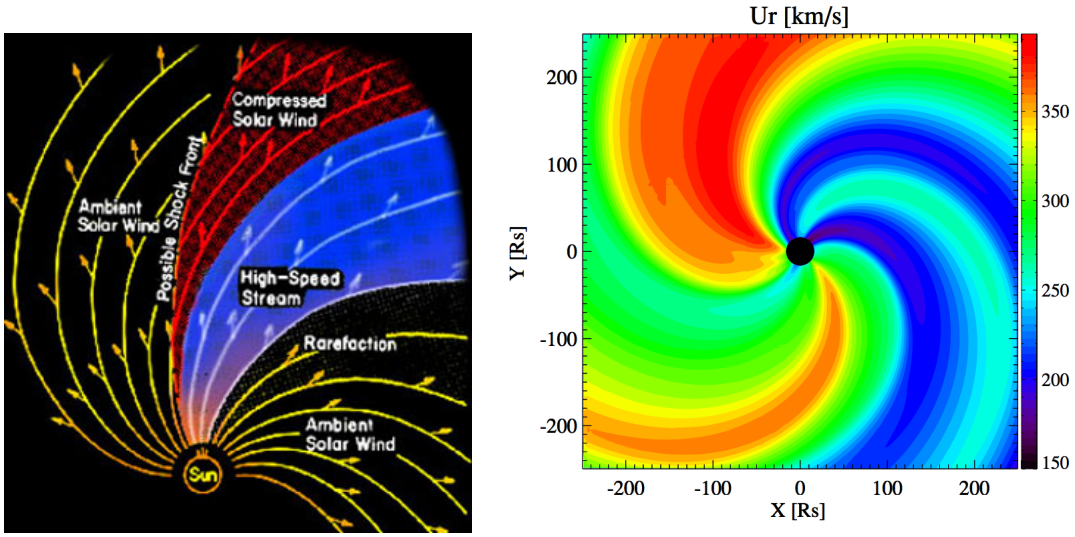

Figure 1.11: Left panel: Cartoon showing the interaction of a fast and a slow stream. Right panel: the realistic stream structure that leads to CIRs in a global MHD solar wind model (*van der Holst et al.*, 2010).

1.2.2.6 Global MHD Modeling of Solar Wind

For the global MHD modeling of solar wind, there are two major issues to be addressed: first, how to account for different sources of solar wind (reproduce the slow/fast solar wind structures); second, how to deal with the thermodynamics of the heliospheric plasma, and the heating mechanism (how to heat solar corona and solar wind). For the first issue, some previous works used an axisymmetric bimodal solar wind to reflect solar minimum conditions (e.g., *Han et al.* 1988; *Odstrčil and Pizzo* 1999; *Wu et al.* 1999; *Groth et al.* 2000; *Gombosi et al.* 2000). Other works incorporated the solar observations (e.g., synoptic magnetogram) to specify the inner boundary condition and utilized the WSA empirical model (*Wang et al.*, 1990; *Arge and Pizzo*, 2000) to relate flux tube expansion and solar wind speed at 1 AU (*Odstrcil et al.*, 2005; *Cohen et al.*, 2007; *van der Holst et al.*, 2010). *van der Holst et al.* (2010) further utilized the differential emission measure tomography (DEMT) method (*Frazin et al.*, 2009; *Vásquez et al.*, 2010) to obtain the inner boundary information for electron temperature and density. Other models that do not use the Wang-Sheeley-

Arge (WSA) relationship involved empirical terms to create a distribution similar to the WSA model (e.g., *Usmanov* 1993; *Roussev et al.* 2003a; *Odstrcil et al.* 2004). Regarding thermodynamics, previous works addressed the solar wind heating by using empirical heating functions (e.g., *Groth et al.* 2000), or variable adiabatic index (e.g., *Roussev et al.* 2003a; *Cohen et al.* 2007). Due to widely observed coronal Alfvén waves in recent observations (e.g., *Tomczyk et al.* 2007; *De Pontieu et al.* 2007), some global MHD solar wind models incorporated Alfvén wave heating mechanism (e.g., *Usmanov et al.* 2000; *Evans et al.* 2009; *van der Holst et al.* 2010; *Sokolov et al.* 2013; *van der Holst et al.* 2014). We will discuss this further in Chapter II–Chapter IV.

1.3 CME Near the Sun

1.3.1 Observations

CMEs are manifest as large-scale ejections of plasma from corona, that are seen in Thomson-scattered white light as measured by coronagraphs. Although the coronagraph was first invented in 1931 by Bernard Lyot, the sensitivity of the instrument was not high enough to detect the faint coronal eruptions from the ground. The first space-based coronagraph was on board OSO-7, with which the first CME was observed from space (*Tousey et al.*, 1973). In the following several decades, there were many missions with coronagraphs that kept monitoring ejections from the Sun (e.g., Skylab, Solar Maximum Mission, SOHO, STEREO). When CMEs were first observed, they were called "solar transients". The first appearance of the term "coronal mass ejection" was by *Gosling et al.* (1976). In Figure 1.12, the timeline of CME discoveries are shown. It has been divided into before and during space age (*Howard*, 2011).

With many CME events observed, the typical morphology of a CME shown in Figure 1.13 exhibits a three-part structure of leading front surrounding a low den-

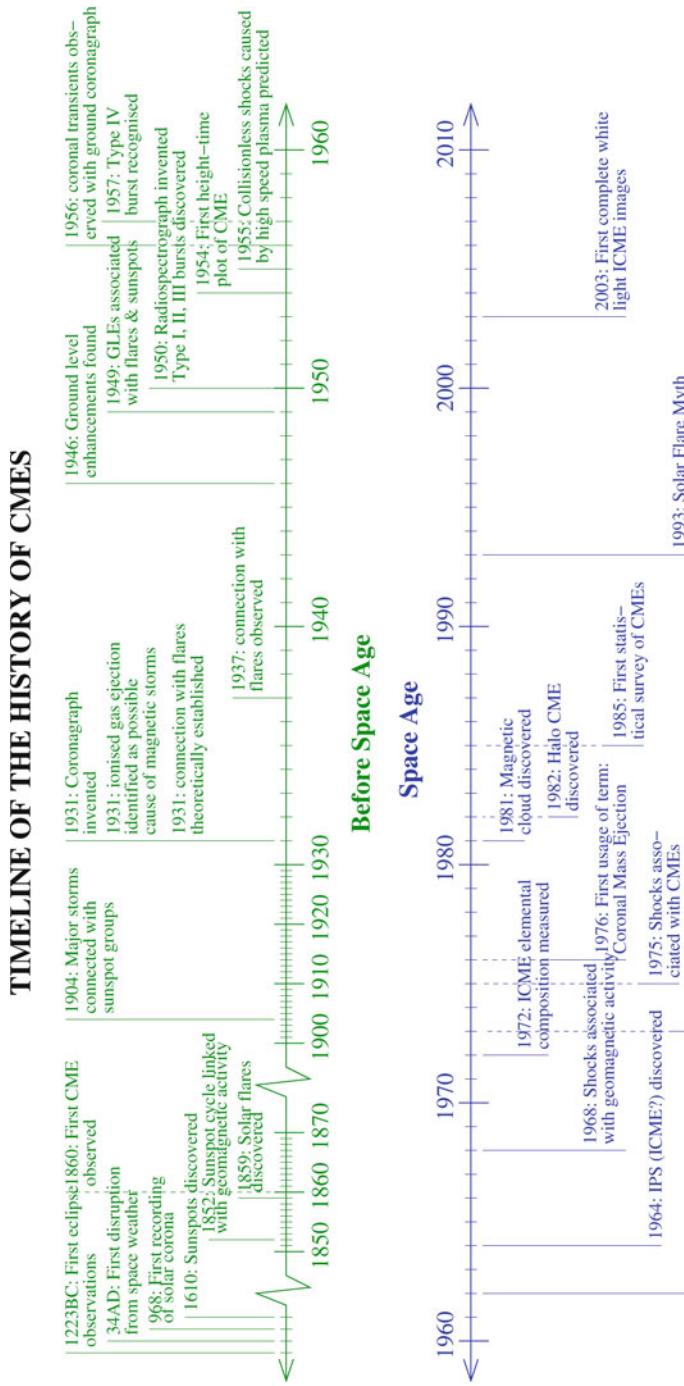

Figure 1.12: Timeline of CME discoveries before and during space age (*Howard*, 2011).

sity cavity containing a high-density core. The leading front is a bright shell that is observed to be ten times denser than the background corona, therefore it cannot be produced by the MHD shock, which has an upper limit of factor 4. It is more likely produced by the pile-up of the plasma in front of the flux rope. The bright core corresponds to the erupting filament material. More than half of all CMEs are associated with a filament eruption. Filaments (sometime also called prominence if seen above the solar limb) are filamentary, cloud-like structures containing plasma that is typically 100 times cooler and denser than the background solar corona. Filaments can form in the weak field of the quiet Sun, so called quiescent filaments may extend to a height of $\sim 10^5$ km above the solar surface. Filaments also form in active regions, which may erupt to form a high speed CME, while the eruption of quiet region filaments tend to produce slow to moderate speed CMEs (*Low*, 2001). The dark cavity is a low-density region between the leading front and the bright core. It is believed to contain the magnetic flux rope. In some fast CME cases, the CME-driven shock can be detected in the white light image with a density compression ratio from 1.2 to 2.5 (*Vourlidas and Howard*, 2006), which is consistent with the prediction of MHD theory (In Chapter III and IV, we will discuss this issue in more detail).

Most CMEs are associated with solar flares and it is has been gradually accepted that the CMEs and solar flares (specifically two-ribbon flares) are manifestations of the same eruptive process. During a CME/flare, there are many phenomena that can be observed near the Sun: intense H_α, X-ray, and radio emissions. In some cases, EUV waves across a large region of the Sun can be observed (*Moses et al.*, 1997; *Thompson et al.*, 1998, 1999). Soft X-ray emission is produced by the hot flare loops with temperature larger than 10^7 K. The loop footpoints can map to the H_α ribbons. Both the soft X-ray and H_α emission can last for hours. The plasma that produces the soft X-ray emission is from chromospheric evaporation[5] (*Hirayama*,

[5]The chromospheric evaporation is caused by the released energy during solar flare that heats the chromospheric material and induces an upward mass motion along magnetic loops.

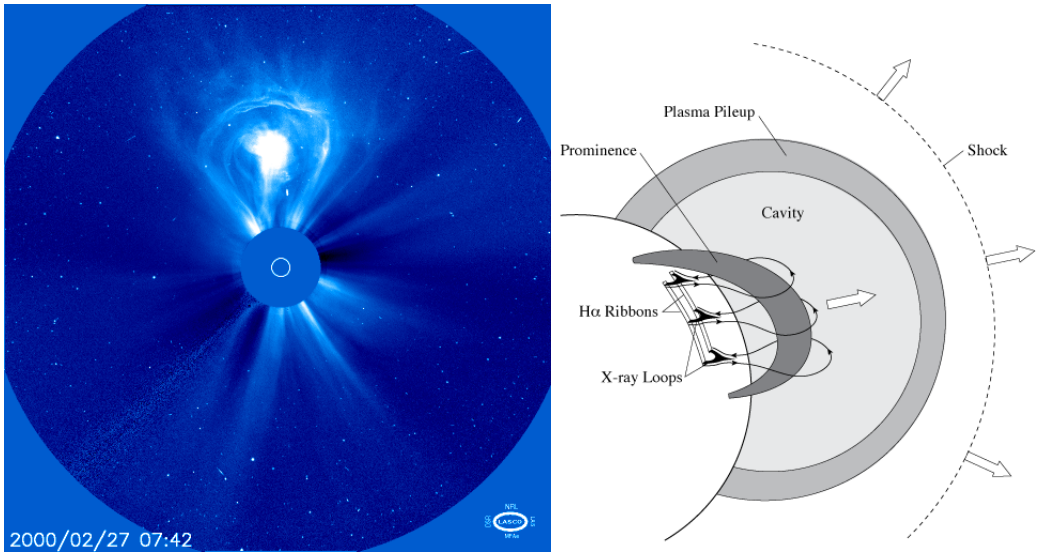

Figure 1.13: Left panel: The typical 3-part CME as observed by the SOHO/LASCO coronagraph: leading edge, dark cavity, and the bright core. The white circle represent the surface of the Sun, while the grey disk is the occulter of the coronagraph. Right panel: The cartoon diagram of 3-part CME.

1974; *Doschek and Warren*, 2005; *Jin and Ding*, 2008). The hard X-ray emission (> 20 keV) appears during the impulsive phase of the solar flare, which is produced by non-thermal electrons through thick-target Bremsstrahlung. Hard X-ray emission is typically observed to have a two-footpoint structure and the intensity of the footprints can be different (e.g., *Jin and Ding* 2007). Figure 1.14 shows the hard X-ray double footpoints in the 2005 January 5 event (*Jin and Ding*, 2007).

The typical energy required for large flares and high-speed CMEs is $\sim 10^{32}$ ergs. In Figure 1.15, the characteristic coronal energy densities are shown. We can see that the magnetic energy density is three orders of magnitude greater than any other energy form. Therefore, the magnetic energy is the only major source of energy for CMEs/flares (*Forbes*, 2000). During the CME/flare, the maximum magnetic energy that can be released is called free magnetic energy, which is the difference between the magnetic energy of the given field and that of the potential field matching the same boundary conditions. The potential field component is produced by the current sources below the solar surface (i.e., convection zone). Considering the Alfvén speed

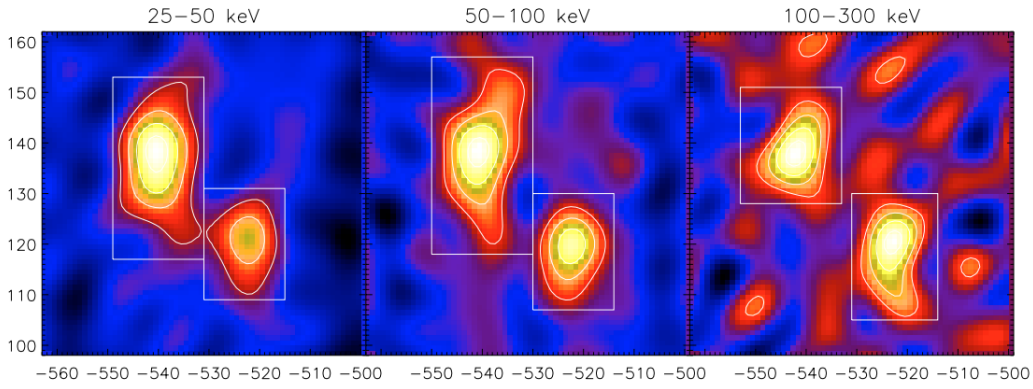

Figure 1.14: Hard X-ray emission from 2005 January 5 event observed by RHESSI (*Jin and Ding*, 2007).

Energy type	Formula	Value (J/m^3)	Parameter values
Magnetic	$B^2/2\mu$	40	$B = 100$ gauss
Thermal	nkT	0.01	$n = 10^{15}$ m^{-3}, $T = 10^6$ K
Bulk kinetic	$m_p n v^2/2$	10^{-6}	$n = 10^{15}$ m^{-3}, $v = 1$ km/s
Gravitational	$m_p n g h$	0.04	$n = 10^{15}$ m^{-3}, $h = 10^8$ m

Figure 1.15: Characteristic coronal energy densities (*Schrijver and Siscoe*, 2012).

($\sim$2 km s^{-1}) of the convection zone and the size of the active region ($\sim 10^5$) km, the dynamic time scale of potential field is about 14 hours (*Priest*, 1982). In contrast, the non-potential component is produced by currents in the solar corona (e.g., sheared arcades, flux ropes) where the time scale of non-potential dynamics is several minutes. The total free magnetic energy is released when all the coronal currents are dissipated.

Figure 1.16 shows some statistical properties of observed CMEs. The average CME speed and angular width[6] are 407 km s^{-1} and 47°, respectively. The largest CME speed observed is over 3000 km s^{-1}, and slowest one is less than 50 km s^{-1}. With regards to space weather, "halo CMEs" with angular widths of 360° are more important due to their traveling direction toward the Earth. The distribution of CME

[6]The CME angular width is defined as the position angle extent of the CME in the sky plane.

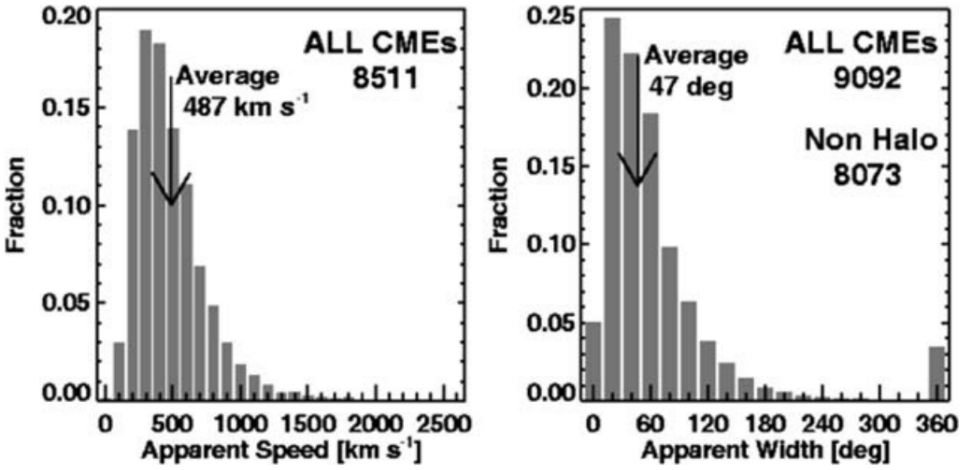

Figure 1.16: Distribution of the apparent speeds (left panel) and widths (right panel) of CMEs observed by the SOHO/LASCO between 1996 and 2004 (*Schwenn et al.*, 2006).

kinetic energy roughly follows a power-law distribution (*Yashiro et al.*, 2008), which is similar to solar flares (*Hudson*, 1991). This may indicate the size and energy of CMEs can extends below the observable threshold (e.g., *Schrijver* 2007).

1.3.2 CME Initiation Models

1.3.2.1 Storage Models

In the storage models, a CME occurs when the slowly evolving coronal magnetic field reaches a point where a stable equilibrium is no longer possible. The slow evolution of the corona is controlled by the motion at the photosphere and below. Because the eruption releases the free magnetic energy stored in the corona, this type of model is called a storage model. The CME breakout model and flux-emergence model are examples of storage models. For the breakout model (*Antiochos et al.*, 1999; *MacNeice et al.*, 2004; *Lynch*, 2006), a quadrupolar initial magnetic field is assumed to form an X-line in the corona. Figure 1.17 shows a sketch of CME breakout by *Antiochos et al.* (1999). The initial magnetic field does not contain electric currents, therefore the system begins with no free energy. A slow shear flow is applied in the central

arcade that gives rise to stressed loops that push outward against the overlaying arcade. At a certain point, magnetic reconnection will occur at high altitude near the pre-existing X-line where a current sheet has formed, which releases the magnetic stress that drives the eruption. Note that not all the field lines are opened in the breakout model, which avoids the Aly-Sturrock hypothesis[7].

In flux-emergence models, CMEs are triggered by magnetic reconnection between emerging field and a stressed coronal field. *Chen and Shibata* (2000) describe a 2D flux-emergence model where an eruption is triggered by forming a current sheet below an emerging flux rope. *Manchester et al.* (2004a) used a fully 3D MHD model to simulate the buoyant flux rope emergence below the surface. They found that slow reconnection plays a key role in transforming the flux rope. The simulation also demonstrated that the shear flows along the polarity inversion line of filaments are a natural consequence of the Lorentz force during the flux rope emergence. Figure 1.18 shows the magnetic field configuration and current density during the flux emergence. *Fan and Gibson* (2007) used a pre-stressed field of an emerging flux rope to model a CME. They start with a flux rope below the surface and slowly emerge it into the corona. The flux rope may or may not erupt depending on the flux rope parameters.

1.3.2.2 Pre-eruption Current Sheet Models

These kinds of models assume there are pre-existing current sheets in the corona. The gas pressure within the current sheet will balance the strong magnetic field outside. And if the current sheet is sufficiently thin, then the high temperature and density cannot be observed. The eruption can be triggered by the introduction of new magnetic flux into the system that causes the current sheet to grow. When the current density exceeds some critical value, a micro-instability is triggered that leads to a dramatic increase in the electrical resistivity and rapid reconnection will then

[7]Aly-Sturrock hypothesis states that the global magnetic energy of a force free field reaches maximum when the field is completely open (*Aly*, 1984, 1991; *Sturrock*, 1991).

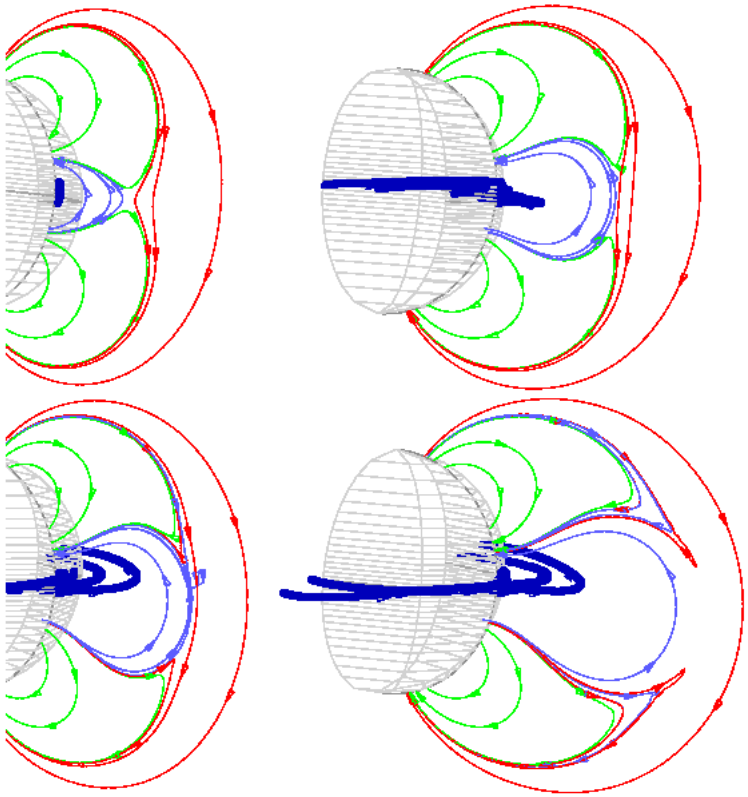

Figure 1.17: A sketch of CME breakout model (*Antiochos et al.*, 1999).

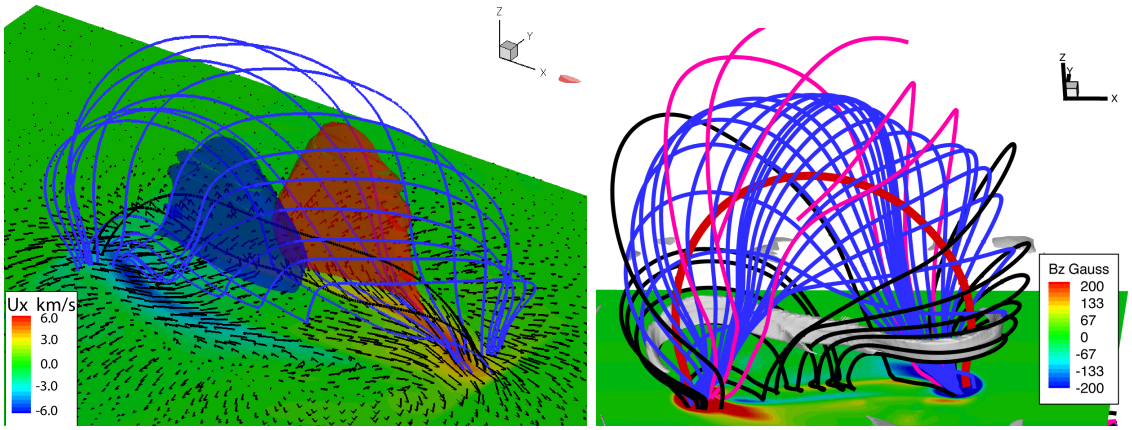

Figure 1.18: Left panel: the background shows the magnitude of the shear velocity (Ux) on the photosphere, with arrows showing the direction of the horizontal flows. The translucent isosurfaces are drawn at -20 km s^{-1} (blue) and 20 km s^{-1} (red). Right panel: the magnetic field configuration during the flux emergence. The bright, ribbon-like structure shows the position of the current sheet *Manchester et al.* (2004a).

occur (*Cassak et al.*, 2006). The last stage is similar to the storage models.

1.3.3 CME-driven Shocks

If the speed of a CME is fast enough, it will drive shocks near the Sun. We have mentioned the shock detection in the white light images in the beginning of the section. In addition to white light observations, there are at least two other techniques that can be used to detect CME-driven shocks. Strong radio emission is known to be associated with propagating shock waves in the solar corona and heliosphere (*Wild and Smerd*, 1972; *Cane et al.*, 1981; *Nelson and Melrose*, 1985; *Lengyel-Frey et al.*, 1997). Just as Langmuir waves can be generated by the electrons from a solar flare, they can also be produced by electrons accelerated by CME-driven shocks, which is called a type II radio burst. Type II emission has a long duration and decreases in frequency with time (the emission is at the plasma frequencies that drop in time as the shock expands into lower density plasma), which provides information on the speed of the CME. CME driven shocks can also be detected with observations of UV spectral

line profiles, which can be used to diagnose the bulk expansion and thermal status of the shocked plasma ahead of a CME. Due to the temporal and spatial resolution limits of spectral observations, the number of observed cases is much smaller than those found with white-light and radio observations. *Ciaravella et al.* (2006) observed 22 halo/partial halo CME events using UVCS observations and found the signatures of CME-driven shocks in 7 cases.

The numerical simulation of CME-driven shocks has been performed by many studies in the past several decades (e.g., *Usmanov and Dryer* 1995; *Wu et al.* 1999; *Groth et al.* 2000; *Odstrcil et al.* 2002; *Riley et al.* 2002). It was found that the CME-driven shock can interact with the bimodal solar wind and form a dimple during the propagation (*Manchester et al.*, 2004b,c; *Lugaz et al.*, 2005). These studies also indicate how the shock is distorted during its propagation from the Sun to the Earth. *Manchester et al.* (2005) investigated the evolution of a CME-driven shock in an ambient solar wind and found the θ_{Bn}[8] changes for magnetic field lines at different heliographic latitude. They also suggested that the compressed field lines in the CME sheath can contribute to the acceleration of energetic particles (*Kóta et al.*, 2005).

1.3.4 Particle Acceleration

The CME-driven shocks[9] can accelerate particles during their propagation in the heliosphere. Such shocks are believed to provide the circumstances necessary for gradual solar energetic particle (SEP) events observed at the Earth(*Reames*, 1999). The particle fluxes during gradual events are typically observed to rise within one to several hours after onset. Given the long decay phase (1-2 days), gradual events are more important for space weather than impulsive events. It is believed that the CME-driven shocks accelerate particles through the diffusive shock acceleration (DSA) mechanism

[8]The angle between the direction of the magnetic field and the shock normal.

[9]Due to the high-speed of CMEs, fast-mode (super-Alfvénic) MHD shocks are most common and are thought to accelerate energetic particles. The fast-mode shock compresses both the plasma and magnetic field.

(*Axford et al.*, 1977; *Bell*, 1978a,b). To understand this acceleration process, we need to start from Fermi acceleration.

Fermi (1949) explained the acceleration of cosmic-ray particles by reflections on moving magnetized clouds. This idea is valid for any moving boundary with higher magnetic fields due to the magnetic mirroring effect that produces a reflection for adiabatic particle motion. Fermi also derived a power law function for the energy spectrum based on statistical arguments that a head-on collision between a particle and a moving magnetic field is more likely than an overtaking one. Therefore, the average particle will be accelerated. The ratio of the reflected to the incident kinetic energy can be calculated in the rest frame of the shock (*Aschwanden*, 2005):

$$\frac{v^2}{u^2} = 1 + (1+\alpha)^2 \frac{\cos^2\theta_{vn}}{\cos^2\theta_{Bn}} - 2(1+\alpha)\frac{\cos\theta_{Bv}\cos\theta_{vn}}{\cos\theta_{Bn}} \tag{1.13}$$

where $\alpha = -\mathbf{v}_{\parallel}/\mathbf{u}_{\parallel}$, θ_{vn} is the angle between $\mathbf{v}$ and shock normal, θ_{Bv} is the angle between the magnetic field and $\mathbf{v}$. For quasi-perpendicular shocks ($\theta_{Bn} \sim 90°$), the second term becomes dominant and leads to large increases of the kinetic energy of the reflected particles ($v^2 >> u^2$). Therefore, we can see that the fast-mode shocks/quasi-perpendicular shocks can accelerate particles effectively, while the slow shocks/quasi-parallel shocks yield little amount of acceleration.

The problem of Fermi acceleration is the energy gain in a single encounter is limited by the shock jump condition. This limitation can be overcome in an inhomogeneous plasma, where particles are scattered back and forth across the shock front many times thereby gaining a large amount of energy. The energy spectra of ions accelerated in DSA were calculated by *Ramaty* (1979) which could reproduce observed γ-ray and interplanetary particle spectra. DSA can accelerate ions up to 100 MeV within less than 1 s. Most of DSA simulations are for cosmic rays (e.g., *Baring et al.* 1994; *Kang and Jones* 1995). Many previous works also tried to simulate DSA under the

planar shock assumption (*Tylka et al.*, 2005; *Li et al.*, 2009; *Guo et al.*, 2010). *Sokolov et al.* (2004, 2009) solved the DSA equation along a selected field line connecting the observer to the Sun and predicted the SEP spectra at 1 AU.

1.4 CME in the Heliosphere – Interplanetary CME (ICME)

1.4.1 Observations and Associated Phenomenon

The ICME[10] is the counterpart of the CME, when it is at much larger distances from the Sun. The methods of ICME detection include interplanetary scintillation, radio burst observations, and *in situ* measurements. Interplanetary scintillation is the oldest method that involves the analysis of radio sources at the meter-wavelength level and tracking the changes to their signals as a dense transient (i.e., ICMEs) passes them. Type II Radio burst observation can monitor the frequency variation of the source as a result of particle acceleration by the shock related to ICMEs. Therefore, this method can track the ICME shock through the heliosphere. Figure 1.19 shows an example of type II and III radio burst related to a CME event. The *in situ* observations (e.g., magnetic field, plasma parameters) can be achieved when the spacecraft moves through the ICMEs. The widely accepted ICME structure was proposed by *Burlaga et al.* (1981). They identified a smoothly rotating magnetic field following an interplanetary shock for an ICME observed by 5 different spacecraft (Voyager 1 & 2, Helios 1 & 2, and IMP-8). The "magnetic cloud" was first used to describe it. Figure 1.20 shows their sketch about this event, including the typical structures of a modern ICME: a shock, a sheath region, and the magnetic cloud.

Long before the discovery of the CME, people started to measure the interplanetary shocks through the radio emission of the accelerated particles. The first *in situ* observation of interplanetary shocks was by the Mariner 2 spacecraft (*Sonett et al.*,

[10]The term "ICME" was first used by Xuepu Zhao (*Zhao*, 1992)

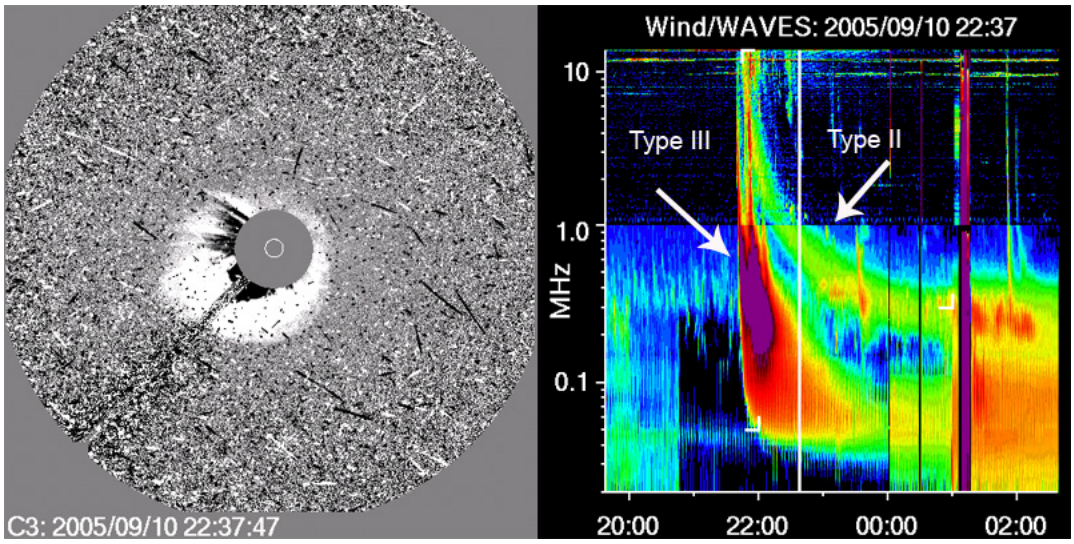

Figure 1.19: Left panel: CME observed by SOHO/LASCO C3. Right panel: A radio dynamic spectrum showing a type II and type III radio burst caused by CME-driven shock acceleration (Credit NASA/ESA).

1964). There are two general classifications of interplanetary shocks: forward shock and reverse shock. A forward shock can be identified in the *in situ* data by a sudden increase in the plasma parameters (solar wind speed, plasma density, temperature, and magnetic field). In some cases, a reverse shock can be observed by a sharp decrease of magnetic field strength, density, and temperature but an increase in solar wind speed. In the left panel of Figure 1.21, an example of *Ulysses* observed forward and reverse shock pair is shown. The right panel shows the forward and reverse shock pair in the MHD simulation by *Manchester and Zurbuchen* (2006).

Magnetic clouds are sometimes observed behind the interplanetary shocks. They contain a large-scale, highly structured magnetic field, which is believed to be the counterpart of the flux rope of the CME. The first direct association between interplanetary shocks and CMEs was made by *Gosling et al.* (1975). They compared a CME observed by *Skylab* with an interplanetary shock detected by Pioneer 9. *Klein and Burlaga* (1982) presented a statistical study of 45 magnetic clouds and confirmed the relationship between the magnetic cloud and ICMEs. Also, they established the characteristics of magnetic clouds in the *in situ* data which is still widely used today:

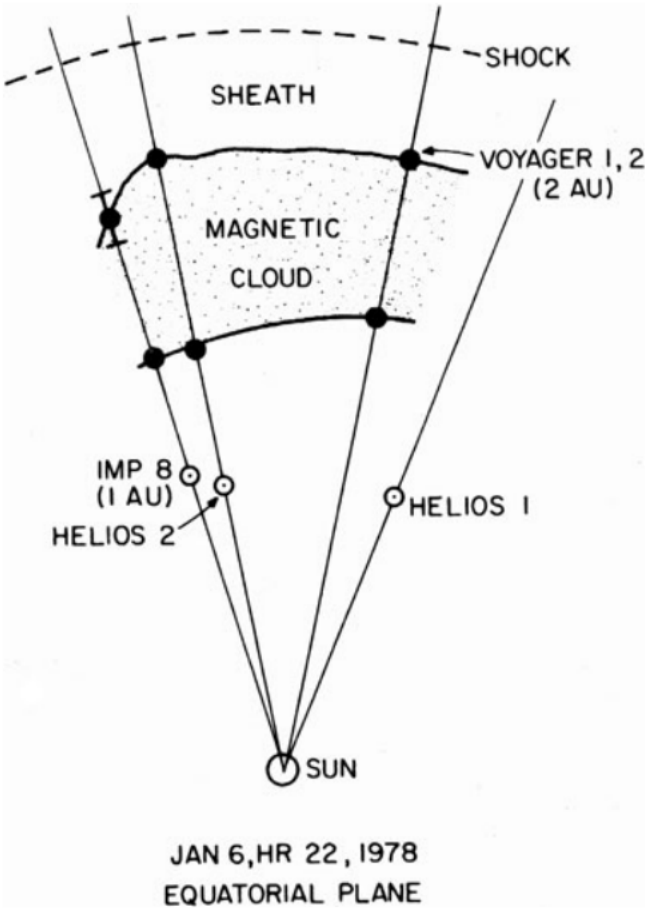

Figure 1.20: Sketch of magnetic cloud observed by *Burlaga et al.* (1981).

1) low plasma temperatures; 2) high magnetic field strength; 3) smoothly rotating magnetic field vector. Magnetic clouds also have a long duration, typically around 10-48 hours with an average of 27 hours. Therefore, they are effective in generating strong geomagnetic activity at Earth when there is a strong sustained southward Bz and a substantial pressure increase associated with the CME-driven shock that compresses the magnetosphere. Since only point observations are available, the 3D structure of magnetic clouds needs to be reconstructed by assuming a flux rope structure with a circular/elliptical cross-section. *Riley et al.* (2004) reviewed many methods to reconstruct the magnetic cloud structures. In Figure 1.22, solar wind plasma and magnetic field parameters across two ICMEs at *Wind* are shown. The first ICME

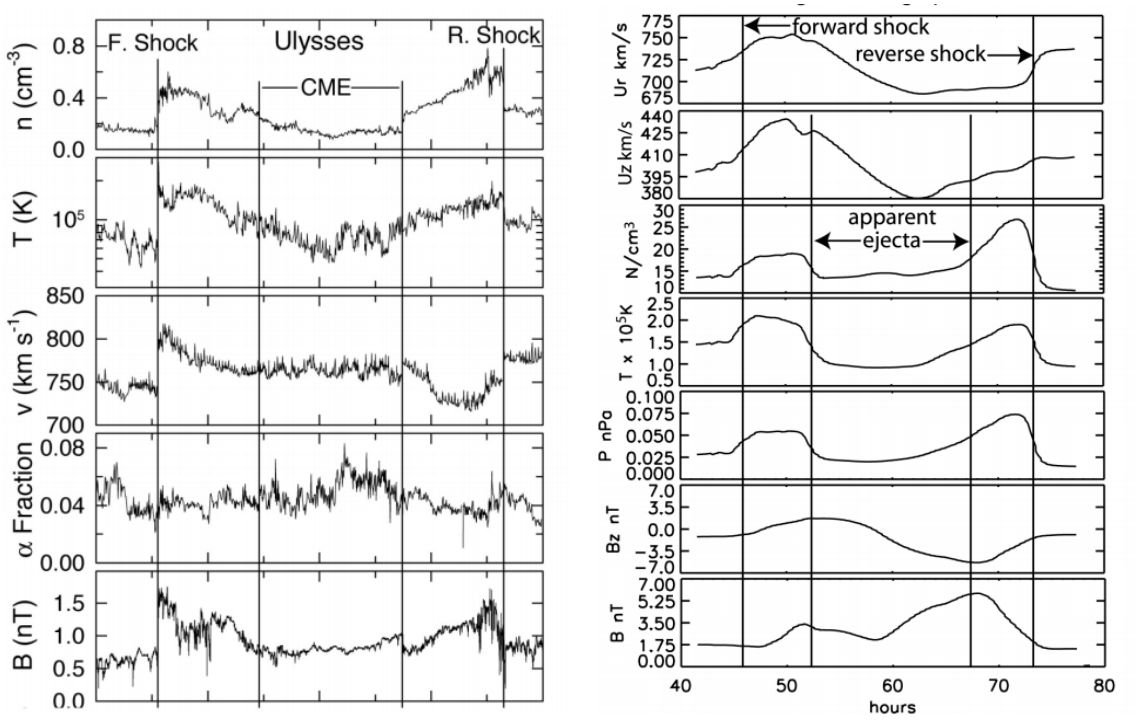

Figure 1.21: Left panel: A forward and reverse shock pair observed by *Ulysses*. Right panel: A forward and reverse shock pair in the MHD simulation (*Manchester and Zurbuchen*, 2006).

and its preceding shock are produced by the 2012 March 7 event. The second ICME and its preceding shock are produced by the 2012 March 10 event.

1.4.1.1 Solar Energetic Particle Events

With fast CMEs, SEP events are always observed at 1 AU. Here shows a physical picture about how we can interpret the *in situ* observations for an SEP event (Figure 1.23): the CME-driven shock is formed very close the Sun, due to the quasi-perpendicular nature of the shock, it can effectively accelerate particles to high energies in minutes. These high-energy particles escape from the upstream of a CME and move through the interplanetary space much faster than the CME and CME-driven shock. Therefore, the energetic particles are seen at 1 AU earlier than the shock arrival. Later, the CME-driven shock crosses the spacecraft and particles are still

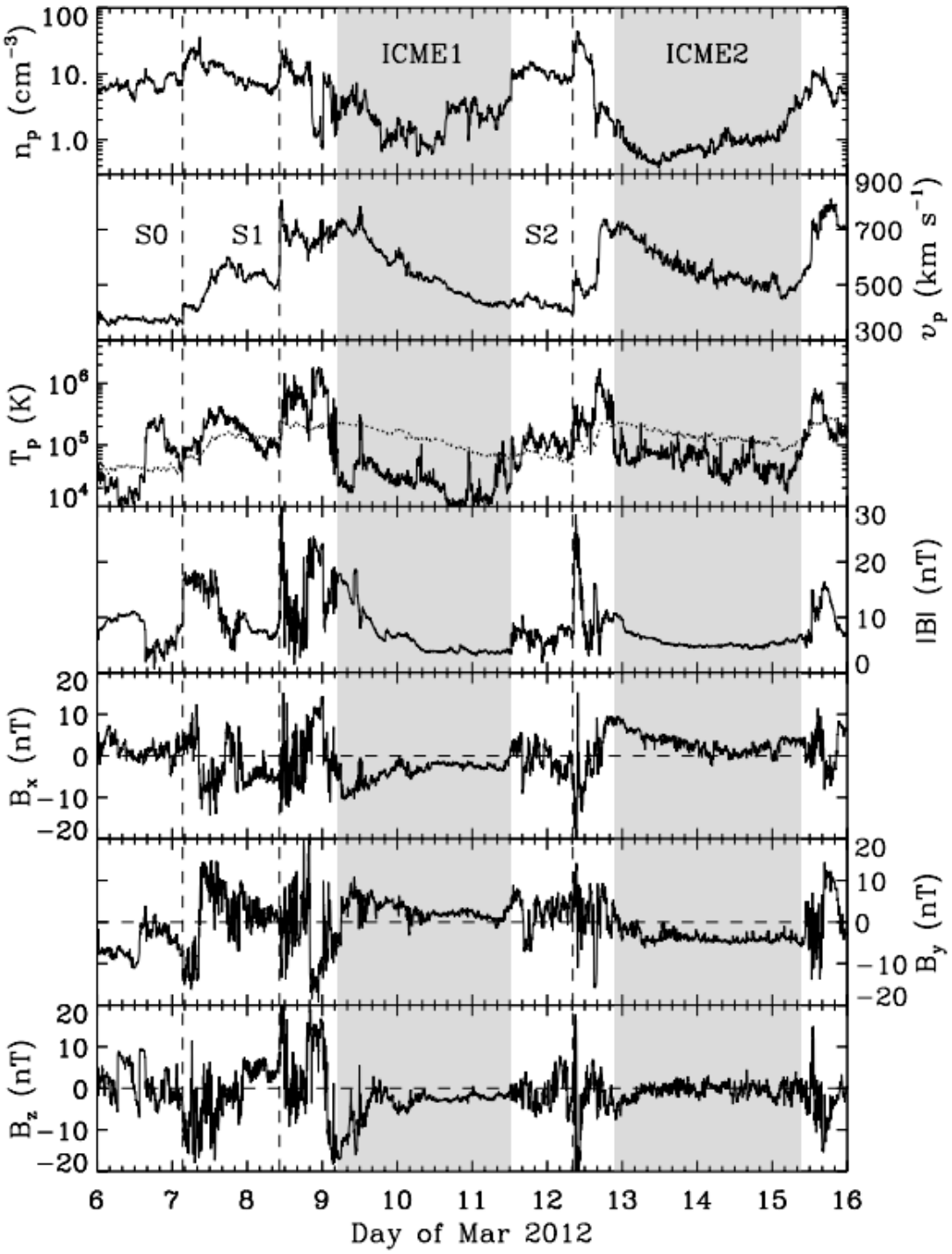

Figure 1.22: Solar wind plasma and magnetic field parameters across two ICMEs observed at *Wind* (*Liu et al.*, 2013).

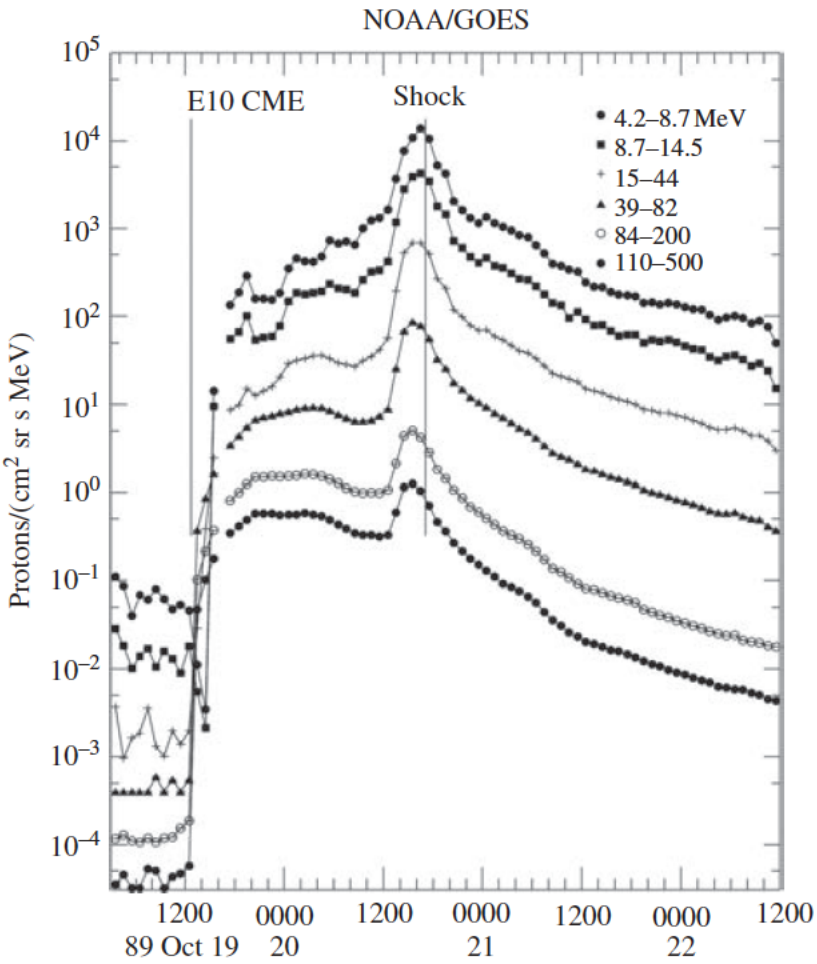

Figure 1.23: The intensity of energetic protons as a function of time for an SEP event associated with a CME on October 19, 1989 (*Reames*, 1999).

being accelerated by the shock and trapped by turbulence in its vicinity, which leads to increased intensity. At last, due to the diffusion and adiabatic cooling effects, the particle intensity decreases. Note that the details of the SEP profile at 1 AU depend on many factors (e.g., location of the source on the Sun, shock strength, solar wind structure).

1.4.2 ICME interaction with Planets and Comets

During the propagation of ICMEs in the heliosphere, they can interact with other bodies in the solar system. The effects of ICMEs on the planets highly depends on the

magnetic field features of the planet. For Mercury, due to its weak magnetosphere, the atmosphere can be stripped away by the solar wind/ICMEs and photoionization processes. Models of Hermean magnetosphere response to the solar wind disturbance have been investigated by *Killen et al.* (2001, 2004). CMEs have been observed at Venus by Pioneer Venus Orbiter (e.g., *Lindsay et al.* 1994; *Luhmann et al.* 2007) and Venus Express (e.g., *Luhmann et al.* 2008a). Due to the lack of magnetic field, ICMEs can enhance the atmospheric ionization on Venus (*Kar et al.*, 1986). Also, the pressure pulse from the ICME shock can decrease the size of Venus ionosphere (*Dryer et al.*, 1982) and expose the neutral atmosphere to the solar wind plasma (*Zhang et al.*, 2008). For Mars, due to the longer distance from the Sun, the ICME should not be strong enough to have an impact on Mars' weak magnetosphere. However, it was found that strong ICMEs can enhance the dayside magnetic field of Mars (*Crider et al.*, 2005). After passing Mars, the ICMEs begin to interact more with CIRs. So it becomes difficult to identify individual events. Also, the magnitude of ICME magnetic fields becomes insufficient compared with the magnetic field of outer planets. From the observation of Jupiter and Saturn, the ICMEs show an impact in the form of aurora intensity enhancement (*Prangé et al.*, 2004).

The ICMEs are also reported to be responsible for the comet disconnection events, during which the tail of the comet appears to be disconnected from its head and moves independently through the solar wind (*Brandt et al.*, 1999; *Jones and Brandt*, 2004). By using the data from SMEI, *Kuchar et al.* (2008) identified 6 disconnection events, in which there is at least one case with an observed ICME passing.

1.4.3 The Fate of ICMEs

At large distance from the Sun, the interaction of different CIRs is possible due to the expansion of CIRs/ICMEs and the overall speed differences between the solar wind structures. When this occurs far from the Sun, the CIRs form a complex

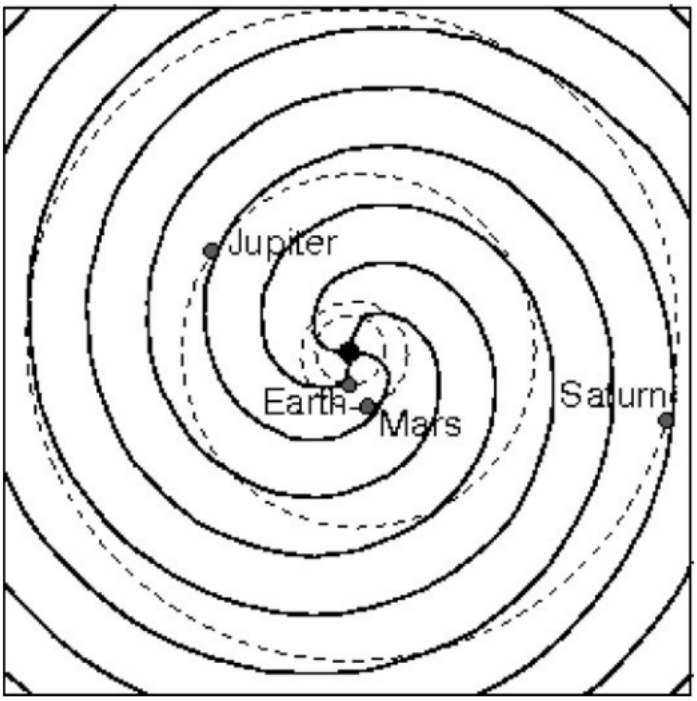

Figure 1.24: Diagram of Parker spirals in the ecliptic plane to 10 AU (*Howard*, 2011).

structures called merged interaction regions (MIRs). MIRs are believed to form at large distance from the Sun (∼5 AU), where the Parker spirals begin to resemble circles centered at the Sun (Figure 1.24). *Burlaga* (1995) demonstrated that ICMEs may eventually merge with MIRs somewhere in the heliosphere. After merging, it becomes a ring around the Sun with large dense structure slowly moving outward. The new coming CMEs will replenish its inner edge. There are studies about the evolution of ICMEs into MIRs (*Burlaga et al.*, 2001; *Whang et al.*, 2001; *Richardson et al.*, 2002). *Richardson et al.* (2002) tracked a CME from the Sun to 58 AU, where its merged structures were observed by Voyager 2. At even greater distance, the MIRs may dissipate to form the background turbulence in the outer heliosphere. Where this occurs is still unknown. However, the MIRs are observed as far as near the termination shock (*Roelof et al.*, 2010).

1.5 Motivations and Outstanding Questions

The motivations of this dissertation are mainly from two perspectives. First, even with the latest CME/ICME detection technology, the information about the CME propagation between the Sun and 1 AU is only obtained through the remote sensing white light images, from which we can only monitor the structure and kinematic evolution of CME/ICME. In order to investigate the internal structures of CME/ICME as well as understand the multiple physical processes involved during their interaction with the solar corona and interplanetary medium, a physics-based, first-principles numerical model is needed. Second, the development of a reliable space weather forecast model is a high national priority for both civilian and national security purposes. As the source of the most destructive space weather, realistic CME modeling is critical for accurate space weather forecasting. In this dissertation, by simulating a realistic event from the chromosphere to 1 AU and comparing with observations, the capability of the global MHD model as a powerful tool for space weather forecasting is shown. The knowledge gained from these studies will go a long way toward the development of physics-based, first-principles space weather forecasting models for CMEs.

There are many unsolved questions about CME/ICME; I list several of them to which this dissertation contributes:

- Most of the CME models are based on the single temperature assumption. However, due to the large difference between the electron and proton mass, they have completely different thermodynamics in the solar wind plasma. How does this thermodynamical difference influence the CME and CME-driven shock structures?

- The CME is embedded in the solar wind plasma, so solar wind structures (e.g., CIR, HCS) have important influence on the CME/CME-driven shock structures. How is the geometry of CMEs and CME-driven shocks affected by their

interaction with plasma and field structures of the solar wind as they propagate through the heliosphere? How are the shock properties (shape, parameters) modified?

- A large fraction of ICMEs observed in the heliosphere appear not to have the flux rope structure (e.g., *Cane and Richardson* 2003), the so-called non-magnetic cloud events or driverless events. The global MHD model has the advantages of highly sophisticated background solar wind and realistic flux rope geometry. Therefore, a complete heliospheric evolution of the simulated CME event can be captured and analyzed to address the driverless events. What is the role of large magnetic structure in the solar corona (e.g., coronal hole) in this process?
- How do CME-driven shocks extend in the heliosphere?
- When, and at what distance, are the shock and the driver separated?

1.6 Organization of the Dissertation

In Chapter II, I performed a multi-spacecraft validation study for a global two-temperature corona and inner heliosphere model, in which different observation and validation techniques are described. For example, for the first time, I compared ionic charge states of carbon, oxygen, silicon, and iron observed by ACE/SWICS with those predicted by our model. The validation results suggest that most of the model outputs can fit the observations very well, which will lead to a great improvement for CME/CME-driven shock modeling. In Chapter III, by employing the validated background solar wind model in both one-temperature (1T) and two-temperature (2T) modes, I performed a numerical study of a CME event that occurred on 2011 March 7. I compared the propagation of fast CMEs and the thermodynamics of CME-driven shocks in both the 1T and 2T modes. Because there is no distinction between electron and proton temperatures, heat conduction in the 1T model creates

an unphysical temperature precursor in front of the CME-driven shock and makes the shock parameters (e.g., shock Mach number, compression ratio) incorrect. The results demonstrate the importance of the electron heat conduction in conjunction with proton shock heating in order to produce physically correct CME structures and CME-driven shocks. In Chapter IV, I present the global MHD simulation results of the CME that occurred on 2011 March 7 by using the newly developed Alfvén Wave Solar Model (AWSoM) in Space Weather Modeling Framework (SWMF). Comprehensive validation work is done using both remote as well as the *in situ* observation from SDO, SOHO, STEREOA/B, and OMNI. Our results show that the new model can reproduce most of the observed features near the Sun (e.g., CME-driven EUV waves, deflection of the flux rope from the coronal hole, "double-front" in the white light images) and in the heliosphere (e.g., CME-CIR interaction, shock properties at 1 AU). By fitting the CME speeds near the Sun with observations, the CME-driven shock arrival time is within 1 hour of the observed arrival time and all the *in situ* parameters are correctly simulated, which suggests the global MHD model is a powerful tool for the space weather forecasting. In Chapter V, I summarize the conclusion reached by this dissertation, followed by the limitations of current studies as well as suggestions for future work.

CHAPTER II

A Global Two-Temperature Corona and Inner Heliosphere Model: A Comprehensive Validation Study

Of all tools, an observatory is the most sublime...What is so good in a college as an observatory? The sublime attaches to the door and to the first stair you ascend; – that this is the road to the stars.

– Ralph Waldo Emerson, *1865*

2.1 Introduction

As the source of coronal mass ejections (CMEs) as well as solar wind, understanding the solar corona is critical for space weather forecasts. Although the physical origin of the hot corona and the expanding solar wind is still in debate, Alfvén wave acceleration of solar wind has been considered as one of the possible mechanisms (*Belcher*, 1971; *Jacques*, 1977). In this type of model, the wave pressure gradient will accelerate the solar wind while the gradual dissipation of the waves can heat the plasma (*Hollweg*, 1986). In the past two decades, a number of coronal models have been created that use Alfvén waves: e.g., *Suzuki* (2006), constructed a 1D model

that forecasts the solar wind speed at 1AU, while e.g. *Lou* (1994); *Ofman and Davila* (1995); *Bravo and Stewart* (1997); *Ruderman et al.* (1998); *Usmanov et al.* (2000) analyzed the Alfvén waves in 2D. *Usmanov et al.* (2000) for the first time developed 2D global axisymmetric solar wind models with Alfvén waves. Fully 3D solar wind models with Alfvén waves have been studied by e.g. *Evans et al.* (2009) for the surface Alfvén wave damping mechanism, and *van der Holst et al.* (2010) developed a 3D solar wind model from Sun to 1 AU that utilizes observational data for the boundary conditions. *Sokolov et al.* (2009) coupled the frequency-resolved transport equations for the Alfvén waves to the magnetohydrodynamics (MHD) equations for an arbitrary 3D domain. Partial reflection of Alfvén waves has also been investigated (e.g., *Chandran and Hollweg* 2009; *Cranmer* 2010; *Verdini et al.* 2010). Note that there are other mechanisms that could be responsible for coronal heating. One is reconnection between open and closed field lines. Reconnection is considered the most likely channel to convert magnetic energy to heat (e.g., *Priest and Forbes* 2000). Since only a small fraction of the coronal magnetic field is open to the heliosphere, the dominant source of energy should come from the stochastic reconnections between open and closed field lines (e.g., *Fisk et al.* 1999, *Schwadron et al.* 2006). Reconnection heating is more difficult for numerical modeling than wave heating mechanisms due to the multi-scale nature of magnetic reconnection. To accurately model the interaction between closed and open field lines, a fully 3D coronal magnetic field is needed. Some initial work with reconnection heating mechanism can be found in *Fisk* (2005); *Tu et al.* (2005). *Parker* (1983, 1988) also proposed a nanoflare coronal heating model, and there are many discussions and works since then (e.g., *Cargill* 1994; *Klimchuk* 2006; *Aschwanden* 2008; *Janse and Low* 2009). In nanoflare heating models, ohmic dissipation of electric currents is responsible for the coronal heating, which would preferentially heat electrons.

Another property that is important in the modeling of the solar corona as well as

of the inner heliosphere is the different temperatures of electrons and protons. This occurs beyond $\sim$2 $R_\odot$ where the collisions between these two species are infrequent (*Hartle and Sturrock*, 1968). Different temperatures between electrons and ions have been found by SOHO/SUMER and SOHO/UVCS (*Seely et al.*, 1997; *Tu et al.*, 1998). A more thorough investigation of different temperature between electrons and ions is made by *Landi* (2008); *Landi and Cranmer* (2009). The model effects have been extended to both 1D and 2D (e.g., *Tu and Marsch* 1997; *Laitinen et al.* 2003; *Vainio et al.* 2003; *Endeve et al.* 2004; *Hu et al.* 2003a,b). The 2D two-temperature model of *Hu et al.* (2003a,b) shows good agreement with *Ulysses in situ* observations of protons at 1AU.

By separating electron and proton temperatures and heating protons by Kolmogorov wave dissipation (*Hollweg*, 1986), *van der Holst et al.* (2010) developed a new global 3D two-temperature corona and inner heliosphere model. In this model, the collisions between the electrons and protons are taken into account as well as the anisotropic thermal heat conduction of the electrons. While *Lionello et al.* (2009) and *Downs et al.* (2010) used a boundary formulation that starts from the chromosphere, in the model of *van der Holst et al.* (2010) this boundary was elevated to $r = 1.035R_\odot$ for computational speed. Moreover, the inner boundary of the initial state is specified by observational data. This model uses a synoptic GONG (Global Oscillation Network Group) magnetogram and the potential field source surface (PFSS) model to determine the initial magnetic field configuration. The PFSS model can be solved by spherical harmonics or a finite difference method, see *Tóth et al.* (2011a). The differential emission measure tomography (DEMT) method (*Frazin et al.*, 2009; *Vásquez et al.*, 2010) is applied to EUV images observed by Extreme UltraViolet Imager (EUVI; *Howard et al.* 2008) on the Solar Terrestrial Relations Observatory (STEREO) A/B in order to provide the electron temperature and density at the inner boundary, while the Alfvén wave pressure is determined via the empirical Wang-Sheeley-Arge

(WSA) model (*Arge and Pizzo*, 2000). The set of two-temperature MHD equations is then numerically solved in the heliographic rotating frame by shock-capturing MHD BATS-R-US code (*Powell et al.*, 1999). To obtain the solution from the Sun to the Earth, we couple the Solar Corona (SC; to $24R_{\odot}$) and Inner Heliosphere (IH; to $250R_{\odot}$) components in the SWMF. The inner boundary of the IH is located at $r = 16R_{\odot}$ such that the two components overlap. The inner boundary conditions of the IH are obtained from the SC. The model output can provide all plasma parameters (e.g., density, velocity, temperature, pressure, and magnetic field), which will be compared with the observations.

The partition of turbulent energy between electrons and protons is still under debate. However, the partition could be a key factor to improving the physical realism as well as the model forecast accuracy. The early works from both the observational analysis (*Pilipp et al.*, 1990) and theoretical predictions (*Leamon et al.*, 1999) suggest that the *in situ* electron heating should be on the same order as the proton heating. *Stawarz et al.* (2009) compare the energy cascade rates with proton heating rates at 1 AU using Advanced Composition Explorer (ACE; *Stone et al.* 1998) observations. They find that the energy cascade rates are consistently higher than the energy required for the observed proton heating. Therefore, they postulate that the electron heating by the turbulent cascade is less than or at most equal to the rate of proton heating. With the comparison to *Ulysses* data, *Breech et al.* (2009) point out that 60% of the turbulence energy goes into proton heating while 40% goes into electron heating. *Cranmer et al.* (2009) obtain the similar results from *Helios* and *Ulysses* data. More recently, *Usmanov et al.* (2011) developed an axisymmetric steady-state solar wind model in which they suggest a similar heating rate division as *Breech et al.* (2009). Based on a turbulent energy cascade model (*Howes et al.*, 2008), *Howes* (2011) predicts the proton-to-total plasma heating in the fast solar wind. The result is consistent with *Cranmer et al.* (2009) for $R \gtrsim 0.8AU$. The discrepancy for

$R \lesssim 0.8AU$ can be explained by considering proton cyclotron damping. In the solar wind model of *van der Holst et al.* (2010), the dissipation of Alfvén waves is assumed to heat only the protons. In the present work, we will distribute the dissipation energy between electrons and protons, allocating 40% of such energy to the electrons as suggested by *Breech et al.* (2009). This value is treated as a global constant in our simulation. However, given the lack of observational constraints between the Sun and 1 AU, the value could change closer to the Sun.

In this Chapter, we compare our model output for the solar minimum Carrington rotation 2077 (2008 November 20 through December 17) with a comprehensive set of space observations from ACE, STEREO A/B, as well as Venus Express. Since there were very few CMEs during this rotation, it is ideal for the solar wind model validation. Near the Sun (1.035 $R_\odot$ – 1.22 $R_\odot$), we compare the model output with the electron temperature and density derived by the DEMT method using EUVI images observed by STEREO A/B. We also use Large Angle and Spectrometric Coronagraph C2 (LASCO; *Brueckner et al.* 1995a) tomography method to derive the electron density between 2.3 $R_\odot$ and 6.0 $R_\odot$ and compare it with the model electron density. In the inner heliosphere, the proton states (density, temperature, velocity) and magnetic field are compared for all the *in situ* observations from ACE, STEREO A/B, and Venus Express. Furthermore, we apply the ion composition model developed by *Gruesbeck et al.* (2011) by using the electron temperature, density, and wind velocity predicted by our model to calculate for the first time the ionic charge states of C , O , Si , and Fe at 1 AU and compare them with the *in situ* observations of the Solar Wind Ion Composition Spectrometer (SWICS; *Gloeckler et al.* 1998) onboard ACE. The electron density and temperature obtained from Hinode/EIS spectral data are also compared with DEMT and model output near the Sun.

The Chapter is organized as follows. In Section 2, we compare the electron heating model output with the former model output without electron heating. The validation

results are presented in Section 3, followed by the summary and conclusions in Section 4.

2.2 The Two-Temperature Model with Electron Heating

The newly developed two-temperature model (*van der Holst et al.*, 2010) is implemented in the MHD BATS-R-US code (*Powell et al.*, 1999) within the Space Weather Modeling Framework (SWMF, *Tóth et al.* 2005, 2012). Compared to the previous version of Solar Corona (SC) and Inner Heliosphere (IH) models (*Cohen et al.*, 2007) in SWMF, the new model uses a uniform $\gamma = 5/3$ for SC and IH, and thus avoids the decrease of γ in the *Cohen et al.* (2007) SC model that could distort the propagation of CMEs and CME-driven shocks. New observations from Hinode/EIS found that the effective adiabatic index for electrons in the corona is 1.10 ± 0.02 due to thermal conduction and coronal heating (*Van Doorsselaere et al.*, 2011). However, since the reduced heat conduction for ions and decoupling between ions and electrons, the γ for ions should be $\sim 5/3$, which is also consistent with the shock compression ratios determined from SOHO/LASCO observations (*Ontiveros and Vourlidas*, 2009).

In this study, we use the new two-temperature model and partition 40% of the dissipation energy to heat electrons to better reproduce the conditions in the space environment. We also double the magnetic field observed by GONG at the inner boundary in order to compensate for the uncertainties of the synoptic magnetogram observation, especially in the polar region, as well as increase the magnetic strength at 1 AU (*Cohen et al.*, 2007). We keep the rest of the model setup the same as described in the previous paper (*van der Holst et al.*, 2010).

In Figure 2.1, a comparison between the SC output and SOHO/EIT observation is shown. The left image in Figure 2.1 shows the EIT 195 Å observation on 2008 November 29. In general, the Sun is very quiet except for a weak active region close to the north pole (without AR number). A large disk coronal hole region can

be seen clearly around the equator, which extends to high latitude in the northern hemisphere. The middle and right images in Figure 2.1 show the SC output for the radial magnetic field and proton density at r = 1.055 $R_\odot$ with selected field lines. For the radial magnetic field image, the field lines are colored by the electron temperature. We can see that the 3D topology of the solar magnetic field near the surface at solar minimum is characterized by open magnetic flux with lower temperatures at the two polar coronal hole regions, and closed magnetic field lines with higher temperatures in the low latitudes. The active region can generate hot coronal loops. The existence of on-disk coronal holes (including polar and low-latitude coronal holes) is one of the major features of the solar corona during solar minimum (See review paper by *Cranmer*, 2009). Therefore, the comparison of on-disk coronal holes between the observation and model is helpful for the model validation. In the right image of Figure 2.1, we show the proton density at r = 1.055 $R_\odot$. The on-disk coronal hole regions shown in EIT 195 Å image can be seen as the low density regions in the model output. The field lines of the right panel are colored by radial solar wind velocity, which suggests that the fast solar wind mainly comes from polar open field line regions and the slow solar wind originates near the solar equator. In general, the model output near the Sun reproduces many observed features.

In Figure 2.2, the meridional slice of the SC ($-24R_\odot \leq (x, y, z) \leq 24R_\odot$) shows the electron temperature (top left), proton temperature (top right), radial solar wind velocity (bottom left), and proton density (bottom right). The model output without electron heating can be found in Figure 5 and 6 in *van der Holst et al.* (2010). Both the electron and proton temperatures are increased from *van der Holst et al.* (2010) model due to the change of the magnetic strength at the inner boundary. The electrons and protons near the Sun are in temperature equilibrium due to the Coulomb collisions. With the decrease of the density away from the Sun, the collisions become infrequent, therefore the electron and proton temperatures become different. For the electron

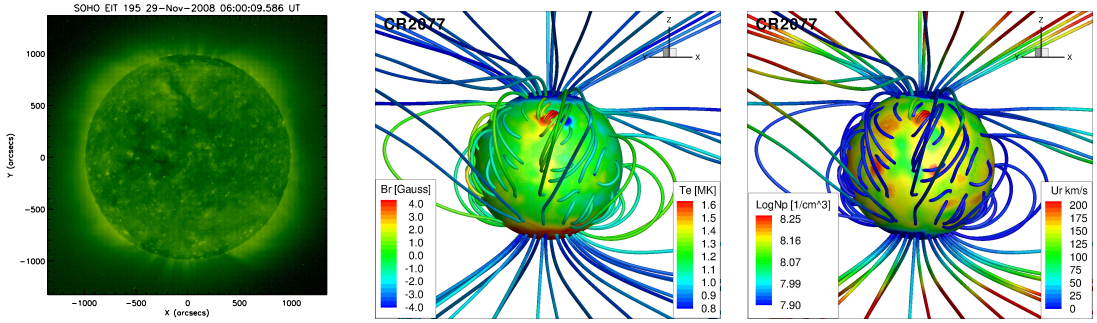

Figure 2.1: Comparison between the SC output and SOHO/EIT observation. *Left*: SOHO/EIT 195 Å observation on 2008 November 29. *Middle*: Radial magnetic field at r = 1.055 $R_\odot$ with selected field lines. The field lines are colored by the electron temperature. *Right*: Proton density at r = 1.055 $R_\odot$ with selected field lines. The field lines are colored by the radial solar wind velocity.

temperature, we can still see the high temperature (above 1MK) in the streamer region due to the electron heat conduction. The most obvious difference of electron temperatures between the models with and without electron heating lies in the coronal hole region. Without electron heating, the electron temperature decreases due to cooling by the adiabatic expansion of the solar wind plasma. With electron heating, the electrons maintain a high temperature ($\sim$ 1 MK) within $\sim$10 $R_\odot$ which then gradually decreases. The proton temperature shows similar bimodal structure. Due to the dissipation of Alfvén waves, the protons are hotter in the fast wind than in the slow wind. The proton temperature reaches $\sim$4 MK at $\sim$5 $R_\odot$. There is no evident change to the solar wind velocity after adding the electron heating. The fast wind at high latitude reaches 700 km s^{-1} and the slow wind speed at low latitude is below 400 km s^{-1}. The square boxes in the velocity figure show the adaptive mesh blocks. The refinement is made near the Sun and at the heliospheric current sheet (HCS). From the proton density figure, that latitude is also the region with the highest plasma density.

In the velocity map of Figure 2.2, we also show some critical surfaces calculated

from the model. The white contour line shows the critical surface where the solar wind speed equals the poloidal Alfvén speed (the Alfvén Mach number is unity). We can see that the radius of the Alfvén critical surface is $\sim$10 $R_\odot$ outside of the streamer belt. Within the streamer belt, due to the increased density, the critical surface location drops to $\sim$5 $R_\odot$. The black and red contour lines show the two critical surfaces where solar wind speeds are the same as the fast and slow magnetosonic-wave speeds, respectively. From the three critical surfaces, we can see clearly the Alfvén and fast magnetosonic critical surfaces coincide with each other at the polar regions, which is due to the fact that Alfvén speed is larger than sound speed. Similarly at the equator, the Alfvén and slow magnetosonic critical surfaces coincide because Alfvén speed is smaller than sound speed. Our results can be compared with some previous studies (*Keppens and Goedbloed*, 1999; *Usmanov et al.*, 2000). The critical surfaces are very important for both theoretical and simulation studies. Beyond the critical surface, the inward propagating waves cannot exist due to the faster outward moving solar wind plasma. To further validate the critical surface results, we need observations nearer to the Sun. Future missions (e.g., Solar Probe[1]) could bring us more valuable information about this issue.

[1]http://solarprobe.gsfc.nasa.gov/

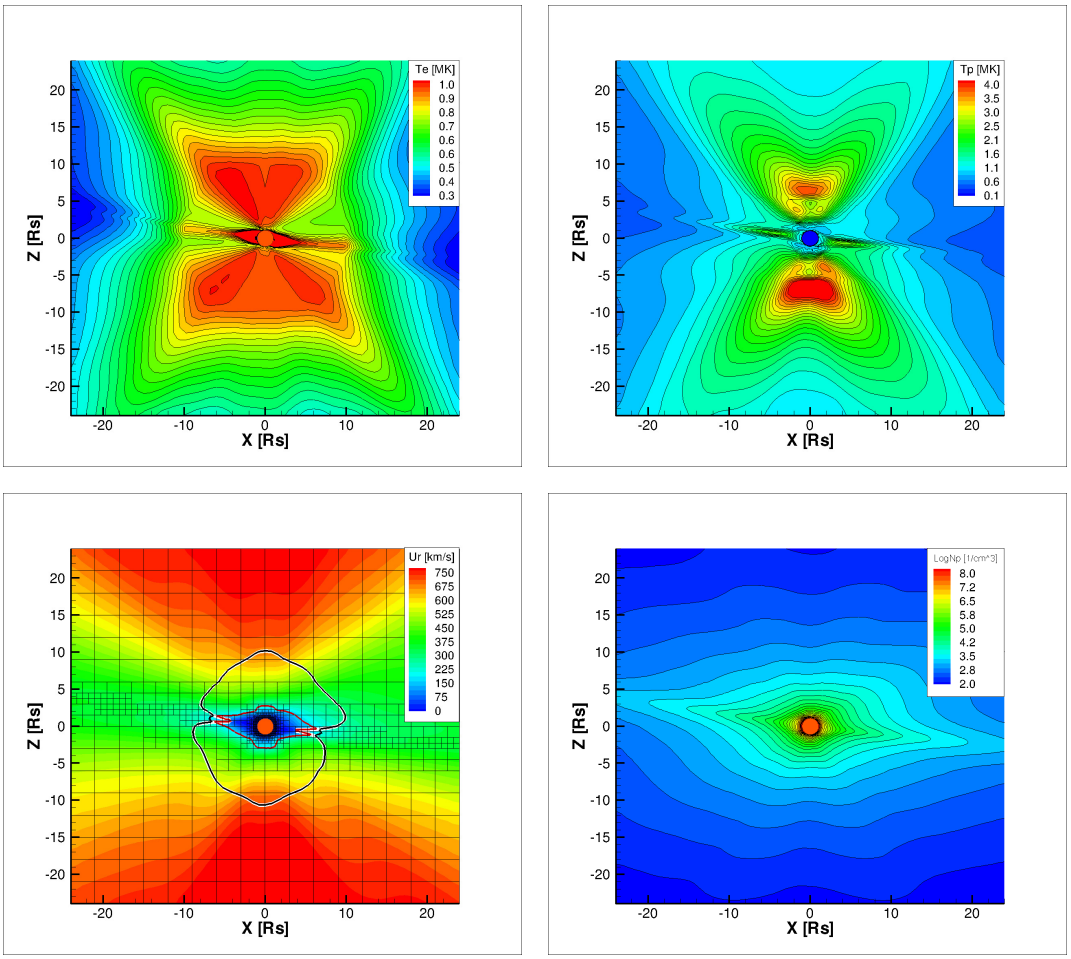

Figure 2.2: Meridional slice of the SC showing the electron temperature (top left), proton temperature (top right), radial solar wind velocity (bottom left), and proton density (bottom right). The square boxes in the velocity figure represent the grid blocks, showing adaptive mesh refinement near the Sun and the current sheet. The white contour line shows the critical surface where the solar wind speed equals the poloidal Alfvén speed. The black (red) contour line shows the critical surface where the solar wind speed equals the poloidal fast (slow) magnetosonic-wave speed.

In order to evaluate the electron heating effect in the two-temperature model near the Sun, we compare the model output with electron heating to the electron temperature and density derived from EUV images of the Sun by using the DEMT method (*Frazin et al.*, 2009; *Vásquez et al.*, 2010). In general, the DEMT method uses a time series of EUV images under the assumption of no time variation and

uniform solar rotation to derive 3D emissivity distribution in each EUV band. By Local Differential Emission Measure (LDEM) analysis, the 3D distribution of the electron density and temperature can be obtained. The DEMT method assumes the plasma is optically thin. In this study, we use three bands of EUV observation (171, 195, and 284 $\mathring{A}$) from EUVI on the STEREO A and B spacecrafts.

The top panels of Figure 2.3 shows the comparison between the model output and the DEMT derived electron temperature (left panel) and number density (right panel) near the Sun. In both panels, the ring between r = 1.035 $R_\odot$ and 1.225 $R_\odot$ shows the ratio between the model and DEMT output. Outside this ring, the two-temperature model output is shown. At the center, the iso-surface of the Sun is taken at R = 1.055 $R_\odot$ with the radial magnetic field shown on the surface. Some of the DEMT data points are set to zero due to the dynamic variation of the corona. These regions are marked by white. The temperature ratio is between $\sim$0.9 and $\sim$1.1 for most of the region. The relatively larger differences are shown outside the north polar region where the DEMT data shows two hot belts where the temperature is $\sim$40% hotter than the model. These two hot belts are associated with active regions, which our model (in its current form) cannot reproduce via Alfvén wave dissipation in closed field line regions. Due to the electron heating by the Alfvén waves dissipation, the electron temperature of the solar wind model increases in the coronal hole above $\sim$1 MK, which is also seen in the tomography. The ratio between the model and DEMT density is $\sim 0 - 0.3$ in log-scale ($\sim 1 - 2$ in normal scale) for most of the region. In the middle and bottom panels of Figure 2.3, we show the temperature and density curves at 1.1 $R_\odot$ as well as along the Y- and Z-axis. This demonstrates that the electron heating is sufficient and the density scale height reproduces the observations.

Although the results suggest a quantitative agreement between the model output and DEMT reconstruction, the assumptions of DEMT make it hard to evaluate the accuracy of the results. First, DEMT used 3/4 of a Carrington rotation's data to

reconstruct the density and temperature maps, while assuming no dynamic evolution of the corona. Also DEMT assumes a fixed iron abundance, to which the derived electron density is inversely proportional. In this work, we assume $[\mathrm{Fe}]/[\mathrm{H}] = 1.26 \times 10^{-4}$, which is 4 times higher than the photospheric value (*Grevesse and Sauval*, 1998) due to the low first ionization potential (FIP) (*Feldman et al.*, 1992). The derived electron temperature is not affected by this caveat, but by the assumed ionization equilibrium fractions of the Fe ions. In the DEMT results here included (*Vásquez et al.*, 2010), we used the ionization equilibrium calculations by *Arnaud and Raymond* (1992) to compute the EUVI bands' temperature responses. Therefore, we need further observational data to compare with and validate our model output. To achieve this, we use the spectral observation from the EUV imaging spectrometer (EIS) onboard Hinode to derive the electron density and temperature for a certain location and time during CR2077 and compare the result with model and DEMT output.

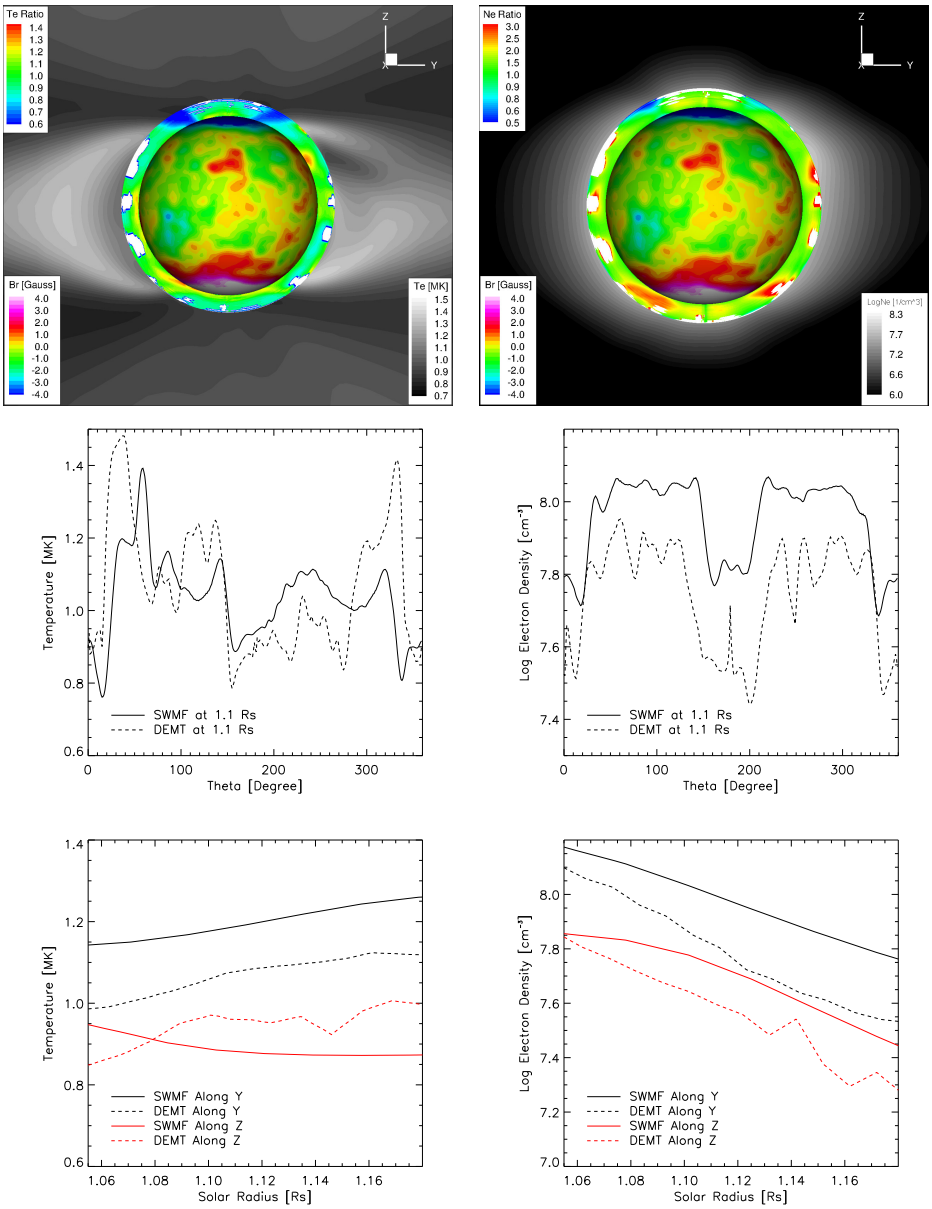

Figure 2.3: Comparison between the meridional slices of the SC and DEMT output near the Sun for electron temperature (left panel) and log electron number density (right panel). The inner ring shows the ratio between the model and DEMT output from 1.035 $R_\odot$ to 1.225 $R_\odot$ and outside background shows the model output. The iso-surface of the Sun is taken at R = 1.055 $R_\odot$ with the radial magnetic field shown at that layer. Middle Left: Model and DEMT electron temperature at 1.1 $R_\odot$. Middle Right: Model and DEMT electron number density at 1.1 $R_\odot$. The angle is measured clockwise from positive Z direction. Bottom Left: Model and DEMT electron temperature along Y- and Z-axis. Bottom Right: Model and DEMT derived electron number density along Y- and Z-axis.

The west limb was observed on 3 December 2008 by the Hinode/EIS. A description of the EIS instrument can be found in *Culhane et al.* (2007). The observations were carried out using the 1″ slit, and the central 128″ of the EIS detectors were downloaded. The EIS pointing was moved along the E-W direction 128 times with 1″ steps, so that the nominal field of view was 128″×128″. For each pointing, an exposure time of 90s was used. The entire wavelength range of each EIS channel was downloaded, resulting in a full solar spectrum in the 166-212 Å and 245-291 Å wavelength ranges for each pointing. The center of the slit was pointed at $(1025'', 14'')$, and a tiny portion of the limb was included in the field of view. Figure 2.4 shows the EIS field of view at three different temperatures using lines from He II (formed at $T \simeq 50,000$ K), Fe VIII (formed at $T \simeq 400,000$ K) and Fe XII (formed at $T \simeq 1,500,000$ K). The sharp decrease of the He II intensity gives an approximate indication of the location of the solar limb; the intensity of all lines decreases exponentially beyond it. The data were reduced, cleaned and calibrated using the standard EIS software available in SolarSoft. A wavelength-dependent shift along the N-S direction was applied to the images to account for the CCD spatial offset of the images; this was also calculated using the standard EIS software.

Figure 2.4 shows the EUV image observed by *SOHO*/EIT on 3 December 2008. The white box shows the EIS field of view. The EIS observation suggests that the field of view is quite unstructured at transition region (i.e. Fe VIII) temperatures, but shows two brighter areas and a darker lane at coronal temperatures. We have thus selected three datasets ("A", "B" and "C") to carry out the analysis, each including one of these features, and averaged the observed emission along the N-S direction at each position in the E-W scan. The position of the these three regions are marked by white dashed lines in Figure 2.4. The resulting dataset consisted of three series of full EIS spectra as a function of height. The signal-to-noise becomes so low above 1.08 $R_\odot$ that line intensities are too uncertain to derive physical properties of the

emitting plasma. We also are interested only in data above 1.02 $R_\odot$, to match the lowest height reached by tomographic reconstructions. We thus studied the spectra in the 1.02-1.07 $R_\odot$ range only.

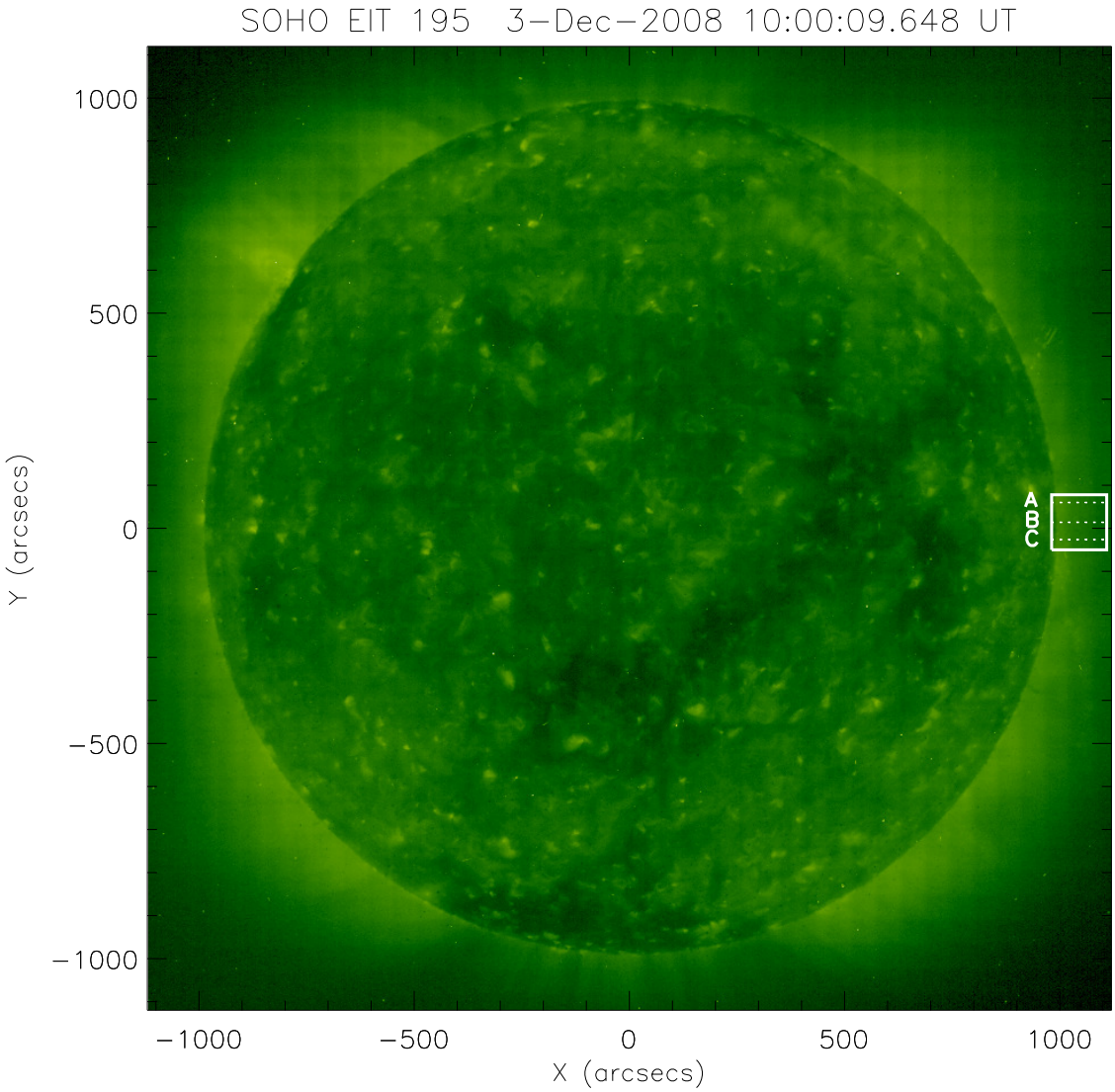

Figure 2.4: SOHO/EIT 195 Å observation on 2008 December 3. The white box shows the EIS field of view. The white dashed lines show the positions of the datasets used in this study.

We measured the plasma electron density and thermal structure applying stan-

dard diagnostic techniques to EIS spectral line intensities. We measured the electron density using line intensity ratios, while we determined the plasma distribution with temperature for each region at each height by measuring the so-called Differential Emission Measure (DEM) of the plasma using the iterative technique developed by *Landi and Landini* (1997). In our analysis, we used Version 6.0.1 of the CHIANTI database (*Dere et al.*, 1997, 2009), and calculated the line emissivities adopting the ion fractions of *Bryans et al.* (2009) and the coronal abundances from *Feldman et al.* (1992).

Several ions provide line intensity ratios that can be used to measure the plasma electron density. However, signal to noise limited the maximum height where each ratio was able to provide meaningful electron density measurements. The Fe XII 186.8/195.1 intensity ratio proved to be the less noisy and allowed us to determine the electron density throughout the entire range of heights spanned by the observations. Figure 2.5 shows the results: the electron density decreases exponentially with height; no significant difference is observed between the three regions. If we assume that the plasma is plane parallel and in hydrostatic equilibrium, the rate of density decrease in the 1.02-1.07 $R_\odot$ range corresponds to a plasma electron temperature of $T \simeq 3.8 \times 10^6$ K, significantly larger than typical quiet Sun coronal temperatures (*Phillips et al.* 2008 and references therein).

The plasma DEM curves were measured for all three datasets and the results are shown in Figure 2.6. There are a few comments to the results. First, all three regions show qualitatively the same plasma distribution, although region C has slightly lower DEM curves. Second, all DEM curves are peaked around $\log T = 6.05$, with a full width half maximum $\Delta \log T \simeq 0.07$: the plasma along the line-of-sight (LOS) is rather tightly clustered around the peak temperature. The DEM peak temperature is a factor $\simeq 3$ lower than the temperature derived by the density scale height. Third, the DEM peak values decrease monotonically with height but they do not significantly

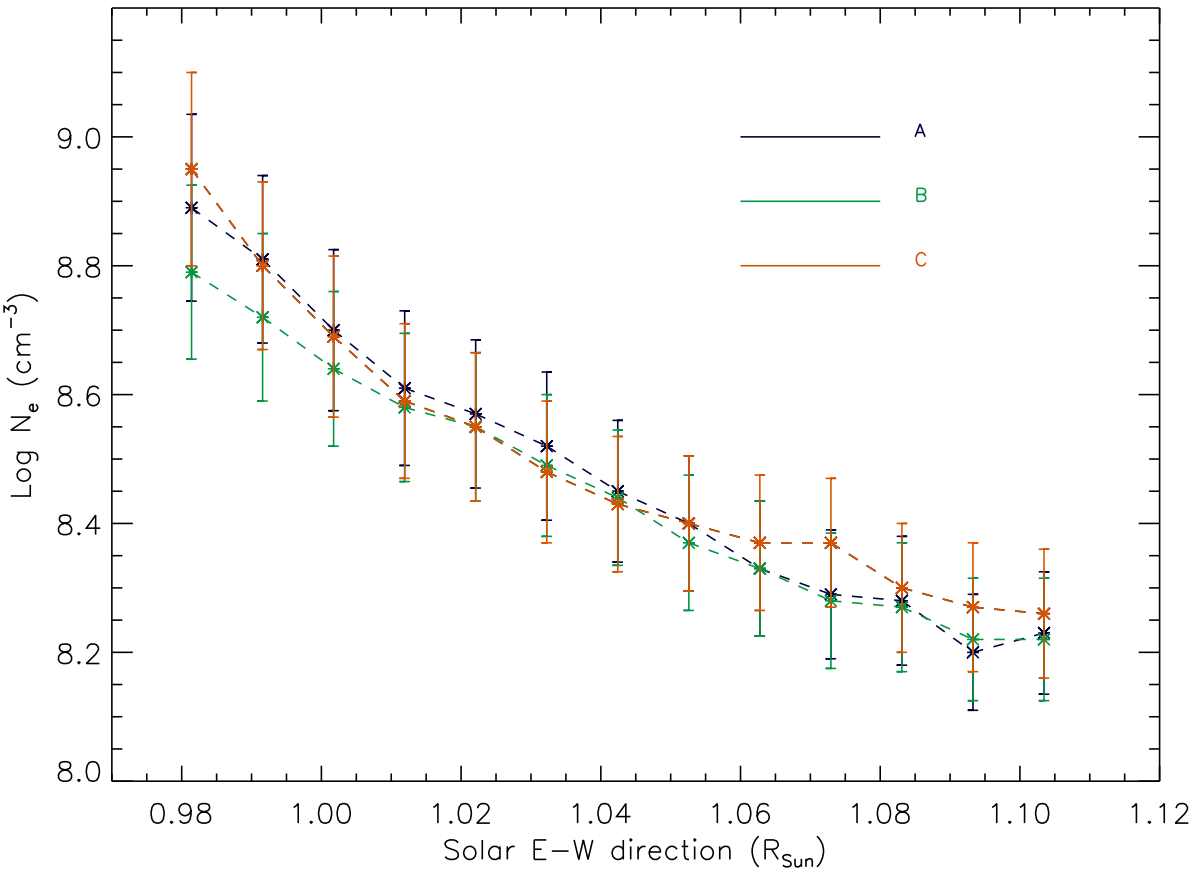

Figure 2.5: Electron number density values measured as a function of distance from the Sun center using the Fe XII 186.6Å/195.1Å intensity ratio. The "A", "B", and "C" curves represent the three selected datasets shown in Figure 2.4.

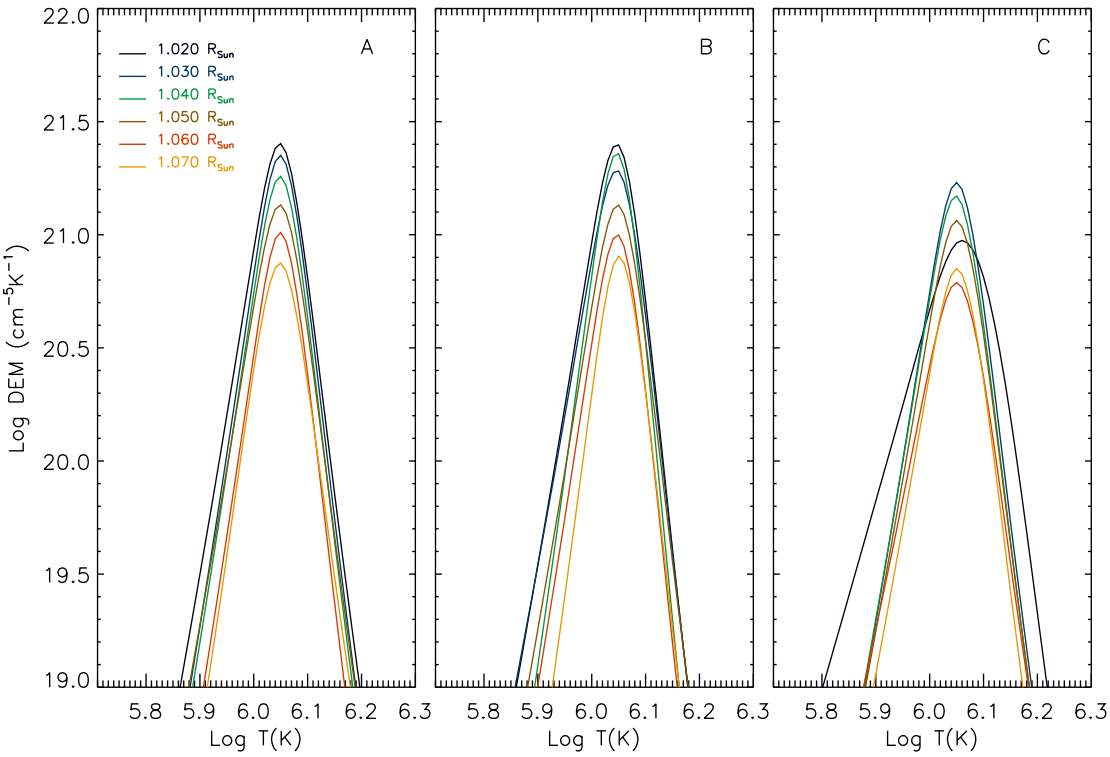

Figure 2.6: DEM curves versus temperature measured for each region as function of distance from Sun center.

change their shape, with the only exception of the curve at 1.02 $R_\odot$ in the C dataset.

To compare the electron density obtained by EIS, DEMT, and the model, we extract the LOS density at several locations around B dataset in the EIS observation for different solar radii from 1.042 to 1.103 $R_\odot$. For the EIS observation, we show both the density derived from Fe XII and Fe XIII. The comparison result is shown in Figure 2.7. Since the location of EIS observation is quiet Sun region, there are no significant differences at different locations for the densities predicted by the SC model and DEMT. The densities provided by SC and DEMT are very close as already shown in Figure 2.3. However, the density derived from EIS Fe XII is higher than the model and DEMT density by a factor of ∼2, while the density derived by the Fe XIII ratio is in good agreement. The disagreement between Fe XII and Fe XIII derived by EIS ratios was noted before (*Young et al.*, 2009; *Watanabe et al.*, 2009). In all cases Fe XII densities were higher than Fe XIII ones. The comparison made in this study

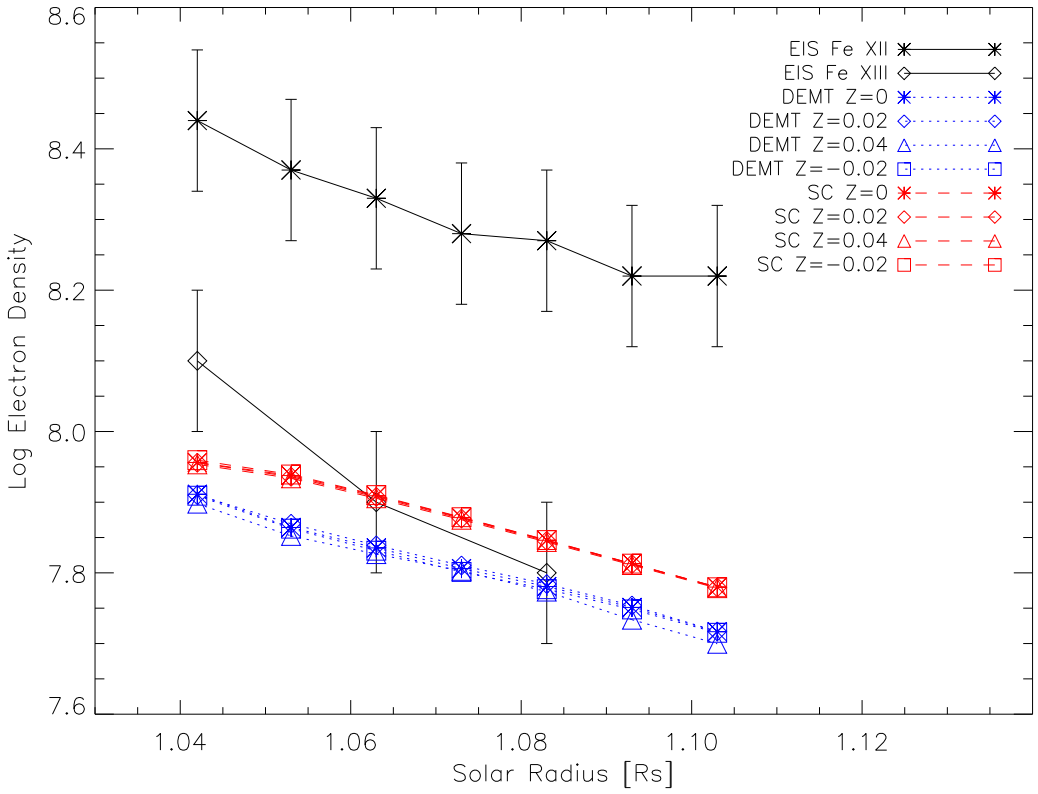

Figure 2.7: Line-of-Sight (LOS) density comparison among SC output, DEMT, and EIS derivations.

shows that the Fe XIII derived densities are more consistent with model and DEMT than Fe XII derived densities. The agreement between the Fe XIII and DEMT density values, obtained with different techniques, reinforces the conclusion drawn by *Young et al.* (2009) and *Watanabe et al.* (2009) that Fe XII line intensities are affected by atomic physics problems. The EIS derived temperature is around $\log T = 6.05$ for all locations, which is well matched with the model output in Figure 2.3.

As the final evaluation of the two-temperature model near the Sun, we compare the model result with the tomography derivation (*Frazin*, 2000; *Frazin and Janzen*, 2002) from SOHO/LASCO-C2. Using the LASCO-C2 observation, the tomographic method can obtain the electron density between 2.3 $R_\odot$ and 6.0 $R_\odot$. The electron density ratio between the model and the LASCO-C2 tomographic output is then

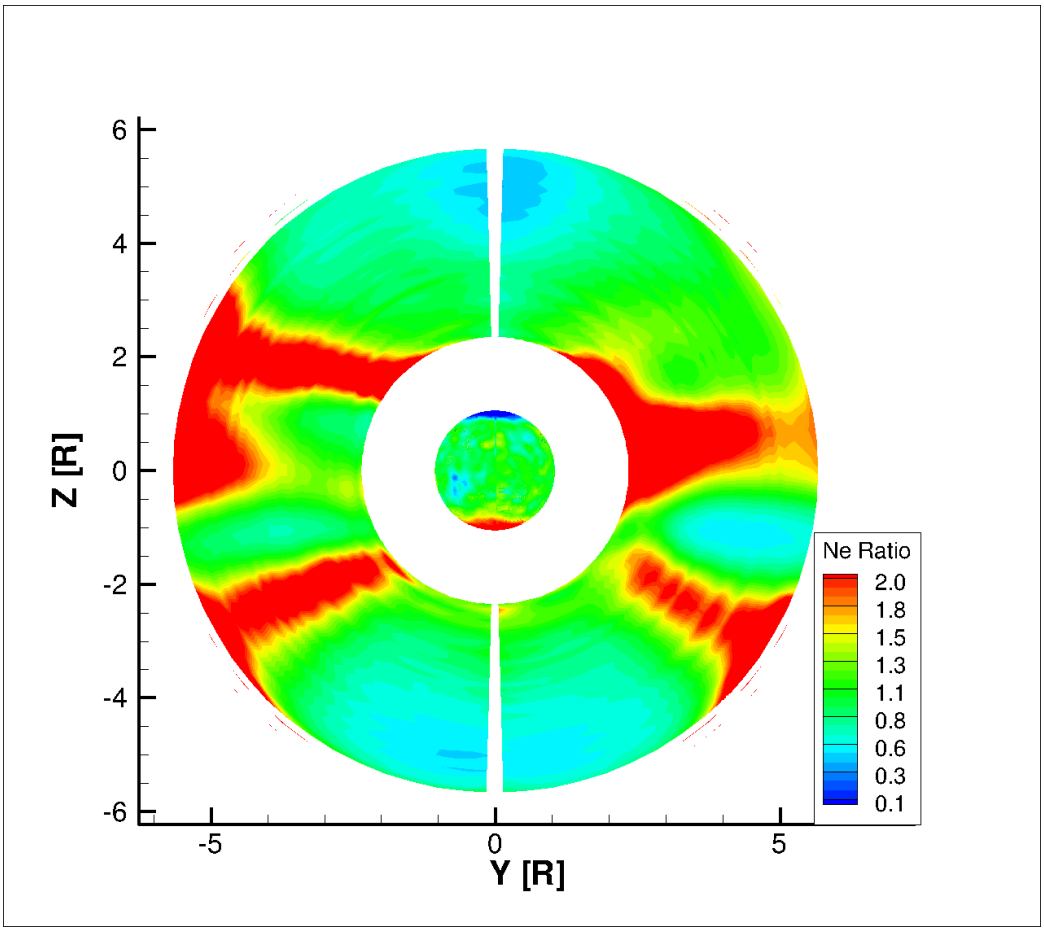

Figure 2.8: The electron density ratio between the two-temperature model and the LASCO-C2 tomography output between 2.3 $R_\odot$ and 6.0 $R_\odot$. The boundary data near ~6.0 $R_\odot$ is eliminated because of the relatively larger uncertainty of the tomography derivation near the boundary.

calculated and shown in Figure 2.8. The data near ~6.0 $R_\odot$ are eliminated due to the relatively larger uncertainty of the tomography derivation near the boundary. In Figure 2.8, we can see that most of the regions have Model/C2 ratio around 1.0, which means the model and C2 tomographic data are well matched. The four red streams that have a Model/C2 ratio are related to the time variation on the Sun that cannot be well captured by the steady state solar wind model as well as the solar rotational tomography.

2.3 Model Validation Using Multispacecraft Observation

In this Section, we will use multispacecraft observation from Venus Express (*Titov et al.*, 2006), STEREO A/B, and ACE to validate our two-temperature model with electron heating in the heliosphere. Figure 2.9 shows the trajectories of the four spacecraft in the Carrington coordinate system (Heliographic Rotating Coordinate, HGR)[2]. We can see that in the frame rotating with the Sun, the satellite trajectories encircle the Sun in a full Carrington rotation period. Venus Express is at ∼0.7 AU from the Sun. The other three satellites are at ∼1 AU. In Figure 2.9, three velocity iso-surfaces from the model are also shown. These three iso-surfaces show the radial solar wind speed of 250 km s^{-1}, 500 km s^{-1}, and 700 km s^{-1}. The corotating interaction regions (CIRs) that have been studied for several decades (see e.g., *Jian et al.*, 2006; *Mason et al.*, 2009, and references therein) are evident in our simulation results. In Figure 2.9, the CIRs are shown by the iso-surface velocity of 250 km s^{-1}, which are the slow streams. Figure 2.10 shows the comparison of the model with Venus Express observations at ∼0.7 AU. The proton parameters (solar wind speed and proton temperature) are observed by Ion Mass Analyzer (IMA) of the Analyser of Space Plasma and Energetic Atoms (ASPERA) onboard Venus Express. The magnetic field strength is obtained by Magnetometer (MAG) onboard Venus Express. Since solar wind monitoring is not the Venus Express goal, the instruments onboard Venus Express are switched on one hour before bow shock crossing and switched off one hour after. In this study, in order to exclude the influence of the atmosphere of Venus on the solar wind, we only use the first data point after switch on and the last data point before switch off. For the solar wind speed, the model agrees with the magnitude of ∼400 km s^{-1}, but differs in the speed variation. For the temperature, the model produces the same trend as the observation but with lower

[2]HGR is a Sun-centered, solar coordinate system that rotates in a sidereal frame exactly once every 25.38 days.

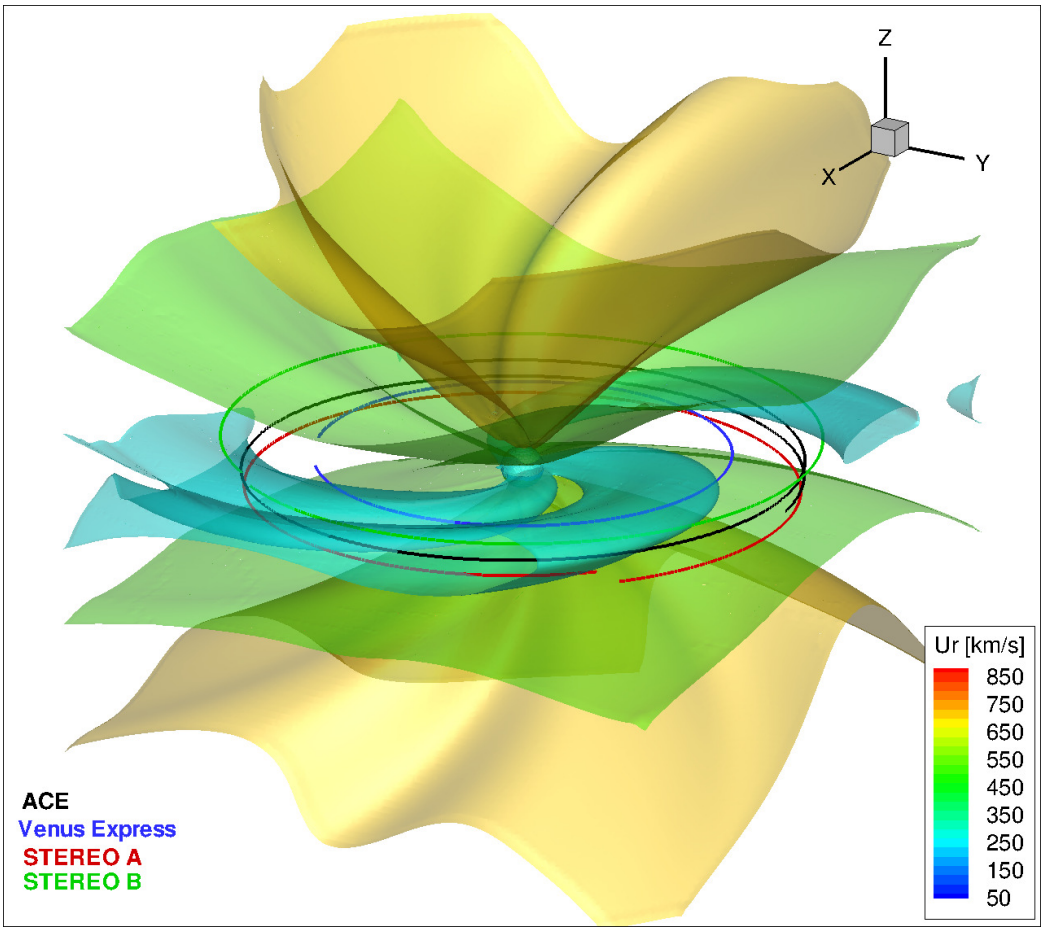

Figure 2.9: The satellite trajectories in the Carrington coordinate system shown with the iso-surface velocity of the two-temperature model. The three iso-surfaces show the radical solar wind speed of 250 km s^{-1}, 500 km s^{-1}, and 700 km s^{-1}.

magnitude. The possible reasons for the discrepancy have been discussed by *van der Holst et al.* (2010). We will discuss it further in Section 4. For the magnetic field strength, both the model and observation give the same magnitude ∼5 nT.

Figure 2.11 shows the comparison between the model and the STEREO A observation. The proton parameters are observed by Plasma And Supra-Thermal Ion Composition Investigation (PLASTIC) instrument onboard STEREO. The magnetic field data is provided by In-situ Measurements of Particles and CME Transients (IMPACT) instrument onboard STEREO. The cyan lines in the figure show the original observational data with a time resolution of 10 mins. There are many fine structures

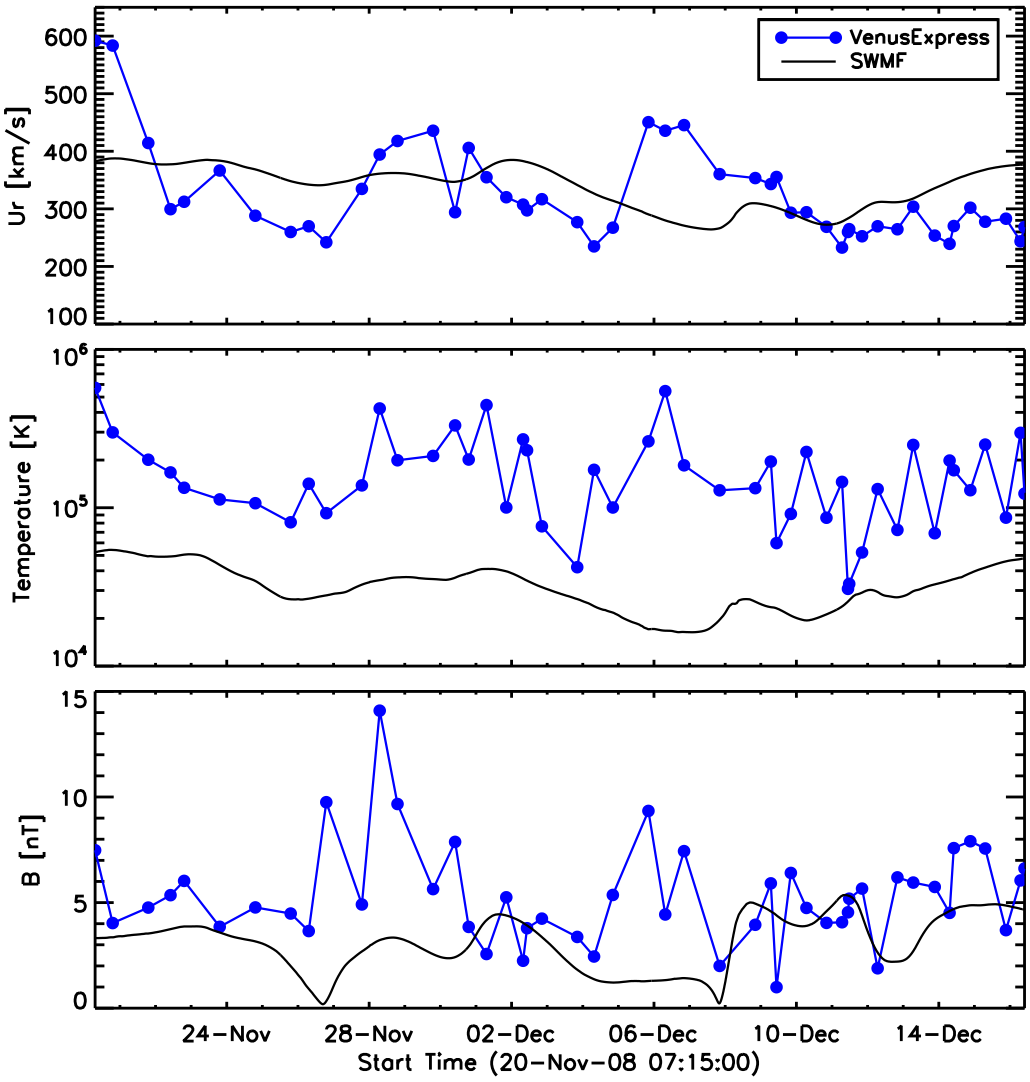

Figure 2.10: Comparison of Venus Express observed solar wind speed, proton density, proton temperature, and magnetic field with the two-temperature model output for CR2077.

that cannot be captured by the steady state MHD solutions. In order to compare the model output with the observation, a daily average of the observational data is shown with red dashed lines. In general, our model agrees to within a factor of two with STEREO observations in all the comparison parameters but some peaks are missing in our model. Some of these peaks might be related to eruptive events in the heliosphere that cannot be simulated by the steady state solar wind model. Similar results are shown in Figure 2.12 for the comparison between the model and STEREO B observations.

Figure 2.13 shows the comparison between the model and ACE observations. We use the hourly averaged ACE data obtained from the Coordinated Data Analysis Web. Such a validation with ACE was also demonstrated by *van der Holst et al.* (2010) using the two-temperature model without electron heating. Comparing results, the model with electron heating can get similar features (e.g., CIRs) but with a higher magnitude which is more consistent with the observations. We can see the simulated solar wind speed has a peak above $\sim$400 km s^{-1}, and an average $\sim$350 km s^{-1}. The average proton temperature at 1 AU is higher and in better agreement with the ACE average temperature than the previous model presented in *van der Holst et al.* (2010), but several temperature peaks from the ACE data are no longer captured.

We next use the freeze-in code developed by *Gruesbeck et al.* (2011) to calculate the ion charge state at 1 AU for the solar wind model, which we then compare to the observed values found by ACE/SWICS. As the solar wind plasma propagates outward from the Sun, the density significantly drops, which shuts down the ionization and recombination processes causing the freeze-in of the ionic charge state very close to the Sun. Lighter elements freeze-in closer to the Sun while heavier elements freeze-in further out (*Geiss et al.*, 1995; *Buergi and Geiss*, 1986). *Esser et al.* (1998) first presented a model of ion charge state in the solar wind by solving the ionization evolution equations. Recently, *Laming* (2004) and *Laming and Lepri* (2007)

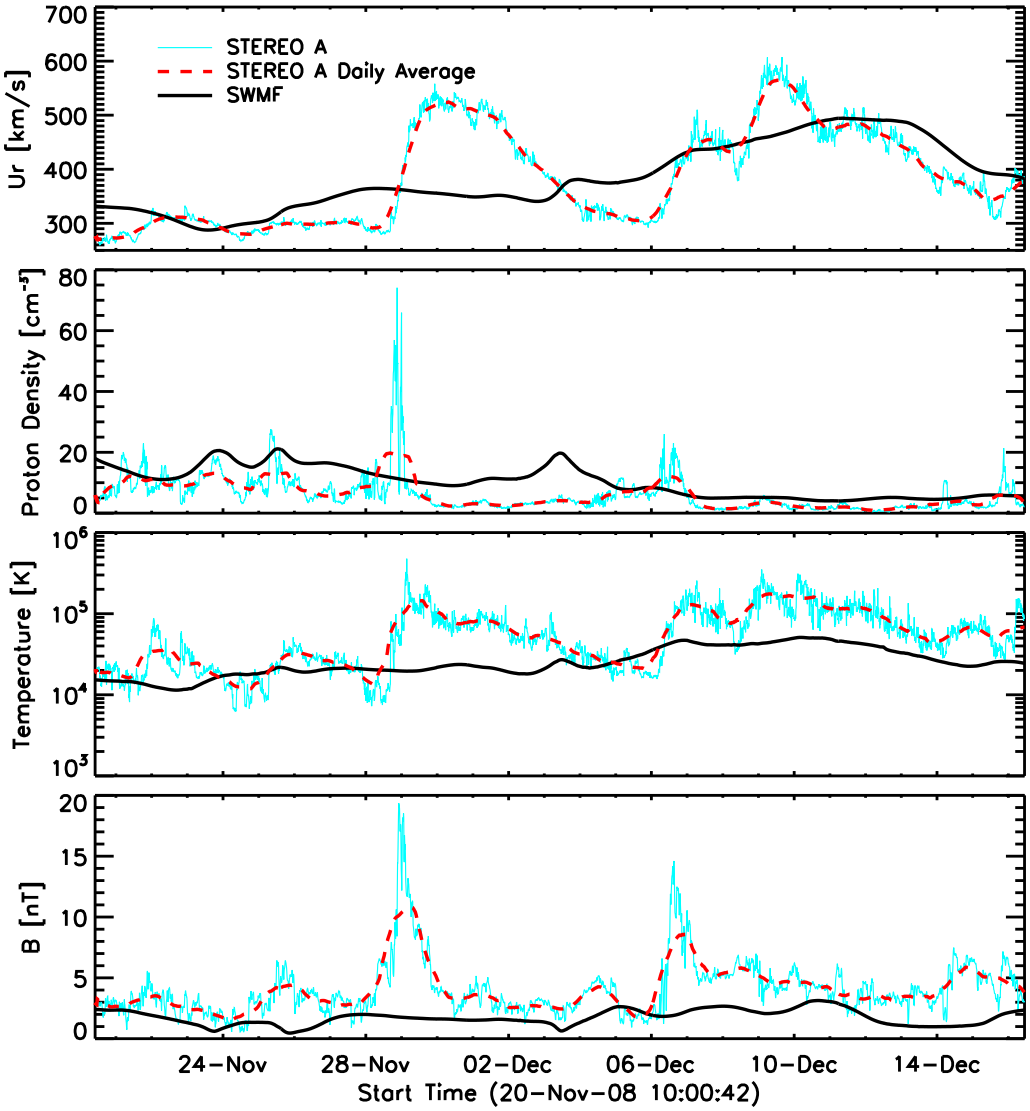

Figure 2.11: Comparison of STEREO A observed solar wind speed, proton density, proton temperature, and magnetic field with the two-temperature model output for CR2077.

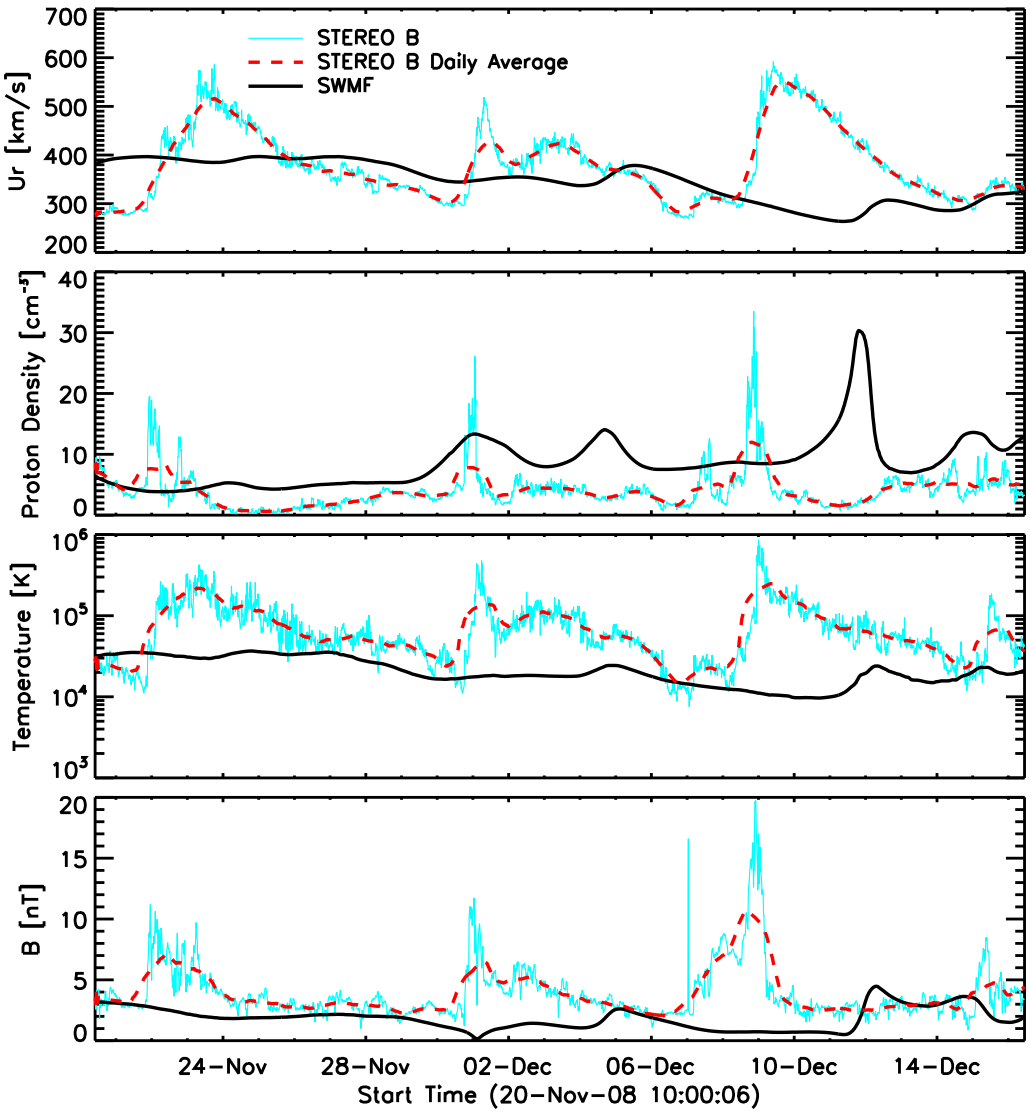

Figure 2.12: Comparison of STEREO B observed solar wind speed, proton density, proton temperature, and magnetic field with the two-temperature model output for CR2077.

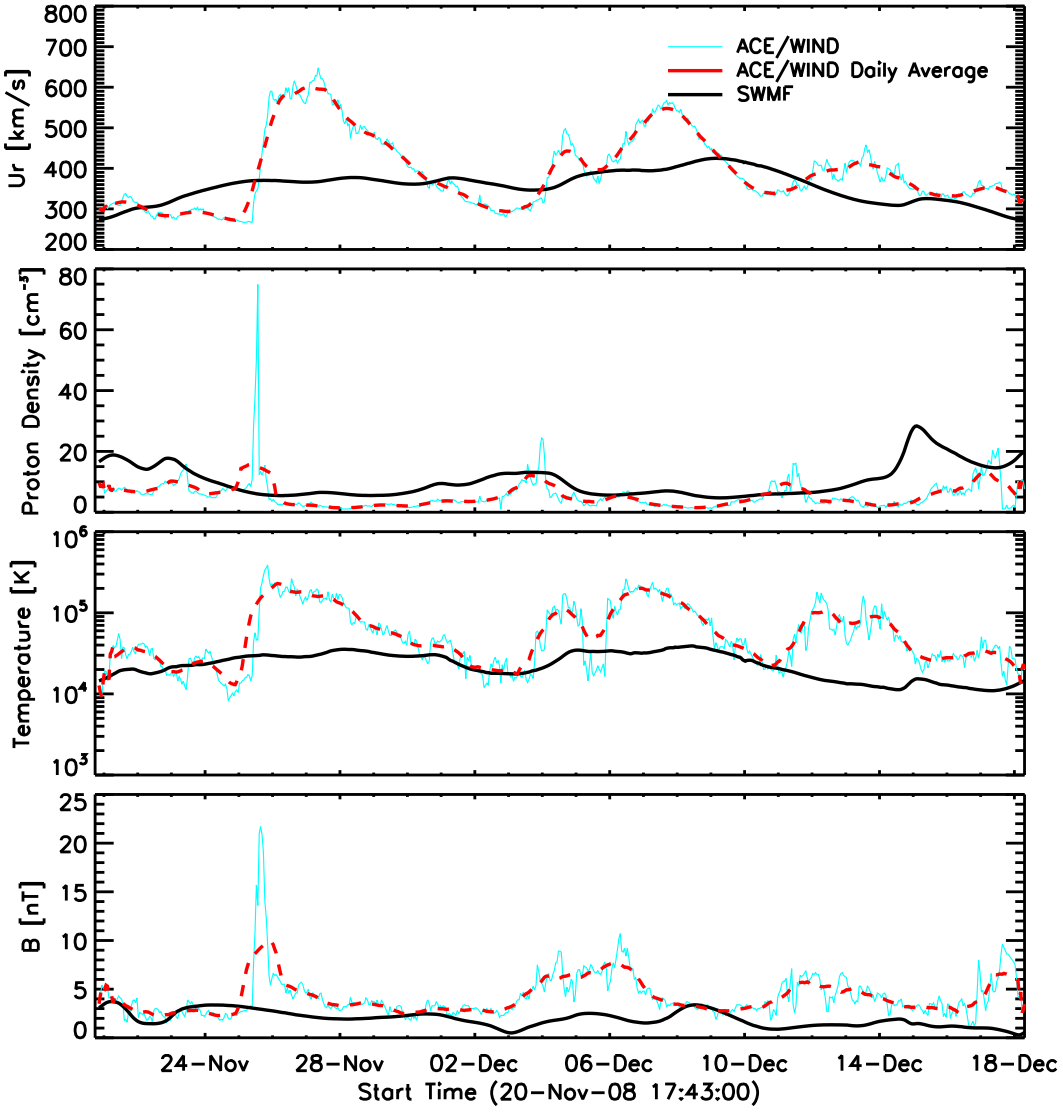

Figure 2.13: Comparison of ACE observed solar wind speed, proton density, proton temperature, and magnetic field with the two-temperature model output for CR2077.

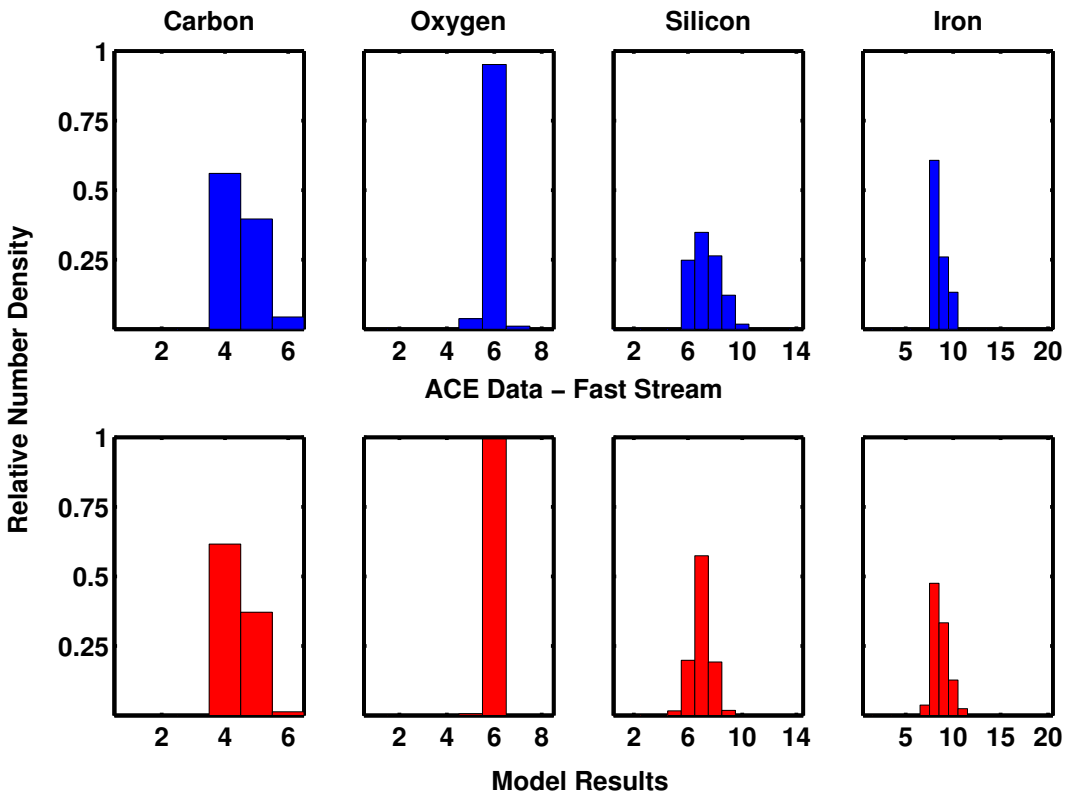

Figure 2.14: Comparison of ACE/SWICS observed ionic charge states of C , O , Si , and Fe with the model predicted result for CR2077.

suggested a model to interpret the increased ionization of charge states in the fast solar wind. The freeze-in code uses the solar wind model's electron temperature and density as inputs to the ionic charge state equation, while the model velocity is input into the continuity equation which is solved for the plasma trajectory along a field line in the fast wind. The freeze-in code solves this series of equations using a 4th order Runge-Kutta scheme, optimized for solving stiff sets of equations. The code is applied to separately calculate the charge state distribution of each atomic species as it propagates away from the Sun at the speed of the bulk velocity determined by the solar wind model. The ionization and recombination rate coefficients of specific ions are taken from *Mazzotta et al.* (1998).

The model's predicted freeze-in heights for C , O , Si , and Fe Are approxi-

mately 1.13 Rs, 1.13 Rs, 1.45 Rs, and 1.51 Rs, respectively, illustrating the trend that has been theorized. As can be seen in the Figure 2.14, there is a strong qualitative agreement between the ACE/SWICS observations from a fast wind stream and the freeze-in code's results from the fast wind of the model. For all four elements inspected, the major charge state peak matches that of the ACE observation. The close match indicates that the model's coronal electrons temperature, density, and velocity are close to that of the solar corona. To determine the nature of the electron temperature discrepancy between the predicted and observed charge state levels is beyond the scope of this work, but will be taken up in subsequent papers. Also, we notice that the freeze-in heights for C And O Are very close to the inner boundary of the simulation domain. Therefore, in order to have a more reliable result for these two elements, we may need to extend the inner boundary to the lower coronal region.

2.4 Summary and Conclusions

We performed a validation study for the new 3D solar wind model (*van der Holst et al.*, 2010) using observations from STEREO A/B, ACE, Venus Express, Hinode, and SOHO of CR2077. We include electron heating in the new model by partitioning 40% of the Alfvén wave energy to the electrons. By comparing the model output with the DEMT electron temperature and density, LASCO-C2 tomographic density, and Hinode/EIS electron density and temperature, we suggest the model with electron heating is more physically reliable and consistent with observations than a single fluid model. The simulation results near the Sun reproduce many observational features (e.g., the open and closed field regions, low and high density regions, the fast and slow solar wind, streamer belt) and get all the plasma parameters with the right magnitude (within a factor of $\sim$2).

Using the *in situ* observations from STEREO, ACE, and Venus Express, we compare the solar wind velocity, proton density, temperature, and magnetic field in the

inner heliosphere with the model output. In general, the validation results for CR2077 are encouraging. The heliosphere observational features (e.g., CIRs) are demonstrated in the simulation: the new model with electron heating also gets the right value of the solar wind speed, proton density, and the magnetic field strength for all of the *in situ* observations. Moreover, we validate the model with derived ionic charge states at 1 AU by using the newly developed freeze-in code by *Gruesbeck et al.* (2011). Our results show that the temperature profile of the model near the Sun can reproduce the ionic charge state observed by ACE/SWICS, which suggests the physical reliability of the new model.

However, there is still room for the improvement of the model. From the *in situ* observations, we notice that our model output has a relatively low magnitude at most CIR peaks for solar wind speed, density, temperature, and heliospheric magnetic field. The reason for this discrepancy is the quite extended slow wind region shown in Figure 2.2. This extended slow wind region positions the satellites in the slow wind for a longer period than occurred in reality and therefore causes the relatively low magnitude of plasma parameters. The wide slow wind region is caused by the difficulty of using the WSA model to obtain the Alfvén wave energy at the inner boundary in order to reproduce the final velocity distribution at 1 AU. The Alfvén wave pressure prediction is determined along the PFSS magnetic field, while the final obtained field line topology of the solar wind model departs from this PFSS field so that the velocity profile at 1 AU is likely to be different from the WSA predicted values. Actually, some studies found the WSA model yields higher solar wind speed at the source surface than the MHD model does (*Feng et al.*, 2010). To overcome this issue, we may need a self-consistent method to treat the inner boundary for Alfvén wave energy. An improved solar wind model in SWMF will start from the top of the chromosphere and will be independent of WSA for the terminal solar wind speed. Also, including couterpropagating Alfvén waves (e.g., *Chandran and Hollweg* 2009;

Cranmer 2010) may improve the heating and acceleration of the solar wind plasma.

In this validation study, in order to compensate for the uncertainty of the synoptic magnetogram observation and get the right magnetic strength at 1 AU, we double the magnetic field of the GONG based synoptic magnetogram. How to create reliable and precise global solar magnetograms is still an open issue. With more observations from space by different satellites (e.g., SDO, high temporal and spatial resolution; Solar Orbiter, polar region magnetic field measurement), as well as the development of new methods (e.g., helioseismology, *Zhao* 2007), the model can be improved by using more precise magnetograms.

There are also some ongoing DEMT improvements that include: (1) Removing scattered light within the EUV telescopes, which is particularly important for fainter features such as the off-limb, coronal holes, and filament cavities; (2) Including the *Bryans et al.* (2009) ionization fractions, which will imply changes in derived DEMT temperatures, specially in the hotter streamer regions. The new computation will change the EUVI responses and shift their peak location to higher temperatures. Therefore, the mean electron temperature from the inverted LDEM will increase too. For the Te $>$ 1 MK regions, the median increase of the temperature is $\sim$15 %, which could result in a better agreement between the two-temperature model and DEMT output; (3) Extending the technique to incorporate the SDO/AIA data, which provides more extensive temperature constraints than EUVI. Currently, a comparative study of EUVI and AIA based DEMT results is being conducted for the current rising phase of solar cycle 24.

For future work, we need to validate the new solar corona model for solar maximum conditions. There are two difficulties for simulating solar maximum. First, the solar corona at solar maximum is more dynamic, which makes the boundary conditions based on potential field model and DEMT data less accurate. We also need to initiate CME events from different active regions in order to compare with observa-

tions. Moreover, our model does not take into account the coronal heating mechanism by ohmic dissipation associated with magnetic reconnection of which interchange reconnection is one example. Since interchange reconnections occur frequently during solar maximum, we need to see how it will influence our simulation results. Also note that a complete description of coronal electrons requires a kinetic treatment that can address the suprathermal electrons that are observed in situ. Furthermore, the core population has a nearly constant temperature of 100,000 K at 1 AU, which requires additional heating mechanisms for our model to reproduce. After the validation work, we will start to simulate eruptive events including CMEs and CME-driven shocks. In the previous solar wind model (*Cohen et al.*, 2007) in the SWMF, the CME-driven shocks are not well described due to the reduced adiabatic index. The new model uses $\gamma = 5/3$ globally. Therefore, improvements in modeling CMEs and CME-driven shocks can be expected. Furthermore, by coupling the coronal model with the flux emergence convection zone model (*Fang et al.*, 2010) with the SWMF, we can achieve self-consistent CME simulations in the future.

CHAPTER III

Numerical Simulations of Coronal Mass Ejection on 2011 March 7: One-Temperature and Two-Temperature Model Comparison

The only way of discovering the limits of the possible is to venture a little way past them into the impossible.

– Arthur C. Clarke

3.1 Introduction

Coronal mass ejections (CMEs) are a major source of potentially destructive space weather conditions, in which 10^{15}–10^{16} g of plasma is ejected from the Sun with a kinetic energy of order 10^{31}–10^{32} ergs (*Hundhausen*, 1993). Fast CMEs can drive shocks in the heliosphere (e.g., *Sime and Hundhausen* 1987; *Vourlidas et al.* 2003; *Vourlidas and Ontiveros* 2009) that are believed to be responsible for gradual solar energetic particle (SEP) events (e.g., *Reames* 1999). The SEPs can pose major hazards for the spacecraft and human life in outer space. Therefore, understanding CME and CME-driven shock dynamics is critical for space weather forecast. However, due to the limitations of observations (e.g., temporal and spatial resolution, sensitivity etc.), it

is very hard to test and verify our theories about CMEs and CME-driven shocks solely from the observations. Global magnetohydrodynamic (MHD) simulation provides a great tool to investigate the CME-related phenomena in detail.

There are three major physical processes for energy balance in the solar corona: coronal heating, thermal conduction, and radiative cooling. The coronal heating is still an open issue of solar physics at this time. Many numerical models addressed this issue by using empirical heating functions (e.g., *Mikić et al.* 1999; *Groth et al.* 2000), or variable adiabatic index (e.g., *Wu et al.* 1999; *Roussev et al.* 2003b; *Cohen et al.* 2007; *Jacobs and Poedts* 2011). Although, these assumptions can reproduce many observational features (e.g., EUV images, 1 AU in-situ plasma parameters), the assumptions limit the physical self-consistency of the simulation. When shocks are present in the simulation, the variable adiabatic index assumption alters the jump conditions therefore leading to an unrealistic shock structure. Inspired by observed wave-like phenomena, there are other models that address the heating term by mimicking Alfvén-wave dissipation (e.g., *Usmanov et al.* 2000; *Suzuki* 2006; *Evans et al.* 2009; *van der Holst et al.* 2010). The advantage of this type of model is fewer free parameters in the simulation and therefore a more physically self-consistent solution. *Sokolov et al.* (2013) further implemented balanced Alfvén-wave turbulence at the top of closed field lines in the global 3D MHD simulations. For the thermal conduction, most of the models use the Spitzer form of heat conduction (*Spitzer*, 1962) for near-Sun plasmas. For models that extend to the chromosphere, the radiative cooling process should be considered (*Lionello et al.*, 2009; *Downs et al.*, 2010). How to treat these processes in the simulation is very important and can lead to different thermodynamic evolution. *Pomoell and Vainio* (2012) simulated CMEs with different heating functions. They found that CME-driven shocks can be significantly altered by different heating prescriptions. *Shiota et al.* (2005) found that the heat conduction is important for reproducing the observational features in the MHD simulation

of CMEs.

Although the complexity keeps increasing, most of the global MHD models assume a single temperature for all particle species. However, in the low corona, the densities sufficiently high that Coulomb collision thermally couple electrons and protons on a time scale of order of tens of seconds. As the density decreases away from the Sun, electrons and protons gradually decouple and attain different temperatures, because of a variety of physical processes that are dependent on particle mass. To capture this complex behavior Van der Holst et al. (2010) developed the first global 2T solar wind model, which dramatically changes the thermodynamics of the evolving plasma. First, the thermal velocity of electrons is more than ∼40 times greater than that of protons so that the heat conduction by electrons completely dominates that of protons, which is thus omitted in our model. Second, Alfvén waves primarily heat protons by Kolmogorov dissipation (*Hollweg*, 1986). Third, CME-driven shocks (∼100 – 3000 km s^{-1}) are supersonic only with respect to the proton thermal speed (c_p ∼100 km s^{-1}). Therefore, protons are shock-heated while electrons are not (c_e ∼5000 km s^{-1}). This work follows the first 1D two-temperature (2T) CME-driven shock model of *Kosovichev and Stepanova* (1991), in which the authors found that the ion temperature can reach 5×10^7 K and may exceed the electron temperature by more than an order of magnitude for strong shocks. Using the model of *van der Holst et al.* (2010), *Manchester et al.* (2012) confirmed this temperature inequality behind CME-driven shocks and found much more complex behavior of field-aligned heat conduction in complex 3D magnetic fields. In particular, heat can propagate on open field lines to form an electron high-temperature shock precursor. A more detailed description about the temperature features of the shock wave in a plasma can be found in *Zel'dovich and Raizer* (1967). A recent application in the multi-material radiation hydrodynamics shows these temperature features in the high energy density regime (*van der Holst et al.*, 2011).

In this study, we investigate the thermodynamical differences between 1T and 2T CME/CME-driven shocks based on a newly developed Alfvén Wave Solar Model (AWSoM; *Sokolov et al.* 2013). Similar to that of *van der Holst et al.* (2010), this model employs Alfvén wave damping to heat the corona and describes separate electron and proton temperatures with electron heat conduction. *Sokolov et al.* (2013) further developed the model by incorporating the balanced turbulence at the top of the closed field lines and by extending it down to the chromosphere and including radiative cooling. The CME simulations described here are based on the CME event that occurred on 2011 March 7th. We initiate the CME by implementing a Titov-Démoulin (TD) flux rope in the steady state solar wind (*Titov and Démoulin*, 1999). The flux rope erupts due to the initial state of force imbalance. The synthesized white light images of 1T and 2T CMEs are compared with SOHO/LASCO observations. Based on the simulation results, we emphasize the importance of a 2T model for CME simulations. This chapter is organized as follows: In Section 2, we describe the background solar wind model as well as the CME initiation model we used. The 1T and 2T CME comparison results are shown in Section 3, followed by the summary and conclusion in Section 4.

3.2 Models

This study is based on the Space Weather Modeling Framework (SWMF) developed in the Center for Space Environment Modeling (CSEM), which provides a high-performance computational capability to simulate the space weather environment from the upper solar atmosphere to the Earth's upper atmosphere and/or the outer heliosphere (*Tóth et al.*, 2005, 2012). The framework contains several components that represent the different physical domains of the space environment and each component can have multiple models available. In this study, we use the Solar Corona (SC) and Eruptive Event Generator (EE) components. The SC component is used to

obtain the background solar wind solution with the newly developed AWSoM model (*Sokolov et al.*, 2013) and is solved by Block-Adaptive Tree Solarwind Roe-type Upwind Scheme (BATS-R-US) code (*Powell et al.*, 1999). The inner boundary condition of magnetic field is specified by a synoptic map obtained from the Helioseismic and Magnetic Imager (HMI) instrument on board the *Solar Dynamics Observatory* (SDO) spacecraft (*Schou et al.*, 2012). The polar field correction for this map is done with a 2D 3-order polynomial spatial fitting of available data above 60 degree (*Sun et al.*, 2011). The initial magnetic field configuration is calculated by the Potential Field Source Surface (PFSS) model using a finite difference method (*Tóth et al.*, 2011b). The Alfvén wave turbulence is launched at the inner boundary and scaled with the surface magnetic field. In the open field line region, the solar wind is heated by Kolmogorov wave dissipation. At the top of the closed field lines, balanced turbulent cascade is dominant.

The governing equations for the 2T model can be summarized as below (see also in *Sokolov et al.* 2013) :

$$\frac{\partial \rho}{\partial t} + \nabla \cdot (\rho \mathbf{u}) = 0 \tag{3.1}$$

$$\frac{\partial (\rho \mathbf{u})}{\partial t} + \nabla \cdot \left(\rho \mathbf{u}\mathbf{u} - \frac{\mathbf{B}\mathbf{B}}{4\pi} \right) + \nabla \left(p_p + p_e + \frac{w_+ + w_-}{2} + \frac{B^2}{8\pi} \right) = -\rho \frac{GM_\odot}{r^2} \mathbf{e_r} \tag{3.2}$$

$$\frac{\partial \left(\frac{p_e}{\gamma - 1} \right)}{\partial t} + \nabla \cdot \left(\frac{p_e}{\gamma - 1} \mathbf{u} \right) = -p_e \nabla \cdot \mathbf{u} + \frac{1}{\tau_{pe}} (p_p - p_e) - \nabla \cdot \mathbf{q_e} - Q_{rad} + \alpha Q_w \tag{3.3}$$

$$\frac{\partial\left(\frac{p_p}{\gamma-1}\right)}{\partial t}+\nabla\cdot\left(\frac{p_p}{\gamma-1}\mathbf{u}\right)=-p_p\nabla\cdot\mathbf{u}+\frac{1}{\tau_{pe}}(p_e-p_p)+(1-\alpha)Q_w \tag{3.4}$$

$$\frac{\partial w_\pm}{\partial t}+\nabla\cdot[w_\pm(\mathbf{u}\pm\mathbf{u_A})]=-\frac{w_\pm}{2}\nabla\cdot\mathbf{u}-\Gamma_\pm w_\pm \tag{3.5}$$

$$\frac{\partial\mathbf{B}}{\partial t}-\nabla\times(\mathbf{u}\times\mathbf{B})=0 \tag{3.6}$$

where ρ is the mass density; $\mathbf{u}$ is the velocity; r is the radial distance from the center of the Sun; G is the gravitational constant; $M_\odot$ is the mass of the Sun; p_e and p_p represent the electron and proton pressures; $w_\pm$ are the Alfvén wave energy densities propagating along and against the magnetic field direction; $\mathbf{B}$ is the magnetic field; $\gamma = 5/3$ is the adiabatic index; τ_{pe} is the characteristic time of collisional energy exchange between the electrons and protons; $\mathbf{q_e}$ is the electron thermal heat flux; Q_{rad} represents the radiative loss; $Q_w = \Gamma_+ w_+ + \Gamma_- w_-$ represents the wave dissipation; $\mathbf{u_A} = \mathbf{B}/\sqrt{\mu_0\rho}$ is the Alfvén wave speed; $\Gamma_\pm$ is the dissipation rate coefficient; α represents the wave dissipation energy partition between the electrons and protons. The $\pm$ sign represents the two Alfvén waves propagating in opposite directions along the magnetic field lines.

The 2T model separates electron and proton temperatures by solving different energy equations while the two species are coupled by Coulomb collisions. The equations are solved in conservative form such that all dissipated energy from shocks is converted to proton thermal energy. The conservative form of the energy equation can be expressed as:

$$\frac{\partial \varepsilon}{\partial t}+\nabla\cdot\left[\left(\varepsilon+p_p+p_e+\frac{w_++w_-}{2}+\frac{B^2}{8\pi}\right)\mathbf{u}-\frac{\mathbf{BB}\cdot\mathbf{u}}{4\pi}+\mathbf{q_e}\right]=-\rho\mathbf{u}\cdot\frac{GM_\odot}{r^3}\mathbf{e_r}+Q_w-Q_{rad} \tag{3.7}$$

where

$$\varepsilon=\frac{\rho u^2}{2}+\frac{p_p+p_e}{\gamma-1}+\frac{B^2}{8\pi}+w_++w_- \tag{3.8}$$

This proton heating is the physically correct approximation since the thermal speed of protons (c_p ~100 km s^{-1}) is much less than that of electrons (c_e ~5000 km s^{-1}) so that only the protons are shocked, while the electrons are only heated adiabatically and due to the proton-electron energy exchange.

The characteristic time of collisional energy exchange can be calculated based on the following equation:

$$\tau_{pe}=\frac{2m_p\epsilon_0^2(2\pi k_B)^{3/2}T_e^{3/2}}{n_e e^4\sqrt{m_e}\ln\Lambda} \tag{3.9}$$

where m_p, m_e, n_e, and T_e are the proton mass, electron mass, electron density, and electron temperature, respectively. e, ϵ_0, and k_B are the electron charge, permittivity of free space, and Boltzmann's constant, respectively. $\ln\Lambda$ is the Coulomb logarithm. In this study, we assume a spatially uniform value of 20.

For the 1T model, there is only one energy equation with thermal heat conduction, radiative loss, and wave heating:

$$\frac{\partial \varepsilon}{\partial t}+\nabla\cdot\left[\left(\varepsilon+p+\frac{w_++w_-}{2}+\frac{B^2}{8\pi}\right)\mathbf{u}-\frac{\mathbf{BB}\cdot\mathbf{u}}{4\pi}+\mathbf{q_e}\right]=-\rho\mathbf{u}\cdot\frac{GM_\odot}{r^3}\mathbf{e_r}+Q_w-Q_{rad} \tag{3.10}$$

where

$$\varepsilon=\frac{\rho u^2}{2}+\frac{p}{\gamma-1}+\frac{B^2}{8\pi}+w_++w_- \tag{3.11}$$

The wave dissipation rate calculation is based on the following form:

$$\Gamma_{\pm} = \frac{\sqrt{|\mathbf{B}|}}{(L_{\perp} \cdot \sqrt{|\mathbf{B}|})} \sqrt{\frac{\max(w_{\mp}, C_{refl}^2 w_{\pm})}{\rho}} \tag{3.12}$$

The derivation of the formula can be found in *Sokolov et al.* (2013). The C_{refl} is the wave reflection coefficient that specifies the ratio of the reflected wave amplitude to the bulk wave amplitude. In the coronal holes and bottom of closed field lines, the onset of turbulence cascade is due to wave reflection while at the top of the closed field line regions, the turbulent cascade is balanced. Also, we distribute 40% of the Alfvén wave dissipation energy to heat electrons ($\alpha = 0.4$; *Jin et al.* 2012) in the 2T model as suggested by *Breech et al.* (2009) from *Ulysses* data.

The model starts from upper chromosphere with a fixed temperature, $T = 50{,}000$ K, and $n = 2{\times}10^{17}$ m^{-3}. Also, field-aligned Spitzer electron conduction and radiative cooling are included. In this study, we assume the collisional formulation of the Spitzer heat flux:

$$\mathbf{q_e} = -\kappa_e T_e^{5/2} \frac{\mathbf{BB}}{B^2} \cdot \nabla T_e \tag{3.13}$$

where the $\kappa_e \approx 9.2 \times 10^{-12}$ Wm^{-1}K$^{-7/2}$. The heat conduction flux of protons is neglected in the model, since many investigations suggest a much smaller proton heat conduction coefficient than for electrons (e.g., *Braginskii* 1965; *Sandbaek and Leer* 1995; *Olsen and Leer* 1996). *Cranmer et al.* (2009) found the difference between the heating rates of the models with and without proton heat conduction is less than 5%. Note that the Spitzer heat conduction formula no longer applies beyond 10 R$_{\odot}$ when the plasma becomes collisionless (*Landi and Pantellini*, 2003). Therefore, in this study, the heat conductivity is prescribed to smoothly go to zero beyond 10 R$_{\odot}$.

The radiative losses are estimated based on the optically thin plasma assumption:

$$Q_{rad} = N_e N_p \Lambda(T_e) \tag{3.14}$$

The loss function, $\Lambda(T_e)$, is calculated using the CHIANTI version 7.1 radiative loss routines (*Landi et al.*, 2013).

We first obtain a steady state solar wind solution for CR2107. A spherical grid is used in the simulation that reaches 24 $R_\odot$. In total, 5.5×10^4 blocks are used with 5.3×10^6 cells. Adaptive mesh refinement is performed to resolve the heliospheric current sheet (HCS). We obtain the solutions for both the 1T and 2T models. In Figure 3.1, we show the steady state solar wind speed of a meridional slice at $X = 0$. In the left panel of Figure 3.1, the black line shows the block boundary and the white line shows the cell boundary. The smallest cell is $\sim$0.003 $R_\odot$ (i.e. about 2100 km) in the radial direction and $\sim$0.02 $R_\odot$ in the angular direction near the Sun. The largest cell is $\sim$0.5 $R_\odot$ near the outer boundary. In 1T model, the fast wind speed reaches $\sim$700 km s^{-1} which is 100 km s^{-1} slower than the 2T model solution. The velocity difference is due to the heat conduction. In the 2T model, the dissipated proton energy cannot effectively conduct back to the Sun therefore more energy can be transferred to accelerate the solar wind. However, the solutions near the Sun are very close for the 1T and 2T models. In the right panel of Figure 3.1, the solar wind speed within 4 $R_\odot$ is shown with selected magnetic field lines in white. Toward solar maximum, the configuration of the magnetic field is much more complex than during solar minimum conditions. In Figure 3.2, we show the solar wind temperature for 1T and 2T models. The left panel of Figure 3.2 shows the temperature of 1T model. The middle and right panels of Figure 3.3 show the 2T electron and proton temperatures, respectively. The proton temperature in the 2T model reaches 4 MK in the streamer belt regions and coronal holes. Because both wave heating and electron heat conduction are applied to the single fluid in the 1T model, the resulting temperature structure resembles the electron temperature in the 2T model.

The EE component is used to initiate the CME event. Here, we use the Titov-Démoulin (TD) analytical flux rope model (*Titov and Démoulin*, 1999), with which

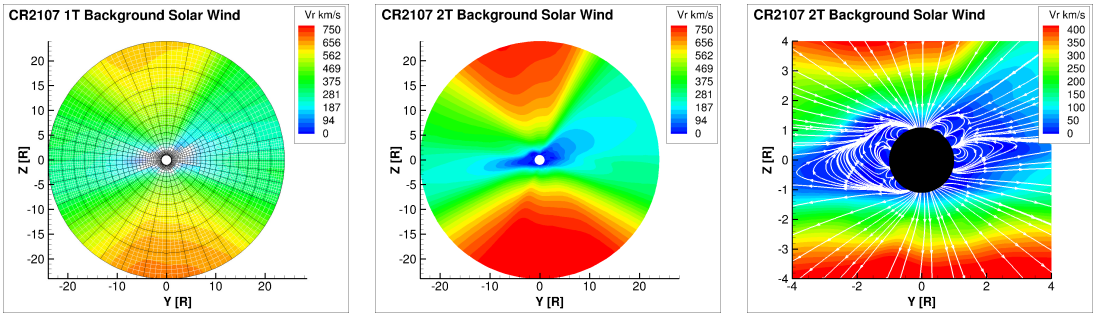

Figure 3.1: 1T and 2T steady state solar wind radial velocity of the meridional slice at X=0. Left: 1T solar wind radial velocity. The black boxes show the blocks and the white boxes show the cells. Middle: 2T solar wind radial velocity. Right: The 2T solar wind radial velocity from -4 $R_\odot$ to 4 $R_\odot$ with field lines.

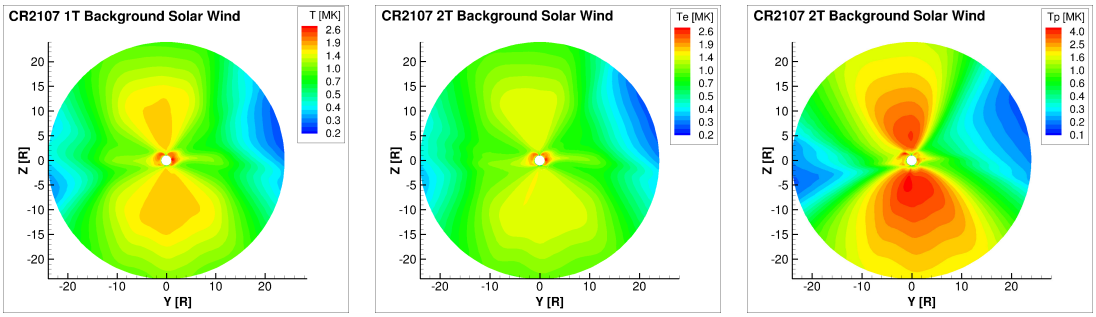

Figure 3.2: 1T and 2T steady state solar wind temperature of meridional slice at X=0. Left: 1T solar wind temperature. Middle: 2T solar wind electron temperature. Right: 2T solar wind proton temperature.

the flux rope will eject due to force imbalance after implementation. The TD flux rope model has been successfully used to simulate CMEs in many studies (e.g., *Roussev et al.* 2003c; *Tóth et al.* 2007; *Lugaz et al.* 2007; *Manchester et al.* 2008; *Loesch et al.* 2011; *Evans et al.* 2011). Since the initiation mechanism of TD flux rope model is by force imbalance of the flux rope, the initial acceleration process may not be correctly caught. However, in this study, our scientific focus is the CME/CME-driven shock propagation and thermodynamics. The usage of TD flux rope should not influence our conclusions. The location of the flux rope is chosen to match the position of the large filament that exists before the eruption, along the polarity inversion line (PIL).

The left panel of Figure 3.3 shows the H_α observation on 2011 March 7, 07:53:37 UT that is $\sim$ 12 hours before the CME. The H_α image is obtained from *Solarmonitor.org* (*Gallagher et al.*, 2002). We can see the filament in AR 11164 clearly. In the right panel of Figure 3.3, the position and configuration of the flux rope in the simulation are shown. The current of the flux rope is set to 2.0×10^{12} A. The length is 60 Mm and the radius is 9 Mm. The total mass of plasma in the flux rope is set to 10^{16} g, which is within the typical range of observed CME mass (*Howard et al.*, 1985) and a good estimation for large ones (e.g., *Jin et al.* 2009). Based on these parameters, the total free energy included in this flux rope is calculated to be 3.9×10^{33} ergs. For this active region, the free energy of the flux rope is a bit more energetic than reality.

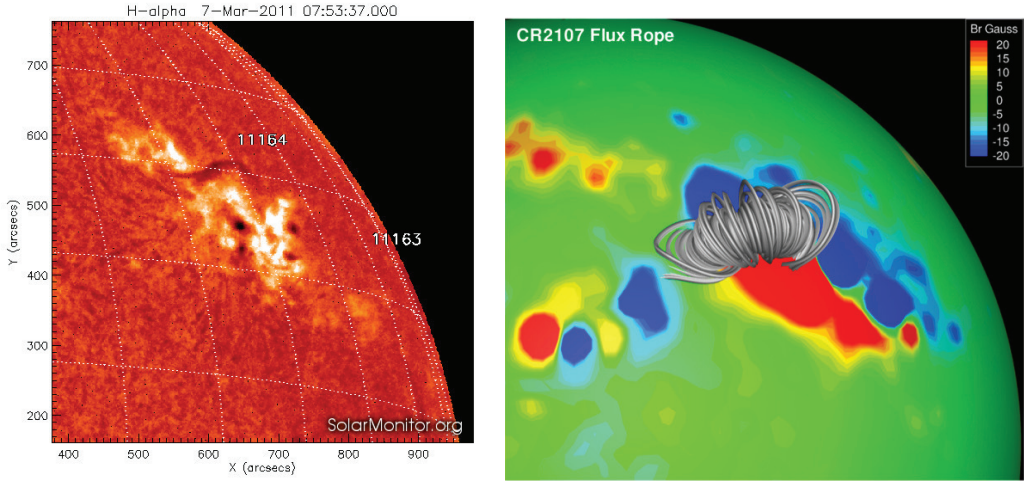

Figure 3.3: Left: The H_α observation on 2011 March 7 showing the filament location. Right: The Titov-Démoulin flux-rope setup in the model. The color scale on the Sun shows the radial magnetic field strength.

3.3 Results

We run the simulation for 20 min during which the CME propagates to $\sim$5 $R_\odot$. In order to investigate the different thermodynamics of the 1T and 2T CME, in Figure 3.4, we show the temperature structures on the CME propagation plane for both 1T

and 2T models at T = 15 min. In the 1T model, we can see the heat precursor extending far beyond the CME and CME-driven shock (marked with dashed line in Figure 3.4) to $\sim$10 $R_{\odot}$ beyond which the heat conduction coefficient becomes insignificant. The highest temperature inside the heat precursor and behind the shock reaches $\sim$10 MK. The heat precursor is caused by electron heat conduction applied to the single shock-heated fluid along open field lines. In the 2T model, we can still see the heat precursor in the electron temperature due to the energy exchange between shock-heated protons and electrons near the Sun as well as the adiabatic compression at the shock. However, the strength of the heat precursor is much smaller than in the 1T case, with the highest temperature inside the heat precursor is less than 2 MK. For the proton temperature, the shock structure is well captured. Due to the shock heating, the proton temperature reaches $\sim$85 MK at the shock region. Particle collisions are too infrequent to affect the large difference in the proton and electron temperatures found behind the shock. The electron and proton temperature difference was found in both the CME observations (*Raymond et al.*, 2000; *Mancuso et al.*, 2002) and many other astronomical collisionless shocks (e.g., supernova remnant; *Michael et al.* 2002). With the increasing of the shock speed, the difference between electron and proton temperatures becomes larger. An interesting phenomenon is the high temperature structure behind the shock in the 2T model (marked as the reconnection site in Figure 3.4). This structure is caused by numerical reconnection, which in our model heats only the protons. Since the heat conduction is not applied to protons, the dissipated energy cannot transfer back to the Sun, which explains the high proton temperature. This numerical issue can be solved with a finer grid as well as using explicit resistivity for the Joule heating of the electrons in the reconnection region. However, since it is unrelated to the shock structures, we will not address it in this study.

We further show the temperature evolution along a radial line crossing the CME

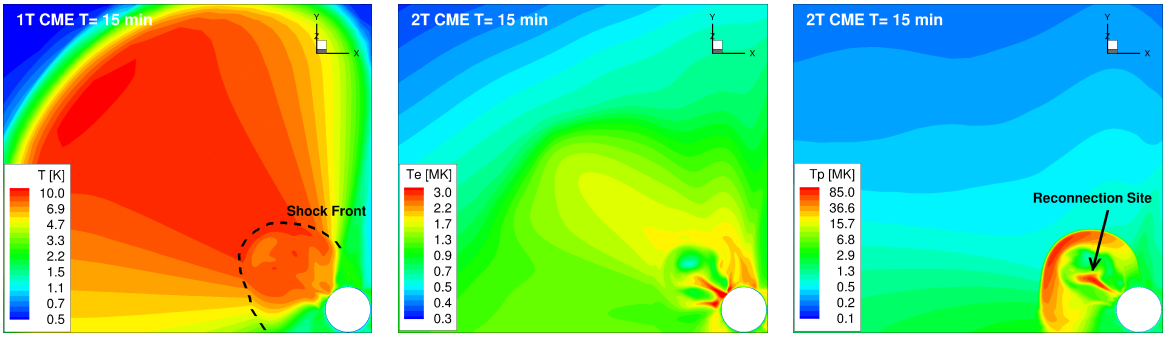

Figure 3.4: The 2D slice cut of the CME propagation plane. Left: 1T model temperature. The dashed line shows the position of the shock front. Middle: 2T model electron temperature. Right: 2T model proton temperature. The arrow shows the reconnection site.

shock structure at 1 min, 5 min, 10 min, 15 min, and 20 min in Figure 3.5. In the 1T model, after the shock-heating starts, the heat precursor immediately propagates to ∼15 $R_\odot$ where the heat conduction coefficient is prescribed to go to zero as the plasma becomes collisionless. The temperature then cools down with time. We notice there is a slight lift of the profiles at the front of the heat precursor. That is caused by the increased thermal relaxation time associated with the gradually decreasing heat conduction coefficient after 8 $R_\odot$. For the 2T model, the highest electron temperature reaches 4 MK at 5 min, while the proton temperature reaches ∼ 120 MK at the same time. The strength of the heat precursor in the 2T model is much less than the 1T model and is mainly caused by the CME compression instead of shock-heating.

In Figure 3.6, we show the evolution of various plasma parameters in the CME. In the first panel, the density evolution is shown. Comparing the 1T and 2T models, the major difference is the compression ratio. The compression ratio in the 1T model is much larger than in the 2T model (we will discuss it later in this session). Moreover, there are more density disturbances behind the shock structure in the 2T model. In the second panel, we show the velocity evolution of the CME. There is ∼500 km s^{-1} difference between the 1T and 2T CME speed. Since we initiate the CMEs with identical flux ropes, the energy input is the same in the 1T and 2T models. The speed

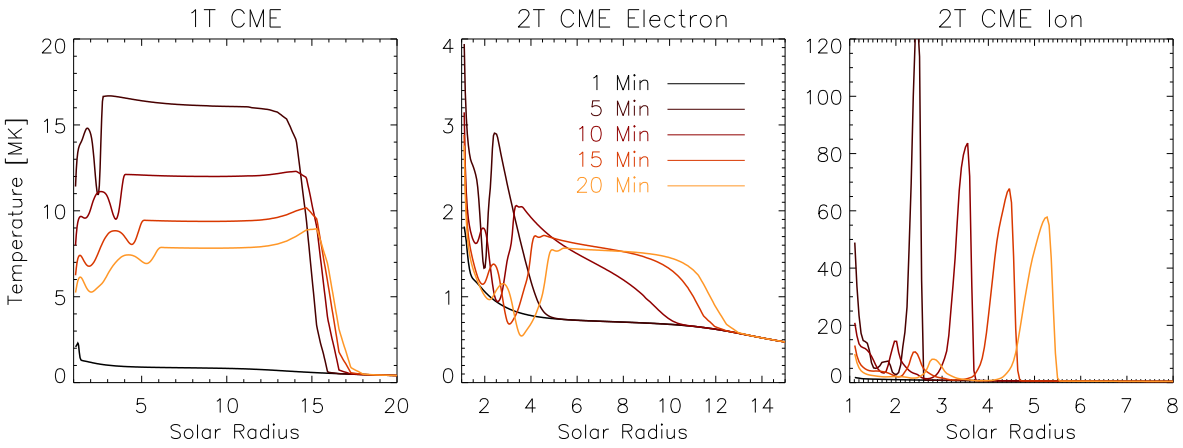

Figure 3.5: Line profiles along the CME propagation path at different times. Left: 1T model temperature. Middle: 2T model electron temperature. Right: 2T model proton temperature.

difference is mainly caused by the non-radial flow in the 2T CME (we will discuss this non-radial flow later in this Session). In the third panel, the local Mach number evolution is shown. As we can see, the heat precursor has a major influence on the thermodynamics of the CME-driven shock. For the 1T CME, the high temperature of the heat precursor dramatically increases the local sound speed and decreases local Mach number in front of the CME, while this phenomenon is not seen in the 2T model.

The shock Alfvén Mach number, compression ratio, and θ_{Bn} (the angle between the magnetic field and shock normal) are three key parameters for the diffusive shock acceleration (DSA) of SEPs (e.g., *Sokolov et al.* 2006). The higher shock Alfvén Mach number and higher compression ratio can result in the higher energy of the accelerated SEPs. In Figure 3.7, we show shock speed and shock Alfvén Mach number for the 1T and 2T CME. Comparing 1T and 2T models, there are two major differences. First, in the 1T model, the shock has already attained maximum speed. However, in the 2T model, the acceleration process is evident. The maximum shock speeds (∼3000 km s^{-1}) are similar in the 1T and 2T models. The other difference is the magnitude

of the shock Alfvén Mach number. In the 2T CME, the shock achieves larger shock Alfvén Mach number than in the 1T CME. The shock Alfvén Mach number of 1T CME is $\sim$4 – 5 during the whole evolution, while in the 2T case the Alfvén Mach number is larger than $\sim$5 with maximum of $\sim$7.

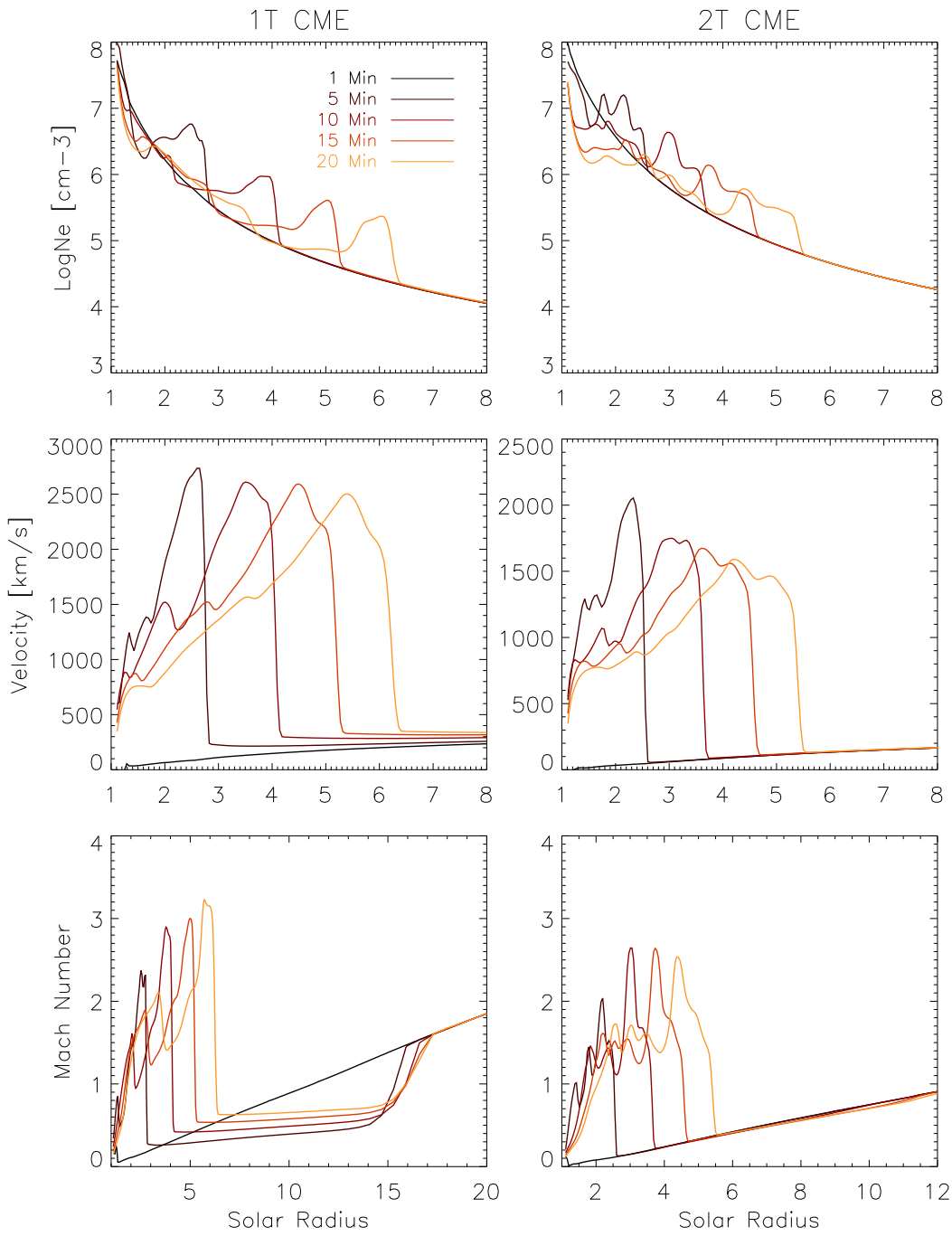

Figure 3.6: Line profiles along the CME propagation path at different times. First panel: density evolution. Second panel: velocity evolution. Third panel: local Mach number evolution.

In order to understand the gradual SEP events that are believed to be accelerated by the DSA mechanism, the compression ratio variation during the shock propagation is needed and usually cannot be obtained from observations (e.g., *Tylka and Lee* 2006).

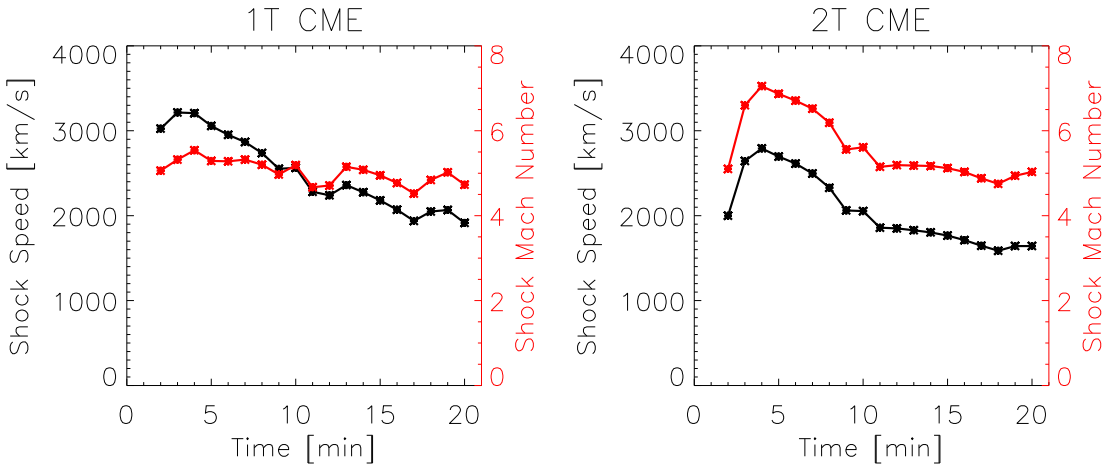

Figure 3.7: The shock speed and shock Alfvén Mach number evolution in the 1T and 2T CME models. The black lines show the shock speed and the red line show the shock Alfvén Mach number.

In Figure 3.8, we show the compression ratio evolution of the shocks from the 1T and 2T CME models. Based on the energy conservation across the shock, the maximum shock compression ratio in the strong shock limit is 4 for $\gamma = 5/3$. For the 1T CME, the compression ratio is always larger than 4, and the maximum value reaches >10. For the 2T CME, the compression ratio is around 4 during the whole evolution. The much higher compression ratio in the 1T model is caused by the heat conduction that very effectively reduces the temperature of the plasma behind the shock, which results in compression and an increased plasma density. Therefore, although the 1T model has a higher compression ratio, it is highly unphysical. Based on the Alfvén Mach number and compression ratio comparison between the 1T and 2T CMEs, in the perspective of particle acceleration (especially by diffusive shock acceleration), the shock formed in the 2T model can be a better accelerator than the shock in the 1T model.

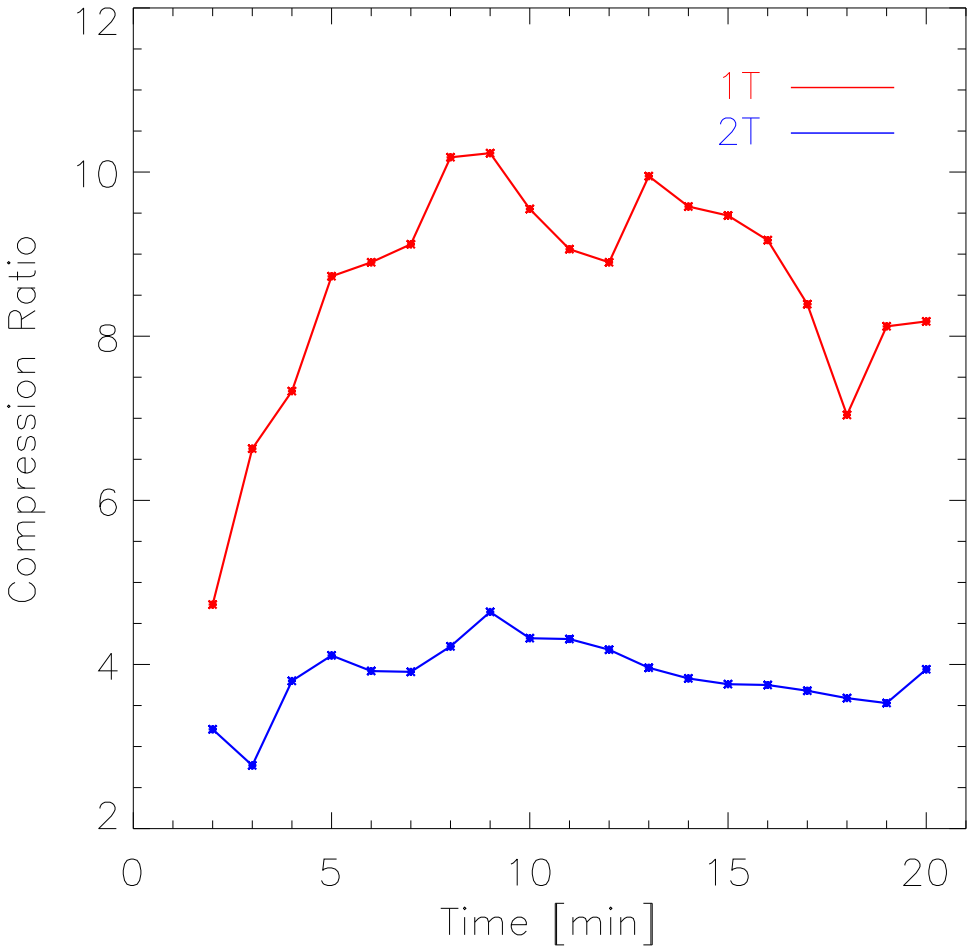

Figure 3.8: The compression ratio evolution of the shock calculated from the 1T and 2T CME models. The red line represents 1T model and the blue line represents the 2T model.

Figure 3.9 shows the 3D CME evolution for both 1T and 2T models at 5 min, 10 min, and 20 min after the initiation. The isosurfaces represent the radial velocity of 1000 km s^{-1}. The color scale on the isosurfaces show the temperature (1T)/proton temperature (2T). The field lines are colored by the density so that we can roughly see the propagation of the CME material as well as the shock positions. The gray

scale on the surface of the Sun shows the magnetic field strength. In the 1T model, the plasma is heated by the shock and cools by heat conduction to reach 15 MK at 5 min and gradually cools down due to the adiabatic expansion and heat conduction behind the CME-driven shock. In the 2T model, since the CME driven shocks exceed the proton sound speed, the protons are dissipatively heated by the shock and reach ∼90 MK at 5 min.

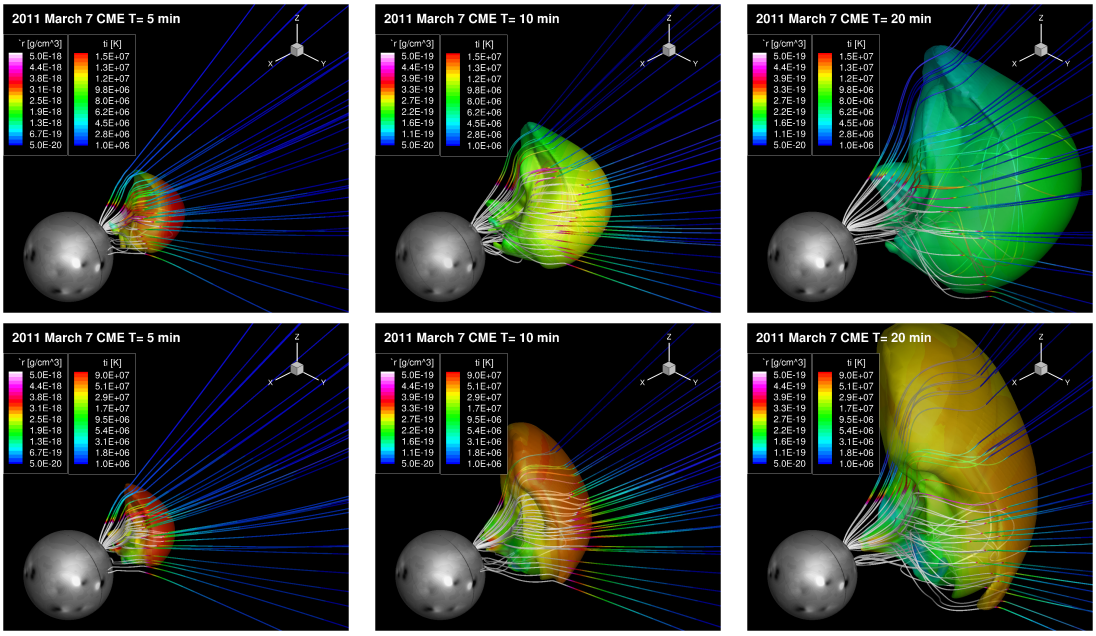

Figure 3.9: 3D CME evolution of 1T and 2T models. The isosurface represents Vr = 1000 km/s. The color on the isosurface shows the proton temperature. The field lines are colored by plasma density.

We notice the morphology of the CME is quite different in the 1T and 2T models after ∼10 min. In the 1T model, the shape of the velocity isosurface shows a radial expansion, while in the 2T model it seems that the expansion has a non-radial component. This non-radial flow is caused by the thermal pressure gradient in the CME sheath. Since the proton population is not falsely attributed electron heat conduction, the energy of shock-heated protons cannot be effectively transferred from behind the shock. Therefore, the thermal pressure and pressure gradient in the 2T model is much higher than the 1T model. This pressure gradient pushes the plasmas poleward and

causes the non-radial flows. The non-radial flows are only evident in near the pole due to the simpler magnetic structure and smaller density in this region. Such non-radial CME expansion was first found from Skylab CME observations (*MacQueen et al.*, 1986). With more observations available from Solar and Heliospheric Observatory (SOHO)/Large Angle and Spectrometric Coronagraph (LASCO; *Brueckner et al.* 1995b), there are many event studies (e.g., *Gosling et al.* 1998, *Gopalswamy et al.* 2000) and statistical studies (e.g., *St. Cyr et al.* 1999, *Wang et al.* 2011). The observed non-radial flows have latitudinal dependence that the poleward expansion is more preferred than the equator ward expansion. Our 2T CME simulation result is consistent with these observations. Also, there are some observations suggesting that the strong magnetic field of the coronal holes can deflect CMEs (*Gopalswamy et al.*, 2009). In our simulation, the field strength in the coronal hole is not strong enough compared with the pressure gradient to deflect the CMEs. One evident effect of this non-radial flow is the slower CME speed in the 2T model. The non-radial flow causes larger mass accumulation and therefore drags down the CME speed.

Since we simulate a realistic CME event, the model-data comparison can provide a general evaluation about the model performance. More importantly, the comparison between 1T and 2T model results can deepen our understanding of the thermodynamics behind the models. In Figure 3.10, we show the comparison between the SOHO/LASCO C2 (1.5 – 6.0 $R_\odot$) CME white light image with both the 1T and 2T model synthesized white light images. The color scale shows the relative intensity changes. In this study, we use TD flux rope to initiate the CME, therefore the 3-component structure of the CME cannot be correctly reproduced (*Illing and Hundhausen*, 1985). For the TD flux rope model, the flux rope structure and erupting filament material coincide with each other. However, in the 3-component structure, they are represented by "dark cavity" and "bright core", respectively. Instead, we will focus on the comparison of CME-driven shocks. A more comprehensive and precise

comparison will be performed in Chapter IV. For this event, the CME-driven shock has a typical "double-front" morphology (*Vourlidas and Ontiveros*, 2009), in which the faint front is caused by the shock and the bright front is the coronal plasma piled up at the top of the erupting flux rope. In both the 1T and 2T models, we can see the bright front. However, the faint front is not obvious in the 1T model but is evident in the 2T model. There are some fine structures behind the shock which could be related to the disturbance after the shock passing.

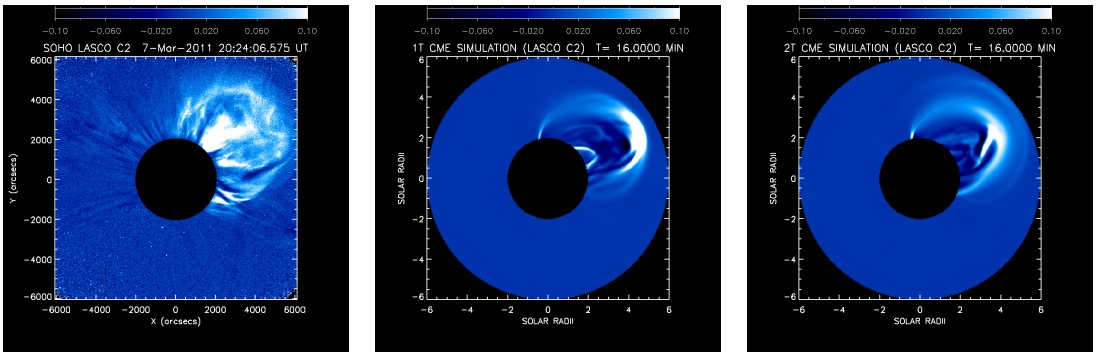

Figure 3.10: Comparison between the SOHO/LASCO C2 CME white light image (left panel) with the 1T (middle panel) and 2T (right panel) model synthesized images for the 2011 March 7 CME event. The color scale shows the relative intensity changes.

3.4 Summary & Conclusion

In this study, we simulated the fast CME event that occurred on 2011 March 7 using the newly developed AWSoM model and investigated the different thermodynamic behavior between the one- and two-temperature models. In both the 1T and 2T models, the background solar wind is heated by the Alfvén wave dissipation and accelerated by the same pressure. For the 1T model, the thermal heat conduction, radiative loss, and wave heating act on the single plasma temperature. For the 2T model, we separate the energy equations for electrons and protons. The thermal heat conduction and radiative loss are only applied to the electrons, while 40% of the wave

dissipation energy goes to electrons and 60% of the energy goes to protons. The electrons and protons are only coupled by Coulomb collisions. We further assume that all dissipated energy from shocks is converted to heat protons, while electrons are heated adiabatically. The thermodynamics of the CME and CME-driven shocks are analyzed in detail, especially some key parameters (e.g., shock Alfvén Mach number, compression ratio) in light of the diffusive shock acceleration mechanism. Also, the white light observation from SOHO/LASCO is used to compare with the model synthesized images. We summarize the major findings as follows:

1. The major thermodynamical difference between the 1T and 2T models is the existence of high temperature heat precursor in front of the 1T CME. This heat precursor is due to the heat conduction along the open magnetic field lines in front of the CME-driven shock. When separating the electron and proton temperatures, this heat precursor is greatly reduced in the 2T electron temperature because the absence of shock heating for the electrons.

2. The fast CME-driven shock can effectively heat the plasmas. When the electron and proton temperatures are separated, the proton temperature can reach ∼120 MK at 5 min. In the 1T CME, the highest temperature is ∼15 MK. Our results are consistent with the 1D model results by *Kosovichev and Stepanova* (1991) and 3D model results by *Manchester et al.* (2012).

3. The expansion of CME structures are different for the 1T and 2T models. The 1T CME shows a more radial expansion while the 2T CME shows non-radial poleward expansion at the later stage of evolution. This non-radial expansion is caused by the higher thermal pressure and pressure gradient behind the shock in the 2T model. Due to the simpler magnetic structure and more tenuous plasmas in the pole region, the non-radial flows shows poleward expansion instead of equator ward. The magnetic strength in the coronal hole is not strong enough to deflect the CME in our simulation.

4. The shock structures reflected by the synthesized white-light images are also

different for the 1T and 2T CME. For the 2T CME, we can see the "double-front" morphology in the synthesized images while that feature is missing in the 1T CME.

5. The compression ratio of the 1T CME well exceeds the strong shock limit value of 4, while the 2T CME has a compression ratio is approximately 4 during the whole evolution. The much higher compression ratio in the 1T model is caused by the heat conduction behind the shock that cools down the plasma efficiently and allows the density to increase.

6. The 2T CME achieves a higher shock Alfvén Mach number than the 1T CME and exhibits a more gradual acceleration. Although the 1T CME has a much larger compression ratio than the 2T CME, this large compression ratio is unphysical as stated above. Therefore, our result suggest that 2T CME-driven shock should be applied for the SEPs by DSA mechanism in the future.

Based on the above findings, we conclude that the 1T model produces significant errors in CME-driven shocks. Because collisions are so infrequent that the electrons and protons thermally decouple on the time scale of the CME propagation. In order to produce the physically correct CME structures and CME-driven shocks, explicit treatment of electron heat conduction in conjunction with proton shock heating is needed in the CME simulation. There are still some drawbacks for the 2T model used in this study. First, since the electron heat conduction is treated with a diffusive formulation, the heat flux can transfer with speeds higher than the electron thermal speed, which is unrealistic. In the future work, we will apply the heat flux limiter (e.g., *van der Holst et al.* 2011) to the electron heat conduction to prevent the extremely fast transport. Second, the Joule heating of the electrons in the reconnection region also needs to be addressed by using explicit resistivity instead of energy conservation. Third, the Spitzer heat condition is only applicable to the collision-dominated regions near the Sun. After $\sim$10 $R_\odot$, the plasmas become free-streaming due to infrequent collisions. The electron heat flux will then travel with the plasma bulk flow speed

(*Hollweg*, 1974; *Canullo et al.*, 1996). We will apply collision-less electron heat conduction assumption (e.g., *Lionello et al.* 2001), with which the propagation of CME from the Sun to 1 AU can be simulated.

CHAPTER IV

Global MHD Simulation of the Coronal Mass Ejection on 2011 March 7: from Chromosphere to 1 AU

Some think that solar work is pretty well played out. In reality, it is only beginning.

– George Ellery Hale, *1893*

All that you did on his behalf
Has caused the lovely Sun to laugh.

– Albert Einstein, *1929*

4.1 Introduction

Coronal mass ejections (CMEs) are a major source of potentially destructive space weather conditions, in which 10^{15}–10^{16} g of plasma is ejected from the Sun with a kinetic energy of order 10^{31}–10^{32} erg. The interplanetary CMEs (ICMEs) that pass Earth can disturb the Earth's magnetosphere and trigger geomagnetic storms (*Gosling*, 1993). Also, fast CMEs can drive shocks in the heliosphere (e.g., *Sime and*

Hundhausen 1987; *Vourlidas et al.* 2003) that are responsible for gradual solar energetic particle (SEP) events (*Reames*, 1999) through the diffusive shock acceleration (DSA) mechanism. The SEPs can pose major hazards for spacecraft and human life in outer space. Due to the limited observations of CME/ICME, numerical models play a vital role for interpreting observations, testing theories, and providing forecasts. Especially, the ability to realistically simulate events by global MHD models is critical for accurate space weather forecasts.

The first attempt to predict the CME evolution was achieved by empirical kinematic models. These kind of models utilize the remote observations near the Sun to predict the arrival time of the CME at 1 AU. By using the SOHO coronagraph measurements of CMEs, *Gopalswamy et al.* (2001) established an empirical model to estimate the arrival time of the CMEs at 1 AU with an average uncertainty of $\sim$10.7 hours. Another successful example is the kinematic 3-D Hakamada-Akasofu-Fry version 2 (HAFv.2) model (*Hakamada and Akasofu*, 1982; *Fry et al.*, 2001; *Dryer et al.*, 2004), in which the type II radio burst, soft X-ray, and solar image data are used to derive the shock speed and direction. The prediction error of the HAFv.2 model is also around 10 hours. The most frequently used predictive kinematic model is the cone model, which fits the CME observations with three free parameters: angular width, speed, and central CME position (*Zhao et al.*, 2002). With the STEREO observation, the cone model was improved to use information from stereoscopic fitting (*Odstrcil and Pizzo*, 2009) as well as the non-uniform density and velocity (*Hayashi et al.*, 2006). The cone model has been widely used to predict the CME/CME-driven shock velocity and arrival time in the space weather forecasting.

However, due to the empirical nature of the kinematic models, the accuracy and predictable parameters are limited. In order to provide more accurate forecast, the kinematic models were combined with 3D MHD models. Typically, the kinematic models will provide the inner boundary conditions (e.g., velocity, pressure) to the

MHD models. Then the CME disturbance in the MHD model can propagate to 1 AU and provide the forecast. Successful examples include combining the ENLIL heliosphere model with the CME cone model (e.g., *Odstrcil et al.* 2005; *Xie et al.* 2004) or coupling the 3D MHD model by *Han et al.* (1988) with the HAFv.2 model (*Wu et al.*, 2007a,b). Both model combinations give density, temperature and velocity predictions at 1 AU with an arrival time error is in the order of 10 hours. While very useful, this type of models does not include the magnetic field of the CME and cannot capture the CME structures formed in the low corona since the heliosphere MHD model always starts outside of the magnto-sonic point.

In order to improve the capability of the forecasting models, especially the ability to forecast the geomagnetic storms, the magnetic structure of the CME has to be taken into account. Therefore, the most sophisticated prediction models to the date have inner boundary lower in the solar corona and incorporate the magnetic driven models of CME initiation. Several solar wind model with coronal inner boundary have been developed in the past decade (e.g., *Groth et al.* 2000; *Roussev et al.* 2003a; *Cohen et al.* 2007; *Feng et al.* 2011; *Evans et al.* 2012). By applying the data-driven boundary conditions from the synoptic magnetogram, these solar wind models can reproduce the realistic steady state solar wind. Some data-driven model can also couple with the surface flux transport model to capture the global coronal evolution (*Feng et al.*, 2012).

There are three major types of CME initiation model: the analytical flux rope model, the breakout model, and flux-emergence model. For the first type (e.g., *Titov and Démoulin* 1999; *Gibson and Low* 1998), the flux ropes are implemented into the background solar wind solution and will erupt due to the force-imbalance. For the second type (*Antiochos et al.*, 1999), the photospheric shear flows are applied around the polarity inversion line (PIL) until the reconnection happens. For the flux-emergence model, CMEs are triggered by magnetic reconnection between the emerging field and

a stressed coronal field (e.g., *Chen and Shibata* 2000; *Manchester et al.* 2004a; *Fan and Gibson* 2007). The advantage of the flux rope initiation is that the eruption does not depend on the magnetic configuration of the active regions. Therefore, it is more favorable for the operational space weather forecast models. While the advantage of the breakout model lies on the realistic CME acceleration process during the initiation. Both initiation models have been successfully used in the CME simulations (e.g., *Manchester et al.* 2004b,c; *Roussev et al.* 2004; *Manchester et al.* 2008; *MacNeice et al.* 2004; *van der Holst et al.* 2009; *Karpen et al.* 2012). By initiating a TD flux rope, *Manchester et al.* (2008) simulated the Halloween CME event from the corona to the Earth and did the first quantitative comparison between the synthetic coronagraph images and LASCO observations, in which the strong CME-driven shock was simulated and validated. In the MHD simulation by *Tóth et al.* (2007) for the same event, the arrival time of the simulated CME is within $\sim$1.8 hours comparing with the observed arrival time. Due to the realistic CME and shock structures, this type of model has also been used to investigate the SEP acceleration by the shock (*Roussev et al.*, 2004; *Manchester et al.*, 2005; *Kozarev et al.*, 2013) and CME-CME interaction (*Lugaz et al.*, 2005, 2007, 2013). For a recent review of the numerical modeling of ICMEs, one can refer to *Lugaz and Roussev* (2011).

In this Chapter, we describe a realistic CME simulation for the event occurred on 2011 March 7 from active region (AR) 11164. We will simulate the CME propagation from the Sun to 1 AU by using the state-of-art Alfvén wave solar model (AWSoM; *van der Holst et al.* 2014) while initiating the CME with the Gibson-Low (GL) flux rope model (*Gibson and Low*, 1998). The new ASWoM is a data-driven global MHD model extending from the upper chromosphere to the corona and the heliosphere. It is developed from the previous works (*van der Holst et al.*, 2010; *Jin et al.*, 2012; *Sokolov et al.*, 2013; *Oran et al.*, 2013). The new model has the advantage of physically self-consistent treatment of Alfvén wave turbulence. By separating the electron and

proton thermodynamics, the CME and CME-driven shocks can be correctly simulated (*Manchester et al.*, 2012; *Jin et al.*, 2013).

The 2011 March 7 CME event is fast, with a speed over 2000 km s^{-1}. It drives a shock and produces a strong SEP event. Good observation coverage of this event from SDO, SOHO, and STEREO A/B, provides an excellent opportunity to validate our CME simulation from the Sun to 1 AU. Also, the detailed analysis of the simulation and observation data will help us get a better understand about the important physical processes during the CME propagation in the heliosphere. The Chapter is organized as follows: In Section 2, we describe the AWSoM for the background solar wind as well as the GL flux rope model for the CME initiation. The 2011 March 7 CME event simulation results and the validation by observations are shown in Section 3, followed by the summary and conclusion in Section 4.

4.2 Models

4.2.1 Background Solar Wind Model

The solar wind model used in this study is newly developed AWSoM (*van der Holst et al.*, 2014), which is a data-driven global MHD model extending from the upper chromosphere to the corona and the heliosphere. The inner boundary condition of the magnetic field is specified by the GONG synoptic magnetogram, while the initial magnetic field configuration is calculated by the Potential Field Source Surface (PFSS) model using a finite difference method (*Tóth et al.*, 2011b). The model starts from upper chromosphere with fixed temperature T = 50,000 K and density $n = 2\times10^{17}$ m^{-3}. The dense plasma at the boundary can provide a source of material for chromospheric evaporation. The correct physics (radiation cooling and heat conduction) self-consistently produce the proper density and temperature structure of the transition region and corona independent of the boundary conditions. The Alfvén

wave turbulence is launched at the inner boundary with the Poynting flux scaling with the surface magnetic field. The solar wind is heated by Alfvén wave dissipation and accelerated by the Alfvén wave pressure. The electron heat conduction and radiative cooling are also included in the model. In order to produce physically correct solar wind and CME structures such as shocks, the electron and proton temperatures are separated. Thus while the electrons and protons are assumed to have the same bulk velocity heat conduction is applied only to the electrons owing to their much higher thermal velocity. Note that the AWSoM also works for three temperatures to include the ion pressure anisotropy (*van der Holst et al.*, 2014).

There are three major improvements to the model that should be mentioned: First, the Alfvén wave turbulence dissipation rate is revised to incorporate physically consistent wave reflection and dissipation. The new dissipation rate can be expressed as:

$$\Gamma_{\pm} = \max\left(\mathcal{R}_{imb}, \frac{2\sqrt{|\mathbf{B}|}}{(L_{\perp}\cdot\sqrt{|\mathbf{B}|})}\sqrt{\frac{w_{\mp}}{\rho}}\right) \tag{4.1}$$

$$\mathcal{R}_{imb} = \sqrt{[(\mathbf{V_A}\cdot\nabla)\log V_A]^2 + [\mathbf{b}\cdot(\nabla\times\mathbf{u})]^2} \tag{4.2}$$

where $w_{\mp}$ is the wave energy densities. The $+$ sign is for waves propagating in the direction parallel to magnetic field $\mathbf{B}$, while the $-$ sign is for waves propagating antiparallel to $\mathbf{B}$. $\mathbf{V_A} = \mathbf{B}/\sqrt{\mu_0\rho}$ is the Alfvén speed and $\mathbf{b} = \mathbf{B}/|\mathbf{B}|$. ρ is the mass density, $\mathbf{u}$ is the velocity. $\mathcal{R}_{imb}$ represents the wave reflection rate, which is due to Alfvén speed gradient and vorticity along the field lines. Second, instead of using a constant value for the heat partitioning between the electrons and protons, the results of linear wave theory and stochastic heating are used (*Chandran et al.*, 2011). With this specification, the majority wave heating goes to electrons near the Sun and around the Heliospheric Current Sheet (HCS), while ion heating dominates away from the Sun and HCS due to the stochastic heating mechanism. For the detailed

calculation of the heat partitioning, please refer to the Appendix B of *van der Holst et al.* (2014). Finally, a collisionless electron heat conduction formulation as suggested by *Hollweg* (1978) is taken into account and combined with the collisional Spitzer heat conduction:

$$\mathbf{q}_e = f_s \mathbf{q}_{e,S} + (1 - f_s)\mathbf{q}_{e,H} \tag{4.3}$$

where the Spitzer heat conduction can be expressed as:

$$\mathbf{q}_{e,S} = -\kappa_e T_e^{5/2} \frac{\mathbf{BB}}{B^2} \cdot \nabla T_e \tag{4.4}$$

And the collisionless electron heat conduction is:

$$\mathbf{q}_{e,H} = \frac{3}{2} \alpha p_e \mathbf{u} \tag{4.5}$$

The f_s specifies the fraction of Spitzer heat flux, which is a function of r:

$$f_s = \frac{1}{1 + (r/r_H)^2} \tag{4.6}$$

where $r_H = 5R_\odot$, $\alpha = 1.05$, and $\kappa_e \approx 9.2 \times 10^{-12}$ W m^{-1} K$^{-7/2}$. For the detailed implementation of the collisionless electron heat conduction in the model, we refer to the Appendix C of *van der Holst et al.* (2014).

4.2.2 CME Initiation Model

Based on the steady state solar wind obtained in §4.2.1, we can initiate the CME using two different mechanisms (flux rope model and breakout model) implemented in the EE component. For the flux rope model, two different analytical models can be used: Titov-Démouline (TD) flux rope (*Titov and Démoulin*, 1999) and Gibson-Low (GL) flux rope (*Gibson and Low*, 1998). By applying the analytical flux rope to the active region along the PIL in a state of force imbalance, it will erupt immediately.

For the breakout model (*Antiochos et al.*, 1999), the CME is triggered by breakout reconnection in a quadrupolar field configuration. Instead of a flux rope, photospheric shear flows are applied around the PIL until the reconnection happens. Comparing with the flux rope model, the breakout model can capture a more realistic energy buildup and subsequent CME initiation and acceleration processes.

In this study, we choose the GL flux rope as the CME initiation model. The analytical solution of the GL flux rope is obtained by finding a solution to $(\nabla \times \mathbf{B}) \times \mathbf{B} - \nabla p - \rho \mathbf{g} = 0$ and $\nabla \cdot \mathbf{B} = 0$, and applying a mathematical stretching transformation to an axisymmetric spherical ball of twisted magnetic flux in the pressure equilibrium. During this process, the flux rope will acquire a geometrically complex configuration. At the same time, the Lorentz forces will be introduced, which supports dense filament plasma in the solar gravitational field. There are several advantages of choosing the GL flux rope: First, it can be implemented easily into any magnetic configurations so that the realization in the operational space weather forecast is easier than the breakout model that requires a special field configuration. Second, the most important feature of the GL flux rope is that it captures the typical 3-part density structure of the CME in the observation (*Illing and Hundhausen*, 1985). Third, compared with the TD flux rope, the magnetic structure of the GL flux rope is less diffusive (*Manchester et al.*, 2004c) and leads to a better *in situ* comparison at 1 AU.

For this simulation, the GL flux rope parameters are specified as follows: the stretching parameter $a = 0.6$; the radius of the flux rope torus $r_0 = 0.8R_\odot$; the distance of torus center from the center of the Sun $r_1 = 1.8R_\odot$; the flux rope field strength parameter $\alpha = 2.25$. The flux rope is placed 27 degree latitude and 155 degree longitude into the AR 11164. The flux rope is rotated 270 degree to match the PIL position of the pre-existing filament before the eruption in H_α observation (*Gallagher et al.*, 2002).

4.2.3 Model Implementation

First, the steady state solar wind solution is obtained for Carrington Rotation (CR) 2107 with the local time stepping and second-order shock-capturing scheme (*Tóth et al.*, 2012). The SC model uses 3D spherical grid from 1 $R_\odot$ to 24 $R_\odot$. The grid blocks consist of 6×4×4 mesh cells. The smallest radial cell size is $\sim 10^{-3}$ $R_\odot$ near the Sun to resolve the steep density and temperature gradients in the upper chromosphere. The largest radial cell size in SC is $\sim R_\odot$. Inside $r = 1.7$ $R_\odot$, the angular resolution is $\sim 1.4°$, outside that region, the grid is coarsened by one level. The IH model uses Cartesian grid to reach 250 $R_\odot$ with grid blocks consisting of 4×4×4 mesh cells. The smallest cell size in IH is $\sim 10^{-1}$ $R_\odot$ and the largest cell size is ~ 8 $R_\odot$. For both the SC and IH, the adaptive mesh refinement (AMR) is performed to resolve the HCS. The number of total cells is $\sim 3\times 10^6$ in SC, and $\sim 1\times 10^6$ in IH. In steady state, both the SC and IH domains are in heliographic rotating coordinates (i.e., Carrington coordinate).

After the steady state solution convergences, the GL flux rope is inserted into the active region, at which point the time-accurate mode starts to capture the CME eruption. Two more levels refinement along the CME path is performed to resolve the CME-driven shock, which doubles the number of total cells in SC to $\sim 6\times 10^6$. The SC runs 1 hour alone to let the CME propagate to ~ 18 $R_\odot$ when the SC-IH coupling begins. In the time-accurate mode, the IH is running under the heliographic inertial coordinate (i.e., heliocentric inertial coordinate). In order to capture the shock structure, especially the shock structure during the satellite-passing, both the grids along the CME path and around the satellite points are refined, which triples the number of total cells in IH to $\sim 3\times 10^6$. The coupling between the SC and IH runs to ~ 8 hours when all the CME structures have passed through the SC into the IH domain. Then the SC is turned off and the IH will run alone till the CME arrives at 1 AU.

4.3 Results

4.3.1 Background Solar Wind & CME Initiation

In order to validate the steady state solution of our model, we compare our model results with the available observations. Near the Sun, the model density and temperature are used to produce synthesized EUV images, which are then compared with the EUV observations from SDO/AIA (*Lemen et al.*, 2012) and STEREO/EUVI (*Howard et al.*, 2008). The comparison results are shown in Figure 4.1. Three EUV lines (SDO AIA 211 Å, STEREOA EUVI 171 Å, and STEREOB EUVI 195 Å) are selected that cover the temperature range from 1 MK to 2 MK. The observation time is at ∼20:00 UT on 2011 March 7. At that time, STEREO A was ∼88° ahead of Earth and STEREO B was ∼95° behind Earth. Since the observations are from three different view points, it covers most area of the Sun. We can see clearly that the model reproduces all the major active regions and the on-disk/polar coronal holes. Compared with our previous model (*Sokolov et al.*, 2013), the intensity of the active region is enhanced, which leads to a better comparison with the observations. The enhanced intensity is due to the increase of the wave reflection around the active regions. Note that in order to resolve the active regions, the 6×6×6 grid block and spatially fifth-order MP5 limiter (*Suresh and Huynh*, 1997) are used. The comparison suggests a quantitative agreement between our model and the observation for the density and electron temperature near in the low corona.

In Figure 4.2, the *in situ* OMNI and STEREO A proton speed, density, and proton/electron temperatures, and magnetic field are shown with the steady state model results for comparison. The OMNI data (obtained from the National Space Science Data Center (NSSDC)) provides selected data from Advance Composition Explorer (ACE), Wind, Geotail, and IMP8 spacecraft. The STEREO A data comes from two instruments on board: the proton parameters are provided by the Plasma

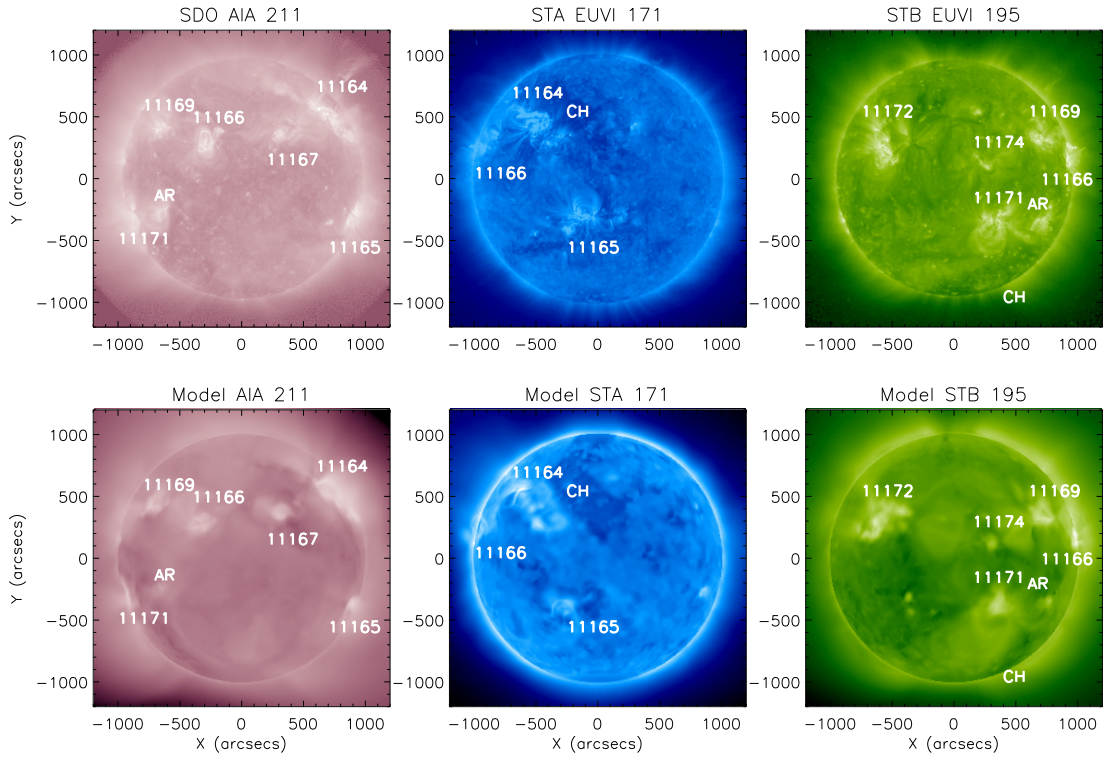

Figure 4.1: The comparison between observations and synthesized EUV images of the steady state solar wind model. Top panels: Observational images from SDO AIA 211 Å, STEREOA EUVI 171 Å, and STEREOB EUVI 195 Å. The observation time is 2011 March 7 ∼20:00 UT. Bottom panels: synthesized EUV images of the model. The active regions and coronal holes are marked both in the observational and synthesized images.

and Supra-Thermal Ion Composition Investigation (PLASTIC; *Galvin et al.* 2008); the magnetic field data is provided by the *in situ* Measurements of Particles and CME Transients (IMPACT; *Luhmann et al.* 2008b). We can see that the model reproduces the solar wind condition at 1 AU. Both the location and plasma parameters of the CIR are captured in the model. Note that for the 2011 March 7 CME event, the co-rotating interaction region (CIR) and the CME-driven shock structures are very close in location and interact with each other. Therefore, to be able to get the CIR structure correct is very important for successful CME event simulation. With the implementation of the collisionless heat conduction, the electron temperature reaches

0.1 MK at 1 AU, which is suggested by previous observations (e.g., *Burlaga* 1971).

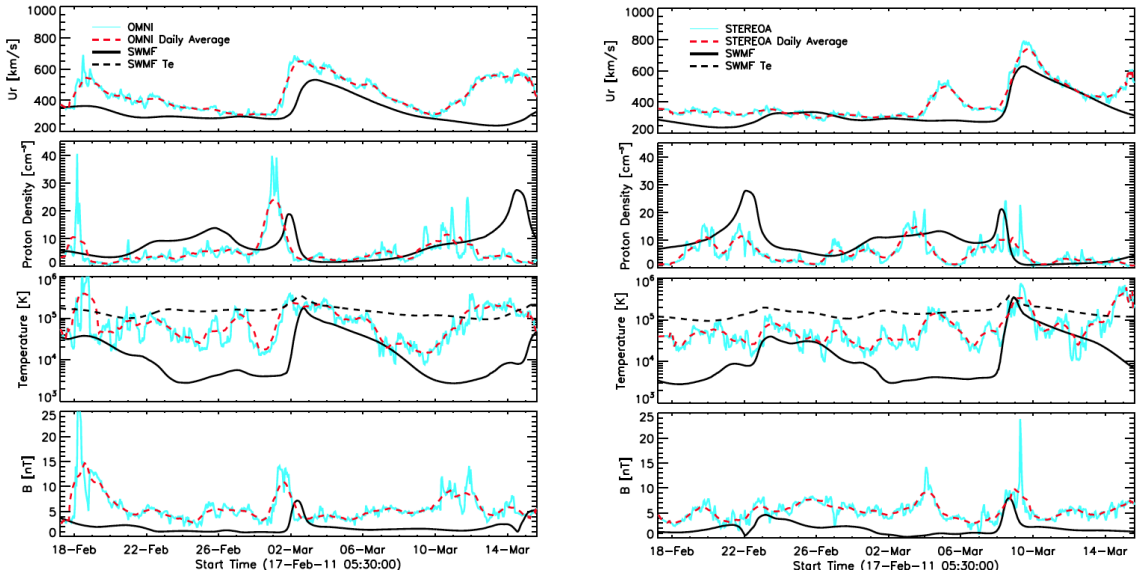

Figure 4.2: Comparison of OMNI and STEREO A observed solar wind speed, proton density, proton/electron temperatures, and magnetic field with the steady state model output for CR2107.

In Figure 4.3, we show the initial GL flux rope configuration based on the steady state solar wind solution. Figure 4.3a shows the 3D GL flux rope structure viewed from the top of the active region AR 11164. The flux rope is implemented along the PIL. In order to mimic the observed filament configuration, the GL flux rope is modified so that both the filament polarity and chirality are matched with the observation (*Martin*, 1998). We can see both the toroidal and poloidal fields from the selected field lines. Also, the filament material is added at the bottom of the GL flux rope. In Figure 4.3b-f, the central planes of the GL flux rope with the mass ratio, proton temperature, total magnetic field, radial velocity, and proton density are shown. The core of the GL flux rope has a higher density and lower temperature than the background, while the cavity of the GL flux rope has a higher magnetic field strength. All these features match the 3-part CME structure in the observation. Due to the insufficient background plasma pressure to offset the magnetic pressure of the

flux rope, it is in a force-imbalance state at the very beginning therefore will erupt immediately after the implementation. The front of the flux rope shows a positive radial velocity of $\sim$150 km s^{-1} at T = 0. In Figure 4.4, we overlap the background solar wind solution with the GL flux rope. The grid information is also shown before the refinement for the CME-driven shock. The flux rope eruption is very close to the north-polar coronal hole and the open-close field boundary.

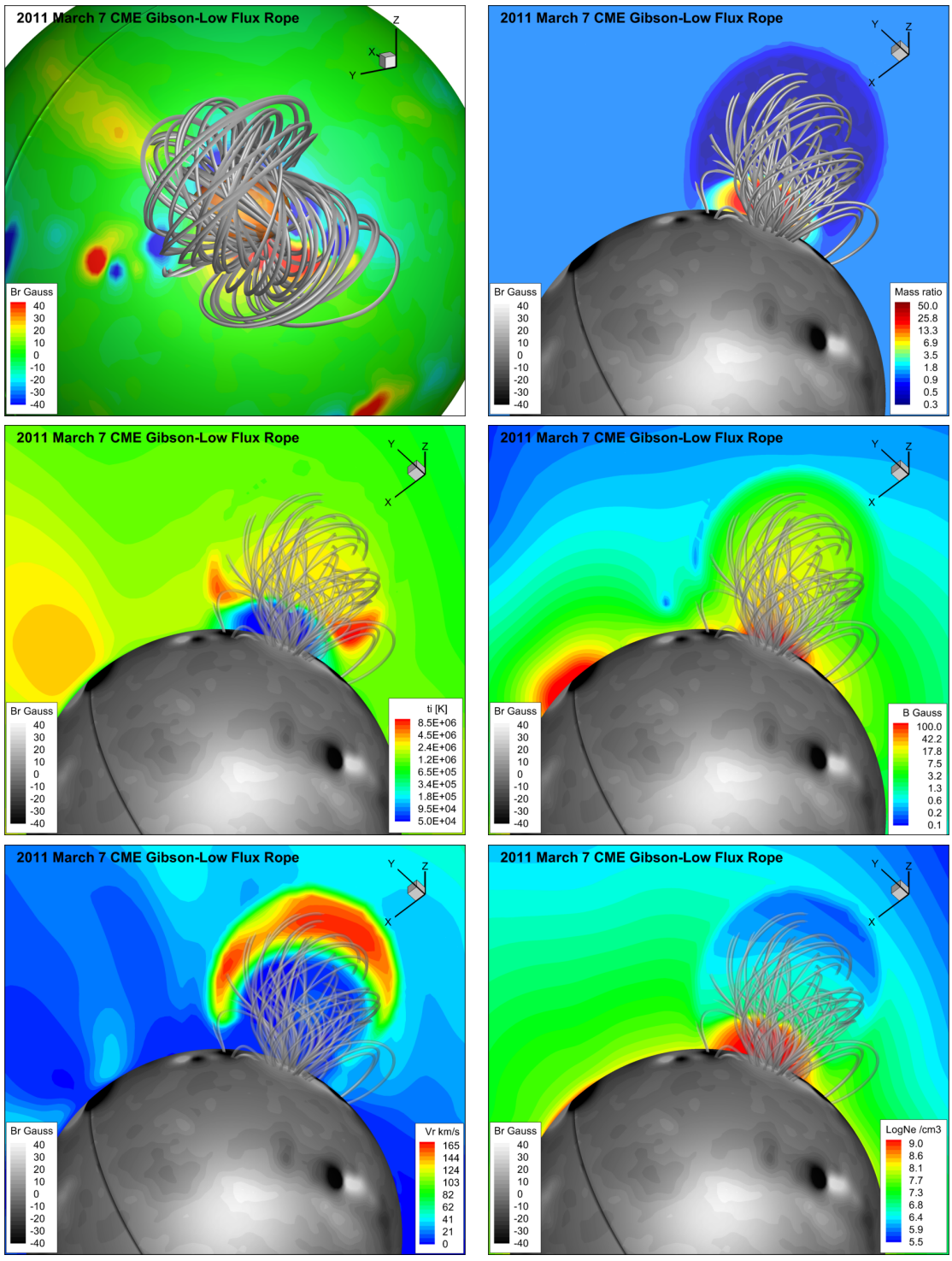

Figure 4.3: The initial GL flux rope configuration for 2011 March 7 CME. (a) 3D GL flux rope configuration viewed from the top of the active region. (b)–(f): central plane of the GL flux rope with mass ratio, proton temperature, total magnetic field, radial velocity, and proton density.

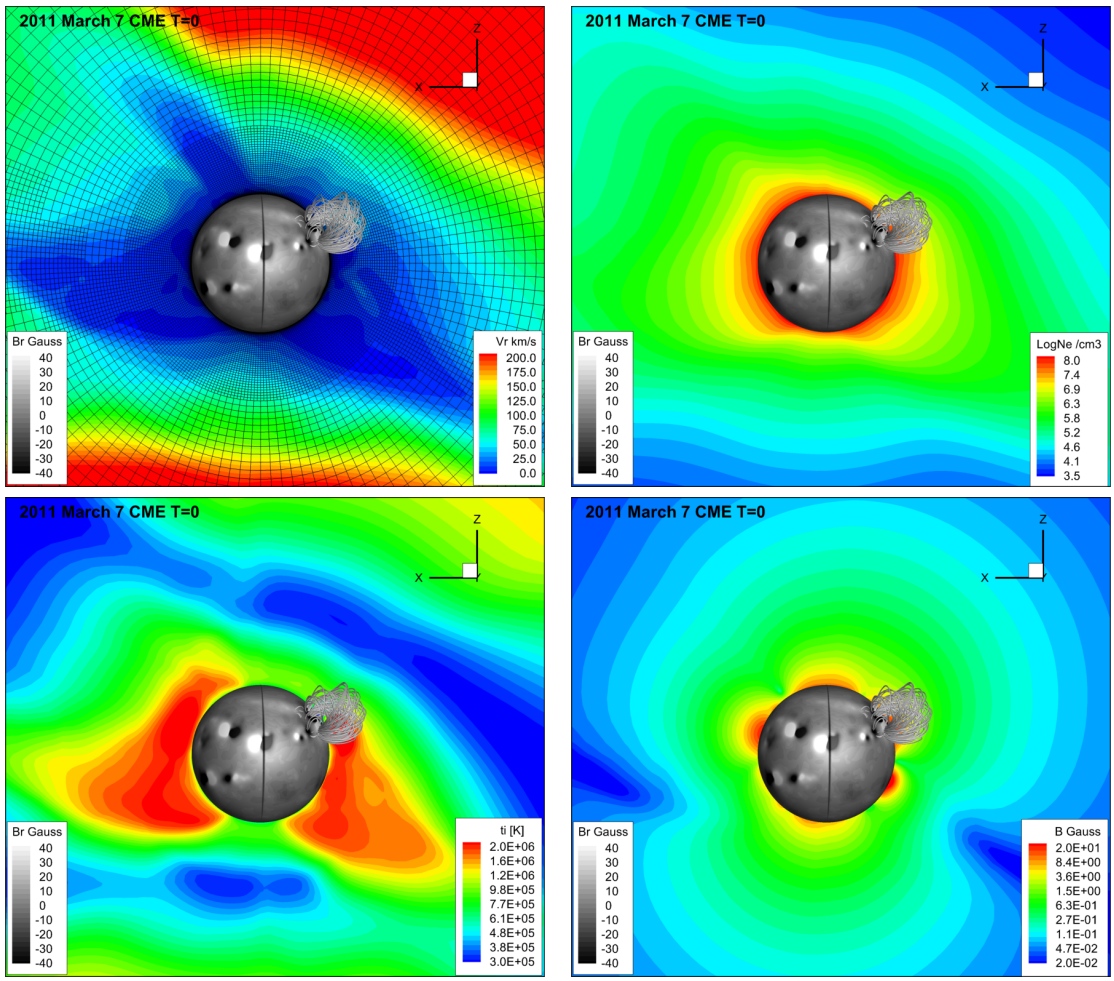

Figure 4.4: Meridional slice of the SC showing the radial velocity (top left), proton density (top right), proton temperature (bottom left), and total magnetic field (bottom right) at T = 0 after GL flux rope implement. The radial magnetic field is shown at r = 1.03 $R_{\odot}$ with gray scale. The black boxes in the velocity map show the grid information for the steady state simulation.

In Figure 4.5, we show the CME-driven shock at T = 5 minutes. We can see that the radial velocity of the CME reaches ∼2500 km $^{-1}$, which has far exceeded the proton thermal speed of ∼100 km s^{-1} in the corona. Therefore, the protons are shock-heated and the temperature reached 200 MK after 5 minutes. Due to the close distance to the polar coronal hole, part of the CME-driven shock is propagating into the fast wind and obtains a higher velocity and proton temperature. The refined grid information for the CME-driven shock is shown in the radial velocity figure.

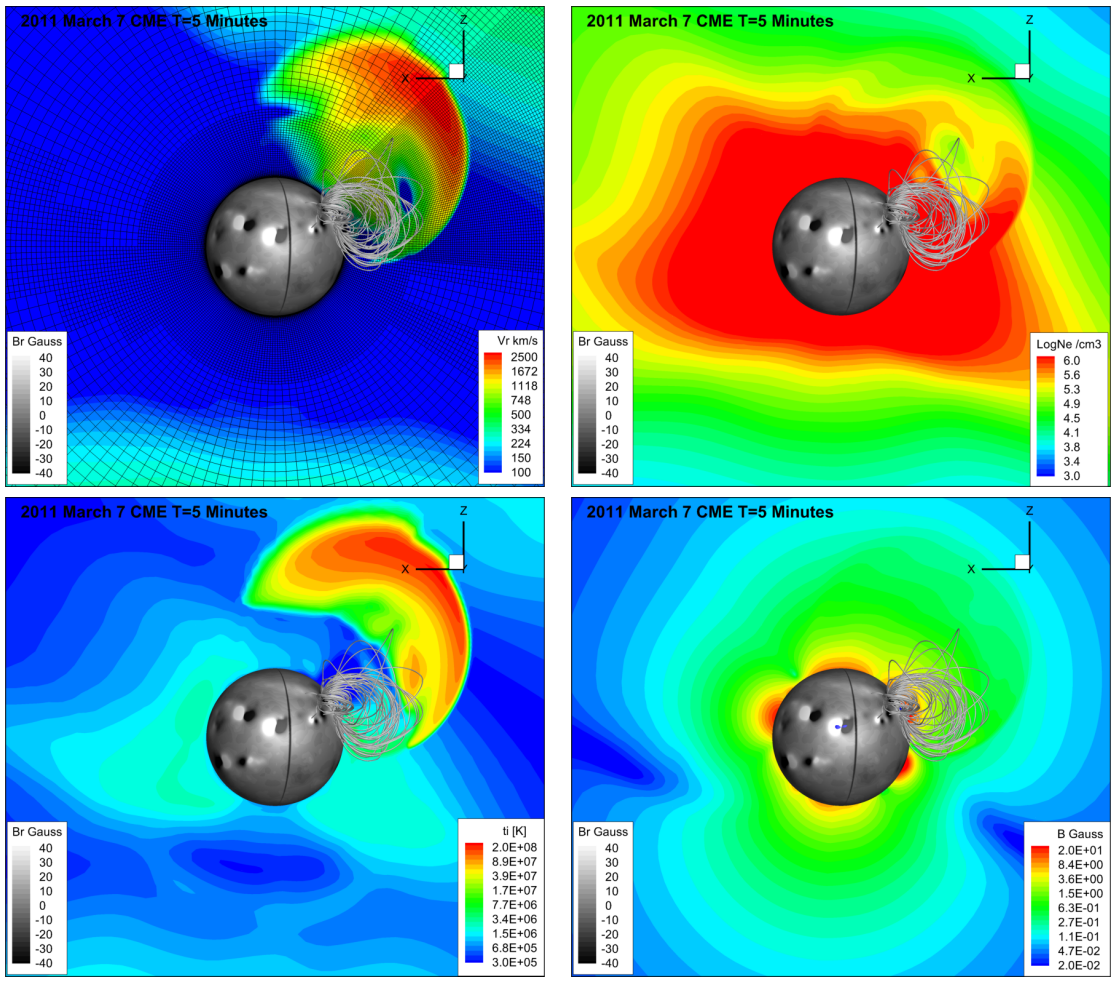

Figure 4.5: Meridional slice of the SC showing the radial velocity (top left), proton density (top right), proton temperature (bottom left), and total magnetic field (bottom right) at T = 5 minutes after GL flux rope implement. The radial magnetic field is shown at r = 1.03 $R_{\odot}$ with gray scale. The black boxes in the velocity map show the grid information used in the CME simulation.

4.3.2 CME from the Sun to 1 AU

In this section, we will describe the CME evolution from the Sun to 1 AU and validate the model with both the remote sensing and *in situ* observations. One of the most intriguing phenomena associated with CMEs is the EUV waves, which was first discovered by *Moses et al.* (1997) and *Thompson et al.* (1998, 1999) using the data from SOHO/EIT (*Delaboudinière et al.*, 1995). The EUV waves are bright fronts

that propagate over the solar disk during CME events. There are extensive studies about the EUV waves in the past (See reviews by *Chen et al.* 2005; *Patsourakos and Vourlidas* 2012). In Figure 4.6, the EUV waves in our simulation and in the SDO/AIA 211 $\mathring{A}$ observation are shown. Both the simulated and observed images are produced by the running difference method. The blue arrows in the figure show the position of the outermost front of the EUV waves while circles show the limb of the Sun. It is clear that our model reproduces many features of the EUV wave in this event: first, the position of the EUV wave front matches the observation. Especially, we notice that part of the wave front is missing in both the simulation and the observation, which is due to an active region (AR 11167 in AIA 211 Å observation of Figure 4.1). Our simulation result is consistent with previous MHD modeling results (e.g., *Cohen et al.* 2009; *Downs et al.* 2011, 2012) that the bright EUV waves are driven by the expanding CME and also have a fast-mode wave nature. A more detailed analysis about the EUV waves in this event will be performed in future work.

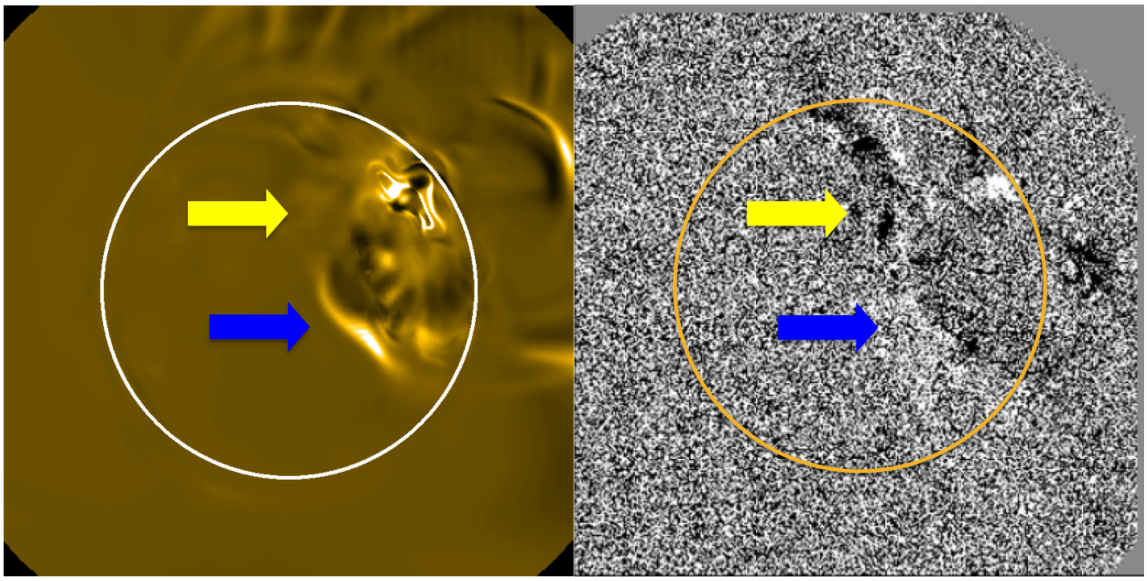

Figure 4.6: The EUV waves in the simulation (left) and in the SDO/AIA 211 Åobservation. Both the simulation and observation images are produced by running difference method. The blue arrows show the positions of the EUV wave fronts in the simulation and observation. The yellow arrows show the region where the EUV wave is impeded by an active region.

For space weather forecasting, attaining the correct propagation direction of the CME is critically important. In order to validate our model's propagation direction, we compare the simulated CME with the CME cone model reconstructed from the observations (*de Koning and Pizzo*, 2010). In Figure 4.7, the dense CME material in the model is represented by the mass ratio iso-surface of 5.0. The black lines show the cone model reconstruction of the CME-driven shock. Two viewpoints are shown so that we can see that the model CME propagates in the same direction as the cone model reconstruction. Also, we show several selected field lines in the model. The color scale on the field lines show the proton temperature. Due to the shock heating, the top of the field lines have the highest temperature ∼10 MK.

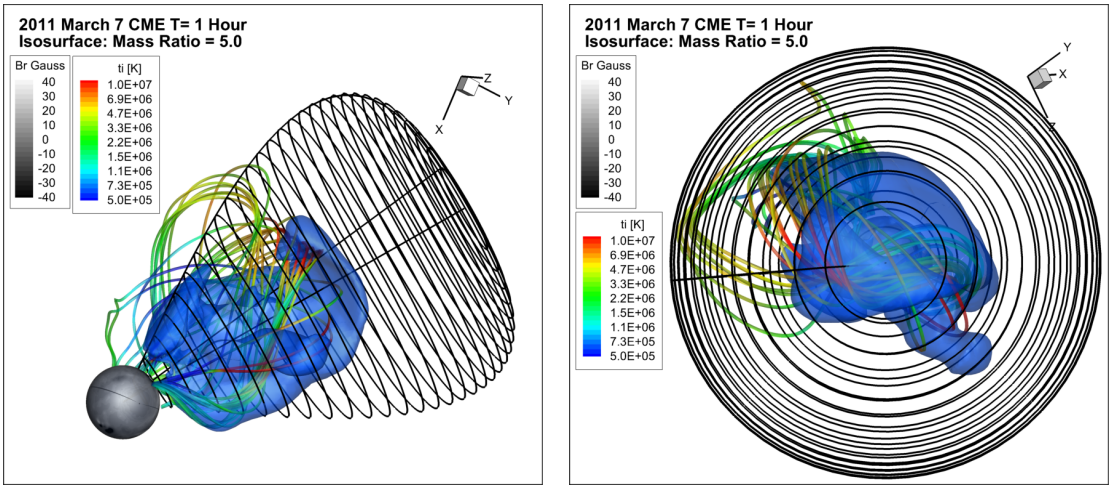

Figure 4.7: The comparison between the simulated CME and the cone model reconstruction of the event from two different viewing angles. The blue isosurface represents the mass ratio of 5. The color scale on the selected field lines shows the proton temperature.

The CME propagation near the Sun and in the heliosphere is mainly observed by the white light coronagraphs. For this event, there are three white light observations available from SOHO/LASCO C2/C3, STEREO A COR1/COR2 and STEREO B COR1/COR2. C2 has a field of view (FOV) from 2 $R_\odot$ to 6 $R_\odot$ and C3 has a FOV from 3 $R_\odot$ to 30 $R_\odot$. The FOV of COR1 is from 1.5 $R_\odot$ to 4 $R_\odot$. The FOV of COR2 is from 3 $R_\odot$ to 15 $R_\odot$. In Figure 4.8 and Figure 4.9, we show a comparison between the observed white light images and the model synthesized images for the 2011 March 7 event. Both the color scale shows the intensity differences divided by the background solar wind solution. In the observation, we can see clearly that the CME has a typical 3-part structure: the bright core that represents the filament material; the dark cavity that corresponds to the flux rope; the bright front that is due to the mass pile-up in front of the flux rope (*Illing and Hundhausen*, 1985). In the model, synthesized images, this 3-part structure is also evident. Moreover, both the observation and model show the second faint front that is the outermost part of the increased intensity region. The "double-front" morphology is consistent with

CME-driven shocks (*Vourlidas et al.*, 2003; *Vourlidas and Ontiveros*, 2009), which has been verified with numerical simulations (*Manchester et al.*, 2008). The white light comparison from three points of view confirms that the simulated CME propagates in the correct direction as observed.

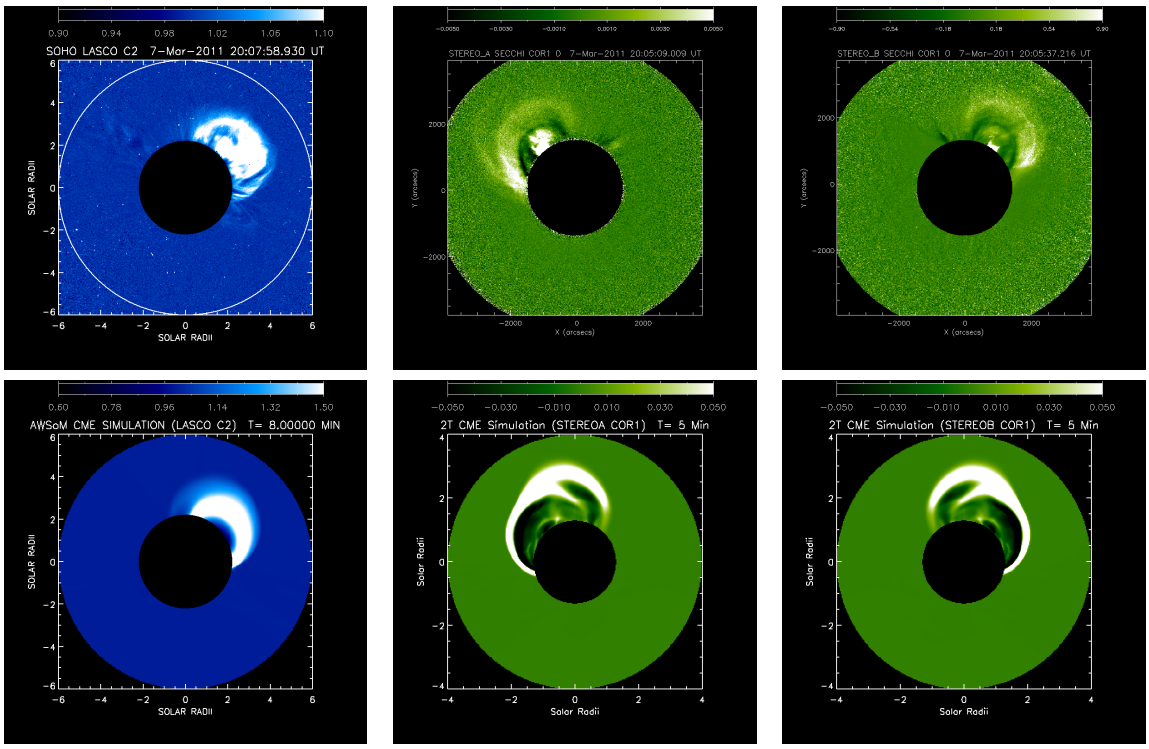

Figure 4.8: Comparison between the LASCO C2, COR1A, and COR1B white light images with the model synthesized images for the 2011 March 7 CME event. The color scale shows the relative intensity changes.

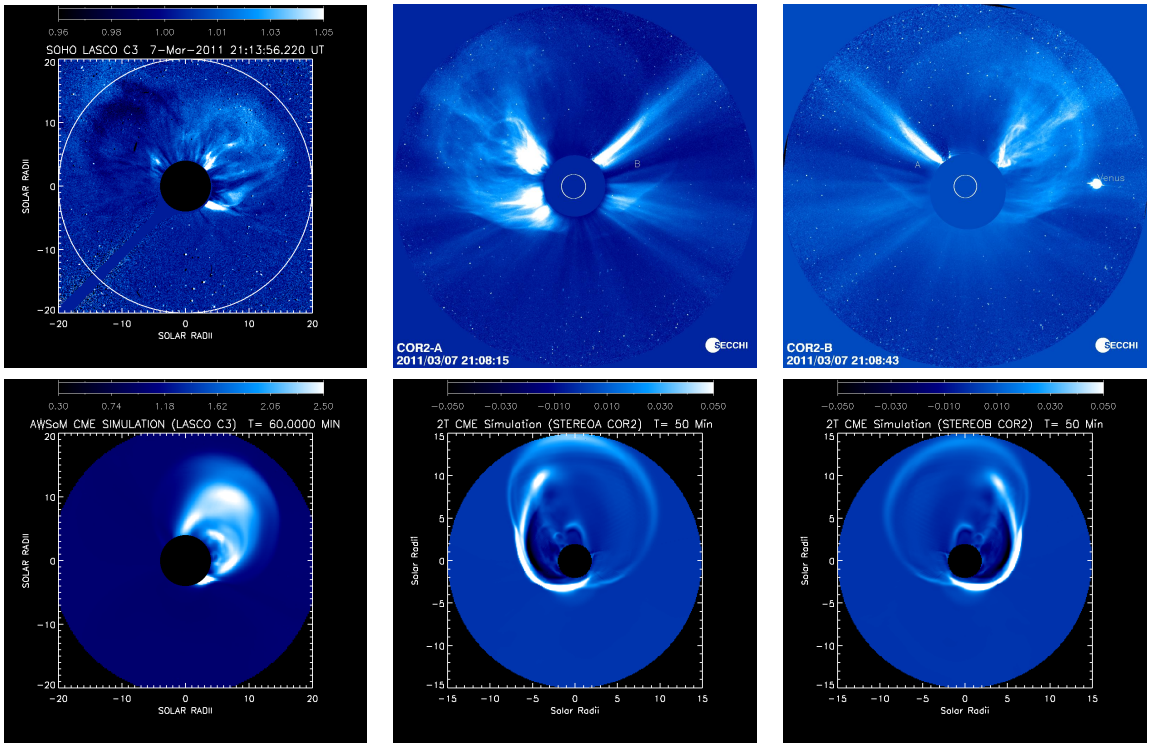

Figure 4.9: Comparison between the LASCO C3, COR2A, and COR2B white light images with the model synthesized images for the 2011 March 7 CME event. The color scale shows the relative intensity changes.

The speed of the CME is another important factor for precise space weather forecasts. From the synthesized white light images, the Height-Time (HT) evolution of different structures (CME-driven shock, flux rope front, and filament) is obtained. Due to the complexity of the observation, only the outermost part of white light observation is used to obtain the HT map. The results are shown in Figure 4.10. In the simulation, the faint front related to the CME-driven shock has the largest speed $\sim$2878 km s^{-1}. The bright front related to the flux rope pile-up has the second largest speed $\sim$2158 km s^{-1}. The filament has the slowest speed $\sim$1089 km s^{-1}. The observed CME speed (outermost front) is $\sim$2275 km s^{-1}, which is close to the speed of the bright front in the simulation, while $\sim$600 km s^{-1} less than the speed of the outermost front in the simulation. Due to the force-imbalance nature of the initial state of the flux rope, all the structures in the simulation experience a deceleration

process in the early stage of propagation, which is not obvious in the observation. In spite of this difference, the model well matches the observed CME speed in low solar wind.

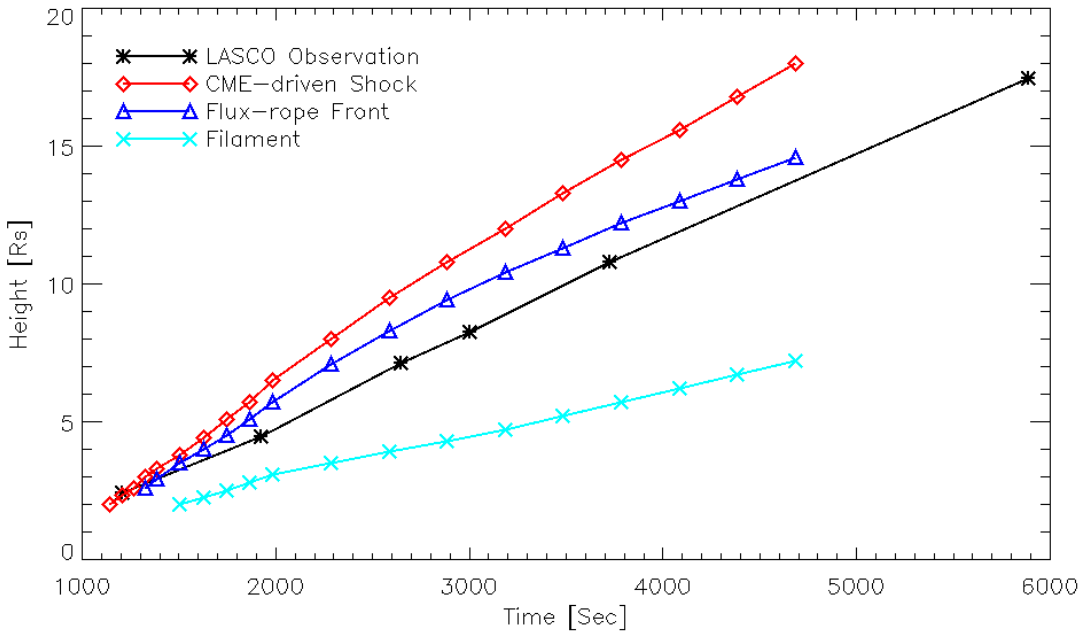

Figure 4.10: CME speed comparison between the simulation and LASCO observation.

Due to the physically consistent treatment of the Alfvén wave turbulence in the AWSoM, the new model has the capacity to investigate the turbulence interaction with CME-driven shocks, which has never been studied in a global CME model. We show the new features of the model related to Alfvén wave dissipation around the CME-driven shock in Figure 4.11. The left panel shows the Alfvén wave dissipation rate and the right panel shows the wave reflection. The selected magnetic field lines are overlapped to show the flux rope structure as well as the field line direction. We can see clearly the enhanced wave reflection around the CME-driven shock. This is caused by the larger Alfvén speed gradient (See Eq. 2) at the shock. The enhanced wave reflection then leads to a larger wave dissipation rate. Due to the focus and length of this Chapter, we will leave the detailed analysis about this turbulence

phenomenon to future work.

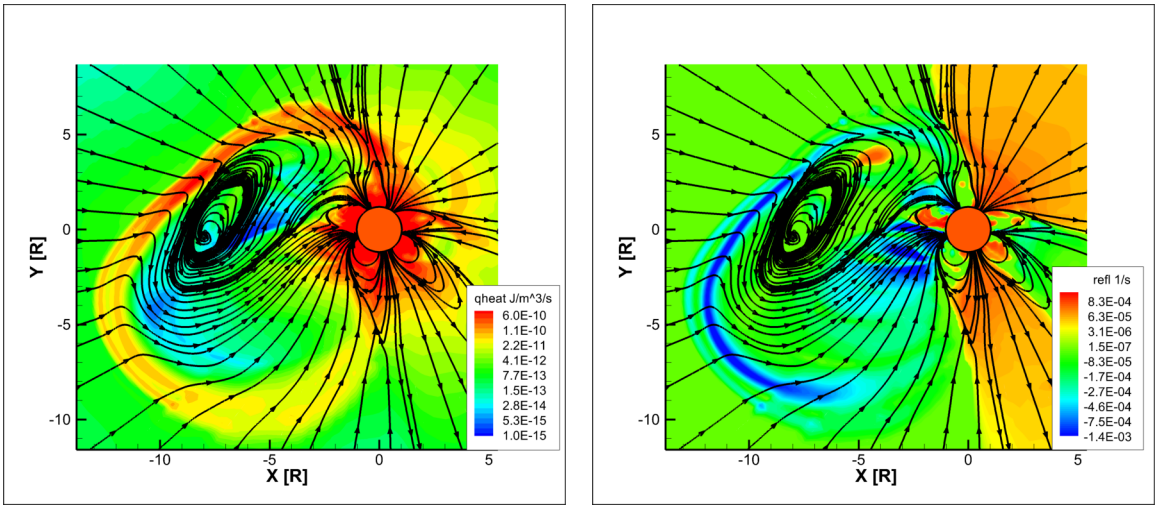

Figure 4.11: The Alfvén wave dissipation rate (left panel) and wave reflection (right panel) in the simulated CME. The selected magnetic field lines are shown as black arrows.

In Figure 4.12, we show the CME-driven shock structure both near the Sun and in the heliosphere. In the left panel, the slice shows the proton temperature at T = 20 minutes, while the isosurface (mass density ratio of 5.0 relative to the background) shows the electron temperature. Due to the decoupling between the electrons and protons, their temperatures are an order of difference at the same location (*Kosovichev and Stepanova*, 1991; *Manchester et al.*, 2012; *Jin et al.*, 2013). The CME-driven shock heats the protons to ∼130 MK, while the electrons are only heated by adiabatic compression at the shock. In the right panel, the slice shows the proton temperature at T = 28 hours, while the isosurface shows the mass density ratio 3.0. Again, we see the difference between the electron and proton temperatures.

The Earth, STEREO A, and STEREO B positions are shown in the figure, which provide the multi-viewpoints of the CME event. We can see in the model that the CME-driven shock mainly propagates toward the STEREO A, and that the slower flank of the shock propagates toward the Earth. This picture is highly consistent with

the shock reconstruction from the observations (see CME2 in Figure 2 from *Wood et al.* 2012).

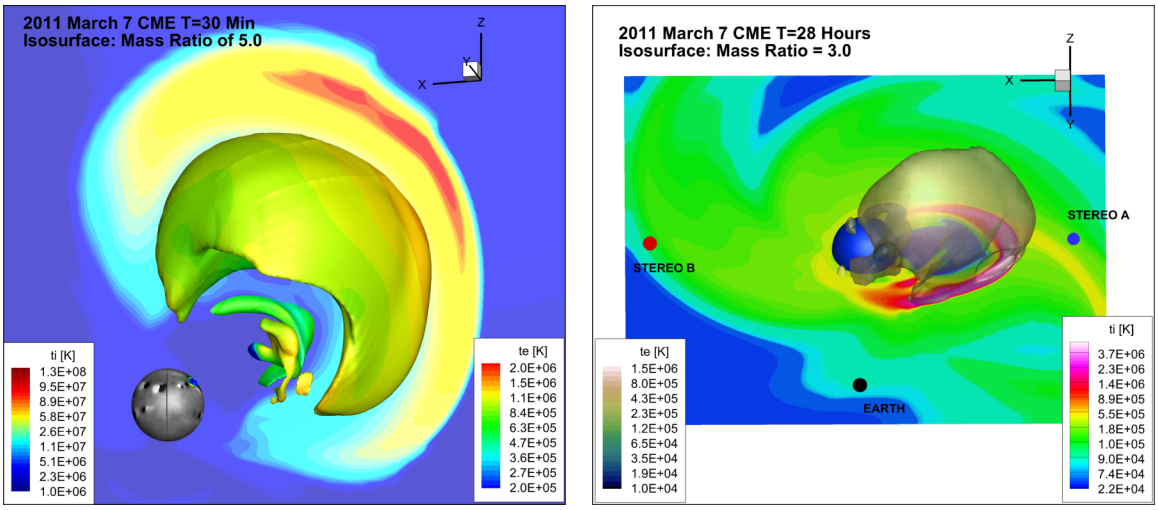

Figure 4.12: Left panel: CME-driven shock structure in SC at T = 30 Minutes. Right panel: CME-driven shock structure in IH at T = 28 Hours. The isosurface in SC shows the mass ratio of 5. The isosurface in IH shows the mass ratio of 3. The background shows the proton temperature and the color scale on the isosurface shows the electron temperature. The Earth, STEREO A and STEREO B positions are shown in IH with different color spots.

Another interesting feature of this CME event is the CME-CIR interaction during the CME propagation in the heliosphere as can be see in Figure 4.12 and 4.13. The CME-CIR interaction phenomenon has been observed in many cases (e.g., *Gómez-Herrero et al.* 2011) and is believed to be related to the enhanced local ion acceleration in the hundred-keV energy range (*Giacalone et al.*, 2002). The ICMEs that interact with CIRs can be difficult to identify in observations due to their distorted structure after interaction (e.g., *Richardson and Cane* 2004; *Riley et al.* 2006). The CME-CIR interaction acts as shock-shock collisions (e.g., CME-CME interaction; *Lugaz et al.* 2008) and will amplify the magnetic fields, plasma temperature, and density of the CIR. We can see the effect of CIR-CME interaction in Figure 4.13. This phenomenon is also found in the interaction of high Mach-number shocks in laser-produced plasma

(*Morita et al.*, 2013). We also notice that the CME-driven shock propagates into both the fast and slow velocity streams in this event. The fast velocity stream can be traced back to the on-disk corona hole (CH in STA observation in Figure 4.1). Since the CME happens just east of the corona hole (AR 11164 in STA observation in Figure 4.1), the CME-driven shock expends into the fast stream and propagates toward the STA, while the CME-driven shock in the slow velocity stream propagates toward the Earth.

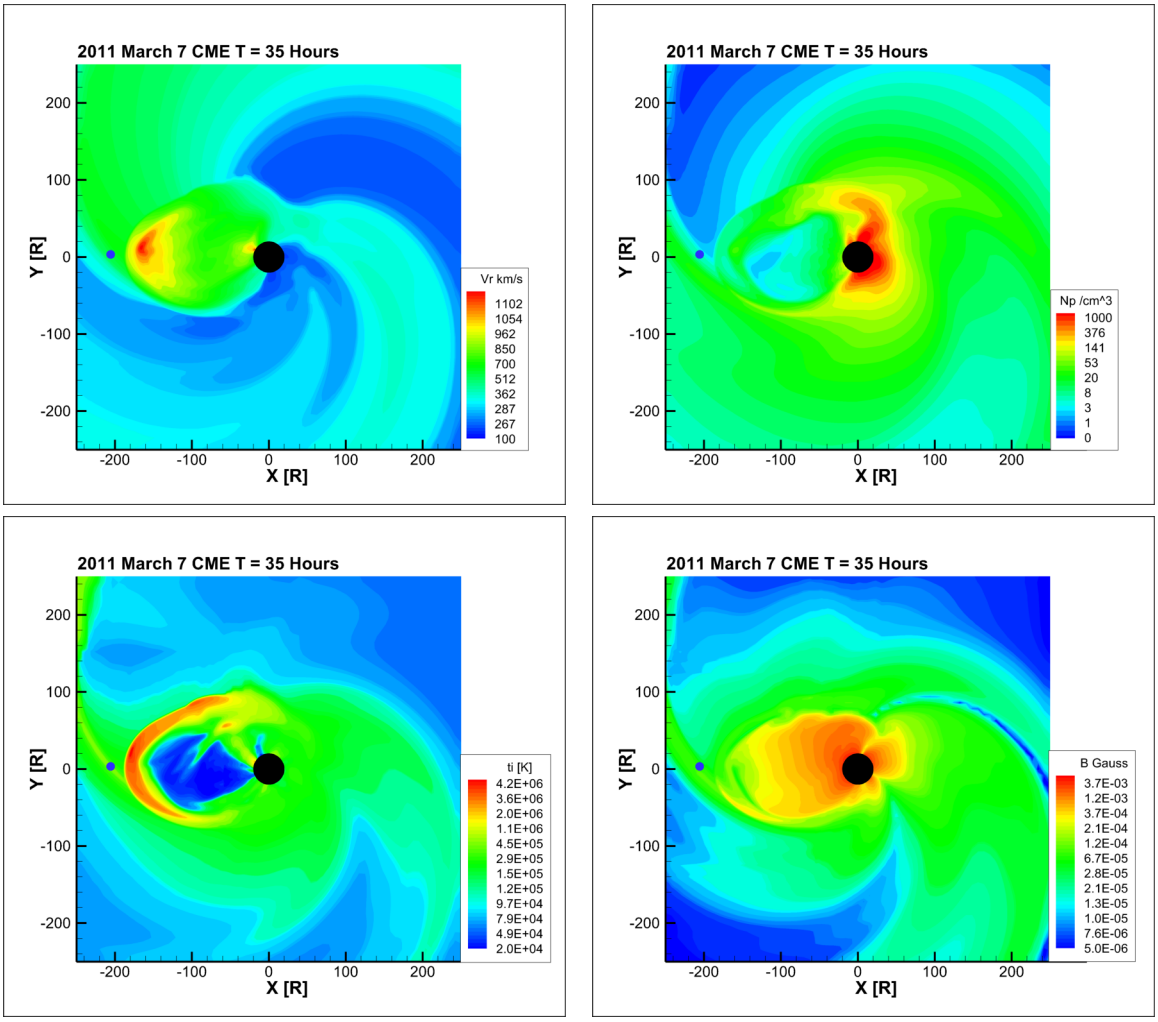

Figure 4.13: The radial velocity, proton density, proton temperature, and total magnetic field of the simulated CME at T = 35 hours.

In Figure 4.14, we show the comparison of the CME *in situ* observations with the

simulation for radial velocity, proton density, proton temperature, and total magnetic field strength. The CME-driven shock hits STA at ∼6:50 UT on 2011 March 9, while the simulated shock arrives within ∼1 hour later. In the radial velocity comparison, we can see that the simulation reproduces the velocity jump of ∼200 km s^{-1} at the shock and the gradually decreasing velocity after the shock passing. The main difference is that in the simulation there is another velocity increase of ∼200 km s^{-1} after the shock, which causes the velocity to be higher than what is observed. This velocity difference is due to the numerical reconnection behind the shock, which is also responsible for the density peak at 14:00 UT in the simulation. In the observed density plot, there are two peaks. The first one is related to the CIR structure and the second one is related to the CME-driven shock. The density jump at the shock is ∼4 in the observation, while it is ∼2 in the simulation. The relatively smaller density jump in the simulation is caused by the CIR-CME interaction. The broader CIR structure in the simulation could lead to a reduction in the Mach number of the CME-driven shock and therefore a smaller compression ratio when the shock arrives at STA. The proton temperature at the shock jumps from ∼0.1 MK to ∼1 MK in the observation, while in the simulation it jumps from ∼0.3 MK to ∼3 MK. Both the magnetic field in the simulation and observation has a jump of factor ∼2.5 at the shock with the magnitude slightly smaller in the simulation.

The correct CME arrival time at 1 AU is achieved by matching the flux rope front speed with LASCO observation near the Sun as shown in Figure 4.10. The discrepancy between the CME-driven shock speed in the simulation and in the observation near the Sun indicates that the simulated shock suffers more deceleration in the heliosphere than the observed shock. This effect could be caused by the relatively higher background solar wind density in the simulation along the CME propagation path.

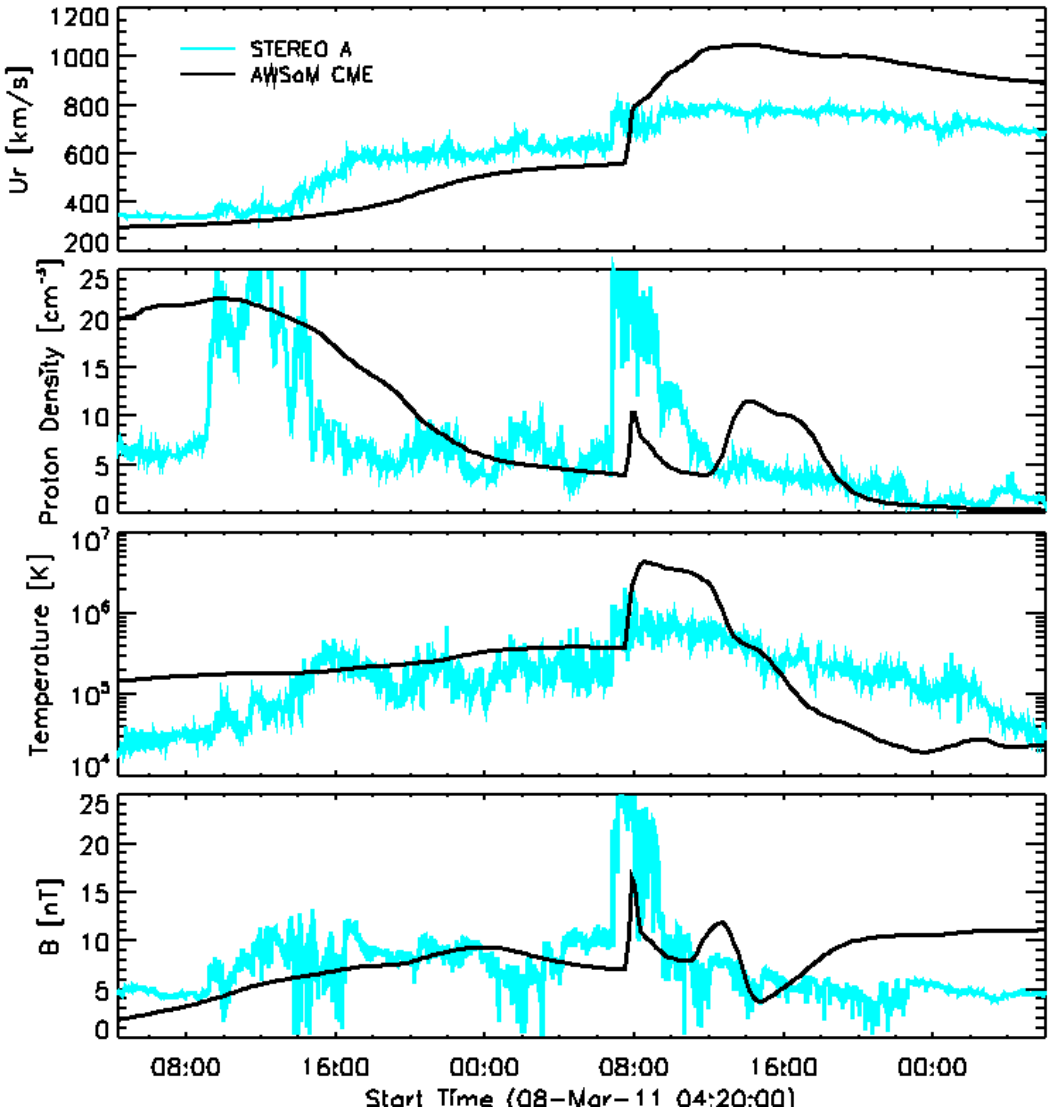

Figure 4.14: Comparison of the CME *in situ* observation with the simulation for radial velocity, proton density, proton temperature, and total magnetic field.

In Figure 4.15, we further compare the three components of the magnetic field between the simulation and observation. As we can see, the simulation successfully captures the variation of the magnetic field at the shock passing. The Bx component has a positive change at the shock, while the By and Bz have negative changes. The negative Bz does not last long in this event at STA. In Figure 4.16, we show the comparison of velocity components between the simulation and observation. Again, our

simulation shows consistency with the observations for all three velocity components. The velocity information is critically important to determine the shock normal. Based on the comparison, our simulation catches the shock normal correctly at STA for this event.

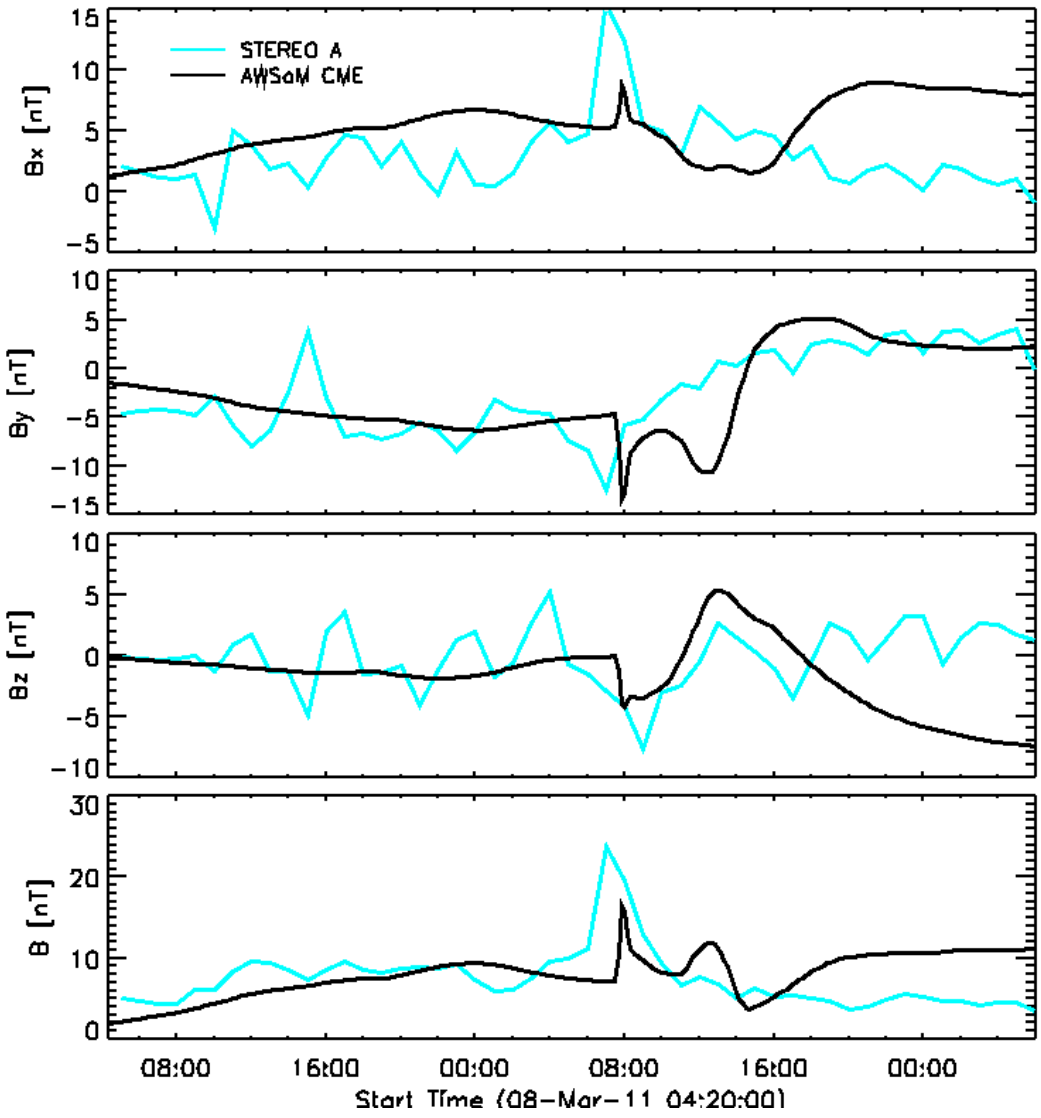

Figure 4.15: Comparison of the CME *in situ* observation with the simulation for Bx, By, Bz, and total magnetic field.

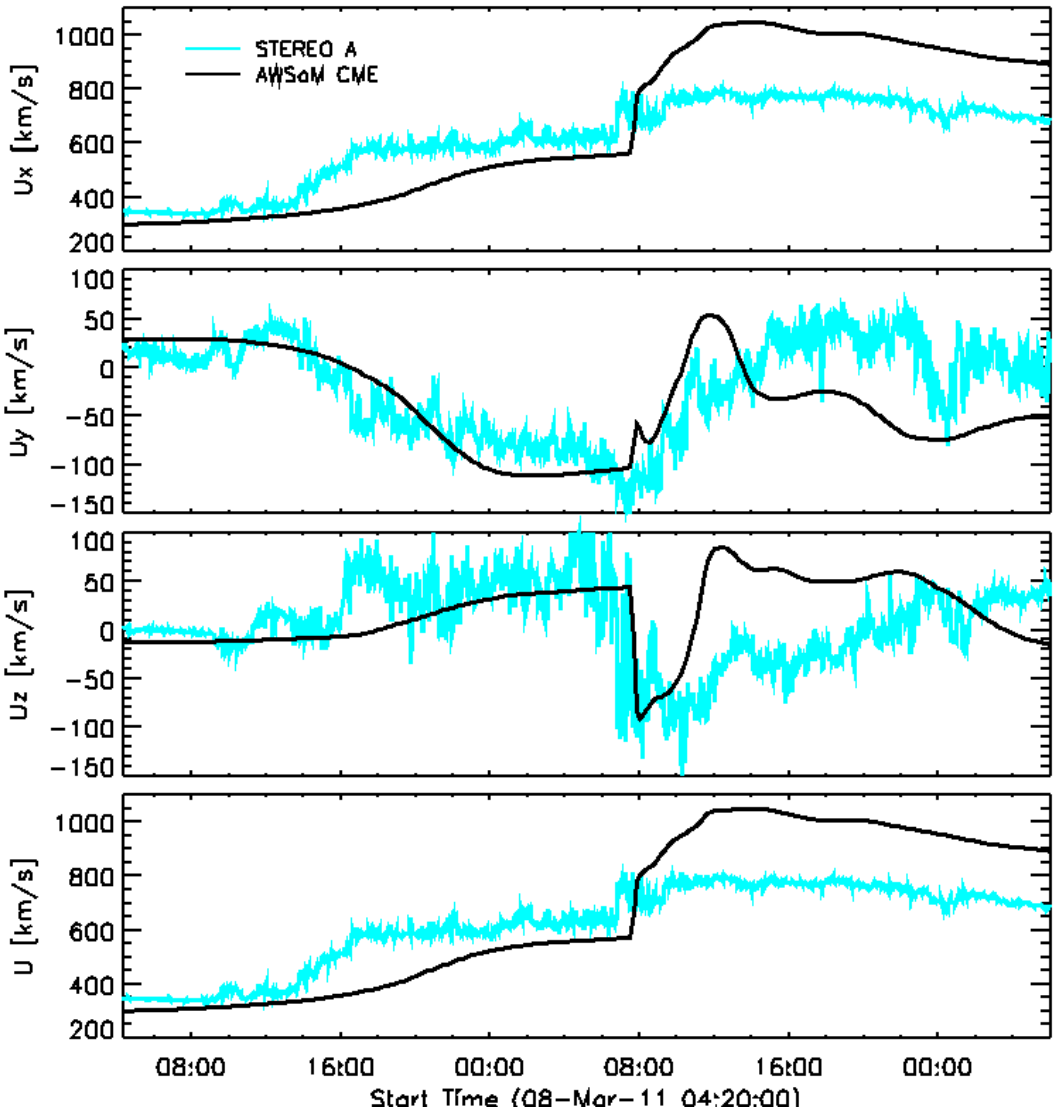

Figure 4.16: Comparison of the CME *in situ* observation with the simulation for Vx, Vy, Vz, and total total velocity field.

Based on the *in situ* observation as well as the simulation, we conclude that the CME-driven shock passes the STA without the flux rope/magnetic cloud structure behind the shock. In general, magnetic clouds correspond to enhanced magnetic field magnitude, low field variance, and low ion temperature (e.g., *Burlaga* 1988). Note that only 30 – 40% of ICMEs are with magnetic clouds (*Gosling*, 1990). This type of ICME is studied in detail by *Gopalswamy et al.* (2009). They found that in each case

there is at least one coronal hole nearby that plays a role in deflecting the CMEs (flux rope) away from the Sun-Satellite line so that only the shock arrives at the satellite. Our study confirms this point in the 2011 March 7 event simulation. The CME source region is located just to the east of a coronal hole from the STA observation (Figure 4.1). The flux rope is deflected from this coronal hole and does not pass through by STA. The CME-driven shock in the slow speed stream did hit the Earth at 7:44 UT on 2011 March 10, with a lengthy period of negative Bz and triggered a geomagnetic storm of Kp = 6. However, this is combined with another slow CME event before the one we simulate in this study (*Wood et al.*, 2012). In order to reproduce the *in situ* data in the simulation at the Earth, a double CME initiation should be included. Therefore, we do not show the *in situ* comparison at Earth in this study.

4.4 Summary & Conclusion

In this study, the 2011 March 7 CME event is simulated from chromosphere to 1 AU using the newly developed AWSoM model. Comparing the model with previous work (*Jin et al.*, 2013), we find the new AWSoM model incorporates physically consistent wave reflection/dissipation and spatially dependent heat partitioning based on the linear wave theory and stochastic heating. Moreover, collisionless electron heat conduction is taken into account and combined with the collisional Spitzer heat conduction. Our simulation results are validated using multi-spacecraft observations from SOHO, SDO, STEREO A/B, and OMNI, which show that the new model can reproduce most of the observed features near the Sun and in the heliosphere. The CME arrival time is correctly simulated, which combined with the correct speed near the Sun suggests the global MHD model can be used as a powerful forecasting tool. We summarize the major conclusions as follows:

1. Near the Sun, the synthesized EUV images of the model can reproduce most of the active regions and on-disk/polar coronal holes. Also, the intensity of the active

region is comparable with the observation thanks to the enhanced wave reflection around the active regions.

2. The cone model comparison and white-light comparison from three different viewpoints show that the simulated CME propagates in the same direction as the observed event to a very high degree. The GL flux rope shows the capacity to reproduce the observed white-light features of the CME (e.g., double-front morphology, dark cavity, dense core), which also showed in the previous works by *Lugaz et al.* (2005). Within 20 $R_\odot$, the observed outermost CME front is $\sim$600 km^{-1} slower than the simulated CME-driven shock front, but the speed is comparable with the second front in the simulation.

3. With the physically consistent treatment of the Alfvén wave turbulence, we find the enhanced wave reflection around the CME-driven shock. This is caused by the larger Alfvén speed gradient at the shock and leads to an increased wave dissipation rate.

4. We find the CME-CIR interaction is evident in this event, which increases the magnetic field, plasma temperature, and density of the CIR. The CME parameters are also affected significantly. Therefore, we emphasize the importance of the correct CIR structure for the precise global MHD simulation of CME propagation.

5. A comprehensive 1 AU *in situ* comparison shows that our simulation captures all the shock features of this event. Our simulation confirms the effect of the on-disk coronal hole on the CME propagation. In this event, the CME flux rope is deflected by the nearby coronal hole, while the shock expands into the coronal hole's fast outflow and finally hits the STA. Therefore, only the CME-driven shock is observed both in the simulation and observation.

Based on these promising results, our future work will be focus on the following directions: First, to further improve the forecast capability of our CME model, we will conduct more benchmark case studies as suggested by *Möstl et al.* (2012) to

validate the CME-driven shocks from multiple *in situ* observations (*Liu et al.*, 2013). Second, the gradual SEP events are believed to be accelerated by CME-driven shocks through the diffusive shock acceleration mechanism (*Reames*, 1999). *Mewaldt et al.* (2008) pointed out that the total energy budget of the energetic particles can be 10% or more of the CME kinetic energy. Therefore, it is very important to couple the CME model with the SEP model (*Sokolov et al.*, 2004, 2009) in the next step. By separating the electron and proton temperatures in our CME model, the CME-driven shock is well reproduced both near the Sun and in the heliosphere, which could lead to an effective acceleration by DSA. Finally, the AWSoM shows a new capacity of investigating the turbulence phenomenon related to CME-driven shocks for which we have shown some preliminary results. With higher temporal and spatial resolution in the simulation as well as with pressure anisotropy (*van der Holst et al.*, 2014), we will soon investigate CME-turbulence interactions with comparison to observations (e.g., *Liu et al.* 2006).

CHAPTER V

Summary & Future Work

"Are we having fun yet?" Professor Gombosi said, "You bet!"

– Tamas I. Gombosi, *in an AOSS Seminar*

5.1 Summary

The subject of this dissertation is understanding the fundamental physical processes involved in the solar wind and coronal mass ejections by closely utilizing both the numerical simulations and observations. The dissertation work involved model development, model validation, thermodynamic analysis, and realistic CME/ICME event simulation. The background solar wind solution is comprehensively validated using available observations. Several advanced methods are used to deduce useful information from the observations (e.g., DEMT) or from the simulations (Ionic charge states). Furthermore, by comparing the CME in the 1T and 2T models, the results show the importance of separating electron and proton temperatures in order to produce physically correct CME structures and CME-driven shocks. Finally, based on the newly developed AWSoM with physics-based Alfvén wave turbulence dissipation and integrated collisional/collisionless heat conduction, a realistic CME event on 2011 March 7 was simulated from the chromosphere to 1 AU. By detailed analysis of

this event from the observation, the model shows the capability to reproduce most of the observed features (e.g., EUV waves, double-front in white light coronagraph images, CME-CIR interaction). We also analyzed the turbulence phenomena around the CME-driven shock front. The CME arrival time and all *in situ* plasma quantities are consistent with the observations, which shows a promising potential for the next generation of first-principles space weather forecasting models.

The main contributions of this dissertation can be summarized as follows:

1. **A comprehensive solar wind model validation with both the remote-sensing and *in situ* observations.** Model validation is one of the most important steps during numerical model development. Due to the limited observations, extracting more information from the available observations is critical for a better evaluation of the model. We utilize several advanced techniques to realize this goal (e.g., white-light tomography, DEMT, spectral inspection). Moreover, for the first time, we use the model to calculate ionic charge state abundances of carbon, oxygen, silicon, and iron and compare these with observations to provide a new constraint on the numerical model. The results not only show good agreement between the simulation and observation for both solar minimum and maximum conditions, but also show that the electron heating is more physically reliable and consistent with observations than a single fluid model.

2. **Detailed CME-driven shock analysis with and without separating electron/proton temperatures.** Based on a realistic background solar wind solution, the CME is initiated both with 1T and 2T models. A detailed comparison of the propagation of fast CMEs and the thermodynamics of CME-driven shocks in 1T and 2T models is made. Because there is no distinction between electron and proton temperatures in the 1T model, electron heat conduction is incorrectly applied to shock heated protons, which creates an unphysical temperature precursor in front of the CME-driven shock and makes the shock parameters (e.g., shock Mach number,

compression ratio) incorrect. The compression ratio of the 1T CME well exceeds the strong shock limit value of 4, while the 2T CME has a compression ratio of approximately 4 during the whole evolution. The much higher compression ratio in the 1T model is caused by the heat conduction behind the shock that cools down the plasma efficiently and allows the density to increase. The results demonstrate the importance of the electron heat conduction in conjunction with proton shock heating in order to produce the physically correct CME structures and CME-driven shocks.

3. **A realistic CME event simulation from the chromosphere to 1 AU based on a physically self-consistent global MHD model.** The capability of simulating realistic solar eruptions as well as validating the model with observations is important for the accurate space weather forecasting. We simulate the CME that occurred on 2011 March 7 with the newly developed global MHD AWSoM in SWMF. The background solar wind starts from the upper chromosphere and extends to 240 $R_\odot$ with heat conduction (both collisional and collisionless formulation) and radiative cooling. The magnetic field of the inner boundary is specified with a synoptic magnetogram from the Global Oscillation Network Group (GONG). The solar wind is driven by Alfvén-wave pressure and heated by Alfvén-wave dissipation. The Alfvén-wave behavior is physically consistent, including non-WKB physics-based reflection and physics-based apportioning of turbulence dissipation. We initiate the CME by using the Gibson-Low (GL) analytical flux rope model. We simulate two days of CME propagation at which time it has passed 1 AU. A comprehensive validation study is done by using remote as well as *in situ* observations from SDO, SOHO, STEREO A/B spacecraft and OMNI data set. Our results show that the new model can reproduce most of the observed features near the Sun (e.g., CME-driven EUV waves, deflection of the flux rope from the coronal hole, "double-front" in the white light images) and in the heliosphere (e.g., CME-CIR interaction, and shock properties at 1 AU). With the physically consistent treatment of the Alfvén wave turbulence, we

find enhanced wave reflection around the CME-driven shock. This is caused by the larger Alfvén speed gradient at the shock and leads to an increased wave dissipation rate. By fitting the CME speeds near the Sun with observations, the CME-driven shock arrival time is within 1 hour of the observed arrival time and all the *in situ* parameters are correctly simulated, which suggests the global MHD model is a powerful tool for space weather forecasting.

5.2 Limitations of this Work

Although the CME simulation in this dissertation shows very promising results for the first-principles space weather forecast, there are several places where the model can be improved in the future to achieve a more realistic event simulation:

1. *Data-driven inner boundary condition improvements.* In the present model, the Carrington magnetogram is used to specify the inner boundary condition for the magnetic field. Because of the time-averaged nature of the magnetogram, it can only reflect the large-scale magnetic structures over the whole Carrington rotation (some 25 days). The variation of the magnetic field (e.g., flux emergence, flux cancellation) is missing. In order to capture the dynamics of the solar corona and solar wind, the model requires an estimate of the instantaneous magnetic field at the inner boundary. The difficulty lies in how to estimate the far-side magnetic field that cannot be directly observed. Flux transport models are widely used to simulate the evolution of the magnetic field, which in the the case of *DeVore et al.* 1985, is accomplished by solving a linear, inhomogenous transport equation. Some more sophisticated flux transport models also incorporate flux emergence, random-walk dispersal, meridional advection, differential rotation, and removal of flux via cancellation (*Schrijver and De Rosa*, 2003). There are some ongoing efforts toward this direction. One example is the Air Force Data Assimilative Photospheric Flux Transport (ADAPT) model (*Arge et al.*, 2010, 2011). The ADAPT model utilizes the modified flux transport model by

Worden and Harvey (2000) to approximate the instantaneous magnetic flux distribution using well known surface flow patterns (e.g., differential rotation) and super granular diffusion. Recently, this model has been improved to assimilate far-side active region data from SDO/HMI through helioseismic technique (e.g., *Lindsey and Braun* 1997; *Zhao* 2007). And it is found that the observed and modeled 1 AU data are in better agreement when including the far-side active regions (*Arge et al.*, 2013). Recently, *Upton and Hathaway* (2014) developed a new surface flux transport model. By combing with data assimilated from full-disk magnetograms, this model can produce full surface maps of the Sun's magnetic field and show the ability to predict the Sun's polar magnetic fields. By utilizing these instantaneous magnetogram data to implement a time-varying inner boundary condition, the AWSoM performance can be improved to catch the dynamics of solar wind evolution as well as to provide a more accurate forecast.

2. *The CME initiation model needs to be revised to catch the early acceleration process of the CME.* In this dissertation, we use both the TD flux rope (Chapter III) and GL flux rope (Chapter IV) to initiate the CME events. Although both analytical flux rope models can reproduce many observed features near the Sun and in the heliosphere, the initial acceleration process ($<$ 2-3 $R_\odot$) is due to the force-imbalance and could be unrealistic in some cases. A better initiation model should be a data-driven model and use as many observations as possible. However, to drive an MHD model, there are at least three challenges: first, a time-series of vector magnetogram observations is needed. With the vector magnetograms from SDO/HMI, this requirement is fulfilled. But there are still some issues that need further work (e.g., 180-degree ambiguity of the vector magnetogram); second, in addition to the magnetic field information, the MHD model also needs velocity field information at the photosphere, which cannot be directly observed. A technique called local correlation tracking (LCT: *Chae* 2001; *Démoulin and Berger* 2003) has been developed

to obtain the vector velocity field. It infers the transverse velocity of the plasma from the motion of magnetic features by finding the shift that maximizes the local correlation function between the successive observations. With ideal MHD assumption, flows along the magnetic field cannot affect the evolution of magnetic structures (*Welsch et al.*, 2004). This leads to an algebraic solution for all three components of the velocity field; finally, MHD requires the magnetic field information through the volume that is consistent with the observed vector field at the inner boundary. To realize this objective, some extrapolation methods should be used to calculate the field information from the inner boundary magnetogram (e.g., non-linear force-free field extrapolation). With the data-driven CME initiation model, the initial acceleration process will be physical consistently captured.

3. *Including more physics in the model.* One of the most important physical features missing in the global MHD solar wind model is anisotropic proton pressure. The remote observations from UVCS have confirmed that the perpendicular ion temperature in the coronal holes is much larger than the parallel ion temperature (*Kohl et al.*, 1998; *Li et al.*, 1998). The *in situ* observation from *Helio* also show the temperature anisotropy in the heliosphere (*Marsch et al.*, 1982). There are many 1D and 2D modeling efforts that take into account the effect of temperature anisotropy in the past (*Leer and Axford* 1972; *Chandran et al.* 2011; *Vásquez et al.* 2003; *Li et al.* 2004). *Meng et al.* (2012a,b) implemented the ion temperature anisotropy in a global magnetosphere model in SWMF. *van der Holst et al.* (2014) further applied the temperature anisotropy in the solar wind model. In Figure 5.2, we can see that the three temperatures have very different behaviors: The perpendicular ion heating is dominant in the coronal hole due to the stochastic heating mechanism; the parallel ion heating is only significant close to the HCS where the plasma β is high; while the electron heating is important near the Sun and around the HCS. Therefore, the temperature anisotropy is very important for the solar wind plasma simulation. Also,

in order to investigate the turbulence phenomenon in the heliosphere and around the CME-driven shocks, the temperature anisotropy has to be taken into account. Although the AWSoM has included the temperature anisotropy, there is still a numerical difficulty when simulating CME-driven shocks. In order to correctly simulate the shocks, the conservative form of the energy equations should be solved. With the three temperatures, finding the conservative form of the energy equations will be a challenging task.

For the present model, only electron and proton species are considered with the same velocity. However, at least one more species should be taken into account, which is the α particles. Observations show that the fractional number density of solar wind alpha particles ranges from 0.1% – 40% with typical concentration of 2 – 6% (*Neugebauer*, 1981). Therefore, the α particle represents almost 20% of the solar wind mass density. Moreover, in the fast solar wind, the α particles are observed to have higher velocity and temperature than the protons (*Marsch*, 2006). In order to describe this system including electrons, protons, and α particles, a multi-fluid MHD model should be used. Also, by including the α particles, many new heating mechanisms can be investigated (e.g., ion cyclotron heating). Through a statistical study of solar wind proton and α particle temperatures, *Kasper et al.* (2008) found direct evidence for the local heating of ions through the dissipation of kinetic alfvén waves by cyclotron resonances. With a multi-fluid solar wind model, we can investigate this mechanism numerically.

5.3 Future Work

5.3.1 SEP Simulation

Fast CMEs can drive shocks in the heliosphere (e.g., *Sime and Hundhausen* 1987) that are believed to be responsible for the gradual SEP events (*Reames*, 1999) through

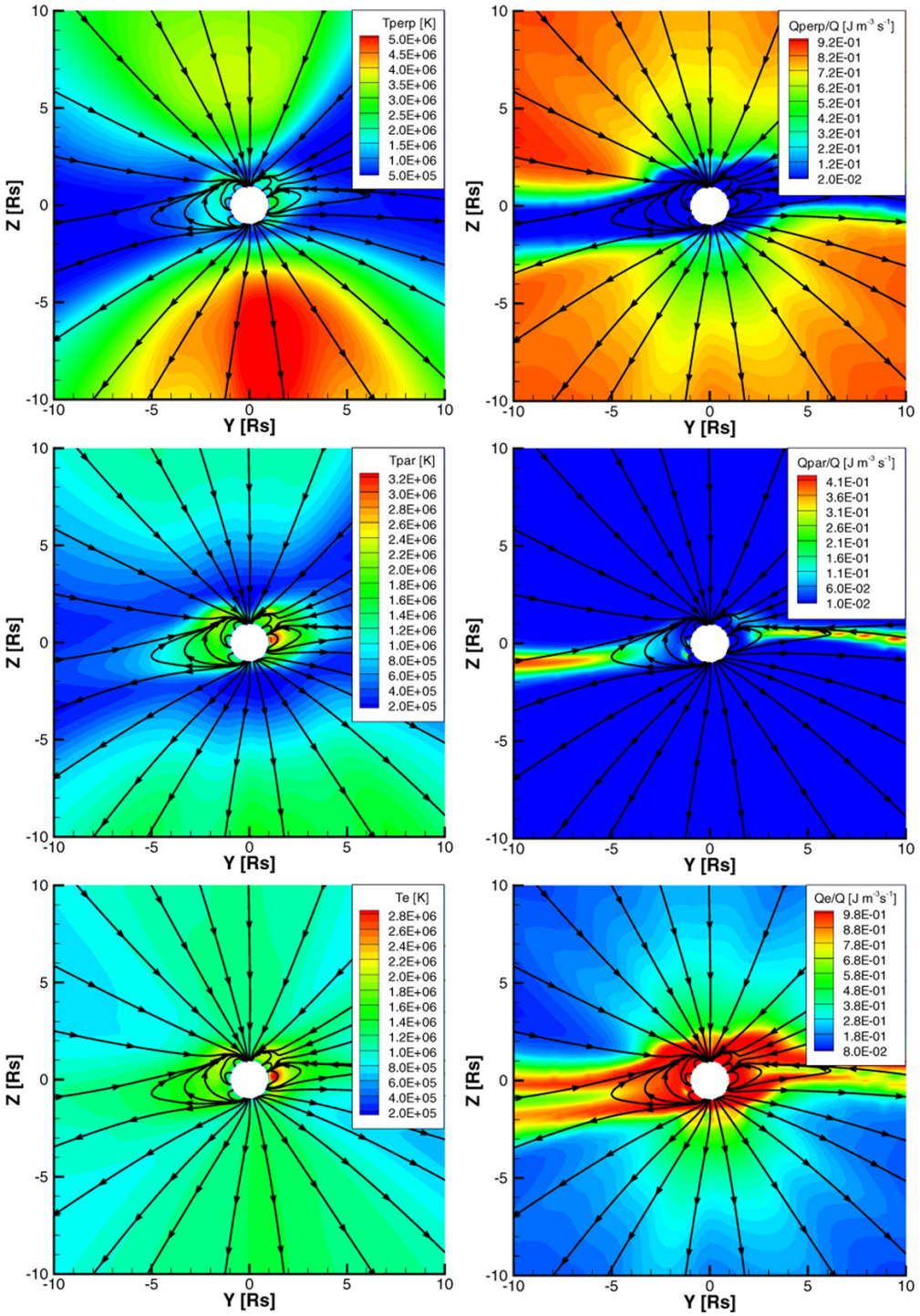

Figure 5.1: *AWSoM model with temperature anisotropy. Left panel: perpendicular ion temperature, parallel ion temperature, and electron temperature. Right panel: the ratio of the perpendicular ion, parallel ion, and electron coronal heating with the total turbulence dissipation (van der Holst et al., 2014).*

the diffusive shock acceleration (DSA) mechanism (*Axford et al.*, 1977; *Bell*, 1978a,b; *Blandford and Ostriker*, 1978). Based on this physical understanding, we require a model capable of addressing the evolution of a fast CMEs from the low corona to 1 AU. The earliest attempt to model an observed CME propagating from the Sun to the Earth is by *Wu et al.* (1999). However this 2D model did not capture the structure of the solar wind or the active region. More recent modeling efforts have been in 3D but treat CME propagation outside of the magneto-sonic point (e.g., *Zhao et al.* 2002; *Odstrcil et al.* 2005; *Odstrcil and Pizzo* 2009). While very useful, this type of model cannot capture the CME structures formed in the low corona that are relevant to SEP acceleration. Other models include the low corona and so that physical initiation mechanisms can be adapted (e.g., *Usmanov and Dryer* 1995; *Riley et al.* 2003; *Chané et al.* 2006). The simulations based on these types of models were used to study the CME-driven shock structures and interpret the SEPs (e.g., *Roussev et al.* 2004; *Manchester et al.* 2005). By implementing a pre-existing out-of-equilibrium flux rope, *Tóth et al.* (2007); *Manchester et al.* (2008) simulated the Halloween CME event from the corona to the Earth and did the first quantitative comparison between the synthetic coronagraph images and LASCO observations, in which the strong CME-driven shock was simulated and validated.

As model complexity keeps increasing, how to address the thermodynamics of heliospheric plasmas is still an open question. Previous work addressed this issue by using empirical heating functions (e.g., *Groth et al.* 2000), or variable adiabatic index (e.g., *Roussev et al.* 2003a; *Cohen et al.* 2007). These assumptions limit the physical self-consistency of the simulation. When shocks are present in the simulation, the variable adiabatic index assumption alters the jump conditions therefore leading to an unrealistic shock structure. Moreover, the single species assumption is also problematic since the electrons should not be shock-heated due to their much higher sonic speed than protons. With the newly developed AWSoM (*van der Holst et al.*, 2014),

the electron and proton temperatures are separated and the Alfvén wave dissipation and reflection are physically consistently treated. In Chapter IV, the simulation results suggest an accurate representation of CME-driven shocks. With this realistic shock structure, we can finally simulate the detailed evolution of the observed gradual SEP events with a DSA model.

For these gradual events, SEP fluxes during the event are typically observed to rise within one to several hours after onset. Given the long decay phase (1–2 days), gradual events are more important for space weather than impulsive events. Many previous works tried to understand DSA using numerical simulations under the planar shock assumption (e.g., *Tylka et al.* 2005; *Li et al.* 2009; *Guo et al.* 2010). However, to predict the SEP observations and achieve forecast capability, the particles need to be accelerated by a realistic CME-driven shock that has complex geometry and temporal evolution. In future studies, we will couple the AWSoM model with the Field Line Advection Model for Particle Acceleration (FLAMPA) developed by *Sokolov et al.* (2004, 2009). The MHD model provides the magnetic configurations as well as the plasma parameters, while the FLAMPA solves the transport equation for protons in the DSA limit along individual field lines. We will further improve FLAMPA by allowing for multiple field line calculations that will enable the simulation of SEP evolution at 1 AU over a longer time range than the single field line calculation. By frequent coupling between the MHD simulation and FLAMPA, the SEP spectrum and its evolution from the Sun to the Earth can be obtained. A detailed analysis of the model results and comparison with the observations (e.g., GOES) will be performed.

Based on the above-mentioned models, we will finally achieve a forecast capability by simulating the "hypothetical" CMEs/SEPs based on remote observations of the CME eruptions[1]. We will simulate the "hypothetical" CMEs for each active region on the Sun and determine whether and when the point of interest (Earth or other

[1]Note that the prediction of initiation is not addressed here, but rather the forecasting capability at 1 AU after initiation

locations in the heliosphere) will be affected by the CME/SEPs. If the point of interest is not significantly affected by the "hypothetical" CME, an "all clear" forecast can be announced for the next day or so. By repeating the procedure daily, a probabilistic forecast can be made for the next 24 hours. Such a forecast would be a great step toward a first-principles-based forecasting capability and will also be invaluable for supporting NASA's robotic exploration and mission planning.

By this investigation, we will address the following fundamental questions in the CME and SEP research: 1) How do different CME initiation mechanisms influence the CME/CME-driven shock structure as well as their role in the SEP acceleration? 2) The formation time and strength of the shock near the Sun is crucial for the particle acceleration. We will find at what altitude in the corona the shock can form and accelerate particles. 3) How the shock-accelerated SEP spectra evolve in the dynamically changing magnetic field configuration with both parallel and perpendicular shock geometrics. 4) What is the shock geometry near the Sun and at 1 AU? 5) What determines the efficiency of the shock acceleration? By answering these questions, we will achieve a better understanding about SEP acceleration/transportation as well as the role of the DSA in the SEPs.

5.3.2 CME Turbulence

The MHD turbulence is one of the most fundamental process in the solar wind plasma (*Biskamp*, 2008), which is critical to understanding the solar wind heating and energy dissipation. Turbulence phenomena in the solar wind have been intensively studied in the past few decades. However, due to the limited observations, turbulence phenomena related to the CME-driven shocks has not been studied in detail. The early observations by ISEE3 showed that there is a huge increase of turbulent power when approaching the interplanetary shock (*Sanderson et al.*, 1985). *Skoug et al.* (2004) found that the downstream turbulence is stronger than upstream turbulence

in the CME-driven shock observations. The turbulent sheath region between the fast ICMEs and their preceding shocks was investigated by *Liu et al.* (2006). They found that this sheath region is often characterized by plasma depletion and mirror wave structures in the observation. The mirror mode waves are generated by an instability due to the temperature anisotropy. Until now, the turbulence related to the CME-driven shocks has not been studied in a global CME model. Due to the physically consistent treatment of the Alfvén wave turbulence in the AWSoM, for the first time, we can investigate this turbulence phenomenon in a global CME model. With higher temporal and spatial resolution in the simulation as well as the pressure anisotropy, we will investigate the CME-related turbulence in more detail and compare it with the observations.

5.3.3 Sympathetic Event Simulation[2]

Finding and understanding the key physical processes that initiate eruptive and explosive phenomena on the Sun (e.g., solar flares, coronal mass ejections (CMEs)) is critical for understanding the Sun-Earth connection as well as space weather. In the past several decades, theoretical models have been proposed to explain the initiation of "isolated" CME events (see the review paper by *Forbes et al.* 2006). There are also "sympathetic" events in which CMEs seem to be spatially coupled. However, due to a lack of prior observational evidence, the hypothetical causal couplings remained speculative. The launch of STEREO A/B and SDO, for the first time, provides near full coverage of the Sun from three different directions, which gives us an unprecedented opportunity to investigate sympathetic events on a global scale. By a comprehensive analysis of the observational data from SDO and STEREO for the 2010 August 1-2 eruptions, *Schrijver and Title* (2011) found that all the active regions involved are

[2]The work proposed in this section will be conducted at the Lockheed Martin Solar and Astrophysics Laboratory with Dr. Carolus J. Schrijver and supported by NASA/UCAR Jack Eddy Postdoctoral Fellowship.

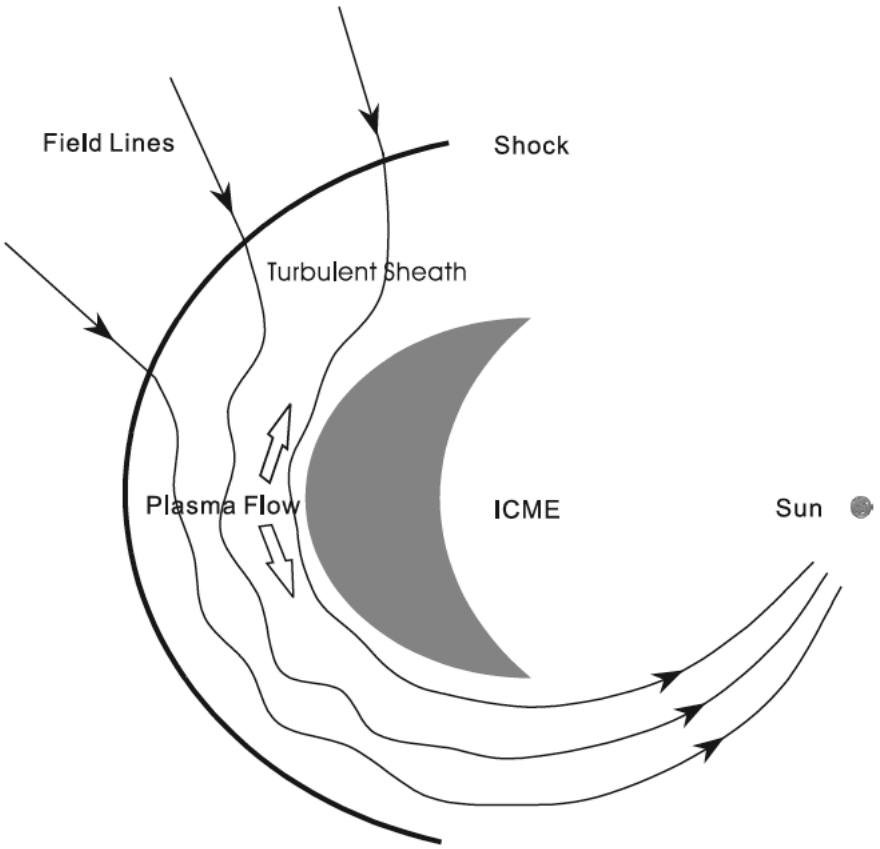

Figure 5.2: Schematic diagram of the turbulent sheath between an ICME and the preceding shock in the solar equatorial plane. (*Liu et al.*, 2006).

connected by some structural features of the magnetic field (e.g., separatrix surfaces, separators, and quasi-separatrix layers). A detailed investigation of the magnetic topology of the source-surface background field by *Titov et al.* (2012) also strongly supports the idea that these structural features are crucial for generating the sympathetic events. These studies suggest that large-scale magnetic coupling plays an important role in initiating eruptive events.

Compared with the established initiation mechanisms for "isolated" events, the mechanisms for "sympathetic" events are still largely unknown, and nascent theories are untested. Many fewer sympathetic events have been extensively observed, so important physical processes remain hidden in the data (e.g., how the perturbation propagates from one region to another; how it interacts with the background magnetic field and triggers an eruption). Global MHD models can play a vital role for interpreting observations and testing theories about sympathetic events. For example, *Török et al.* (2011) reproduces some important aspects of the global sympathetic event on 2010 August 1 in an idealized case and suggests the importance of the pseudo-streamer for producing the "twin-filament" eruptions. Based on the zero beta assumption and "ad hoc" flux cancellation, *Mikić et al.* (2013) reproduced the sympathetic event using the observed magnetic field. However, the a realistic simulation of sympathetic events remains to be done, which will greatly deepen our understanding of large-scale magnetic coupling.

By using the newly developed AWSoM, we can achieve a realistic sympathetic event simulation in the global MHD model. There are several features of the model that are essential for achieving a realistic simulation: 1) It is the first global MHD model that separates electron and proton temperatures. This feature is critical for producing physically correct CME-driven shocks and extreme ultra-violet (EUV) waves (*Manchester et al.*, 2012; *Jin et al.*, 2013). Also, this model allows for the accurate simulation of EUV emissions, which can then be compared to observations.

2) The data-driven boundary condition can capture the realistic global magnetic topology, while the adaptive mesh refinement (AMR) can resolve the magnetic reconnection. 3) The model covers from the upper chromosphere to 1 AU, with which we can not only capture the dynamics of solar lower atmosphere but also achieve a more comprehensive tracking of eruptions and their coupling. This model has been successfully used to simulate the realistic CME event on 2011 March 7 (Chapter IV).

We can initiate the CME using two different mechanisms (flux rope model and breakout model) implemented in the EE component. For the flux rope model, two different analytical models can be used: the Titov-Démouline flux rope (*Titov and Démoulin*, 1999) and the Gibson-Low flux rope (*Gibson and Low*, 1998). Both of them have been successfully used in CME simulations (e.g., *Manchester et al.* 2004b,c; *Roussev et al.* 2004; *Manchester et al.* 2008). For the breakout model (*Antiochos et al.*, 1999), the CME is triggered by breakout reconnection in a quadrupolar field configuration. Instead of a flux rope, photospheric shear flows are applied around the PIL until the reconnection happens. Compared to the flux rope model, the breakout model can capture a more realistic CME acceleration process. There are also many applications of this model (e.g., *MacNeice et al.* 2004; *van der Holst et al.* 2009; *Karpen et al.* 2012). In Figure 5.3, the initial conditions of the three initiation mechanisms are shown. The choice of the eruptive models will depend on the observational features and magnetic configurations.

The CME-driven wave (i.e., EUV wave) that propagates through the corona is an important mechanism that may connect different magnetic structures and trigger sympathetic events (See reviews by *Chen et al.* 2005; *Patsourakos and Vourlidas* 2012). In Figure 4.1 of Chapter IV, we show the model synthesized EUV waves during the 2011 March 7 event and compare it with the observed EUV wave by AIA 211 Å. We can see clearly the propagation direction and position of the wave is correctly reproduced by the model. This shows the capability of global MHD model in

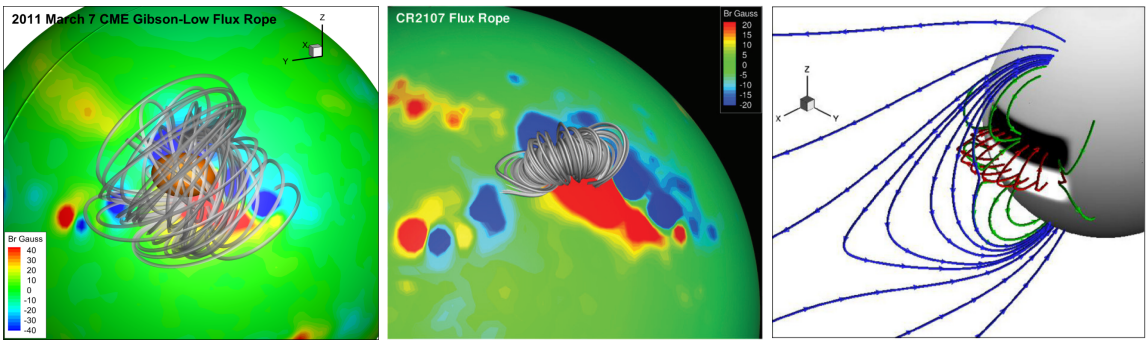

Figure 5.3: The initiation mechanisms of the eruptive events in the model: left panel: Gibson-Low flux rope configuration inserted into an active region (Figure 3a in Chapter IV); middle panel: Titov-Démouline flux rope into the same active region (*Jin et al.*, 2013); right panel: the breakout model configuration in an idealized case (*van der Holst et al.*, 2009).

the study of the wave-related solar sympathetic event. In the previous observations, the CME-driven waves are seen to reach and destabilize the active regions. However, we still need to answer the question that how this process takes place. The MHD models give us a great opportunity to investigate the evolution of interaction between the coronal waves and magnetic structure of the active regions.

The first step of the investigation will be conducted with idealized magnetic configurations in order to understand the fundamental physical processes that can disrupt the magnetic structures and trigger sympathetic eruptions. We will also acquire a better knowledge of the magnetic structures that are in favor of sympathetic eruptions. *Schrijver et al.* (2013) presents detailed case studies by using SDO/AIA observations to show several different coupling processes involved in the sympathetic events: direct magnetic coupling; distortion of the enveloping field; effects of an expansion wave; indirect coupling through an intermediate region. These four destabilizing mechanisms will be studied in detail in idealized simulations. A typical testing process will be like the following: First, flux ropes will be implemented and confined within a closed magnetic structure (e.g., helmet streamer). The external field will be made strong enough to contain the flux rope that may erupt from the torus instability (*Kliem and Török*,

2006), or by magnetic reconnection. Then, another more energetic flux rope will be put in a separate magnetic configuration and set to erupt after implementation. By setting the trigger flux rope in different locations on the Sun as well as different initial energies, we can study in detail the following questions: 1) How the static flux rope be affected by the eruptive one; 2) the location and energy dependences of producing sympathetic events; 3) large-scale changes in field topology.

Based on experience gained from the first step, we will achieve a realistic event simulation in the second step. The eruptions will be initiated based on synthetic magnetograms from SDO/HMI, with which the correct magnetic topology can be represented. The usage of AMR can guarantee the resolution of the magnetic reconnections along the structural features of the magnetic field that are important for initiating eruptions in sympathetic events. A detailed analysis of the observation is important in this stage for generating better input to drive the MHD model (e.g., choice of the CME models, modification of the inner boundary conditions). When propagating into the solar wind, sympathetic events are always prone to CME-CME interaction, which will significantly influence the CME-driven shock structures and the CME/ICME properties (e.g., *Liu et al.* 2012; *Temmer et al.* 2012). The former is directly related to the production of solar energetic particles (SEPs), while the later is closely related to the onset of geomagnetic storms. By propagating sympathetic CMEs to 1 AU in the simulation, we can further investigate the role of sympathetic events in space weather. By using all the available observations, we will achieve a comprehensive validation study.

This investigation will address the following fundamental questions for the solar sympathetic events: 1) How the coronal signals propagate from one region to another and how they trigger eruptions; 2) The importance of the large-scale magnetic coupling in the realistic solar magnetic environment therefore the effects of CME coupling in space weather; 3) When propagating into the heliosphere, how the CME-driven

shocks and CME/ICME properties are influenced by the sympathetic eruptions.

APPENDICES

APPENDIX A

Flux Rope Models

Titov-Démoulin (TD) Flux Rope

In Figure A.1, the three-dimensional TD flux rope is shown. The flux rope is toroidal and has radius of R and minor radius of a. In the original TD flux rope, the magnetic field comprises three parts: first, the field of a constant-current I; second, the overlying coronal arcade created by a pair of magnetic charges $\pm q$. The magnetic charges represent the leading and following sunspots that are located along the flux rope axis at depth d; third, the field of a line current I_0 along the flux rope axis at depth d. This line current can produce a purely toroidal magnetic field parallel to the current I (minor axis of the flux rope). As the value of I_0 increases, the flux rope configuration changes from a highly twisted flux rope to a weakly twisted one. The equilibrium is created by a balance between the outward force of the torus and the inward force of the arcade due to the magnetic charges. The torus instability will happen when $R > \sqrt{2}L$. *Roussev et al.* (2003b) found that the flux rope actually erupts only when $R > 5L$ due to line-tying effect of the poloidal field. Note that in order to let the flux rope escape from the solar corona, I_0 is set to zero in our model.

Therefore, the number of turns in the field lines at the flux rope surface approaches infinity as the distance from the axis increases to a.

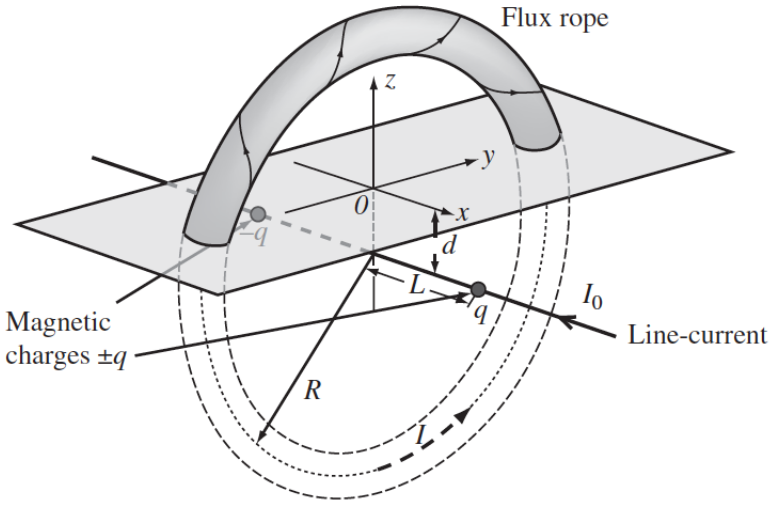

Figure A.1: The three-dimensional TD flux rope model (*Titov and Démoulin*, 1999).

Gibson-Low (GL) Flux Rope

The analytical solution of GL flux rope is obtained by starting from a spheromak field. The flux rope is adjusted to be in equilibrium force balance so as to satisfy the following equations:

$$(\nabla \times \mathbf{B}) \times \mathbf{B} - \nabla 0 - \rho \mathbf{g} = 0 \tag{A.1}$$

$$\nabla \cdot \mathbf{B} = 0 \tag{A.2}$$

The solution of the above equations has the following form:

$$\mathbf{B} = \frac{1}{r \sin\theta} \left(\frac{1}{r} \frac{\partial A}{\partial \theta} \mathbf{e_r} - \frac{\partial A}{\partial r} \mathbf{e}_\theta + \alpha_0 A \mathbf{e}_\phi \right) \tag{A.3}$$

where A is the stream function of magnetic field with the following form:

$$A = \frac{\mu_0 a_1}{\alpha_0^2}\left[\frac{r_0^2}{g(\alpha_0 r_0)} g(\alpha_0 r)\right]\sin^2\theta \tag{A.4}$$

where a_1 is a free parameter to determine the magnetic field strength and plasma pressure of the flux rope. r_0 is the diameter of the initial spherical flux rope. $\alpha_0 r_0 = 5.763459$. r_1 is the distance between the spherical flux rope center and the origin of the heliospheric coordinate system. A mathematical transformation is then performed on the axisymmetric flux rope to make it fully 3D. This is done by the transformation $r \rightarrow r - a$ that distorts the flux rope sphere to a tear-drop shape with the tail pointing toward the Sun. The left panel of Figure A.2 shows the limiting case of $a = r_1 - r_0$. Following the transformation, the new equilibrium requires the plasma pressure to be the following form:

$$p = \left(\frac{\Lambda}{r}\right)^2\left[1 - \left(\frac{\Lambda}{r}\right)^2\right]\left(\frac{B_r^2}{2}\right) + \left(\frac{\Lambda}{r}\right)^2 a_1 A \tag{A.5}$$

where $\Lambda = r + a$. The stretching transformation helps to reproduce the 3-part density structure of the CME. The right panel of Figure A.2 shows an idealized case of 3D GL flux rope embedded in a global dipole field. The yellow iso-surface shows the dense core at the bottom of the GL flux rope.

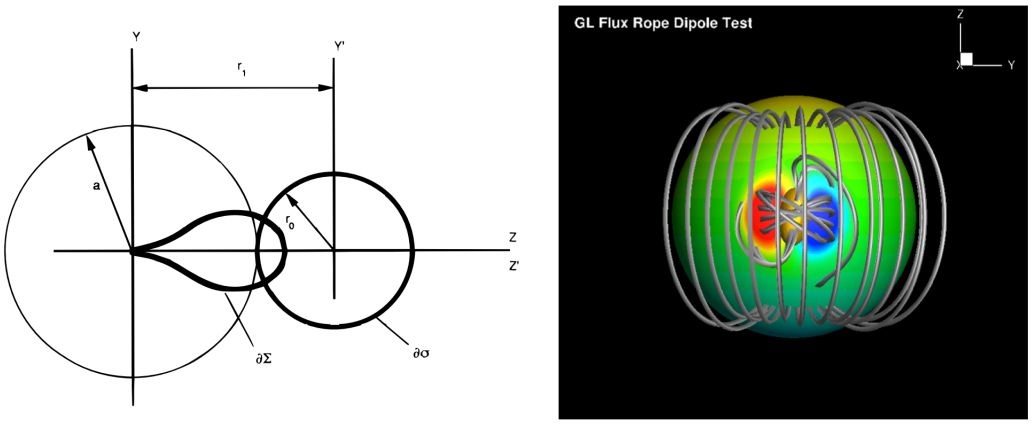

Figure A.2: Left panel: GL flux rope transformation showing a limiting case of $a = r_1 - r_0$ (*Gibson and Low*, 1998). Right panel: 3D GL flux rope embedded in a global dipole field.

APPENDIX B

Collisionless Heat Conduction

Here, we show the collisionless electron heat conduction implementation in the model. For the purpose of the derivation, we neglect the terms of collisional heat conduction, Coulomb collisional heat exchange, radiative cooling, and time variation temporarily. Then, Equation (3.3) with collisionless heat conduction can be written as:

$$\nabla \cdot \left(\frac{p_e}{\gamma - 1} \mathbf{u} \right) + p_e \nabla \cdot \mathbf{u} = -\nabla \cdot \left[\frac{3}{2} \alpha p_e \mathbf{u} \right] + Q_e \tag{B.1}$$

If we combine the first term in the LHS and RHS, then:

$$\nabla \cdot \left(\frac{p_e}{\gamma_H - 1} \mathbf{u} \right) + p_e \nabla \cdot \mathbf{u} = Q_e \tag{B.2}$$

where γ_H is the new polytropic index taking into account the collisionless heat conduction. The γ_H has the following form:

$$\gamma_H = \frac{\gamma + \frac{3}{2}(\gamma - 1)\alpha}{1 + \frac{3}{2}(\gamma - 1)\alpha} \tag{B.3}$$

For the standard values: $\alpha = 1.05$ (*Cranmer et al.*, 2009) and $\gamma = 5/3$, the new $\gamma_H \approx 1.33$. Now, we can write the complete form of Equation (3.3) with collisionless

heat conduction included:

$$\frac{\partial\left(\frac{p_e}{\gamma_e-1}\right)}{\partial t}+\nabla\cdot\left(\frac{p_e}{\gamma_e-1}\mathbf{u}\right)=-p_e\nabla\cdot\mathbf{u}+\frac{1}{\tau_{pe}}(p_p-p_e)-\nabla\cdot\mathbf{q_e^*}-Q_{rad}+Q_e \quad \text{(B.4)}$$

where $\gamma_e=\gamma f_s+\gamma_H(1-f_s)$ interpolates the electron polytropic index γ_e between the collisional region ($\gamma_e=\gamma$) and the collisionless region ($\gamma_e=\gamma_H$). The f_s has the same form as Equation (4.6). The heat conduction term $\nabla\cdot\mathbf{q_e^*}$ now only has the contribution from the collisional heat conduction ($\mathbf{q_e^*}=f_s\mathbf{q_{e,S}}$). Because the collisionless heat conduction is parameterized through γ_e. Note that the spatially varying electron polytropic index should not impact the CME-driven shocks in our simulation. Because only the protons will be shocked and $\gamma=5/3$ for the protons.

APPENDIX C

MHD Shock Properties

The shock wave forms when the disturbance is large enough that the nonlinear effects become important. In that case, the crest of the sound wave moves faster than its leading edge and the steepening process finally causes the formation of a shock. The disturbance itself moves faster than the "signal speed" of the fluids (e.g., sound speed for the hydrodynamics case) while the driver needs not to be. Typically, shocks are thin transition layers across which the fluid properties change rapidly from one state to another. In this section, we summarize some important facts about both the hydrodynamic and MHD shocks.

Hydrodynamic Shocks

Through the conservation of mass, momentum, and energy, the relations between the properties of shocked and unshocked fluids can be obtained (e.g., *Gombosi* 2004; *Priest* 2014):

$$\rho_2 v_2 = \rho_1 v_1 \tag{C.1}$$

$$p_2 + \rho_2 v_2^2 = p_1 v_1^2 \tag{C.2}$$

$$\frac{\gamma p_2}{(\gamma - 1)\rho_2} + \frac{1}{2} v_2^2 = \frac{\gamma p_1}{(\gamma - 1)\rho_1} + \frac{1}{2} v_1^2 \tag{C.3}$$

where the properties ahead and behind of shock are represented by 1 and 2, respectively. Note that the above relations are obtained in the shock frame (frame moving with the shock). These relations are called jump condition or *Rankine-Hugoniot* relations.

The solution of Equation (C.1) to (C.3) can be written as:

$$\frac{\rho_2}{\rho_1} = \frac{(\gamma+1)M_1^2}{2+(\gamma-1)M_1^2} \tag{C.4}$$

$$\frac{v_2}{v_1} = \frac{2+(\gamma-1)M_1^2}{(\gamma+1)M_1^2} \tag{C.5}$$

$$\frac{p_2}{p_1} = \frac{2\gamma M_1^2-(\gamma-1)}{\gamma+1} \tag{C.6}$$

where $M_1 = v_1/c_{s1}$ is the shock Mach number and $c_{s1} = (\gamma p_1/\rho_1)^{\frac{1}{2}}$ is the sound speed.

The second law of thermodynamics states that the entropy of an isolated system must increase. For shock wave, it requires $s_2 \geq s_1$ ($s = c_v \log(p/\rho^\gamma)$). To satisfy this entropy conduction, the shock speed must exceed the sound speed ahead of the shock ($M_1 \geq 1$ and $v_2 \leq c_{s2}$). In the shock frame, the flow is supersonic ahead of the shock but subsonic behind of it. Also, we have $p_2 \geq p_1$, $\rho_2 \geq \rho_1$, $v_2 \leq v_1$, $T_2 \geq T_1$. Therefore, we can see that the shock slows down the flow but heats it up (transferring flow kinetic energy to thermal energy). As the shock Mach number increases, the compression ratio ρ_2/ρ_1 has a limit of $(\gamma+1)/(\gamma-1)$.

MHD Shocks

With the presence of a magnetic field, the shock properties become much more complex than the hydrodynamic case. The **B** and **v** can be inclined away from the shock normal. Therefore, the magnetic field and velocity in the jump conditions will have both normal and tangential components. In general, the *Rankine-Hugoniot*

relations for MHD shocks can be expressed as (e.g., *Gombosi* 2004; *Priest* 2014):

$$\rho_2 v_{n2} = \rho_1 v_{n1} \tag{C.7}$$

$$\rho_2 v_{n2}^2 + p_2 + \frac{B_{t2}^2}{2\mu_0} = \rho_1 v_{n1}^2 + p_1 + \frac{B_{t1}^2}{2\mu_0} \tag{C.8}$$

$$\rho_2 v_{n2} \mathbf{v_{t2}} - \frac{\mathbf{B_{t2}} B_{n2}}{\mu_0} = \rho_1 v_{n1} \mathbf{v_{t1}} - \frac{\mathbf{B_{t1}} B_{n1}}{\mu_0} \tag{C.9}$$

$$\begin{aligned} \left(\frac{\gamma}{\gamma-1}\frac{p_2}{\rho_2} + \frac{v_2^2}{2}\right)\rho_2 v_{n2} + \frac{v_{n2}B_{t2}^2}{\mu_0} - \frac{B_{n2}(\mathbf{B_{t2}}\cdot\mathbf{v_{t2}})}{\mu_0} = \\ \left(\frac{\gamma}{\gamma-1}\frac{p_1}{\rho_1} + \frac{v_1^2}{2}\right)\rho_1 v_{n1} + \frac{v_{n1}B_{t1}^2}{\mu_0} - \frac{B_{n1}(\mathbf{B_{t1}}\cdot\mathbf{v_{t1}})}{\mu_0} \end{aligned} \tag{C.10}$$

$$B_{n2} = B_{n1} \tag{C.11}$$

$$(\mathbf{v}\times\mathbf{B})_{\mathbf{t2}} = (\mathbf{v}\times\mathbf{B})_{\mathbf{t1}} \tag{C.12}$$

The simplest case of an MHD shock is the perpendicular shock. For the perpendicular shock, both the shock normal and velocities are perpendicular to the magnetic field. From the jump conditions, it is easy to find out that the shock speed v_1 must exceed the fast magnetosonic speed $(c_{s1}^2 + v_{A1}^2)^{1/2}$, where $v_{A1} = B_1/(\mu\rho_1)^{1/2}$ is the Alfvén speed for the unshocked plasma. The upper limit for the compression ratio is the same as the hydrodynamic case $\rho_2/\rho_1 < (\gamma+1)/(\gamma-1)$. However, we should note that the effect of magnetic field is to reduce the compression ratio below its hydrodynamic value. Because the kinetic energy of the flow can be transferred into magnetic energy as well as thermal energy now.

If the magnetic field and velocity contain components both perpendicular and parallel to the shock normal, these are called oblique shocks. When analyzing the oblique shocks, a special frame called de Hoffman-Teller frame is often used to simplify the jump conditions. In this frame, the velocity component along the shock front is chosen to make the velocity and magnetic field parallel to each other on both sides of the shock. For the oblique shocks, there are three different modes: slow shock, fast

shock, and intermediate wave. For slow shock, $\mathbf{B_2} < \mathbf{B_1}$ and it makes the magnetic field rotate toward the shock normal, while the fast shock has the opposite effect. As the normal component vanishes, the fast shock becomes a perpendicular shock, while the slow shock reduces to a tangential discontinuity. In another case, when there is no flow across the boundary ($v_{2n} = v_{1n} = 0$), it is called contact (entropy) discontinuity. For the intermediate wave mode, the wave front propagates at the Aflvén speed so that the compression ratio is unity. Both the tangential components of magnetic field and velocity have the same magnitude across the boundary but the direction changes. Therefore, it is also called a rotational discontinuity.

When analyzing the shock data, the shock normal can be determined through the upstream and downstream magnetic fields:

$$\mathbf{n_s} = \frac{(\mathbf{B_1} - \mathbf{B_2}) \times (\mathbf{B_1} \times \mathbf{B_2})}{|(\mathbf{B_1} - \mathbf{B_2}) \times (\mathbf{B_1} \times \mathbf{B_2})|} \tag{C.13}$$

and then the shock speed can be calculated:

$$v_s = \frac{\rho_2 v_2 - \rho_1 v_1}{\rho_2 - \rho_1} \cdot \mathbf{n_s} \tag{C.14}$$

BIBLIOGRAPHY

BIBLIOGRAPHY

Aly, J. J. (1984), On some properties of force-free magnetic fields in infinite regions of space, *ApJ*, *283*, 349–362, doi:10.1086/162313.

Aly, J. J. (1991), How much energy can be stored in a three-dimensional force-free magnetic field?, *ApJ*, *375*, L61–L64, doi:10.1086/186088.

Antiochos, S. K., C. R. DeVore, and J. A. Klimchuk (1999), A Model for Solar Coronal Mass Ejections, *ApJ*, *510*, 485–493, doi:10.1086/306563.

Arge, C. N., and V. J. Pizzo (2000), Improvement in the prediction of solar wind conditions using near-real time solar magnetic field updates, *J. Geophys. Res.*, *105*, 10,465–10,480, doi:10.1029/1999JA900262.

Arge, C. N., C. J. Henney, J. Koller, C. R. Compeau, S. Young, D. MacKenzie, A. Fay, and J. W. Harvey (2010), Air Force Data Assimilative Photospheric Flux Transport (ADAPT) Model, *Twelfth International Solar Wind Conference*, *1216*, 343–346, doi:10.1063/1.3395870.

Arge, C. N., C. J. Henney, J. Koller, W. A. Toussaint, J. W. Harvey, and S. Young (2011), Improving Data Drivers for Coronal and Solar Wind Models, in *5th International Conference of Numerical Modeling of Space Plasma Flows (ASTRONUM 2010)*, *Astronomical Society of the Pacific Conference Series*, vol. 444, edited by N. V. Pogorelov, E. Audit, and G. P. Zank, p. 99.

Arge, C. N., C. J. Henney, I. G. Hernandez, W. A. Toussaint, J. Koller, and H. C. Godinez (2013), Modeling the corona and solar wind using ADAPT maps that include far-side observations, in *American Institute of Physics Conference Series*, *American Institute of Physics Conference Series*, vol. 1539, edited by G. P. Zank, J. Borovsky, R. Bruno, J. Cirtain, S. Cranmer, H. Elliott, J. Giacalone, W. Gonzalez, G. Li, E. Marsch, E. Moebius, N. Pogorelov, J. Spann, and O. Verkhoglyadova, pp. 11–14, doi:10.1063/1.4810977.

Arnaud, M., and J. Raymond (1992), Iron ionization and recombination rates and ionization equilibrium, *ApJ*, *398*, 394–406, doi:10.1086/171864.

Aschwanden, M. J. (2005), *Physics of the Solar Corona. An Introduction with Problems and Solutions (2nd edition)*.

Aschwanden, M. J. (2008), An Observational Test That Disproves Coronal Nanoflare Heating Models, *ApJ*, *672*, L135–L138, doi:10.1086/527297.

Axford, W. I., E. Leer, and G. Skadron (1977), The acceleration of cosmic rays by shock waves, *International Cosmic Ray Conference*, *11*, 132–137.

Baker, D. N., et al. (2013), A Long-Lived Relativistic Electron Storage Ring Embedded in Earth's Outer Van Allen Belt, *Science*, *340*, 186–190, doi: 10.1126/science.1233518.

Baring, M. G., D. C. Ellison, and F. C. Jones (1994), Monte Carlo simulations of particle acceleration at oblique shocks, *ApJS*, *90*, 547–552, doi:10.1086/191873.

Belcher, J. W. (1971), ALFVÉNIC Wave Pressures and the Solar Wind, *ApJ*, *168*, 509–+, doi:10.1086/151105.

Bell, A. R. (1978a), The acceleration of cosmic rays in shock fronts. I, *MNRAS*, *182*, 147–156.

Bell, A. R. (1978b), The acceleration of cosmic rays in shock fronts. II, *MNRAS*, *182*, 443–455.

Biermann, L. (1951), Kometenschweife und solare Korpuskularstrahlung, *ZAp*, *29*, 274.

Birkeland, K., and W. H. Dall (1915), Scientific Books: The Norwegian Aurora Polaris Expedition, 1902-03. Vol. I.: On the Cause of Magnetic Storms and the Origin of Terrestrial Magnetism, *Science*, *41*, 29, doi:10.1126/science.41.1044.29.

Biskamp, D. (2008), *Magnetohydrodynamic Turbulence*.

Blandford, R. D., and J. P. Ostriker (1978), Particle acceleration by astrophysical shocks, *ApJ*, *221*, L29–L32, doi:10.1086/182658.

Braginskii, S. I. (1965), Transport Processes in a Plasma, *Reviews of Plasma Physics*, *1*, 205.

Brandt, J. C., F. M. Caputo, J. T. Hoeksema, M. B. Niedner, Y. Yi, and M. Snow (1999), Disconnection Events (DEs) in Halley's Comet 1985-1986:. The Correlation with Crossings of the Heliospheric Current Sheet (HCS), *Icarus*, *137*, 69–83, doi: 10.1006/icar.1998.6030.

Bravo, S., and G. A. Stewart (1997), Fast and Slow Wind from Solar Coronal Holes, *ApJ*, *489*, 992–+, doi:10.1086/304789.

Breech, B., W. H. Matthaeus, S. R. Cranmer, J. C. Kasper, and S. Oughton (2009), Electron and proton heating by solar wind turbulence, *Journal of Geophysical Research (Space Physics)*, *114*, 9103–+, doi:10.1029/2009JA014354.

Brueckner, G. E., et al. (1995a), The Large Angle Spectroscopic Coronagraph (LASCO), *Sol. Phys.*, *162*, 357–402, doi:10.1007/BF00733434.

Brueckner, G. E., et al. (1995b), The Large Angle Spectroscopic Coronagraph (LASCO), *Sol. Phys.*, *162*, 357–402, doi:10.1007/BF00733434.

Bryans, P., E. Landi, and D. W. Savin (2009), A New Approach to Analyzing Solar Coronal Spectra and Updated Collisional Ionization Equilibrium Calculations. II. Updated Ionization Rate Coefficients, *ApJ*, *691*, 1540–1559, doi:10.1088/0004-637X/691/2/1540.

Buergi, A., and J. Geiss (1986), Helium and minor ions in the corona and solar wind - Dynamics and charge states, *Sol. Phys.*, *103*, 347–383, doi:10.1007/BF00147835.

Burlaga, L., E. Sittler, F. Mariani, and R. Schwenn (1981), Magnetic loop behind an interplanetary shock - Voyager, Helios, and IMP 8 observations, *J. Geophys. Res.*, *86*, 6673–6684, doi:10.1029/JA086iA08p06673.

Burlaga, L. F. (1971), Hydromagnetic Waves and Discontinuities in the Solar Wind, *Space Sci. Rev.*, *12*, 600–657, doi:10.1007/BF00173345.

Burlaga, L. F. (1988), Magnetic clouds and force-free fields with constant alpha, *J. Geophys. Res.*, *93*, 7217–7224, doi:10.1029/JA093iA07p07217.

Burlaga, L. F. (1995), Interplanetary magnetohydrodynamics., *Interplanetary magnetohydrodynamics, by L. F. Burlag. International Series in Astronomy and Astrophysics, Vol. 3, Oxford University Press. 1995. 272 pages; ISBN13: 978-0-19-508472-6*, *3*.

Burlaga, L. F., R. P. Lepping, K. W. Behannon, L. W. Klein, and F. M. Neubauer (1982), Large-scale variations of the interplanetary magnetic field - Voyager 1 and 2 observations between 1-5 AU, *J. Geophys. Res.*, *87*, 4345–4353, doi:10.1029/JA087iA06p04345.

Burlaga, L. F., N. F. Ness, J. D. Richardson, and R. P. Lepping (2001), The Bastille day Shock and Merged Interaction Region at 63 au: Voyager 2 Observations, *Sol. Phys.*, *204*, 399–411, doi:10.1023/A:1014269926730.

Cane, H. V., and I. G. Richardson (2003), Interplanetary coronal mass ejections in the near-Earth solar wind during 1996-2002, *Journal of Geophysical Research (Space Physics)*, *108*, 1156, doi:10.1029/2002JA009817.

Cane, H. V., R. G. Stone, J. Fainberg, J. L. Steinberg, S. Hoang, and R. T. Stewart (1981), Radio evidence for shock acceleration of electrons in the solar corona, *Geophys. Res. Lett.*, *8*, 1285–1288, doi:10.1029/GL008i012p01285.

Canullo, M. V., A. Costa, and C. Ferro-Fontan (1996), Nonlocal Heat Transport in the Solar Wind, *ApJ*, *462*, 1005, doi:10.1086/177214.

Cargill, P. J. (1994), Some implications of the nanoflare concept, *ApJ*, *422*, 381–393, doi:10.1086/173733.

Carrington, R. C. (1859), Description of a Singular Appearance seen in the Sun on September 1, 1859, *MNRAS*, *20*, 13–15.

Cassak, P. A., J. F. Drake, and M. A. Shay (2006), A Model for Spontaneous Onset of Fast Magnetic Reconnection, *ApJ*, *644*, L145–L148, doi:10.1086/505690.

Chae, J. (2001), Observational Determination of the Rate of Magnetic Helicity Transport through the Solar Surface via the Horizontal Motion of Field Line Footpoints, *ApJ*, *560*, L95–L98, doi:10.1086/324173.

Chandran, B. D. G., and J. V. Hollweg (2009), Alfvén Wave Reflection and Turbulent Heating in the Solar Wind from 1 Solar Radius to 1 AU: An Analytical Treatment, *ApJ*, *707*, 1659–1667, doi:10.1088/0004-637X/707/2/1659.

Chandran, B. D. G., T. J. Dennis, E. Quataert, and S. D. Bale (2011), Incorporating Kinetic Physics into a Two-fluid Solar-wind Model with Temperature Anisotropy and Low-frequency Alfvén-wave Turbulence, *ApJ*, *743*, 197, doi:10.1088/0004-637X/743/2/197.

Chané, E., B. van der Holst, C. Jacobs, S. Poedts, and D. Kimpe (2006), Inverse and normal coronal mass ejections: evolution up to 1 AU, *A&A*, *447*, 727–733, doi:10.1051/0004-6361:20053802.

Chapman, S., and H. Zirin (1957), Notes on the Solar Corona and the Terrestrial Ionosphere, *Smithsonian Contributions to Astrophysics*, *2*, 1.

Chen, P. F., and K. Shibata (2000), An Emerging Flux Trigger Mechanism for Coronal Mass Ejections, *ApJ*, *545*, 524–531, doi:10.1086/317803.

Chen, P. F., C. Fang, and K. Shibata (2005), A Full View of EIT Waves, *ApJ*, *622*, 1202–1210, doi:10.1086/428084.

Ciaravella, A., J. C. Raymond, and S. W. Kahler (2006), Ultraviolet Properties of Halo Coronal Mass Ejections: Doppler Shifts, Angles, Shocks, and Bulk Morphology, *ApJ*, *652*, 774–792, doi:10.1086/507171.

Cohen, O., et al. (2007), A Semiempirical Magnetohydrodynamical Model of the Solar Wind, *ApJ*, *654*, L163–L166, doi:10.1086/511154.

Cohen, O., G. D. R. Attrill, W. B. Manchester, IV, and M. J. Wills-Davey (2009), Numerical Simulation of an EUV Coronal Wave Based on the 2009 February 13 CME Event Observed by STEREO, *ApJ*, *705*, 587, doi:10.1088/0004-637X/705/1/587.

Cranmer, S. R. (2009), Coronal Holes, *Living Reviews in Solar Physics*, *6*, 3–+.

Cranmer, S. R. (2010), An Efficient Approximation of the Coronal Heating Rate for use in Global Sun-Heliosphere Simulations, *ApJ*, *710*, 676–688, doi:10.1088/0004-637X/710/1/676.

Cranmer, S. R., W. H. Matthaeus, B. A. Breech, and J. C. Kasper (2009), Empirical Constraints on Proton and Electron Heating in the Fast Solar Wind, *ApJ*, *702*, 1604–1614, doi:10.1088/0004-637X/702/2/1604.

Crider, D. H., J. Espley, D. A. Brain, D. L. Mitchell, J. E. P. Connerney, and M. H. AcuñA (2005), Mars Global Surveyor observations of the Halloween 2003 solar superstorm's encounter with Mars, *Journal of Geophysical Research (Space Physics)*, *110*, A09S21, doi:10.1029/2004JA010881.

Crooker, N. U., G. L. Siscoe, S. Shodhan, D. F. Webb, J. T. Gosling, and E. J. Smith (1993), Multiple heliospheric current sheets and coronal streamer belt dynamics, *J. Geophys. Res.*, *98*, 9371–9381, doi:10.1029/93JA00636.

Crooker, N. U., J. T. Gosling, and S. W. Kahler (2002), Reducing heliospheric magnetic flux from coronal mass ejections without disconnection, *Journal of Geophysical Research (Space Physics)*, *107*, 1028, doi:10.1029/2001JA000236.

Culhane, J. L., et al. (2007), The EUV Imaging Spectrometer for Hinode, *Sol. Phys.*, *243*, 19–61, doi:10.1007/s01007-007-0293-1.

de Koning, C. A., and V. J. Pizzo (2010), Three-Dimensional CME Reconstruction Using Geometric and Polarimetric Localization, *AGU Fall Meeting Abstracts*, p. A6.

De Pontieu, B., et al. (2007), Chromospheric Alfvénic Waves Strong Enough to Power the Solar Wind, *Science*, *318*, 1574–, doi:10.1126/science.1151747.

Delaboudinière, J.-P., et al. (1995), EIT: Extreme-Ultraviolet Imaging Telescope for the SOHO Mission, *Sol. Phys.*, *162*, 291–312, doi:10.1007/BF00733432.

Démoulin, P., and M. A. Berger (2003), Magnetic Energy and Helicity Fluxes at the Photospheric Level, *Sol. Phys.*, *215*, 203–215, doi:10.1023/A:1025679813955.

Dere, K. P., E. Landi, H. E. Mason, B. C. Monsignori Fossi, and P. R. Young (1997), CHIANTI - an atomic database for emission lines, *A&AS*, *125*, 149–173, doi:10.1051/aas:1997368.

Dere, K. P., E. Landi, P. R. Young, G. Del Zanna, M. Landini, and H. E. Mason (2009), CHIANTI - an atomic database for emission lines. IX. Ionization rates, recombination rates, ionization equilibria for the elements hydrogen through zinc and updated atomic data, *A&A*, *498*, 915–929, doi:10.1051/0004-6361/200911712.

DeVore, C. R., N. R. Sheeley, Jr., J. P. Boris, T. R. Young, Jr., and K. L. Harvey (1985), Simulations of magnetic-flux transport in solar active regions, *Sol. Phys.*, *102*, 41–49, doi:10.1007/BF00154036.

Doschek, G. A., and H. P. Warren (2005), Chromospheric Evaporation in Solar Flares Revisited, *ApJ*, *629*, 1150–1163, doi:10.1086/431920.

Downs, C., I. I. Roussev, B. van der Holst, N. Lugaz, I. V. Sokolov, and T. I. Gombosi (2010), Toward a Realistic Thermodynamic Magnetohydrodynamic Model of the Global Solar Corona, *ApJ*, *712*, 1219–1231, doi:10.1088/0004-637X/712/2/1219.

Downs, C., I. I. Roussev, B. van der Holst, N. Lugaz, I. V. Sokolov, and T. I. Gombosi (2011), Studying Extreme Ultraviolet Wave Transients with a Digital Laboratory: Direct Comparison of Extreme Ultraviolet Wave Observations to Global Magnetohydrodynamic Simulations, *ApJ*, *728*, 2, doi:10.1088/0004-637X/728/1/2.

Downs, C., I. I. Roussev, B. van der Holst, N. Lugaz, and I. V. Sokolov (2012), Understanding SDO/AIA Observations of the 2010 June 13 EUV Wave Event: Direct Insight from a Global Thermodynamic MHD Simulation, *ApJ*, *750*, 134, doi:10.1088/0004-637X/750/2/134.

Dryer, M., H. Perez-de-Tejada, H. A. Taylor, Jr., D. S. Intriligator, J. D. Mikalov, and B. Rompolt (1982), Compression of the Venusian ionosphere on May 10, 1979, by the interplanetary shock generated by the solar eruption of May 8, 1979, *J. Geophys. Res.*, *87*, 9035–9044, doi:10.1029/JA087iA11p09035.

Dryer, M., Z. Smith, C. D. Fry, W. Sun, C. S. Deehr, and S.-I. Akasofu (2004), Real-time shock arrival predictions during the "Halloween 2003 epoch", *Space Weather*, *2*, S09001, doi:10.1029/2004SW000087.

Endeve, E., T. E. Holzer, and E. Leer (2004), Helmet Streamers Gone Unstable: Two-Fluid Magnetohydrodynamic Models of the Solar Corona, *ApJ*, *603*, 307–321, doi:10.1086/381239.

Esser, R., R. J. Edgar, and N. S. Brickhouse (1998), High Minor Ion Outflow Speeds in the Inner Corona and Observed Ion Charge States in Interplanetary Space, *ApJ*, *498*, 448, doi:10.1086/305516.

Evans, R. M., M. Opher, V. Jatenco-Pereira, and T. I. Gombosi (2009), Surface Alfvén Wave Damping in a Three-Dimensional Simulation of the Solar Wind, *ApJ*, *703*, 179–186, doi:10.1088/0004-637X/703/1/179.

Evans, R. M., M. Opher, and T. I. Gombosi (2011), Learning from the Outer Heliosphere: Interplanetary Coronal Mass Ejection Sheath Flows and the Ejecta Orientation in the Lower Corona, *ApJ*, *728*, 41, doi:10.1088/0004-637X/728/1/41.

Evans, R. M., M. Opher, R. Oran, B. van der Holst, I. V. Sokolov, R. Frazin, T. I. Gombosi, and A. Vásquez (2012), Coronal Heating by Surface Alfvén Wave Damping: Implementation in a Global Magnetohydrodynamics Model of the Solar Wind, *ApJ*, *756*, 155, doi:10.1088/0004-637X/756/2/155.

Fan, Y., and S. E. Gibson (2007), Onset of Coronal Mass Ejections Due to Loss of Confinement of Coronal Flux Ropes, *ApJ*, *668*, 1232–1245, doi:10.1086/521335.

Fang, F., W. Manchester, W. P. Abbett, and B. van der Holst (2010), Simulation of Flux Emergence from the Convection Zone to the Corona, *ApJ*, *714*, 1649–1657, doi:10.1088/0004-637X/714/2/1649.

Feldman, U., P. Mandelbaum, J. F. Seely, G. A. Doschek, and H. Gursky (1992), The potential for plasma diagnostics from stellar extreme-ultraviolet observations, *ApJS*, *81*, 387–408, doi:10.1086/191698.

Feng, X., L. Yang, C. Xiang, S. T. Wu, Y. Zhou, and D. Zhong (2010), Three-dimensional Solar WIND Modeling from the Sun to Earth by a SIP-CESE MHD Model with a Six-component Grid, *ApJ*, *723*, 300–319, doi:10.1088/0004-637X/723/1/300.

Feng, X., S. Zhang, C. Xiang, L. Yang, C. Jiang, and S. T. Wu (2011), A Hybrid Solar Wind Model of the CESE+HLL Method with a Yin-Yang Overset Grid and an AMR Grid, *ApJ*, *734*, 50, doi:10.1088/0004-637X/734/1/50.

Feng, X., C. Jiang, C. Xiang, X. Zhao, and S. T. Wu (2012), A Data-driven Model for the Global Coronal Evolution, *ApJ*, *758*, 62, doi:10.1088/0004-637X/758/1/62.

Fermi, E. (1949), On the Origin of the Cosmic Radiation, *Physical Review*, *75*, 1169–1174, doi:10.1103/PhysRev.75.1169.

Fisk, L. A. (1996), Motion of the footpoints of heliospheric magnetic field lines at the Sun: Implications for recurrent energetic particle events at high heliographic latitudes, *J. Geophys. Res.*, *101*, 15,547–15,554, doi:10.1029/96JA01005.

Fisk, L. A. (2005), The Open Magnetic Flux of the Sun. I. Transport by Reconnections with Coronal Loops, *ApJ*, *626*, 563–573, doi:10.1086/429957.

Fisk, L. A., N. A. Schwadron, and T. H. Zurbuchen (1998), On the Slow Solar Wind, *Space Sci. Rev.*, *86*, 51–60, doi:10.1023/A:1005015527146.

Fisk, L. A., N. A. Schwadron, and T. H. Zurbuchen (1999), Acceleration of the fast solar wind by the emergence of new magnetic flux, *J. Geophys. Res.*, *104*, 19,765–19,772, doi:10.1029/1999JA900256.

Forbes, T. G. (2000), A review on the genesis of coronal mass ejections, *J. Geophys. Res.*, *105*, 23,153–23,166, doi:10.1029/2000JA000005.

Forbes, T. G., et al. (2006), CME Theory and Models, *Space Sci. Rev.*, *123*, 251–302, doi:10.1007/s11214-006-9019-8.

Frazin, R. A. (2000), Tomography of the Solar Corona. I. A Robust, Regularized, Positive Estimation Method, *ApJ*, *530*, 1026–1035, doi:10.1086/308412.

Frazin, R. A., and P. Janzen (2002), Tomography of the Solar Corona. II. Robust, Regularized, Positive Estimation of the Three-dimensional Electron Density Distribution from LASCO-C2 Polarized White-Light Images, *ApJ*, *570*, 408–422, doi:10.1086/339572.

Frazin, R. A., A. M. Vásquez, and F. Kamalabadi (2009), Quantitative, Three-dimensional Analysis of the Global Corona with Multi-spacecraft Differential Emission Measure Tomography, *ApJ*, *701*, 547–560, doi:10.1088/0004-637X/701/1/547.

Fry, C. D., W. Sun, C. S. Deehr, M. Dryer, Z. Smith, S.-I. Akasofu, M. Tokumaru, and M. Kojima (2001), Improvements to the HAF solar wind model for space weather predictions, *J. Geophys. Res.*, *106*, 20,985–21,002, doi:10.1029/2000JA000220.

Gallagher, P. T., Y.-J. Moon, and H. Wang (2002), Active-Region Monitoring and Flare Forecasting I. Data Processing and First Results, *Sol. Phys.*, *209*, 171–183, doi:10.1023/A:1020950221179.

Galvin, A. B., et al. (2008), The Plasma and Suprathermal Ion Composition (PLASTIC) Investigation on the STEREO Observatories, *Space Sci. Rev.*, *136*, 437–486, doi:10.1007/s11214-007-9296-x.

Geiss, J., et al. (1995), The Southern High-Speed Stream: Results from the SWICS Instrument on Ulysses, *Science*, *268*, 1033–1036, doi:10.1126/science.7754380.

Giacalone, J., J. R. Jokipii, and J. Kóta (2002), Particle Acceleration in Solar Wind Compression Regions, *ApJ*, *573*, 845–850, doi:10.1086/340660.

Gibson, S. E., and B. C. Low (1998), A Time-Dependent Three-Dimensional Magnetohydrodynamic Model of the Coronal Mass Ejection, *ApJ*, *493*, 460, doi:10.1086/305107.

Gloeckler, G., et al. (1998), Investigation of the composition of solar and interstellar matter using solar wind and pickup ion measurements with SWICS and SWIMS on the ACE spacecraft, *Space Sci. Rev.*, *86*, 497–539, doi:10.1023/A:1005036131689.

Gombosi, T. I. (2004), *Physics of the Space Environment*.

Gombosi, T. I., D. L. DeZeeuw, C. P. T. Groth, K. G. Powell, and Q. F. Stout (2000), Multiscale MHD simulation of a coronal mass ejection and its interaction with the magnetosphere-ionosphere system, *Journal of Atmospheric and Solar-Terrestrial Physics*, *62*, 1515–1525, doi:10.1016/S1364-6826(00)00091-2.

Gómez-Herrero, R., O. Malandraki, N. Dresing, E. Kilpua, B. Heber, A. Klassen, R. Müller-Mellin, and R. F. Wimmer-Schweingruber (2011), Spatial and temporal variations of CIRs: Multi-point observations by STEREO, *Journal of Atmospheric and Solar-Terrestrial Physics*, *73*, 551–565, doi:10.1016/j.jastp.2010.11.017.

Gopalswamy, N., Y. Hanaoka, and H. S. Hudson (2000), Structure and Dynamics of the Corona Surrounding an Eruptive Prominence, *Advances in Space Research*, *25*, 1851–1854, doi:10.1016/S0273-1177(99)00597-9.

Gopalswamy, N., A. Lara, S. Yashiro, M. L. Kaiser, and R. A. Howard (2001), Predicting the 1-AU arrival times of coronal mass ejections, *J. Geophys. Res.*, *106*, 29,207–29,218, doi:10.1029/2001JA000177.

Gopalswamy, N., P. Mäkelä, H. Xie, S. Akiyama, and S. Yashiro (2009), CME interactions with coronal holes and their interplanetary consequences, *Journal of Geophysical Research (Space Physics)*, *114*, A00A22, doi:10.1029/2008JA013686.

Gosling, J. T. (1990), Coronal mass ejections and magnetic flux ropes in interplanetary space, *Washington DC American Geophysical Union Geophysical Monograph Series*, *58*, 343–364.

Gosling, J. T. (1993), The solar flare myth, *J. Geophys. Res.*, *98*, 18,937–18,950, doi:10.1029/93JA01896.

Gosling, J. T., E. Hildner, R. M. MacQueen, R. H. Munro, A. I. Poland, and C. L. Ross (1975), Direct observations of a flare related coronal and solar wind disturbance, *Sol. Phys.*, *40*, 439–448, doi:10.1007/BF00162390.

Gosling, J. T., E. Hildner, R. M. MacQueen, R. H. Munro, A. I. Poland, and C. L. Ross (1976), The speeds of coronal mass ejection events, *Sol. Phys.*, *48*, 389–397, doi:10.1007/BF00152004.

Gosling, J. T., P. Riley, D. J. McComas, and V. J. Pizzo (1998), Overexpanding coronal mass ejections at high heliographic latitudes - Observations and simulations, *J. Geophys. Res.*, *103*, 1941, doi:10.1029/97JA01304.

Grevesse, N., and A. J. Sauval (1998), Standard Solar Composition, *Space Sci. Rev.*, *85*, 161–174, doi:10.1023/A:1005161325181.

Groth, C. P. T., D. L. De Zeeuw, T. I. Gombosi, and K. G. Powell (2000), Global three-dimensional MHD simulation of a space weather event: CME formation, interplanetary propagation, and interaction with the magnetosphere, *J. Geophys. Res.*, *105*, 25,053–25,078, doi:10.1029/2000JA900093.

Gruesbeck, J. R., S. T. Lepri, T. H. Zurbuchen, and S. K. Antiochos (2011), Constraints on Coronal Mass Ejection Evolution from in Situ Observations of Ionic Charge States, *ApJ*, *730*, 103–+, doi:10.1088/0004-637X/730/2/103.

Guo, F., J. R. Jokipii, and J. Kota (2010), Particle Acceleration by Collisionless Shocks Containing Large-scale Magnetic-field Variations, *ApJ*, *725*, 128–133, doi:10.1088/0004-637X/725/1/128.

Hakamada, K., and S.-I. Akasofu (1982), Simulation of three-dimensional solar wind disturbances and resulting geomagnetic storms, *Space Sci. Rev.*, *31*, 3–70, doi:10.1007/BF00349000.

Han, S. M., S. T. Wu, and M. Dryer (1988), A three-dimensional, time-dependent numerical modeling of super-sonic, super-Alfvenic MHD flow, *Computers and Fluids*, *16*, 81–103.

Hartle, R. E., and P. A. Sturrock (1968), Two-Fluid Model of the Solar Wind, *ApJ*, *151*, 1155–+, doi:10.1086/149513.

Hayashi, K., X. P. Zhao, and Y. Liu (2006), MHD simulation of two successive interplanetary disturbances driven by cone-model parameters in IPS-based solar wind, *Geophys. Res. Lett.*, *33*, L20103, doi:10.1029/2006GL027408.

Hirayama, T. (1974), Theoretical Model of Flares and Prominences. I: Evaporating Flare Model, *Sol. Phys.*, *34*, 323–338, doi:10.1007/BF00153671.

Hollweg, J. V. (1974), On electron heat conduction in the solar wind, *J. Geophys. Res.*, *79*, 3845, doi:10.1029/JA079i025p03845.

Hollweg, J. V. (1978), Some physical processes in the solar wind, *Reviews of Geophysics and Space Physics*, *16*, 689–720, doi:10.1029/RG016i004p00689.

Hollweg, J. V. (1986), Transition region, corona, and solar wind in coronal holes, *J. Geophys. Res.*, *91*, 4111–4125, doi:10.1029/JA091iA04p04111.

Howard, R. A., N. R. Sheeley, Jr., D. J. Michels, and M. J. Koomen (1985), Coronal mass ejections - 1979-1981, *J. Geophys. Res.*, *90*, 8173–8191, doi:10.1029/JA090iA09p08173.

Howard, R. A., et al. (2008), Sun Earth Connection Coronal and Heliospheric Investigation (SECCHI), *Space Sci. Rev.*, *136*, 67–115, doi:10.1007/s11214-008-9341-4.

Howard, T. (Ed.) (2011), *Coronal Mass Ejections%*, *Astrophysics and Space Science Library*, vol. 376, doi:10.1007/978-1-4419-8789-1.

Howes, G. G. (2011), Prediction of the Proton-to-total Turbulent Heating in the Solar Wind, *ApJ*, *738*, 40, doi:10.1088/0004-637X/738/1/40.

Howes, G. G., S. C. Cowley, W. Dorland, G. W. Hammett, E. Quataert, and A. A. Schekochihin (2008), A model of turbulence in magnetized plasmas: Implications for the dissipation range in the solar wind, *Journal of Geophysical Research (Space Physics)*, *113*, A05103, doi:10.1029/2007JA012665.

Hu, Y. Q., S. R. Habbal, Y. Chen, and X. Li (2003a), Are coronal holes the only source of fast solar wind at solar minimum?, *Journal of Geophysical Research (Space Physics)*, *108*, 1377, doi:10.1029/2002JA009776.

Hu, Y. Q., X. Li, and S. R. Habbal (2003b), A 2.5-dimensional MHD Alfvén-wave-driven solar wind model, *Journal of Geophysical Research (Space Physics)*, *108*, 1378, doi:10.1029/2003JA009889.

Hudson, H. S. (1991), Solar flares, microflares, nanoflares, and coronal heating, *Sol. Phys.*, *133*, 357–369, doi:10.1007/BF00149894.

Hundhausen, A. J. (1993), Sizes and locations of coronal mass ejections - SMM observations from 1980 and 1984-1989, *J. Geophys. Res.*, *98*, 13,177, doi:10.1029/93JA00157.

Illing, R. M. E., and A. J. Hundhausen (1985), Observation of a coronal transient from 1.2 to 6 solar radii, *J. Geophys. Res.*, *90*, 275–282, doi:10.1029/JA090iA01p00275.

Jacobs, C., and S. Poedts (2011), A polytropic model for the solar wind, *Advances in Space Research*, *48*, 1958–1966, doi:10.1016/j.asr.2011.08.015.

Jacques, S. A. (1977), Momentum and energy transport by waves in the solar atmosphere and solar wind, *ApJ*, *215*, 942–951, doi:10.1086/155430.

Janse, Å. M., and B. C. Low (2009), The Topological Changes of Solar Coronal Magnetic Fields. I. Spontaneous Current Sheets in Three-Dimensional Fields, *ApJ*, *690*, 1089–1104, doi:10.1088/0004-637X/690/2/1089.

Jian, L., C. T. Russell, J. G. Luhmann, and R. M. Skoug (2006), Properties of Stream Interactions at One AU During 1995 2004, *Sol. Phys.*, *239*, 337–392, doi:10.1007/s11207-006-0132-3.

Jin, M., and M. Ding (2008), Loop-Like Hard X-Ray Emission in a 2005 January 20 Flare, *PASJ*, *60*, 835–, doi:10.1093/pasj/60.4.835.

Jin, M., and M. D. Ding (2007), Correlation and asymmetry between solar flare hard X-ray footpoints: a statistical study, *A&A*, *471*, 705–709, doi:10.1051/0004-6361:20077202.

Jin, M., M. D. Ding, P. F. Chen, C. Fang, and S. Imada (2009), Coronal Mass Ejection Induced Outflows Observed with Hinode/EIS, *ApJ*, *702*, 27–38, doi:10.1088/0004-637X/702/1/27.

Jin, M., et al. (2012), A Global Two-temperature Corona and Inner Heliosphere Model: A Comprehensive Validation Study, *ApJ*, *745*, 6, doi:10.1088/0004-637X/745/1/6.

Jin, M., W. B. Manchester, B. van der Holst, R. Oran, I. Sokolov, G. Toth, Y. Liu, X. D. Sun, and T. I. Gombosi (2013), Numerical Simulations of Coronal Mass Ejection on 2011 March 7: One-temperature and Two-temperature Model Comparison, *ApJ*, *773*, 50, doi:10.1088/0004-637X/773/1/50.

Jokipii, J. R., and E. N. Parker (1968), Random Walk of Magnetic Lines of Force in Astrophysics, *Physical Review Letters*, *21*, 44–47, doi:10.1103/PhysRevLett.21.44.

Jones, G. H., and J. C. Brandt (2004), The interaction of comet 153P/Ikeya-Zhang with interplanetary coronal mass ejections: Identification of fast ICME signatures, *Geophys. Res. Lett.*, *31*, L20805, doi:10.1029/2004GL021166.

Kang, H., and T. W. Jones (1995), Diffusive Shock Acceleration Simulations: Comparison with Particle Methods and Bow Shock Measurements, *ApJ*, *447*, 944, doi:10.1086/175932.

Kar, J., K. K. Mahajan, M. V. Srilakshmi, and R. Kohli (1986), Possible effects of solar flares on the ionosphere of Venus from Pioneer Venus Orbiter measurements, *J. Geophys. Res.*, *91*, 8986–8992, doi:10.1029/JA091iA08p08986.

Karpen, J. T., S. K. Antiochos, and C. R. DeVore (2012), The Mechanisms for the Onset and Explosive Eruption of Coronal Mass Ejections and Eruptive Flares, *ApJ*, *760*, 81, doi:10.1088/0004-637X/760/1/81.

Kasper, J. C., A. J. Lazarus, and S. P. Gary (2008), Hot Solar-Wind Helium: Direct Evidence for Local Heating by Alfvén-Cyclotron Dissipation, *Physical Review Letters*, *101*(26), 261103, doi:10.1103/PhysRevLett.101.261103.

Keppens, R., and J. P. Goedbloed (1999), Numerical simulations of stellar winds: polytropic models, *A&A*, *343*, 251–260.

Killen, R. M., A. E. Potter, P. Reiff, M. Sarantos, B. V. Jackson, P. Hick, and B. Giles (2001), Evidence for space weather at Mercury, *J. Geophys. Res.*, *106*, 20,509–20,526, doi:10.1029/2000JE001401.

Killen, R. M., M. Sarantos, and P. H. Reiff (2004), Space weather at Mercury, *Advances in Space Research*, *33*, 1899–1904, doi:10.1016/j.asr.2003.02.020.

Klein, L. W., and L. F. Burlaga (1982), Interplanetary magnetic clouds at 1 AU, *J. Geophys. Res.*, *87*, 613–624, doi:10.1029/JA087iA02p00613.

Kliem, B., and T. Török (2006), Torus Instability, *Physical Review Letters*, *96*(25), 255002, doi:10.1103/PhysRevLett.96.255002.

Klimchuk, J. A. (2006), On Solving the Coronal Heating Problem, *Sol. Phys.*, *234*, 41–77, doi:10.1007/s11207-006-0055-z.

Kohl, J. L., et al. (1998), UVCS/SOHO Empirical Determinations of Anisotropic Velocity Distributions in the Solar Corona, *ApJ*, *501*, L127, doi:10.1086/311434.

Kosovichev, A. G., and T. V. Stepanova (1991), Numerical Simulation of Shocks in the Heliosphere, *Soviet Ast.*, *35*, 646.

Kóta, J., W. B. Manchester, J. R. Jokipii, D. L. de Zeeuw, and T. I. Gombosi (2005), Simulation of SEP Acceleration and Transport at CME-driven Shocks, in *The Physics of Collisionless Shocks: 4th Annual IGPP International Astrophysics Conference*, *American Institute of Physics Conference Series*, vol. 781, edited by G. Li, G. P. Zank, and C. T. Russell, pp. 201–206, doi:10.1063/1.2032697.

Kozarev, K. A., R. M. Evans, N. A. Schwadron, M. A. Dayeh, M. Opher, K. E. Korreck, and B. van der Holst (2013), Global Numerical Modeling of Energetic Proton Acceleration in a Coronal Mass Ejection Traveling through the Solar Corona, *ApJ*, *778*, 43, doi:10.1088/0004-637X/778/1/43.

Kuchar, T. A., et al. (2008), Observations of a comet tail disruption induced by the passage of a CME, *Journal of Geophysical Research (Space Physics)*, *113*, A04101, doi:10.1029/2007JA012603.

Laitinen, T., H. Fichtner, and R. Vainio (2003), Toward a self-consistent treatment of the cyclotron wave heating and acceleration of the solar wind plasma, *Journal of Geophysical Research (Space Physics)*, *108*, 1081–+, doi:10.1029/2002JA009479.

Laming, J. M. (2004), On Collisionless Electron-Ion Temperature Equilibration in the Fast Solar Wind, *ApJ*, *604*, 874–883, doi:10.1086/382066.

Laming, J. M., and S. T. Lepri (2007), Ion Charge States in the Fast Solar Wind: New Data Analysis and Theoretical Refinements, *ApJ*, *660*, 1642–1652, doi:10.1086/513505.

Landi, E. (2008), The Off-Disk Thermal Structure of a Polar Coronal Hole, *ApJ*, *685*, 1270–1276, doi:10.1086/591225.

Landi, E., and S. R. Cranmer (2009), Ion Temperatures in the Low Solar Corona: Polar Coronal Holes at Solar Minimum, *ApJ*, *691*, 794–805, doi:10.1088/0004-637X/691/1/794.

Landi, E., and M. Landini (1997), Simultaneous temperature and density diagnostics of optically thin plasmas, *A&A*, *327*, 1230–1241.

Landi, E., P. R. Young, K. P. Dere, G. Del Zanna, and H. E. Mason (2013), CHIANTI – An Atomic Database for Emission Lines. XIII. Soft X-Ray Improvements and Other Changes, *ApJ*, *763*, 86, doi:10.1088/0004-637X/763/2/86.

Landi, S., and F. Pantellini (2003), Kinetic simulations of the solar wind from the subsonic to the supersonic regime, *A&A*, *400*, 769–778, doi:10.1051/0004-6361:20021822.

Lanzerotti, L. J. (2011), Physical Origins of Space Weather Impacts: Open Physics Questions, *AGU Fall Meeting Abstracts*, p. B1.

Leamon, R. J., C. W. Smith, N. F. Ness, and H. K. Wong (1999), Dissipation range dynamics: Kinetic Alfvén waves and the importance of β_e, *J. Geophys. Res.*, *104*, 22,331–22,344, doi:10.1029/1999JA900158.

Leer, E., and W. I. Axford (1972), A Two-Fluid Solar Wind Model with Anisotropic Proton Temperature, *Sol. Phys.*, *23*, 238–250, doi:10.1007/BF00153907.

Lemen, J. R., et al. (2012), The Atmospheric Imaging Assembly (AIA) on the Solar Dynamics Observatory (SDO), *Sol. Phys.*, *275*, 17–40, doi:10.1007/s11207-011-9776-8.

Lengyel-Frey, D., G. Thejappa, R. J. MacDowall, R. G. Stone, and J. L. Phillips (1997), Ulysses observations of wave activity at interplanetary shocks and implications for type II radio bursts, *J. Geophys. Res.*, *102*, 2611–2622, doi: 10.1029/96JA02871.

Li, B., X. Li, Y.-Q. Hu, and S. R. Habbal (2004), A two-dimensional Alfvén wave-driven solar wind model with proton temperature anisotropy, *Journal of Geophysical Research (Space Physics)*, *109*, A07103, doi:10.1029/2003JA010313.

Li, G., G. P. Zank, O. Verkhoglyadova, R. A. Mewaldt, C. M. S. Cohen, G. M. Mason, and M. I. Desai (2009), Shock Geometry and Spectral Breaks in Large SEP Events, *ApJ*, *702*, 998–1004, doi:10.1088/0004-637X/702/2/998.

Li, X., S. R. Habbal, J. Kohl, and G. Noci (1998), The Effect of Temperature Anisotropy on Observations of Doppler Dimming and Pumping in the Inner Corona, *ApJ*, *501*, L133, doi:10.1086/311428.

Lindsay, G. M., C. T. Russell, J. G. Luhmann, and P. Gazis (1994), On the sources of interplanetary shocks at 0.72 AU, *J. Geophys. Res.*, *99*, 11–17, doi: 10.1029/93JA02666.

Lindsey, C., and D. C. Braun (1997), Helioseismic Holography, *ApJ*, *485*, 895, doi: 10.1086/304445.

Lionello, R., J. A. Linker, and Z. Mikić (2001), Including the Transition Region in Models of the Large-Scale Solar Corona, *ApJ*, *546*, 542–551, doi:10.1086/318254.

Lionello, R., J. A. Linker, and Z. Mikić (2009), Multispectral Emission of the Sun During the First Whole Sun Month: Magnetohydrodynamic Simulations, *ApJ*, *690*, 902–912, doi:10.1088/0004-637X/690/1/902.

Liu, Y., J. D. Richardson, J. W. Belcher, J. C. Kasper, and R. M. Skoug (2006), Plasma depletion and mirror waves ahead of interplanetary coronal mass ejections, *Journal of Geophysical Research (Space Physics)*, *111*, A09108, doi: 10.1029/2006JA011723.

Liu, Y. D., et al. (2012), Interactions between Coronal Mass Ejections Viewed in Coordinated Imaging and in situ Observations, *ApJ*, *746*, L15, doi:10.1088/2041-8205/746/2/L15.

Liu, Y. D., J. G. Luhmann, N. Lugaz, C. Möstl, J. A. Davies, S. D. Bale, and R. P. Lin (2013), On Sun-to-Earth Propagation of Coronal Mass Ejections, *ApJ*, *769*, 45, doi:10.1088/0004-637X/769/1/45.

Loesch, C., M. Opher, M. V. Alves, R. M. Evans, and W. B. Manchester (2011), Signatures of two distinct driving mechanisms in the evolution of coronal mass ejections in the lower corona, *Journal of Geophysical Research (Space Physics)*, *116*, A04106, doi:10.1029/2010JA015582.

Lou, Y. (1994), Compressible fluctuations in the equatorial solar wind with a spiral magnetic field, *J. Geophys. Res.*, *99*, 8491–8504, doi:10.1029/94JA00209.

Low, B. C. (2001), Coronal mass ejections, magnetic flux ropes, and solar magnetism, *J. Geophys. Res.*, *106*, 25,141–25,164, doi:10.1029/2000JA004015.

Lugaz, N., and I. I. Roussev (2011), Numerical modeling of interplanetary coronal mass ejections and comparison with heliospheric images, *Journal of Atmospheric and Solar-Terrestrial Physics*, *73*, 1187–1200, doi:10.1016/j.jastp.2010.08.016.

Lugaz, N., W. B. Manchester, IV, and T. I. Gombosi (2005), Numerical Simulation of the Interaction of Two Coronal Mass Ejections from Sun to Earth, *ApJ*, *634*, 651–662, doi:10.1086/491782.

Lugaz, N., W. B. Manchester, IV, I. I. Roussev, G. Tóth, and T. I. Gombosi (2007), Numerical Investigation of the Homologous Coronal Mass Ejection Events from Active Region 9236, *ApJ*, *659*, 788–800, doi:10.1086/512005.

Lugaz, N., W. B. Manchester, IV, I. I. Roussev, and T. I. Gombosi (2008), Observational evidence of CMEs interacting in the inner heliosphere as inferred from MHD simulations, *Journal of Atmospheric and Solar-Terrestrial Physics*, *70*, 598–604, doi:10.1016/j.jastp.2007.08.033.

Lugaz, N., C. J. Farrugia, W. B. Manchester, IV, and N. Schwadron (2013), The Interaction of Two Coronal Mass Ejections: Influence of Relative Orientation, *ApJ*, *778*, 20, doi:10.1088/0004-637X/778/1/20.

Luhmann, J. G., W. T. Kasprzak, and C. T. Russell (2007), Space weather at Venus and its potential consequences for atmosphere evolution, *Journal of Geophysical Research (Planets)*, *112*, E04S10, doi:10.1029/2006JE002820.

Luhmann, J. G., et al. (2008a), Venus Express observations of atmospheric oxygen escape during the passage of several coronal mass ejections, *Journal of Geophysical Research (Planets)*, *113*, E00B04, doi:10.1029/2008JE003092.

Luhmann, J. G., et al. (2008b), STEREO IMPACT Investigation Goals, Measurements, and Data Products Overview, *Space Sci. Rev.*, *136*, 117–184, doi:10.1007/s11214-007-9170-x.

Lynch, B. J. (2006), Numerical simulations of the breakout model for the initiation of solar coronal mass ejections and in-situ observations of their interplanetary structure, Ph.D. thesis, University of Michigan.

MacNeice, P., S. K. Antiochos, A. Phillips, D. S. Spicer, C. R. DeVore, and K. Olson (2004), A Numerical Study of the Breakout Model for Coronal Mass Ejection Initiation, *ApJ*, *614*, 1028–1041, doi:10.1086/423887.

MacQueen, R. M., A. J. Hundhausen, and C. W. Conover (1986), The propagation of coronal mass ejection transients, *J. Geophys. Res.*, *91*, 31–38, doi:10.1029/JA091iA01p00031.

Manchester, W., IV, T. Gombosi, D. DeZeeuw, and Y. Fan (2004a), Eruption of a Buoyantly Emerging Magnetic Flux Rope, *ApJ*, *610*, 588–596, doi:10.1086/421516.

Manchester, W. B., and T. H. Zurbuchen (2006), Are high-latitude forward-reverse shock pairs driven by CME overexpansion?, *Journal of Geophysical Research (Space Physics)*, *111*, A05101, doi:10.1029/2005JA011461.

Manchester, W. B., T. I. Gombosi, I. Roussev, D. L. de Zeeuw, I. V. Sokolov, K. G. Powell, G. Tóth, and M. Opher (2004b), Three-dimensional MHD simulation of a flux rope driven CME, *Journal of Geophysical Research (Space Physics)*, *109*, A01102, doi:10.1029/2002JA009672.

Manchester, W. B., T. I. Gombosi, I. Roussev, A. Ridley, D. L. de Zeeuw, I. V. Sokolov, K. G. Powell, and G. Tóth (2004c), Modeling a space weather event from the Sun to the Earth: CME generation and interplanetary propagation, *Journal of Geophysical Research (Space Physics)*, *109*, A02107, doi:10.1029/2003JA010150.

Manchester, W. B., IV, T. I. Gombosi, D. L. De Zeeuw, I. V. Sokolov, I. I. Roussev, K. G. Powell, J. Kóta, G. Tóth, and T. H. Zurbuchen (2005), Coronal Mass Ejection Shock and Sheath Structures Relevant to Particle Acceleration, *ApJ*, *622*, 1225–1239, doi:10.1086/427768.

Manchester, W. B., IV, A. Vourlidas, G. Tóth, N. Lugaz, I. I. Roussev, I. V. Sokolov, T. I. Gombosi, D. L. De Zeeuw, and M. Opher (2008), Three-dimensional MHD Simulation of the 2003 October 28 Coronal Mass Ejection: Comparison with LASCO Coronagraph Observations, *ApJ*, *684*, 1448–1460, doi:10.1086/590231.

Manchester, W. B., IV, B. van der Holst, G. Tóth, and T. I. Gombosi (2012), The Coupled Evolution of Electrons and Ions in Coronal Mass Ejection-driven shocks, *ApJ*, *756*, 81, doi:10.1088/0004-637X/756/1/81.

Mancuso, S., J. C. Raymond, J. Kohl, Y.-K. Ko, M. Uzzo, and R. Wu (2002), UVCS/SOHO observations of a CME-driven shock: Consequences on ion heating mechanisms behind a coronal shock, *A&A*, *383*, 267–274, doi:10.1051/0004-6361:20011721.

Marsch, E. (2006), Kinetic Physics of the Solar Corona and Solar Wind, *Living Reviews in Solar Physics*, *3*, 1, doi:10.12942/lrsp-2006-1.

Marsch, E., R. Schwenn, H. Rosenbauer, K.-H. Muehlhaeuser, W. Pilipp, and F. M. Neubauer (1982), Solar wind protons - Three-dimensional velocity distributions and derived plasma parameters measured between 0.3 and 1 AU, *J. Geophys. Res.*, *87*, 52–72, doi:10.1029/JA087iA01p00052.

Martin, S. F. (1998), Filament Chirality: A Link Between Fine-Scale and Global Patterns (Review), in *IAU Colloq. 167: New Perspectives on Solar Prominences*, *Astronomical Society of the Pacific Conference Series*, vol. 150, edited by D. F. Webb, B. Schmieder, and D. M. Rust, p. 419.

Mason, G. M., M. I. Desai, U. Mall, A. Korth, R. Bucik, T. T. von Rosenvinge, and K. D. Simunac (2009), In situ Observations of CIRs on STEREO, Wind, and ACE During 2007 - 2008, *Sol. Phys.*, *256*, 393–408, doi:10.1007/s11207-009-9367-0.

Mazzotta, P., G. Mazzitelli, S. Colafrancesco, and N. Vittorio (1998), Ionization balance for optically thin plasmas: Rate coefficients for all atoms and ions of the elements H to NI, *A&AS*, *133*, 403–409, doi:10.1051/aas:1998330.

McComas, D. J., R. Goldstein, J. T. Gosling, and R. M. Skoug (2001), Ulysses' Second Orbit: Remarkably Different Solar Wind, *Space Sci. Rev.*, *97*, 99–103, doi:10.1023/A:1011826111330.

McComas, D. J., H. A. Elliott, and R. von Steiger (2002), Solar wind from high-latitude coronal holes at solar maximum, *Geophys. Res. Lett.*, *29*, 1314, doi:10.1029/2001GL013940.

McComas, D. J., R. W. Ebert, H. A. Elliott, B. E. Goldstein, J. T. Gosling, N. A. Schwadron, and R. M. Skoug (2008), Weaker solar wind from the polar coronal holes and the whole Sun, *Geophys. Res. Lett.*, *35*, L18103, doi:10.1029/2008GL034896.

Meng, X., G. Tóth, M. W. Liemohn, T. I. Gombosi, and A. Runov (2012a), Pressure anisotropy in global magnetospheric simulations: A magnetohydrodynamics model, *Journal of Geophysical Research (Space Physics)*, *117*, A08216, doi:10.1029/2012JA017791.

Meng, X., G. Tóth, I. V. Sokolov, and T. I. Gombosi (2012b), Classical and semirelativistic magnetohydrodynamics with anisotropic ion pressure, *Journal of Computational Physics*, *231*, 3610–3622, doi:10.1016/j.jcp.2011.12.042.

Mewaldt, R. A., et al. (2008), How Efficient are Coronal Mass Ejections at Accelerating Solar Energetic Particles?, in *American Institute of Physics Conference Series*, *American Institute of Physics Conference Series*, vol. 1039, edited by G. Li, Q. Hu, O. Verkhoglyadova, G. P. Zank, R. P. Lin, and J. Luhmann, pp. 111–117, doi:10.1063/1.2982431.

Michael, E., S. Zhekov, R. McCray, U. Hwang, D. N. Burrows, S. Park, G. P. Garmire, S. S. Holt, and G. Hasinger (2002), The X-Ray Spectrum of Supernova Remnant 1987A, *ApJ*, *574*, 166–178, doi:10.1086/340591.

Mikić, Z., J. A. Linker, D. D. Schnack, R. Lionello, and A. Tarditi (1999), Magnetohydrodynamic modeling of the global solar corona, *Physics of Plasmas*, *6*, 2217–2224, doi:10.1063/1.873474.

Mikić, Z., T. Török, V. S. Titov, C. Downs, J. A. Linker, R. Lionello, and P. Riley (2013), MHD Modeling of the Sympathetic Eruptions Observed on August 1, 2010, *AGU Fall Meeting Abstracts*, p. C8.

Morita, T., et al. (2013), Interaction of high Mach-number shocks in laser-produced plasmas, *High Energy Density Physics*, *9*, 187–191, doi:10.1016/j.hedp.2012.12.008.

Moses, D., et al. (1997), EIT Observations of the Extreme Ultraviolet Sun, *Sol. Phys.*, *175*, 571–599, doi:10.1023/A:1004902913117.

Möstl, C., et al. (2012), Multi-point Shock and Flux Rope Analysis of Multiple Interplanetary Coronal Mass Ejections around 2010 August 1 in the Inner Heliosphere, *ApJ*, *758*, 10, doi:10.1088/0004-637X/758/1/10.

Nelson, G. J., and D. B. Melrose (1985), *Type II bursts*, pp. 333–359.

Neugebauer, M. (1981), Observations of solar-wind helium, *Fund. Cosmic Phys.*, *7*, 131–199.

Neugebauer, M. (1997), Pioneers of space physics: A career in the solar wind, *J. Geophys. Res.*, *102*, 26,887–26,894, doi:10.1029/97JA02444.

Neugebauer, M., and C. W. Snyder (1962), Solar Plasma Experiment, *Science*, *138*, 1095–1097, doi:10.1126/science.138.3545.1095-a.

Odstrcil, D., and V. J. Pizzo (2009), Numerical Heliospheric Simulations as Assisting Tool for Interpretation of Observations by STEREO Heliospheric Imagers, *Sol. Phys.*, *259*, 297–309, doi:10.1007/s11207-009-9449-z.

Odstrcil, D., J. A. Linker, R. Lionello, Z. Mikic, P. Riley, V. J. Pizzo, and J. G. Luhmann (2002), Merging of coronal and heliospheric numerical two-dimensional MHD models, *Journal of Geophysical Research (Space Physics)*, *107*, 1493, doi:10.1029/2002JA009334.

Odstrcil, D., V. J. Pizzo, J. A. Linker, P. Riley, R. Lionello, and Z. Mikic (2004), Initial coupling of coronal and heliospheric numerical magnetohydrodynamic codes, *Journal of Atmospheric and Solar-Terrestrial Physics*, *66*, 1311–1320, doi:10.1016/j.jastp.2004.04.007.

Odstrcil, D., V. J. Pizzo, and C. N. Arge (2005), Propagation of the 12 May 1997 interplanetary coronal mass ejection in evolving solar wind structures, *Journal of Geophysical Research (Space Physics)*, *110*, A02106, doi:10.1029/2004JA010745.

Odstrčil, D., and V. J. Pizzo (1999), Three-dimensional propagation of CMEs in a structured solar wind flow: 1. CME launched within the streamer belt, *J. Geophys. Res.*, *104*, 483–492, doi:10.1029/1998JA900019.

Ofman, L., and J. M. Davila (1995), Alfvén wave heating of coronal holes and the relation to the high-speed solar wind, *J. Geophys. Res.*, *100*, 23,413–23,426, doi:10.1029/95JA02222.

Olsen, E. L., and E. Leer (1996), An eight-moment approximation two-fluid model of the solar wind, *J. Geophys. Res.*, *101*, 15,591–15,604, doi:10.1029/96JA00687.

Ontiveros, V., and A. Vourlidas (2009), Quantitative Measurements of Coronal Mass Ejection-Driven Shocks from LASCO Observations, *ApJ*, *693*, 267–275, doi:10.1088/0004-637X/693/1/267.

Oran, R., B. van der Holst, E. Landi, M. Jin, I. V. Sokolov, and T. I. Gombosi (2013), A Global Wave-driven Magnetohydrodynamic Solar Model with a Unified Treatment of Open and Closed Magnetic Field Topologies, *ApJ*, *778*, 176, doi:10.1088/0004-637X/778/2/176.

Parker, E. N. (1958), Dynamics of the Interplanetary Gas and Magnetic Fields., *ApJ*, *128*, 664, doi:10.1086/146579.

Parker, E. N. (1983), Magnetic Neutral Sheets in Evolving Fields - Part Two - Formation of the Solar Corona, *ApJ*, *264*, 642–+, doi:10.1086/160637.

Parker, E. N. (1988), Nanoflares and the solar X-ray corona, *ApJ*, *330*, 474–479, doi:10.1086/166485.

Parker, E. N. (1997), Mass Ejection and a Brief History of the Solar Wind Concept, in *Cosmic Winds and the Heliosphere*, edited by J. R. Jokipii, C. P. Sonett, and M. S. Giampapa, p. 3.

Parker, E. N. (2014), Reminiscing my sixty year pursuit of the physics of the Sun and the Galaxy, *Research in Astronomy and Astrophysics*, *14*, 1, doi:10.1088/1674-4527/14/1/001.

Patsourakos, S., and A. Vourlidas (2012), On the Nature and Genesis of EUV Waves: A Synthesis of Observations from SOHO, STEREO, SDO, and Hinode (Invited Review), *Sol. Phys.*, *281*, 187–222, doi:10.1007/s11207-012-9988-6.

Phillips, K. J. H., U. Feldman, and E. Landi (2008), *Ultraviolet and X-ray Spectroscopy of the Solar Atmosphere*, Cambridge University Press.

Pilipp, W. G., K. Muehlhaeuser, H. Miggenrieder, H. Rosenbauer, and R. Schwenn (1990), Large-scale variations of thermal electron parameters in the solar wind between 0.3 and 1 AU, *J. Geophys. Res.*, *95*, 6305–6329, doi:10.1029/JA095iA05p06305.

Pneuman, G. W., and R. A. Kopp (1971), Gas-Magnetic Field Interactions in the Solar Corona, *Sol. Phys.*, *18*, 258–270, doi:10.1007/BF00145940.

Pomoell, J., and R. Vainio (2012), Influence of Solar Wind Heating Formulations on the Properties of Shocks in the Corona, *ApJ*, *745*, 151, doi:10.1088/0004-637X/745/2/151.

Powell, K. G., P. L. Roe, T. J. Linde, T. I. Gombosi, and D. L. de Zeeuw (1999), A Solution-Adaptive Upwind Scheme for Ideal Magnetohydrodynamics, *Journal of Computational Physics*, *154*, 284–309, doi:10.1006/jcph.1999.6299.

Prangé, R., L. Pallier, K. C. Hansen, R. Howard, A. Vourlidas, R. Courtin, and C. Parkinson (2004), An interplanetary shock traced by planetary auroral storms from the Sun to Saturn, *Nature*, *432*, 78–81, doi:10.1038/nature02986.

Priest, E., and T. Forbes (Eds.) (2000), *Magnetic reconnection : MHD theory and applications*.

Priest, E. R. (1982), *Solar magneto-hydrodynamics*, 74P pp.

Priest, E. R. (2014), *Magnetohydrodynamics of the Sun*.

Ramaty, R. (1979), Energetic particles in solar flares, in *Particle Acceleration Mechanisms in Astrophysics*, *American Institute of Physics Conference Series*, vol. 56, edited by J. Arons, C. McKee, and C. Max, pp. 135–154, doi:10.1063/1.32074.

Raymond, J. C., et al. (2000), SOHO and radio observations of a CME shock wave, *Geophys. Res. Lett.*, *27*, 1439–1442, doi:10.1029/1999GL003669.

Reames, D. V. (1999), Particle acceleration at the Sun and in the heliosphere, *Space Sci. Rev.*, *90*, 413–491, doi:10.1023/A:1005105831781.

Richardson, I. G., and H. V. Cane (2004), Identification of interplanetary coronal mass ejections at 1 AU using multiple solar wind plasma composition anomalies, *Journal of Geophysical Research (Space Physics)*, *109*, A09104, doi:10.1029/2004JA010598.

Richardson, J. D., K. I. Paularena, C. Wang, and L. F. Burlaga (2002), The life of a CME and the development of a MIR: From the Sun to 58 AU, *Journal of Geophysical Research (Space Physics)*, *107*, 1041, doi:10.1029/2001JA000175.

Riley, P., J. A. Linker, Z. Mikić, D. Odstrcil, V. J. Pizzo, and D. F. Webb (2002), Evidence of Posteruption Reconnection Associated with Coronal Mass Ejections in the Solar Wind, *ApJ*, *578*, 972–978, doi:10.1086/342608.

Riley, P., J. A. Linker, Z. Mikić, D. Odstrcil, T. H. Zurbuchen, D. Lario, and R. P. Lepping (2003), Using an MHD simulation to interpret the global context of a coronal mass ejection observed by two spacecraft, *Journal of Geophysical Research (Space Physics)*, *108*, 1272, doi:10.1029/2002JA009760.

Riley, P., et al. (2004), Fitting flux ropes to a global MHD solution: a comparison of techniques, *Journal of Atmospheric and Solar-Terrestrial Physics*, *66*, 1321–1331, doi:10.1016/j.jastp.2004.03.019.

Riley, P., C. Schatzman, H. V. Cane, I. G. Richardson, and N. Gopalswamy (2006), On the Rates of Coronal Mass Ejections: Remote Solar and In Situ Observations, *ApJ*, *647*, 648–653, doi:10.1086/505383.

Roelof, E. C., S. M. Krimigis, D. G. Mitchell, R. B. Decker, J. D. Richardson, M. Gruntman, and H. O. Funsten (2010), Implications of Generalized Rankine-Hugoniot Conditions for the PUI Population at the Voyager 2 Termination Shock, in *American Institute of Physics Conference Series*, *American Institute of Physics Conference Series*, vol. 1302, edited by J. Le Roux, G. P. Zank, A. J. Coates, and V. Florinski, pp. 133–141, doi:10.1063/1.3529960.

Roussev, I. I., T. I. Gombosi, I. V. Sokolov, M. Velli, W. Manchester, IV, D. L. DeZeeuw, P. Liewer, G. Tóth, and J. Luhmann (2003a), A Three-dimensional Model of the Solar Wind Incorporating Solar Magnetogram Observations, *ApJ*, *595*, L57–L61, doi:10.1086/378878.

Roussev, I. I., T. G. Forbes, T. I. Gombosi, I. V. Sokolov, D. L. DeZeeuw, and J. Birn (2003b), A Three-dimensional Flux Rope Model for Coronal Mass Ejections Based on a Loss of Equilibrium, *ApJ*, *588*, L45–L48, doi:10.1086/375442.

Roussev, I. I., T. I. Gombosi, I. V. Sokolov, M. Velli, W. Manchester, IV, D. L. DeZeeuw, P. Liewer, G. Tóth, and J. Luhmann (2003c), A Three-dimensional Model of the Solar Wind Incorporating Solar Magnetogram Observations, *ApJ*, *595*, L57–L61, doi:10.1086/378878.

Roussev, I. I., I. V. Sokolov, T. G. Forbes, T. I. Gombosi, M. A. Lee, and J. I. Sakai (2004), A Numerical Model of a Coronal Mass Ejection: Shock Development with Implications for the Acceleration of GeV Protons, *ApJ*, *605*, L73–L76, doi:10.1086/392504.

Ruderman, M. S., V. M. Nakariakov, and B. Roberts (1998), Alfven wave phase mixing in two-dimensional open magnetic configurations., *A&A*, *338*, 1118–1124.

Sandbaek, O., and E. Leer (1995), Coronal Heating and Solar Wind Energy Balance, *ApJ*, *454*, 486, doi:10.1086/176500.

Sanderson, T. R., R. Reinhard, P. van Nes, and K.-P. Wenzel (1985), Observations of three-dimensional anisotropies of 35- to 1000-keV protons associated with interplanetary shocks, *J. Geophys. Res.*, *90*, 19–27, doi:10.1029/JA090iA01p00019.

Schou, J., et al. (2012), Design and Ground Calibration of the Helioseismic and Magnetic Imager (HMI) Instrument on the Solar Dynamics Observatory (SDO), *Sol. Phys.*, *275*, 229–259, doi:10.1007/s11207-011-9842-2.

Schrijver, C. J. (2007), A Characteristic Magnetic Field Pattern Associated with All Major Solar Flares and Its Use in Flare Forecasting, *ApJ*, *655*, L117–L120, doi:10.1086/511857.

Schrijver, C. J., and M. L. De Rosa (2003), Photospheric and heliospheric magnetic fields, *Sol. Phys.*, *212*, 165–200, doi:10.1023/A:1022908504100.

Schrijver, C. J., and G. L. Siscoe (2012), *Heliophysics: Space Storms and Radiation: Causes and Effects*.

Schrijver, C. J., and A. M. Title (2011), Long-range magnetic couplings between solar flares and coronal mass ejections observed by SDO and STEREO, *Journal of Geophysical Research (Space Physics)*, *116*, A04108, doi:10.1029/2010JA016224.

Schrijver, C. J., A. M. Title, A. R. Yeates, and M. L. DeRosa (2013), Pathways of Large-scale Magnetic Couplings between Solar Coronal Events, *ApJ*, *773*, 93, doi:10.1088/0004-637X/773/2/93.

Schwadron, N. A., D. J. McComas, and C. DeForest (2006), Relationship between Solar Wind and Coronal Heating: Scaling Laws from Solar X-Rays, *ApJ*, *642*, 1173–1176, doi:10.1086/501066.

Schwenn, R., et al. (2006), Coronal Observations of CMEs. Report of Working Group A, *Space Sci. Rev.*, *123*, 127–176, doi:10.1007/s11214-006-9016-y.

Seely, J. F., U. Feldman, U. Schuehle, K. Wilhelm, W. Curdt, and P. Lemaire (1997), Turbulent Velocities and Ion Temperatures in the Solar Corona Obtained from SUMER Line Widths, *ApJ*, *484*, L87+, doi:10.1086/310769.

Shiota, D., H. Isobe, P. F. Chen, T. T. Yamamoto, T. Sakajiri, and K. Shibata (2005), Self-Consistent Magnetohydrodynamic Modeling of a Coronal Mass Ejection, Coronal Dimming, and a Giant Cusp-shaped Arcade Formation, *ApJ*, *634*, 663–678, doi:10.1086/496943.

Sime, D. G., and A. J. Hundhausen (1987), The coronal mass ejection of July 6, 1980 - A candidate for interpretation as a coronal shock wave, *J. Geophys. Res.*, *92*, 1049–1055, doi:10.1029/JA092iA02p01049.

Skoug, R. M., J. T. Gosling, J. T. Steinberg, D. J. McComas, C. W. Smith, N. F. Ness, Q. Hu, and L. F. Burlaga (2004), Extremely high speed solar wind: 29-30 October 2003, *Journal of Geophysical Research (Space Physics)*, *109*, A09102, doi:10.1029/2004JA010494.

Smith, C. W., and J. L. Phillips (1997), The role of coronal mass ejections and interplanetary shocks in interplanetary magnetic field statistics and solar magnetic flux ejection, *J. Geophys. Res.*, *102*, 249–262, doi:10.1029/96JA02678.

Smith, E. J. (1979), Interplanetary magnetic fields, *Reviews of Geophysics and Space Physics*, *17*, 610–623, doi:10.1029/RG017i004p00610.

Smith, E. J., M. Neugebauer, A. Balogh, S. J. Bame, R. P. Lepping, and B. T. Tsurutani (1995), ULYSSES Observations of Latitude Gradients in the Heliospheric Magnetic Field: Radial Component and Variances, *Space Sci. Rev.*, *72*, 165–170, doi:10.1007/BF00768773.

Snodgrass, H. B. (1983), Magnetic rotation of the solar photosphere, *ApJ*, *270*, 288–299, doi:10.1086/161121.

Sokolov, I. V., I. I. Roussev, T. I. Gombosi, M. A. Lee, J. Kóta, T. G. Forbes, W. B. Manchester, and J. I. Sakai (2004), A New Field Line Advection Model for Solar Particle Acceleration, *ApJ*, *616*, L171–L174, doi:10.1086/426812.

Sokolov, I. V., I. I. Roussev, L. A. Fisk, M. A. Lee, T. I. Gombosi, and J. I. Sakai (2006), Diffusive Shock Acceleration Theory Revisited, *ApJ*, *642*, L81–L84, doi:10.1086/504406.

Sokolov, I. V., I. I. Roussev, M. Skender, T. I. Gombosi, and A. V. Usmanov (2009), Transport Equation for MHD Turbulence: Application to Particle Acceleration at Interplanetary Shocks, *ApJ*, *696*, 261–267, doi:10.1088/0004-637X/696/1/261.

Sokolov, I. V., B. van der Holst, R. Oran, C. Downs, I. I. Roussev, M. Jin, W. B. Manchester, IV, R. M. Evans, and T. I. Gombosi (2013), Magnetohydrodynamic Waves and Coronal Heating: Unifying Empirical and MHD Turbulence Models, *ApJ*, *764*, 23, doi:10.1088/0004-637X/764/1/23.

Sonett, C. P., D. S. Colburn, L. Davis, E. J. Smith, and P. J. Coleman (1964), Evidence for a Collision-Free Magnetohydrodynamic Shock in Interplanetary Space, *Physical Review Letters*, *13*, 153–156, doi:10.1103/PhysRevLett.13.153.

Spitzer, L. (1962), *Physics of Fully Ionized Gases*.

St. Cyr, O. C., J. T. Burkepile, A. J. Hundhausen, and A. R. Lecinski (1999), A comparison of ground-based and spacecraft observations of coronal mass ejections from 1980-1989, *J. Geophys. Res.*, *104*, 12,493–12,506, doi:10.1029/1999JA900045.

Stawarz, J. E., C. W. Smith, B. J. Vasquez, M. A. Forman, and B. T. MacBride (2009), The Turbulent Cascade and Proton Heating in the Solar Wind at 1 AU, *ApJ*, *697*, 1119–1127, doi:10.1088/0004-637X/697/2/1119.

Stone, E. C., A. M. Frandsen, R. A. Mewaldt, E. R. Christian, D. Margolies, J. F. Ormes, and F. Snow (1998), The Advanced Composition Explorer, *Space Sci. Rev.*, *86*, 1–22, doi:10.1023/A:1005082526237.

Sturrock, P. A. (1991), Maximum energy of semi-infinite magnetic field configurations, *ApJ*, *380*, 655–659, doi:10.1086/170620.

Sun, X., Y. Liu, J. T. Hoeksema, K. Hayashi, and X. Zhao (2011), A New Method for Polar Field Interpolation, *Sol. Phys.*, *270*, 9–22, doi:10.1007/s11207-011-9751-4.

Suresh, A., and H. T. Huynh (1997), Accurate Monotonicity-Preserving Schemes with Runge Kutta Time Stepping, *Journal of Computational Physics*, *136*, 83–99, doi:10.1006/jcph.1997.5745.

Suzuki, T. K. (2006), Forecasting Solar Wind Speeds, *ApJ*, *640*, L75–L78, doi:10.1086/503102.

Temmer, M., et al. (2012), Characteristics of Kinematics of a Coronal Mass Ejection during the 2010 August 1 CME-CME Interaction Event, *ApJ*, *749*, 57, doi: 10.1088/0004-637X/749/1/57.

Thompson, B. J., S. P. Plunkett, J. B. Gurman, J. S. Newmark, O. C. St. Cyr, and D. J. Michels (1998), SOHO/EIT observations of an Earth-directed coronal mass ejection on May 12, 1997, *Geophys. Res. Lett.*, *25*, 2465–2468, doi: 10.1029/98GL50429.

Thompson, B. J., et al. (1999), SOHO/EIT Observations of the 1997 April 7 Coronal Transient: Possible Evidence of Coronal Moreton Waves, *ApJ*, *517*, L151–L154, doi:10.1086/312030.

Titov, D. V., et al. (2006), Venus Express science planning, *Planet. Space Sci.*, *54*, 1279–1297, doi:10.1016/j.pss.2006.04.017.

Titov, V. S., and P. Démoulin (1999), Basic topology of twisted magnetic configurations in solar flares, *A&A*, *351*, 707–720.

Titov, V. S., Z. Mikic, T. Török, J. A. Linker, and O. Panasenco (2012), 2010 August 1-2 Sympathetic Eruptions. I. Magnetic Topology of the Source-surface Background Field, *ApJ*, *759*, 70, doi:10.1088/0004-637X/759/1/70.

Tomczyk, S., S. W. McIntosh, S. L. Keil, P. G. Judge, T. Schad, D. H. Seeley, and J. Edmondson (2007), Alfvén Waves in the Solar Corona, *Science*, *317*, 1192–, doi:10.1126/science.1143304.

Török, T., O. Panasenco, V. S. Titov, Z. Mikić, K. K. Reeves, M. Velli, J. A. Linker, and G. De Toma (2011), A Model for Magnetically Coupled Sympathetic Eruptions, *ApJ*, *739*, L63, doi:10.1088/2041-8205/739/2/L63.

Tóth, G., et al. (2005), Space Weather Modeling Framework: A new tool for the space science community, *Journal of Geophysical Research (Space Physics)*, *110*, 12,226–+, doi:10.1029/2005JA011126.

Tóth, G., D. L. de Zeeuw, T. I. Gombosi, W. B. Manchester, A. J. Ridley, I. V. Sokolov, and I. I. Roussev (2007), Sun-to-thermosphere simulation of the 28-30 October 2003 storm with the Space Weather Modeling Framework, *Space Weather*, *5*, 06003, doi:10.1029/2006SW000272.

Tóth, G., B. van der Holst, and Z. Huang (2011a), Obtaining Potential Field Solutions with Spherical Harmonics and Finite Differences, *ApJ*, *732*, 102–+, doi: 10.1088/0004-637X/732/2/102.

Tóth, G., B. van der Holst, and Z. Huang (2011b), Obtaining Potential Field Solutions with Spherical Harmonics and Finite Differences, *ApJ*, *732*, 102, doi:10.1088/0004-637X/732/2/102.

Tóth, G., et al. (2012), Adaptive numerical algorithms in space weather modeling, *Journal of Computational Physics*, *231*, 870–903, doi:10.1016/j.jcp.2011.02.006.

Tousey, R., J. D. F. Bartoe, J. D. Bohlin, G. E. Brueckner, J. D. Purcell, V. E. Scherrer, N. R. Sheeley, Jr., R. J. Schumacher, and M. E. Vanhoosier (1973), A Preliminary Study of the Extreme Ultraviolet Spectroheliograms from Skylab, *Sol. Phys.*, *33*, 265–280, doi:10.1007/BF00152418.

Tu, C., and E. Marsch (1997), Two-Fluid Model for Heating of the Solar Corona and Acceleration of the Solar Wind by High-Frequency Alfven Waves, *Sol. Phys.*, *171*, 363–391.

Tu, C.-Y., E. Marsch, K. Wilhelm, and W. Curdt (1998), Ion Temperatures in a Solar Polar Coronal Hole Observed by SUMER on SOHO, *ApJ*, *503*, 475–+, doi:10.1086/305982.

Tu, C.-Y., C. Zhou, E. Marsch, L.-D. Xia, L. Zhao, J.-X. Wang, and K. Wilhelm (2005), Solar Wind Origin in Coronal Funnels, *Science*, *308*, 519–523, doi:10.1126/science.1109447.

Tylka, A. J., and M. A. Lee (2006), A Model for Spectral and Compositional Variability at High Energies in Large, Gradual Solar Particle Events, *ApJ*, *646*, 1319–1334, doi:10.1086/505106.

Tylka, A. J., C. M. S. Cohen, W. F. Dietrich, M. A. Lee, C. G. Maclennan, R. A. Mewaldt, C. K. Ng, and D. V. Reames (2005), Shock Geometry, Seed Populations, and the Origin of Variable Elemental Composition at High Energies in Large Gradual Solar Particle Events, *ApJ*, *625*, 474–495, doi:10.1086/429384.

Upton, L., and D. H. Hathaway (2014), Predicting the Sun's Polar Magnetic Fields with a Surface Flux Transport Model, *ApJ*, *780*, 5, doi:10.1088/0004-637X/780/1/5.

Usmanov, A. V. (1993), A global numerical 3-D MHD model of the solar wind, *Sol. Phys.*, *146*, 377–396, doi:10.1007/BF00662021.

Usmanov, A. V., and M. Dryer (1995), A Global 3-D Simulation of Interplanetary Dynamics in June 1991, *Sol. Phys.*, *159*, 347–370, doi:10.1007/BF00686537.

Usmanov, A. V., M. L. Goldstein, B. P. Besser, and J. M. Fritzer (2000), A global MHD solar wind model with WKB Alfvén waves: Comparison with Ulysses data, *J. Geophys. Res.*, *105*, 12,675–12,696, doi:10.1029/1999JA000233.

Usmanov, A. V., W. H. Matthaeus, B. A. Breech, and M. L. Goldstein (2011), Solar Wind Modeling with Turbulence Transport and Heating, *ApJ*, *727*, 84–+, doi:10.1088/0004-637X/727/2/84.

Vainio, R., T. Laitinen, and H. Fichtner (2003), A simple analytical expression for the power spectrum of cascading Alfvén waves in the solar wind, *A&A*, *407*, 713–723, doi:10.1051/0004-6361:20030914.

van der Holst, B., W. Manchester, IV, I. V. Sokolov, G. Tóth, T. I. Gombosi, D. DeZeeuw, and O. Cohen (2009), Breakout Coronal Mass Ejection or Streamer Blowout: The Bugle Effect, *ApJ*, *693*, 1178, doi:10.1088/0004-637X/693/2/1178.

van der Holst, B., W. B. Manchester, R. A. Frazin, A. M. Vásquez, G. Tóth, and T. I. Gombosi (2010), A Data-driven, Two-temperature Solar Wind Model with Alfvén Waves, *ApJ*, *725*, 1373–1383, doi:10.1088/0004-637X/725/1/1373.

van der Holst, B., et al. (2011), CRASH: A Block-adaptive-mesh Code for Radiative Shock Hydrodynamics – Implementation and Verification, *ApJS*, *194*, 23, doi:10.1088/0067-0049/194/2/23.

van der Holst, B., I. V. Sokolov, X. Meng, M. Jin, W. B. Manchester, IV, G. Tóth, and T. I. Gombosi (2014), Alfvén Wave Solar Model (AWSoM): Coronal Heating, *ApJ*, *782*, 81, doi:10.1088/0004-637X/782/2/81.

Van Doorsselaere, T., N. Wardle, G. Del Zanna, K. Jansari, E. Verwichte, and V. M. Nakariakov (2011), The First Measurement of the Adiabatic Index in the Solar Corona Using Time-dependent Spectroscopy of Hinode/EIS Observations, *ApJ*, *727*, L32+, doi:10.1088/2041-8205/727/2/L32.

Vásquez, A. M., A. A. van Ballegooijen, and J. C. Raymond (2003), The Effect of Proton Temperature Anisotropy on the Solar Minimum Corona and Wind, *ApJ*, *598*, 1361–1374, doi:10.1086/379008.

Vásquez, A. M., R. A. Frazin, and W. B. Manchester (2010), The Solar Minimum Corona from Differential Emission Measure Tomography, *ApJ*, *715*, 1352–1365, doi:10.1088/0004-637X/715/2/1352.

Verdini, A., M. Velli, W. H. Matthaeus, S. Oughton, and P. Dmitruk (2010), A Turbulence-Driven Model for Heating and Acceleration of the Fast Wind in Coronal Holes, *ApJ*, *708*, L116–L120, doi:10.1088/2041-8205/708/2/L116.

Vourlidas, A., and R. A. Howard (2006), The Proper Treatment of Coronal Mass Ejection Brightness: A New Methodology and Implications for Observations, *ApJ*, *642*, 1216–1221, doi:10.1086/501122.

Vourlidas, A., and V. Ontiveros (2009), A Review of Coronagraphic Observations of Shocks Driven by Coronal Mass Ejections, in *American Institute of Physics Conference Series*, *American Institute of Physics Conference Series*, vol. 1183, edited by X. Ao and G. Z. R. Burrows, pp. 139–146, doi:10.1063/1.3266770.

Vourlidas, A., S. T. Wu, A. H. Wang, P. Subramanian, and R. A. Howard (2003), Direct Detection of a Coronal Mass Ejection-Associated Shock in Large Angle and

Spectrometric Coronagraph Experiment White-Light Images, *ApJ*, *598*, 1392–1402, doi:10.1086/379098.

Wang, Y., C. Chen, B. Gui, C. Shen, P. Ye, and S. Wang (2011), Statistical study of coronal mass ejection source locations: Understanding CMEs viewed in coronagraphs, *Journal of Geophysical Research (Space Physics)*, *116*, A04104, doi: 10.1029/2010JA016101.

Wang, Y.-M., N. R. Sheeley, Jr., and A. G. Nash (1990), Latitudinal distribution of solar-wind speed from magnetic observations of the sun, *Nature*, *347*, 439–444, doi:10.1038/347439a0.

Watanabe, T., H. Hara, N. Yamamoto, D. Kato, H. A. Sakaue, I. Murakami, T. Kato, N. Nakamura, and P. R. Young (2009), Fe XIII Density Diagnostics in the EIS Observing Wavelengths, *ApJ*, *692*, 1294–1304, doi:10.1088/0004-637X/692/2/1294.

Welsch, B. T., G. H. Fisher, W. P. Abbett, and S. Regnier (2004), ILCT: Recovering Photospheric Velocities from Magnetograms by Combining the Induction Equation with Local Correlation Tracking, *ApJ*, *610*, 1148–1156, doi:10.1086/421767.

Whang, Y. C., L. F. Burlaga, N. F. Ness, and C. W. Smith (2001), The Bastille day Shocks and Merged Interaction Region, *Sol. Phys.*, *204*, 253–263, doi: 10.1023/A:1014221210800.

Wild, J. P., and S. F. Smerd (1972), Radio Bursts from the Solar Corona, *ARA&A*, *10*, 159, doi:10.1146/annurev.aa.10.090172.001111.

Wood, B. E., C.-C. Wu, A. P. Rouillard, R. A. Howard, and D. G. Socker (2012), A Coronal Hole's Effects on Coronal Mass Ejection Shock Morphology in the Inner Heliosphere, *ApJ*, *755*, 43, doi:10.1088/0004-637X/755/1/43.

Worden, J., and J. Harvey (2000), An Evolving Synoptic Magnetic Flux map and Implications for the Distribution of Photospheric Magnetic Flux, *Sol. Phys.*, *195*, 247–268, doi:10.1023/A:1005272502885.

Wu, C.-C., C. D. Fry, M. Dryer, S. T. Wu, B. Thompson, K. Liou, and X. S. Feng (2007a), Three-dimensional global simulation of multiple ICMEs interaction and propagation from the Sun to the heliosphere following the 25 28 October 2003 solar events, *Advances in Space Research*, *40*, 1827–1834, doi:10.1016/j.asr.2007.06.025.

Wu, C.-C., C. D. Fry, S. T. Wu, M. Dryer, and K. Liou (2007b), Three-dimensional global simulation of interplanetary coronal mass ejection propagation from the Sun to the heliosphere: Solar event of 12 May 1997, *Journal of Geophysical Research (Space Physics)*, *112*, A09104, doi:10.1029/2006JA012211.

Wu, S. T., W. P. Guo, D. J. Michels, and L. F. Burlaga (1999), MHD description of the dynamical relationships between a flux rope, streamer, coronal mass ejection, and magnetic cloud: An analysis of the January 1997 Sun-Earth connection event, *J. Geophys. Res.*, *104*, 14,789–14,802, doi:10.1029/1999JA900099.

Xie, H., L. Ofman, and G. Lawrence (2004), Cone model for halo CMEs: Application to space weather forecasting, *Journal of Geophysical Research (Space Physics)*, *109*, A03109, doi:10.1029/2003JA010226.

Yashiro, S., G. Michalek, S. Akiyama, N. Gopalswamy, and R. A. Howard (2008), Spatial Relationship between Solar Flares and Coronal Mass Ejections, *ApJ*, *673*, 1174–1180, doi:10.1086/524927.

Young, P. R., T. Watanabe, H. Hara, and J. T. Mariska (2009), High-precision density measurements in the solar corona. I. Analysis methods and results for Fe XII and Fe XIII, *A&A*, *495*, 587–606, doi:10.1051/0004-6361:200810143.

Zel'dovich, Y. B., and Y. P. Raizer (1967), *Physics of shock waves and high-temperature hydrodynamic phenomena*.

Zhang, T. L., et al. (2008), Induced magnetosphere and its outer boundary at Venus, *Journal of Geophysical Research (Planets)*, *113*, E00B20, doi: 10.1029/2008JE003215.

Zhao, J. (2007), Time-Distance Imaging of Solar Far-Side Active Regions, *ApJ*, *664*, L139–L142, doi:10.1086/520837.

Zhao, X. (1992), Interaction of fast steady flow with slow transient flow - A new cause of shock pair and interplanetary B(z) event, *J. Geophys. Res.*, *97*, 15,051, doi:10.1029/92JA01535.

Zhao, X. P., S. P. Plunkett, and W. Liu (2002), Determination of geometrical and kinematical properties of halo coronal mass ejections using the cone model, *Journal of Geophysical Research (Space Physics)*, *107*, 1223, doi:10.1029/2001JA009143.